

PROGRAMA DE DOCTORADO EN INFORMÁTICA

TESIS DOCTORAL

Contribuciones a la gestión óptima de recursos en aplicaciones solares térmicas: CSP y desalación

PhD THESIS

Towards optimal resource management in solar thermal applications: CSP and desalination



Escuela Internacional de
DOCTORADO
Universidad de Almería



UNIVERSIDAD
DE ALMERÍA

AUTOR / AUTORA

JUAN MIGUEL SERRANO RODRÍGUEZ

DIRECTOR / A / ES / AS

LIDIA ROCA SOBRINO

PATRICIA PALENZUELA ARDILA

UNIVERSIDAD DE ALMERÍA

Escuela Internacional de Doctorado de la Universidad de Almería

Almería, 2025

Normal: ω

Bold: $\mathbf{\omega}$

 WORK IN PROGRESS   

Esta sección no está terminada. Siquieres puedes echarle un ojo para ver la estructura y cómo encaja con el resto pero no merece la pena revisarla en detalle en el estado actual.

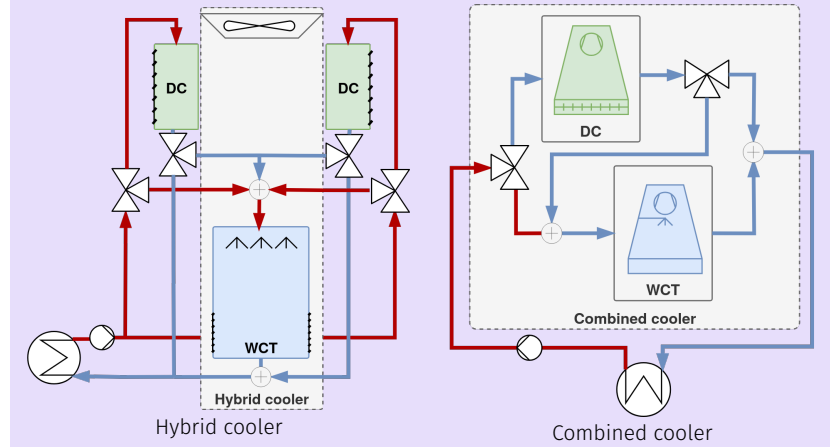
Additional text to add

Kaobox with custom color

What is thiiis

1. Enumerations
2. should
3. be
4. okay

Even fancy figures™.



Hello, here is some text without a meaning. This text should show what a printed text will look like at this place. If you read this text, you will get no information. Really? Is there no information? Is there a difference between this text and some nonsense like "Huardest gefburn"? Kjift – not at all! A blind text like this gives you information about the selected font, how the letters are written and an impression of the look. This text should contain all letters of the alphabet and it should be written in of the original language. There is no need for special content, but the length of words should match the language. Hello, here is some text without a meaning. This text should show what a printed text will look like at this place. If you read this text, you will get no information. Really? Is there no information? Is there a difference between this text and some nonsense like "Huardest gefburn"? Kjift – not at all! A blind text like this gives you information about the selected font, how the letters are written and an impression of the look. This text should contain all letters of the alphabet and it should be written in of the original language. There is no need for special content, but the length of words should match the language.

Model 0.1: Test

$T_{cc,out}, C_e, C_w, T_{c,out} = \text{combined cooler model}(q_c, R_p, R_s, \omega_{dc}, \omega_{wct}, T_{amb}, HR_i, T_v, \dot{m}_v)$

$$T_{cc,in} = T_{c,out}$$

$$T_{dc,in} = T_{cc,in}$$

$$q_{dc} = q_c \cdot (1 - R_p)$$

$$q_{wct,p} = q_c \cdot R_p$$

$$q_{wct,s} = q_{dc} \cdot R_s$$

$$T_{dc,out}, C_{e,dc} = \text{dc model}(q_{dc}, \omega_{dc}, T_{amb}, T_{dc,in})$$

$$q_{wct}, T_{wct,in} = \text{mixer model}(q_{wct,p}, T_{cc,in}, q_{wct,s}, T_{dc,out})$$

As can be seen in Model 0.1, the counter is working. As can be seen in Problem 0.1, the counter is working.

Problem 0.1: Test

Hello, here is some text without a meaning. This text should show what a printed text will look like at this place. If you read this text, you will get no information. Really? Is there no information? Is there a difference between this text and some nonsense like "Huardest gefburn"? Kjift – not at all! A blind text like this gives you information about the selected font, how the letters are written and an impression of the look. This text should contain all letters of the alphabet and it should be written in of the original language. There is no need for special content, but the length of words should match the language.

$$\min_{\mathbf{x}, \mathbf{e}; \boldsymbol{\theta}} J = f(\mathbf{x}, \mathbf{e}; \boldsymbol{\theta}) = f(\mathbf{x})$$

with:

- Model name model

$$out_1, out_2 = f(in_1, in_2, \dots, in_N)$$

- Decision variables

$$\mathbf{x} = [x_1, x_2]$$

- Environment variables

$$\mathbf{e} = [e_1, e_2, \dots, e_3]$$

- Fixed parameters

$$\boldsymbol{\theta} = [\theta_1 = X, \theta_2 = Y]$$

subject to:

- Box-bounds

$$\begin{aligned} \cdot x_1 &\in [\underline{x}_1, \bar{x}_1] \\ \cdot x_2 &\in [\underline{x}_2, \bar{x}_2] \end{aligned}$$

- Constraints

$$\begin{aligned} \cdot |out_x - out_y| &\leq \epsilon_1 \\ \cdot out_x &\leq out_z - \Delta Z \end{aligned}$$

Hello, here is some text without a meaning. This text should show what a printed text will look like at this place. If you read this text, you will get no information. Really? Is there no information? Is there a difference between this text and some nonsense like “Huardest gefburn”? Kjift – not at all! A blind text like this gives you information about the selected font, how the letters are written and an impression of the look. This text should contain all letters of the alphabet and it should be written in of the original language. There is no need for special content, but the length of words should match the language.

TL;DR

Too Long Didn't Read (TL;DR) boxes are defined with the `tldrbox` command. They are equivalent to abstracts or summaries and are placed at the beginning of sections or chapters.

Title of the annotation

Is everything in this life just a wrapped kaobox? What if I told you that a kaobox is just a wrapper of tcolorbox?

Definition 0.0.1 Let (X, d) be a metric space. A subset $U \subset X$ is an open set if, for any $x \in U$ there exists $r > 0$ such that $B(x, r) \subset U$. We call the topology associated to d the set τ_d of all the open subsets of (X, d) .

Remark 0.0.1 Let (X, d) be a metric space. A subset $U \subset X$ is an open set if, for any $x \in U$ there exists $r > 0$ such that $B(x, r) \subset U$. We call the topology associated to d the set τ_d of all the open subsets of (X, d) .

Towards optimal resource management in solar thermal applications

PhD Thesis

**Towards optimal resource management in solar thermal applications:
CSP and desalination**

Juan Miguel Serrano Rodríguez

October 28, 2025

University of Almería

Some rights reserved

 This work is available under the Creative Commons Attribution 3.0 IGO license (CC BY 3.0 IGO) <http://creativecommons.org/licenses/by/3.0/igo>. Under the Creative Commons Attribution license, you are free to copy, distribute, transmit, and adapt this work, including for commercial purposes, under the following conditions:

- ▶ Attribution—Please cite the work as follows: Serrano Juan Miguel, Roca Lidia , Palenzuela Patricia. October 28, 2025. Towards optimal resource management in solar thermal applications: CSP and desalination DOI: [10.1596/XXX](https://doi.org/10.1596/XXX). License: Creative Commons Attribution CC BY 3.0 IGO
- ▶ Translations—if you create a translation of this work, please add the following disclaimer along with the attribution: This translation was not created by Serrano J.M and should not be considered an official Serrano J.M translation. Serrano J.M shall not be liable for any content or error in this translation.
- ▶ Adaptations—if you create an adaptation of this work, please add the following disclaimer along with the attribution: This is an adaptation of an original work by Serrano J.M. Views and opinions expressed in the adaptation are the sole responsibility of the author or authors of the adaptation and are not endorsed by Serrano J.M.
- ▶ Third-party content—Serrano J.M does not necessarily own each component of the content contained within the work. Serrano J.M therefore does not warrant that the use of any third-party-owned individual component or part contained in the work will not infringe on the rights of those third parties. The risk of claims resulting from such infringement rests solely with you. If you wish to re-use a component of the work, it is your responsibility to determine whether permission is needed for that re-use and to obtain permission from the copyright owner. Examples of components can include, but are not limited to, tables, figures, or images.

Available at

DOI: [10.1596/XXX](https://doi.org/10.1596/XXX)

Main repository: <https://github.com/juan11iguel/my-thesis/blob/main>

Mirror repository: <https://github.com/juan11iguel/my-thesis>

Colophon

This document was typeset with the help of KOMA-Script and \TeX using the kaobook class.
The source code of this book class is available at: <https://github.com/fmarotta/kaobook>

Publisher

First printed in October 28, 2025 by University of Almería

The harmony of the world is made manifest in Form and Number, and the heart and soul and all the poetry of Natural Philosophy are embodied in the concept of mathematical beauty.

– D'Arcy Wentworth Thompson

Acknowledgements

Test test test

Juanmi

Preface

The present manuscript is the result of a PhD thesis research work carried out at the Plataforma Solar de Almería, Spain, under the supervision of Dr. Lidia Roca and Dr. Patricia Palenzuela and is ascribed to the Computer Science Doctorate Program at the University of Almería. The research was funded by a scholarship from CIEMAT, a public research organization attached to the Ministry of Science, Innovation and Universities.

The research work was developed within the framework of several national and international research projects, including the European Union's Horizon 2020 research and innovation programme *SFERA-III – Solar Facilities for the European Research Area* (823802) and *Water Mining – Next generation water-smart management systems* (869474), as well as the national project *SOLhycool – Hybrid cooling solutions for water saving in solar thermal applications* (PID2021-126452OA-I00).

Different parts of the research work to be presented in the following, were developed during international stays. In a combined short-stay at the Cyprus Institute (Nicosia, Cyprus - 2023) and attendance to the EDS conference in Limassol, it was matured and presented the initial *Proposal for a standard methodology for performance evaluation in multi-effect distillation processes* under the supervision of Dr. Marios Georgiou (EEWRC). A year later (February – June 2024), the main research stay at the Universidade Federal de Santa Catarina (UFSC), in Florianópolis (Brazil) took place under the supervision of Dr. Julio E. Normey-Rico. There it was completed the *Hybrid model of a solar desalination system, composed of finite state machines coupled to data-driven and first-principles models*. Finally, at the end of the contractual relationship with CIEMAT, in 2025, a one-month stay at the Technische Universität Chemnitz financed by the Erasmus program served to advance the work in *Evaluation and comparison of annual simulations of different cooling alternatives for a case study CSP plant* which would culminate with its presentation at the SolarPACES conference in September 2025.

This manuscript has been prepared with an intention of making it accessible to a non-expert audience, however, it is primarily aimed at researchers and professionals in the fields of renewable energy and water treatment, with the technical parts of the document delving into thermodynamic, mathematical modelling and optimization concepts. The content is structured to provide a comprehensive understanding of the topics discussed, while also being approachable for those who may not have a deep technical background in these areas.

The text is divided into four parts where each contains a number of chapters.

PART ONE introduces the context and motivation of the thesis, the research plan, including the main contributions of this research work, and ends with an introduction of the main research topics used to develop this research work. This introductory part is then followed by two parts with the main contributions, where each part is a complete unit: it describes the problem, presents the proposed solutions and analyses the obtained results.

PART Two is devoted to the cooling of the power block in Concentrated Solar Power (CSP) plants, with a focus on the optimal management of the water resource through the modelling and optimization of alternative combined cooling systems. The work also includes the experimental validation of the proposed solution in a pilot plant.

PART THREE centers around thermal desalination processes, particularly multi-effect distillation. First by analyzing the separation process from a thermodynamic and qualitative perspective in order to standardize its evaluation and later in the part, the process is integrated with a variable energy source: solar thermal energy and its operation is modelled and optimized to manage the solar resource, maximizing fresh water generation and advancing the state of research in this area.

PART FOUR completes the manuscript with a recapitulation of the main conclusions and findings, as well as a discussion on potential future research directions in the studied topics and presents the derived scientific contributions.

Summary

Concentrated Solar Power (CSP) is poised to be a crucial contributor to the energy transition away from fossil fuels. The first phase of this transition is well underway, driven by the massive deployment of low-cost and non-dispatchable renewable technologies such as wind and solar photovoltaics. However, the second and more challenging phase, which involves achieving large-scale dispatchable renewable generation, is still ahead. CSP stands out as a renewable and scalable dispatchable technology with the potential to outcompete combined-cycle and coal-fired power plants.

One of the key challenges in CSP systems lies in cooling the power block, which is typically associated with high water consumption. The first part of this research is therefore dedicated to the efficient management of water resources in CSP plants. An optimal water management strategy is proposed for CSP systems that integrate novel combined cooling configurations. To this end, the annual performance of different cooling alternatives is evaluated for a commercial 50 MW_e CSP plant, Andasol-II, located in southern Spain. Specifically, three cooling systems, all modelled and validated, are compared: the plant's existing Wet Cooling Tower (WCT), and two variants of a novel Combined Cooler (CC) system with dry cooler capacities of 75 % and 100 % of the nominal thermal load of the WCT system.

For each alternative, plant operation is optimized under the same water-scarcity scenario using a proposed multi-stage optimization framework. This framework minimizes the daily cooling cost, which includes both electricity and water expenses, while ensuring that the cooling demand is satisfied. The key challenge lies in effectively managing the limited water resource. Results show that integrating the CC can reduce specific cooling costs by up to 80 % and annual water consumption by about 48 %, with 38 % savings during the driest months. These benefits arise primarily from reduced reliance on costly alternative water sources. The CC alternatives also provide more stable and cost-effective operation throughout the year compared to the WCT, which is highly sensitive to water availability.

Thermal desalination, particularly Multi-Effect Distillation (MED), can play an important role in mitigating water scarcity. Although it may not become the dominant desalination technology, it is well suited for specific applications. Its competitiveness can be improved by leveraging opportunities such as brine mining or industrial wastewater treatment, which enhance both economic feasibility and environmental benefits. MED systems use thermal and electrical energy to separate seawater or contaminated feedwater into fresh water and concentrated brine.

To expand their applicability, MED systems must improve in two directions: (i) by enhancing efficiency through wider operating ranges, or (ii) by adapting to low-temperature applications in which their heat demands can be partially or fully met using low-exergy sources such as waste heat or solar thermal energy. However, the true cost of thermal energy, and consequently the performance of such systems, is often difficult to quantify.

To address this challenge, this research proposes a standardized methodology for evaluating the performance of MED processes, which can also be extended to other thermal separation technologies. The method covers key aspects such as instrumentation requirements, process control, and the suitability of performance metrics. It also includes uncertainty quantification and an algorithm for automatic steady-state detection. The proposed approach enhances the reliability and robustness of experimental evaluations under variable conditions. Experimental results confirm that the methodology is both reliable and consistent, enabling fair comparisons of MED systems across different operating scenarios.

The experimental campaign includes evaluations at high Top Brine Temperatures (TBTs). Results analyzed using several performance metrics and scale formation risks demonstrate that the MED process can operate at high TBTs without significant scaling and can achieve higher concentrations. However, no substantial improvements in thermal performance or reconcentration capacity are observed unless specific design modifications are introduced.

Finally, a novel operational strategy is proposed to enable the seamless, autonomous, and optimal integration of a solar-driven MED system. The method explicitly determines when to start and stop each subsystem while considering a two-day prediction horizon. This allows the optimization to account not only for immediate performance but also for the effect of present decisions on future production. The approach is based on an experimentally validated system model that includes the electrical consumption of each component, combined with the most comprehensive data-driven MED model currently available in the literature. The control architecture follows a hierarchical three-layer structure, in which the upper operational layer solves a Mixed Integer Non-Linear Programming problem aimed at maximizing water production while minimizing operating costs. Results from a week-long system simulation are compared with two alternative strategies, a baseline operation and a fixed-schedule optimized operation. The proposed method

significantly increases water production by XX %, fully leveraging the solar resource and thermal storage capacity while accounting for primary operational costs.

This research encompasses two complementary studies on two intrinsically linked resources: water and energy. The first part focuses on the efficient management of water resources for power generation, while the second explores the efficient use of solar energy for clean water production.

Resumen

La Energía Solar de Concentración (CSP) está destinada a ser un contribuyente crucial en la transición energética hacia el abandono de los combustibles fósiles. La primera fase de esta transición está bien encaminada, impulsada por el despliegue masivo de tecnologías renovables de bajo costo y no gestionables, como la eólica y la solar fotovoltaica. Sin embargo, la segunda y más desafiante fase, que implica lograr una generación renovable gestionable a gran escala, aún está por venir. La CSP se destaca como una tecnología renovable y escalable con capacidad gestionable y el potencial de superar a las plantas de ciclo combinado y de carbón.

Uno de los principales desafíos en los sistemas CSP radica en la refrigeración del bloque de potencia, la cual suele asociarse con un alto consumo de agua. Por ello, la primera parte de esta investigación se dedica a la gestión eficiente de los recursos hídricos en plantas CSP. Se propone una estrategia óptima de gestión del agua para sistemas CSP que integran configuraciones de refrigeración combinada novedosas. Con este fin, se evalúa el rendimiento anual de diferentes alternativas de refrigeración para una planta comercial de 50 MW_e CSP, Andasol-II, ubicada en el sur de España. En concreto, se comparan tres sistemas de refrigeración, todos ellos modelados y validados: la WCT existente de la planta, y dos variantes de un novedoso sistema CC con capacidades de enfriador seco del 75 % y del 100 % de la carga térmica nominal del sistema WCT.

Para cada alternativa, la operación de la planta se optimiza bajo el mismo escenario de escasez de agua utilizando un marco de optimización multi-etapa propuesto. Este marco minimiza el costo diario de refrigeración, que incluye los gastos de electricidad y agua, garantizando al mismo tiempo que se satisfaga la demanda de refrigeración. El desafío clave radica en gestionar eficazmente el recurso hídrico limitado. Los resultados muestran que la integración del CC puede reducir los costos específicos de refrigeración hasta en un 80 % y el consumo anual de agua en alrededor del 48 %, con un ahorro del 38 % durante los meses más secos. Estos beneficios surgen principalmente de la menor dependencia de fuentes de agua alternativas y costosas. Las alternativas CC también ofrecen una operación más estable y rentable a lo largo del año en comparación con la WCT, que es altamente sensible a la disponibilidad de agua.

La desalación térmica, en particular la Destilación Multiefecto (MED), puede desempeñar un papel importante en la mitigación de la escasez de agua. Aunque puede que no llegue a ser la tecnología de desalación dominante, es muy adecuada para aplicaciones específicas. Su competitividad puede mejorarse aprovechando oportunidades como la minería de salmuera o el tratamiento de aguas residuales industriales, que mejoran tanto la viabilidad económica como los beneficios ambientales. Los sistemas MED utilizan energía térmica y eléctrica para separar agua de mar o agua contaminada en agua dulce y salmuera concentrada.

Para ampliar su aplicabilidad, los sistemas MED deben mejorar en dos direcciones: (i) aumentando su eficiencia mediante rangos de operación más amplios, o (ii) adaptándose a aplicaciones de baja temperatura en las que sus demandas térmicas puedan satisfacerse parcial o totalmente mediante fuentes de baja energía, como el calor residual o la energía solar térmica. Sin embargo, el costo real de la energía térmica, y por tanto el rendimiento de estos sistemas, a menudo es difícil de cuantificar.

Para abordar este desafío, esta investigación propone una metodología estandarizada para evaluar el rendimiento de los procesos MED, la cual también puede extenderse a otras tecnologías de separación térmica. El método abarca aspectos clave como los requisitos de instrumentación, el control del proceso y la idoneidad de las métricas de rendimiento. También incluye la cuantificación de incertidumbre y un algoritmo para la detección automática del estado estacionario. El enfoque propuesto mejora la fiabilidad y la robustez de las evaluaciones experimentales bajo condiciones variables. Los resultados experimentales confirman que la metodología es confiable y consistente, lo que permite comparaciones justas entre sistemas MED bajo diferentes escenarios operativos.

La campaña experimental incluye evaluaciones a altas TBTs. Los resultados, analizados mediante diversas métricas de rendimiento y riesgos de formación de incrustaciones, demuestran que el proceso MED puede operar a altas TBTs sin incrustaciones significativas y puede alcanzar mayores concentraciones. Sin embargo, no se observan mejoras sustanciales en el rendimiento térmico o la capacidad de reconcentración, a menos que se introduzcan modificaciones específicas en el diseño.

Finalmente, se propone una estrategia operativa novedosa que permite la integración fluida, autónoma y óptima de un sistema MED impulsado por energía solar. El método determina explícitamente cuándo iniciar y detener cada subsistema, considerando un horizonte de predicción de dos días. Esto permite que la optimización tenga en cuenta

no solo el rendimiento inmediato, sino también el efecto de las decisiones presentes sobre la producción futura. El enfoque se basa en un modelo del sistema validado experimentalmente que incluye el consumo eléctrico de cada componente, combinado con el modelo MED basado en datos más completo disponible actualmente en la literatura. La arquitectura de control sigue una estructura jerárquica de tres niveles, en la que la capa operativa superior resuelve un problema Mixed Integer Non-Linear Programming destinado a maximizar la producción de agua mientras se minimizan los costos operativos. Los resultados de una simulación del sistema durante una semana se comparan con dos estrategias alternativas: una operación base y una operación optimizada con horario fijo. El método propuesto aumenta significativamente la producción de agua en un XX %, aprovechando plenamente el recurso solar y la capacidad de almacenamiento térmico, al tiempo que tiene en cuenta los costos operativos principales.

Esta investigación abarca dos estudios complementarios sobre dos recursos intrínsecamente vinculados: el agua y la energía. La primera parte se centra en la gestión eficiente de los recursos hídricos para la generación eléctrica, mientras que la segunda explora el uso eficiente de la energía solar para la producción de agua limpia.

Contents

Acknowledgements	v
Preface	vii
Summary	ix
Resumen	xi
Contents	xiii
About the author	1
How to read this document	3
INTRODUCTION	5
1 Context	7
2 Research plan	11
2.1 Hypothesis	11
2.2 Objectives	11
2.3 Contributions	12
2.4 Implementation software tools	14
3 Automation overview: modelling, optimization and control	15
3.1 Modelling and simulation	15
3.1.1 First principle modelling	17
3.1.2 Data-driven modelling	17
3.1.3 Discrete modelling by means of Finite-State Machines (FSMs)	22
3.1.4 Forecasting and combinatory nature of FSMs	23
3.1.5 Performance metrics	23
3.2 Optimization	24
3.2.1 Non-Linear Programming (NLP) problems	25
3.2.2 Mixed Integer Non-Linear Programming (MINLP) problems	26
3.2.3 A discussion on constraint handling	26
3.2.4 Multi-objective optimization	27
3.2.5 Optimization algorithms	28
3.3 Control	32
3.3.1 PID controllers	33
3.4 Hierarchical control	34
I ENERGY MANAGEMENT IN MED PROCESSES DRIVEN BY VARIABLE ENERGY SOURCES	37
4 Thermal desalination	41
4.1 Water crisis	41
4.2 Brine concentration and mining	42
4.3 Overview of Desalination Technologies	43
4.3.1 Mechanical Technologies	43
4.3.2 Thermal Technologies	43
4.3.3 Thermal desalination timeline and comparison with Reverse Osmosis (RO)	44
4.4 (Variable) Energy sources for thermal separation processes	46
4.4.1 Solar thermal	46
4.4.2 Waste heat	47
5 SolarMED pilot plant	49
5.1 Solar field	50
5.2 Thermal storage	50

5.3	Multi-Effect Distillation	51
6	Hybrid modelling of a solar driven MED system	55
6.1	Introduction	55
6.2	Dynamic modelling. Process variables	55
6.2.1	Solar field	56
6.2.2	Thermal storage	60
6.2.3	Heat exchanger	64
6.2.4	MED	67
6.3	Discrete modelling. Operation state	71
6.3.1	Heat generation and storage subsystem (sfts)	71
6.3.2	Separation subsystem (med)	71
6.3.3	Validation	73
6.4	Complete system model	74
6.4.1	Validation	76
7	Performance evaluation in MED processes	81
7.1	Process analysis	84
7.2	Performance metrics	85
7.2.1	Separation metrics	85
7.2.2	Energetic metrics	86
7.2.3	Exergetic metrics	88
7.3	Instrumentation	89
7.3.1	Key Process Variables (KPVs)	89
7.3.2	Instrumentation requirements	90
7.3.3	Uncertainty determination	92
7.4	Monitoring and process control	92
7.4.1	Monitoring: steady-state identification	92
7.4.2	Control system	94
7.5	Methodology validation in an experimental campaign	96
8	Towards the optimal coupling and operation of a solar driven MED system	105
8.1	Introduction	105
8.2	Problem description	107
8.2.1	Implementation discussion	108
8.4	Operation plan layer description	111
8.4.1	Candidate problems generation	111
8.4.2	Update times generation	111
8.5	Operation optimization layer description	113
8.6	Optimization results	114
8.6.1	Choosing an algorithm	114
8.6.2	Choosing a candidate problem	114
8.6.3	Simulation results	114
8.6.4	Performance comparison with alternative strategies	117
CONCLUSIONS AND OUTLOOK		119
Conclusions		121
Outlook and future work		121
Derived scientific contributions		122
APPENDIX		125
A	MED Performance Evaluation	127
A.1	Uncertainty estimation through first-order Taylor series approximation	127
A.1.1	Specific Thermal Energy Consumption (STEC)	127
A.1.2	Specific Electrical Energy Consumption (SEEC)	127
A.1.3	Performance Ratio	127
A.1.4	Waste heat performance ratio	128
A.1.5	Recovery ratio	128
A.1.6	Concentration factor	128

A.2	Exergy calculations	128
A.3	Separation metrics calculation	129
A.4	Control system and steady state identification parameters	129
B	MED First-Principles Model	131
B.1	Nomenclature	131
B.1.1	Calibration mode	132
B.1.2	Simulation mode	133
B.2	Implementation	133
B.3	Validation	136
	Bibliography	141

List of Figures

1	Example figure	3
1.1	Shareholders-driven apocalysis	7
1.2	Annual global mean temperature anomalies relative to a pre-industrial (1850–1900) baseline.	
Source: [3]	8
1.3	Extreme weather-related events map. Source: [7]	9
1.4	Aerial view of the pilot plants at Plataforma Solar de Almería (PSA)	10
3.1	Dynamic response (reaction curve) of a process output to changes in its inputs'	17
3.2	Illustration of Gaussian Process Regression. (a) Prior samples drawn from a Gaussian Process with zero mean and smooth covariance, representing the prior belief before observing any data. (b) Posterior samples and mean after conditioning on two observations, showing reduced uncertainty near the observed points. Source: Rasmussen <i>et al.</i> [38]	
3.3	ANN model configurations	19
3.4	Considered ANN architectures	20
3.5	FSM representation of a traffic light	21
3.6	Evolution of different traffic-light FSMs	22
3.7	Constrained optimization problem. The goal is to minimize $y = f(x)$ with the two continuous decision variables x_1 and x_2 constrained to $g(x)$. The problem is NLP with a convex solution-space. Source: Wang <i>et al.</i> [47]	23
3.8	Simulated Annealing. Example illustrating the effect of cooling schedule on the performance of simulated annealing. The problem is to rearrange the pixels of an image so as to minimize a certain potential energy function, which causes similar colors to attract at short range and repel at a slightly larger distance. The elementary moves swap two adjacent pixels. These images were obtained with a fast cooling schedule (left) and a slow cooling schedule (right), producing results similar to amorphous and crystalline solids, respectively. Source: Wikipedia	25
3.9	Particle Swarm Optimization concept. Each particle adjusts its velocity based on its own experience and that of neighboring particles to explore the search space and converge towards optimal solutions. Source: Pagmo 2.19.1 documentation	29
3.10	Illustration of optimization runs for two algorithms	31
3.11	Control diagrams	32
3.12	Hierarchical control architecture	32
3.12	Hierarchical control architecture	34
4.1	Global water stress map. [1ex]Source: Statista. [1ex]	42
4.2	Desalination technologies used at plants worldwide in 2019 [1ex]Source: Panagopoulos <i>et al.</i> [79]	44
4.3	Desalination technologies coupled with renewable energy sources at plants worldwide. Source: Panagopoulos <i>et al.</i> [79]	44
4.4	Greenhouse Gas (GHG)s emissions per cubic meter of freshwater produced Source: Panagopoulos <i>et al.</i> [79].	45
5.1	Solar-driven Multi-Effect Distillation (SolarMED) process diagram	50
5.2	51
5.3	MED plant at PSA with open effects for maintenance	51
5.4	Piping and Instrumentation Diagram (P&ID) representative of the MED-PSA plant with the installed instrumentation, Key Process Variables (KPVs), and implemented control loops (ANSI/ISA 5.1-2022).	54
6.1	Solar field process diagram.	56
6.2	Solar field and thermal storage electrical characterization tests.	58
6.3	Solar field flow for different pump configurations and their associated power consumption. [1ex]	58
6.4	59
6.5	Thermal storage process diagram.	62
6.6	63
6.7	Heat exchanger process diagram.	65
6.8	Heat exchanger model validation for a particular test.	67
6.9	MED process diagram.	68
6.10	MED Gaussian-Process Regression (GPR) model regression for different outputs.	69

6.11	Finite-state machines for the different subsystems	70
6.12	SolarMED FSM states evolution during a test on 20230703	72
6.13	Complete SolarMED model architecture.	74
6.14		76
6.15		77
7.1	Ryznar Stability Index (RSI) of seawater at different temperatures and concentrations	83
7.2	Inputs and outputs variables in an MED process. The dash line delimits the control volume	85
7.3	P&ID with the required instrumentation, KPVs, and basic control loops (ANSI/ISA 5.1-2022) required in an MED plant	91
7.4	Sensitivity index results for different variables. Useful to assess the impact of the different measured variables uncertainty on the performance metrics. KPVs are shown in bold notation	91
7.5	Diagram of the steady-state identification procedure	93
7.6	Flowchart of finite state machines for plant start-up (left) and shutdown (right)	96
7.7		97
7.8		98
7.9	Condenser outlet temperature controller implementation	99
7.10	RSI values as a function of temperature and concentration before (left) and after (right) pretreatment using nanofiltration.	99
7.11	Scaling assessment during high TBT operation	101
7.12	Per effect comparison between low and high TBT operation points	102
8.1	Decision tree resulting from the combinatorial nature of the integer part of the optimization problem. Text in nodes represents system states.	110
8.2	Proposed optimization strategy architecture	110
8.3	Operation plan layer computation and updates distribution	112
8.4	Fitness evolution for a particular startup-problem	115
8.5	A rotated figure	116
B.1	Overall schematic of the MED model with inputs, outputs, main variables and components	132
B.2	MED model <i>calibration mode</i> diagram with inputs and outputs	133
B.3	MED model <i>simulation mode</i> diagram with inputs and outputs	133
B.4	Detailed schematic of a single cell in the MED containing the effect or evaporator (left) and the preheater (right)	134
B.5	Detailed schematic of a single cell in the MED with the effect's equations.	134
B.6	Detailed schematic of a single cell in the MED with the energy source side equations and internal effect condensate flashing.	135
B.7	Detailed schematic of a single cell in the MED with the preheater's equations.	135
B.8	Heat transfer coefficients comparison between <i>calibration mode</i> and <i>simulation mode</i> for the validation set	136
B.9	Detailed schematic of a single cell in the MED with distribution lines for the energy source side and generated steam. Also auxiliary elements like demister and preheater-effect distribution line geometry.	137
B.10		138
B.11		139

List of Tables

1	MED plant at PSA specifications and nominal operating conditions	4
5.1	MED plant at PSA specifications and nominal operating conditions	52
5.2	MED plant available experimental data range.	52
5.3	Characteristics of the instrumentation installed at MED-PSA unit (^a value of the measured temperature in °C, ^b of reading, ^c full scale).	53
6.1	Summary table of the prediction results obtained with the solar field model for different test days and sample times.	60
6.2	Summary table of the prediction results obtained with the thermal storage model for different test days and sample times.	64
6.3	Summary table of the prediction results obtained with the heat exchanger model for different test days and sample times.	66
6.4	Models parameters.	71
6.5	Solar Field and Thermal Storage subsystem (sfts) FSM states definitions. \wedge represents the logical AND operator and \forall represents that all meet the condition.	71
6.6	Separation subsystem (med) FSM states definitions. \wedge represents the logical AND operator, \exists represents that at least one meets the condition, and \forall represents that all meet the condition.	73
6.7	Summary table of the prediction results obtained with the SolarMED model for different test days, sample time set to 400s and different prediction horizons.	79
7.1	Ryznar Stability Index (RSI) values and their interpretation in terms of scaling and corrosion risk [122].	84
7.2	Experimental campaign design specifications	96
7.3	Measured variables and performance metrics for some operation points of the experimental campaign. The values are expressed as mean \pm standard deviation with a coverage factor of 2 (95% confidence interval). D is the duration of the steady state period.	100
8.1	Operation plan. Start-up (1) and shutdown (2) degrees of freedom for changes in the operation state.	111
A.2	Parameters for the Proportional-Integral-Derivative controller (PID) based process control, where <i>i.u.</i> represents the input variable units, and <i>o.u.</i> the output units.	130
A.1	Parameters for the steady-state detection algorithm, where <i>s.u.</i> represents that the parameter has the same units to the related variable	130

About the author

The author of this research work holds a degree in Industrial Engineering with a specialization in Electronics and Automation from the University of Almería (Spain) and a degree in automation by the *Università degli Studi di Brescia* (Italy). In 2021, he was awarded a scholarship by the CIEMAT research center to pursue a PhD within the Solar Thermal Applications Unit at the Plataforma Solar de Almería, where he has conducted his research from 1 February 2021 to 31 January 2025.

Throughout his academic and professional career, he has developed a strong interest in scientific computing, automation, and control systems. His work has provided extensive experience with tools and technologies such as Linux, Python, Docker, LaTeX, and the Robot Operating System (ROS). He is also an advocate of open science and open-source software, supporting initiatives that promote transparency and collaborative research.

For his bachelor's thesis, he established a mobile robotics laboratory at the University of Almería by deploying the Duckietown project. This work provided practical experience with ROS and containerization technologies through Docker. His master's thesis focused on the design and implementation of a SCADA-like monitoring and control system using Python.

During his PhD studies, the author has presented his research at several international conferences, including the IFAC Conference on Advances in Proportional-Integral-Derivative Control, the European Desalination Society (EDS) conferences (2022 and 2023 editions), and the SolarPACES conference (2025 edition). He has also participated in the Doctoral Colloquium program (Sollab), presenting his work in Spain (2021), Switzerland (2022), and Germany (2023), as well as in the annual progress meetings of the University of Almería's Doctorate Program in Computer Science (2021-2025).

Additionally, the author has completed several international research stays: a short stay at the Cyprus Institute (Nicosia, Cyprus) in 2023; a main research stay at the *Universidade Federal de Santa Catarina* (Florianópolis, Brazil) from February to June 2024; and a one-month stay at the *Technische Universität Chemnitz* (Germany) in 2025.

Also, during his time at PSA he participated in different dissemination activities and projects. Being part of the national project *SOLpréndete - Didactics and dissemination of CSP*, participating since his undergraduate period in every edition of the European Researchers Night and giving some talks at high-schools as part of the program *DivulgaCIEMAT*.



How to read this document

TL;DR

This preliminary chapter explains how to read this document, mainly the different environment boxes used throughout the manuscript, why the large margins, what is placed in them, and how to use the interactive features of the manuscript. This is an example of a Too Long; Didn't Read (TL;DR) box. It contains an Abstract/Summary of the main point of the chapter and are placed at the beginning of every chapter.

This \LaTeX template is designed with large margins, on the one hand this allows to have shorter lines, which makes for an easier reading experience but most interestingly, it also allows to place additional information in the margins, such as side notes, side citations, figures, tables... your imagination is the limit! Or rather \LaTeX compilation errors and your patience are. Throughout this manuscript I will add side notes¹ to provide additional information and comments that would otherwise be too distracting and verbose to include in the main text, constantly interrupting the flow of the reading. The side notes are not essential to understand the content of the document, but mostly complementary.

Boxed environments

Both problem definition boxes (e.g. ref) and model definition boxes (e.g. Model 0.2) are countered environments and can (and will) be referenced in the text.

Problem: Problem definition box example

This is an example of a problem definition box. It is used to formally and concisely define an optimization problem.

$$\min_{\mathbf{x}, \mathbf{e}; \theta} J = f(\mathbf{x}, \mathbf{e}; \theta) = \text{XXXX}$$

with:

$$\begin{aligned} \mathbf{out}_1, \mathbf{out}_2 &= f(\mathbf{in}_1, \mathbf{in}_2, \dots, \mathbf{in}_N) \\ \mathbf{out}_1, \mathbf{out}_2 &= f(\mathbf{in}_1, \mathbf{in}_2, \dots, \mathbf{in}_N) \end{aligned}$$

► Decision variables

$$\mathbf{x} = [x_1, x_2]$$

► Environment variables

$$\mathbf{e} = [e_1, e_2, \dots, e_3]$$

► Fixed parameters

$$\theta = [\theta_1 = X, \theta_2 = Y]$$

subject to:

► Box-bounds

$$\begin{aligned} \cdot x_1 &\in [\underline{x}_1, \bar{x}_1] \\ \cdot x_2 &\in [\underline{x}_2, \bar{x}_2] \end{aligned}$$

► Constraints

¹: Like this one! They are like footnotes, but placed in the margin of the page



Figure 1: Example figure. Try clicking or scanning the QR code to access the interactive version.



Table 1: MED plant at PSA specifications and nominal operating conditions

Parameter	Value
Capacity	72 m ³ /day
Number of effects	14
Feed type	Forward feed
Physical arrangement	Vertically stacked
Heat exchanger configuration	90/10 Cu-Ni HTE
Heat source type	Hot water
Top Brine Temperature (TBT)	70 °C
Condenser temperature	35 °C

2: I believe that this is a good way to make the document more accessible and to encourage readers to explore the content in more depth. However, the interactive features are optional and not necessary to understand the content of the document.



3:

[https://github.com/juan11iguel/
my-thesis/blob/main](https://github.com/juan11iguel/my-thesis/blob/main)

4: Like hoarding toilet paper

$$\begin{aligned} & \cdot |out_x - out_y| \leq \epsilon_1 \\ & \cdot out_x \leq out_z - \Delta Z \end{aligned}$$

Model 0.2: Model definition box example

out_1, out_2 = some cool model(in_1, in_2, in_3)

Other boxes

Other boxes are used to highlight important points, or to provide additional information that is not essential to the main text.

In order to make the book more interactive and link-friendly, I have enabled hyperlinks in the PDF. This means that you can click on the references, citations, and links to external resources, and they will take you to the corresponding location. This is standard LaTeX, however to maintain a consistent experience in the physical version, QR codes are inserted in the margin next to the links. The reader is invited to scan them with a QR code reader to access the corresponding online resource². Some figures also include QR codes that link to an interactive (HTML) version of the figure, see Figure 1 as an example.

The additional material as well as the source code of this document are hosted in a [Zenodo repository](#)³. Alternatively, a mirror repository is also available at:

<https://github.com/juan11iguel/my-thesis>

It seems unlikely that both Zenodo and GitHub will go down at a time where this document is still relevant, and if they do, I think there will be more important things to worry about than losing access to the interactive content of this thesis.⁴

INTRODUCTION

Just some phrase, it may be longer, it might
be shorter, but in the end, it's a phrase.
Aren't we all phrases? Well, no

Someone else answering someone

Technological development has undeniably improved material conditions for an important part of humanity. Over the past century, innovations in energy, medicine, transport, and communication have contributed to longer life expectancy, higher productivity, and broader access to goods and services. For some time, it was possible to argue that the rise in CO₂ emissions was closely tied to an overall improvement in material well-being of some societies.

However, this trend has now been reversed. Seven out of ten people live in countries where economic inequality has increased over the past 30 years, and nearly half of the world's wealth —46 %— is concentrated in the hands of just 1 % of the population [1].

We find ourselves in a paradoxical situation: as the planet becomes increasingly uninhabitable, social inequalities continue to deepen. The overall outlook is far from encouraging. Technological progress no longer serves to enhance collective well-being¹ or to effectively build a sustainable future. Instead, the relentless pursuit of endless economic growth —fueled by unchecked consumption, short-term profit seeking, and a shareholder-driven economy dominated by speculation— is propelling us ever closer to catastrophic climate collapse.

One of the main drivers in this direction, consequence of this unchecked growing economy prioritization, is the abuse in use of fossil fuels. Despite the finite nature of fossil fuels, the problem today is not scarcity, but excess —an abundance sufficient to fill the atmosphere with greenhouse gases² at levels incompatible with life. The Paris Agreement has a long-term temperature goal which is to keep the rise in global surface temperature to well below 2 °C above pre-industrial levels. The treaty also states that preferably the limit of the increase should only be 1.5 °C.

A 2024 report from the World Meteorological Organization (WMO) finds an 86 per cent chance that global average temperatures will exceed 1.5 °C above pre-industrial levels in at least one of the next five years (see Figure 1.2), and a one per cent chance of one of those years exceeding 2 °C of warming [3].

Our dependence on fossil fuels is proving lethal, and this is manifesting in multiple ways:

- As of 2024, CO₂ emissions continue to increase, albeit more slowly than in the past. Yet this continued growth has pushed global emissions to another record high [4].
- Between 1999 and 2020, coal-related particulate matter (PM_{2.5}) caused an estimated 460,000 deaths in the United States alone [5].
- Plastic production has [more than doubled](#) in the last two decades [6]. Only a small fraction of this plastic is recycled, and even then, only a limited number of times³
- Studies covering nearly 750 extreme weather-related events and trends (see Figure 1.3) show that 83 % have been influenced by human-induced climate change [7].

Even within this grim context, financial logic seems to prevail. Some investors, motivated not by moral concern but by the growing profitability of renewables, are now turning towards cleaner technologies⁴. Yet at the same time, a new wave of governments has emerged that, despite overwhelming evidence, promotes a return to fossil fuels: leaders who exploit crises to sow confusion and advance regressive agendas⁵. If previous climate measures were insufficient and often reduced to symbolic agreements with limited implementation, e.g.:



Figure 1.1: "Yes, the planet got destroyed. But for a beautiful moment in time, we created a lot of value for shareholders"

Source: Tom Toro – The New Yorker

[1]: Sayer (2016), *Why We Can't Afford the Rich*

1: not that it ever did for a significant amount of people [2]

2: great efforts are also being made in filling both hydrosphere and lithosphere with plastics

[3]: Organization (2025), *State of the Global Climate 2024*

[4]: IEA (2025), *Global Energy Review 2025*

[5]: Henneman et al. (2023), "Mortality Risk from United States Coal Electricity Generation"

[6]: Geyer et al. (2017), "Production, Use, and Fate of All Plastics Ever Made"

3: As environmental engineer [Jenna Jambeck](#) from the University of Georgia notes, "What's the best way to manage waste? To not produce it in the first place."

4: The private sector is driving the energy transition, providing three-quarters of global clean energy investment. However, to meet scale investment in renewables to at least USD₂₀₂₅ 1.4 trillion per year in 2025–2030, more than doubling the invested in 2024 [8]

5: President Trump Prioritizes Fossil Fuel Development and Rolls Back Climate Action in Energy [9]

Confusion over the causes of the blackout intensifies the ideological battle between renewables and nuclear power [10]

Global mean temperature 1850-2024

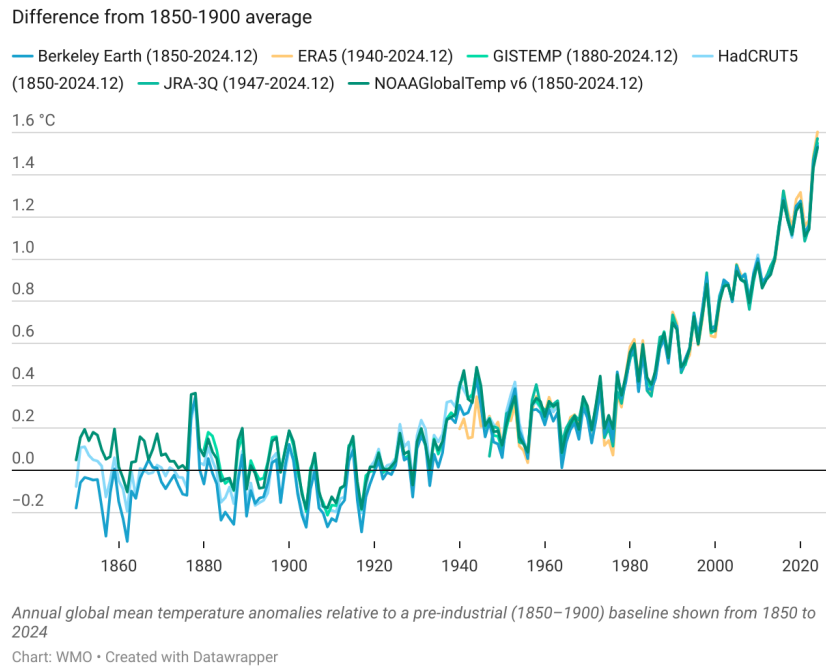


Figure 1.2: Annual global mean temperature anomalies relative to a pre-industrial (1850–1900) baseline. Source: [3]

State health services and pensions are run down and replaced by private health insurance and private pensions. You're on your own, free to choose, free to lose... Instead of seeing ourselves as members of a common society... we are supposed to see ourselves as competing individuals with no responsibility for anyone else.

Andrew Sayer
In *Why We Can't Afford the Rich*

[11]: Amelie (2025), "The Future of Climate Migration"

In Europe, despite targets such as recycling 55 % of plastic packaging waste by 2030, most plastic waste was exported to China, where it ended up in landfills. In 2025, only around 12 % is actually recycled.

The current political landscape shows an even more concerning trend: open denialism. This fuels widespread disenchantment. Society has become increasingly alienated. Trust in collective institutions, including science, is eroding, while conspiracy theories gain traction and shape public opinion. As a result, genuine and complex challenges are neglected, while artificial or symbolic issues dominate public discourse. In Europe and elsewhere, racism and exclusionary politics are resurging, often presented as responses to fabricated threats. Yet the true challenge lies ahead: in the coming decades, climate change is expected to displace millions, as vast regions of the planet become increasingly incompatible with human life [11]. The question remains whether societies will respond with solidarity and structural transformation, or with further division and denial.

Where this research work fits in the current context

After discussing the global environmental challenges of our time, and setting aside their complex socio-political dimensions, the focus can now narrow to a more specific and concrete contribution. The work presented here does not solve such grand challenges, nowhere near, but rather contribute within a limited scope: developing and optimizing technologies that improve the sustainable management of two interconnected resources, energy and water, in two solar-driven processes.

This research is therefore structured in two complementary parts. The first addresses the efficient management of water resources for power generation in Concentrated Solar Power (CSP) plants, through the optimization of a novel combined cooling system. The second explores the efficient use of solar energy

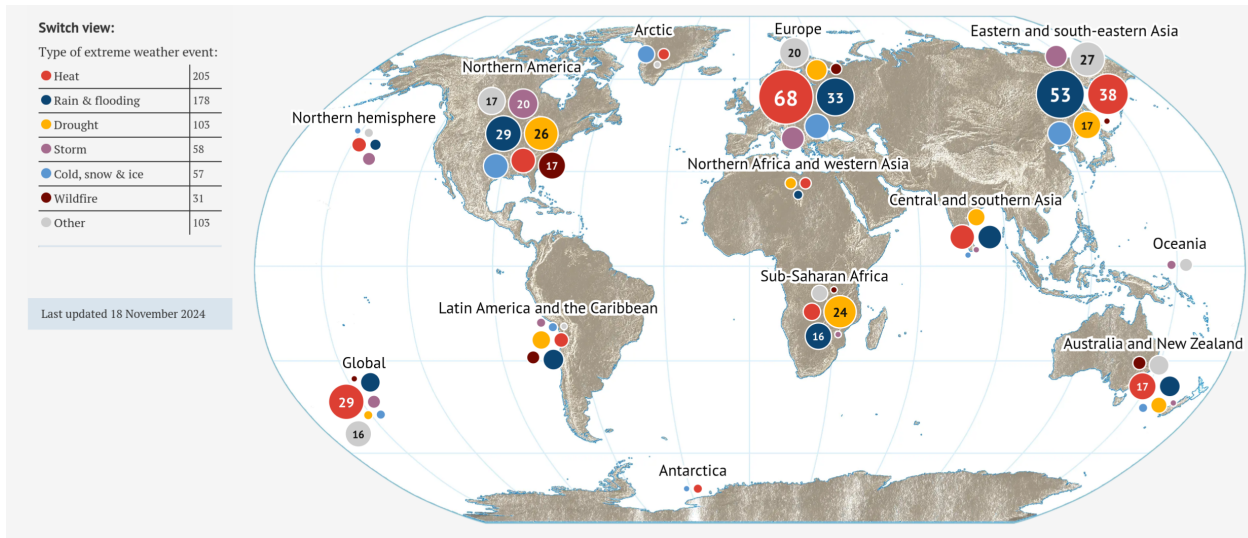


Figure 1.3: Extreme weather-related events map. Source: [7]

for clean water production in a solar-driven multi-effect distillation system with thermal storage, focusing once again on operational optimization.

In an era where almost every idea seems to have been expressed before, originality rarely lies in invention alone, but in the creative integration of existing concepts into meaningful, purposeful solutions. For this reason, implementation plays an increasingly central role even—and perhaps especially—in applied scientific research. Implementation should not remain hidden; it should be shared, documented, and made accessible, allowing others to replicate, verify, and build upon it [12].

Accordingly, the complete implementations of both studies are made available in open repositories, alongside most of the code and supplementary material used to develop this manuscript. The developed work has an important experimentation component (see Figure 1.4). Most experimental and simulated results follow the Findable, Accessible, Interoperable, Reusable (FAIR) data principles⁶ [13], ensuring transparency, accessibility, and reproducibility. Further details are provided in Section 15 (Derived scientific contributions).

[12]: Hicks et al. (2015), “Bibliometrics”

6: And made public at time of publication of this manuscript. The rest may follow soon after

[13]: Wilkinson et al. (2016), “The FAIR Guiding Principles for Scientific Data Management and Stewardship”



Figure 1.4: Aerial view of the pilot plants at Plataforma Solar de Almería (PSA), Spain. The developments presented in this thesis have been developed and validated around two test-rigs: a Combined Cooling System (CCS) and a Solar-driven Multi-Effect Distillation (SolarMED) pilot plant. In the picture, the solar field, the source of energy for all processes, is highlighted in yellow. Below it in purple is the building containing the Multi-Effect Distillation (MED) plant. The bottom two boxes (gray and green) delineate the area of the CCS plant. In gray the condenser and Air-Cooled Condenser (ACC) and in green the combined cooler composed by the Air-Cooled Heat Exchanger (ACHE) and Wet Cooling Tower (WCT) components.

2.1 Hypothesis

The purpose of this thesis is to investigate the following hypotheses:

- i) The cooling solution of choice in a CSP plant is strongly dependent on the specific location of the plant, particularly on its weather conditions and water resources. Restricting the cooling choice to only dry or only wet options penalizes the overall system performance in fulfilling its role in the grid.
- ii) Hybrid or combined cooling systems are a technically feasible compromise between purely wet or dry systems, but they have seen limited deployment due to the increased complexity in design and operation. A general optimization methodology for these alternative cooling solutions could promote their broader adoption.
- iii) Thermal desalination has a role to play in alleviating water scarcity, not necessarily as the dominant desalination technology, but by addressing more niche applications. This can be achieved by making desalination more economically attractive through approaches such as brine mining, and/or by reducing water contamination through the treatment of industrial and mining wastewater streams.
- iv) To serve such applications, thermal desalination (with emphasis on MED) must improve in two directions: either by becoming more efficient through expanded operational ranges, or by adapting to low-temperature applications where its heat demands can partially or fully be met using alternative sources such as low-exergy waste heat, or solar thermal.

2.2 Objectives

The specific objectives and goals set out in the present research work are divided into two main blocks, each corresponding to one of the main contributions of the thesis¹. The first block (**O1**) focuses on the development of a methodology for the modelling and optimization of combined cooling systems, while the second block (**O2**) is centered around MED systems coupled with solar thermal plants.

2.1 Hypothesis	11
2.2 Objectives	11
2.3 Contributions	12
2.4 Implementation software tools	14

¹: And matches the parts in this manuscript

- O1.1** Model and validate various components of combined cooling systems, as well as their integration into a complete combined system.
- O1.2** Propose a methodology for optimizing combined cooling systems.
- O1.3** Experimentally validate the proposed methodology.
- O1.4** Perform a simulation-based analysis of a representative case study comparing different cooling alternatives and integrating the proposed methodology.

- O2.1** Analyze the current performance indices and evaluation criteria used in thermal desalination processes.
- O2.2** Propose a standardized methodology for the experimental evaluation and determination of performance criteria in thermal desalination processes.
- O2.3** Design and assess basic control loops, as well as identify stable operating conditions to ensure the reliability of experimentally obtained evaluation criteria.

- O2.4 Experimentally evaluate improvements (e.g., nanofiltration pretreatment) that enhance efficiency and/or reduce costs in solar desalination systems.
- O2.5 Model and simulate multi-effect desalination plants coupled with solar thermal systems.
- O2.6 Propose a methodology to optimize the operation of solar desalination processes based on selected performance criteria.
- O2.7 Evaluate hierarchical control structures aimed at optimizing desalination processes coupled with solar plants.
- O2.8 Demonstrate that the proposed hierarchical control structures improve the performance indices of desalination plants coupled with solar thermal systems.

2.3 Contributions

Over the years, numerous studies have compared wet and dry cooling systems for CSP plants. Most of these works focus on sensitivity analyses of selected operating parameters [14–19]. A smaller number have addressed the optimization of individual component operation to improve overall cooling system performance. In Martin *et al.* [20, 21], they optimized the year-round operation of the cooling system (wet in [20] and dry in [21]) in a CSP. However, both of their studies relied on monthly average data, which obscure significant daily temperature variations—often exceeding 10 °C—that coincide with peak power production and substantially affect cooling system performance.

In contrast, there has been little discussion in the literature regarding the operational strategies of combined cooling systems. For water-enhanced dry cooling and parallel configurations, the commonly proposed strategy [22–24] is to prioritize the dry section until the condenser pressure reaches a predefined threshold, at which point the wet units are activated. While this approach is simple and robust, it leaves significant performance potential untapped.

Several additional considerations arise when developing an effective operation strategy for combined cooling systems:

- ▶ Humidity is typically higher at night, when ambient temperatures are lower. This partially mitigates the limitations of dry cooling and makes it less unfavorable.
- ▶ The wet cooling section should be fully leveraged when water is plentiful, given its superior efficiency and lower operational cost.
- ▶ The availability and dynamic cost of alternative water sources should be incorporated into the decision process.
- ▶ The operation of combined cooling systems is inherently complex and requires a strategy that, at a minimum, ensures reliable satisfaction of the cooling demand, and ideally, minimizes the total operating cost.

This research work investigates the optimization of different cooling system configurations, focusing on their two main resource consumptions: electricity and water. The optimization problems are formulated to minimize the total cost of cooling a prescribed thermal load, with cost defined as the combined use of these two resources. The thermal load itself is treated as an external requirement and is therefore excluded from the decision space. This work addresses existing gaps in the literature and, for the first time, presents an actual optimization of the operation of a combined cooling system within the context of CSP applications.

Regarding the MED process, its future in desalination and brine concentration applications depends on both its technical development and its integration with other technologies [25, 26]. Performance evaluation plays a central role in this

[14]: Asfand *et al.* (2020), “Thermodynamic Performance and Water Consumption of Hybrid Cooling System Configurations for Concentrated Solar Power Plants”

[15]: Mdallal *et al.* (2024), “Modelling and Optimization of Concentrated Solar Power Using Response Surface Methodology”

[16]: Hu *et al.* (2018), “Thermodynamic Characteristics of Thermal Power Plant with Hybrid (Dry/Wet) Cooling System”

[17]: Tang *et al.* (2013), “Study on Operating Characteristics of Power Plant with Dry and Wet Cooling Systems”

[18]: Asvapoositkul *et al.* (2014), “Comparative Evaluation of Hybrid (Dry/Wet) Cooling Tower Performance”

[19]: Barigozzi *et al.* (2014), “Performance Prediction and Optimization of a Waste-to-Energy Cogeneration Plant with Combined Wet and Dry Cooling System”

[20]: Martín *et al.* (2013), “Optimal Year-Round Operation of a Concentrated Solar Energy Plant in the South of Europe”

[21]: Martín (2015), “Optimal Annual Operation of the Dry Cooling System of a Concentrated Solar Energy Plant in the South of Spain”

[22]: Wiles *et al.* (1978), *Description and Cost Analysis of a Deluge Dry/Wet Cooling System*.

[23]: Zaloudek *et al.* (1976), *Study of the Comparative Costs of Five Wet/Dry Cooling Tower Concepts*

[24]: Rohani *et al.* (2021), “Optimization of Water Management Plans for CSP Plants through Simulation of Water Consumption and Cost of Treatment Based on Operational Data”

[25]: Ghenai *et al.* (2021), “Performance Analysis and Optimization of Hybrid Multi-Effect Distillation Adsorption Desalination System Powered with Solar Thermal Energy for High Salinity Sea Water”

[26]: Son *et al.* (2020), “Pilot Studies on Synergistic Impacts of Energy Utilization in Hybrid Desalination System”

development. Although efforts have been made to propose performance metrics for multi-effect evaporation, there is currently neither consensus on which metrics are the most appropriate [27] nor a standardized methodology for experimental evaluation. The only existing standard for MED processes addresses cost structures and determinants rather than performance assessment [28].

This research proposes a standardized methodology for evaluating the performance of MED processes, which can also be extended to other thermal separation technologies. The method addresses key aspects such as instrumentation requirements, process control, and the suitability of various performance metrics, including the uncertainties associated with their determination. In addition, an algorithm has been developed for the automatic detection of steady-state operation, improving the reliability and robustness of evaluations under variable conditions. Furthermore, the plant is evaluated for the first time at high Top Brine Temperatures (TBTs). The results are analyzed using multiple performance metrics, and the scale formation risk is quantified via the Ryznar Stability Index (RSI).

In terms of process integration, low-exergy solar thermal energy represents a promising heat source. Most existing literature on the automatic control of solar-driven MED systems focuses on low-level control strategies, typically employing simple control loops with either Proportional-Integral-Derivative controller (PID) controllers [29] or Model Predictive Control (MPC) schemes [30], whose primary goal is to maintain temperature setpoints—usually at the heat source inlet. A number of works have also addressed the optimization of the MED process in isolation [31, 32]. However, optimizing the MED subsystem independently neglects its coupling with the energy supply and storage systems.

A MED plant, like any thermal separator, requires both heat and electricity. While electricity costs can be directly assigned, the cost of thermal energy depends on its source. When the heat is supplied by a variable source such as solar energy, the situation becomes more complex: solar availability is intermittent, and the operation and efficiency of the solar field are closely linked to how the MED load is managed. This coupling is further complicated by the presence of thermal storage, which allows temporal shifting of heat usage and introduces additional operational decisions.

Several studies have addressed this broader problem at varying levels of complexity. González et al. [30] proposed a receding-horizon optimal control strategy with economic objectives—maximizing water production while minimizing electricity costs—but relied on a simplified linear model that optimized only the solar field flow, keeping the MED inlet temperature constant. The most advanced optimization efforts in the literature, however, have been developed for Membrane Distillation (MD) rather than MED. Gil et al. [33] recognized that a solar MD plant operates through distinct modes (*e.g.*, solar field heating, thermal storage charging, and MD operation), dictated by solar and thermal conditions. However, in their work, the transitions between these modes were hardcoded in the control rules, meaning that the choice of when to start or stop each subsystem was not treated as a decision variable but as part of the environment.

In many studies, either the decision space is too limited, the models are overly simplified, or key variables are treated as uncontrollable. Moreover, thermal storage decouples heat usage from solar availability, within certain limits, making the timing of subsystem operation—both solar field and thermal separator—critical for maximizing system performance over multiple days. Using a fixed irradiance threshold to trigger startup is therefore suboptimal, as it ignores the state of thermal storage and forecasts of future solar availability, which could enable more flexible and efficient operation.

In this work, the operation of a solar-driven MED system is optimized with these aspects explicitly accounted for. The formulation includes decision variables

[27]: Burgess et al. (2000), “Solar Thermal Powered Desalination: Membrane versus Distillation Technologies”

[28]: Pinto et al. (2017), “Desalination Projects Economic Feasibility”

[29]: Roca et al. (2008), “Solar Field Control for Desalination Plants”

[30]: González et al. (2014), “Economic Optimal Control Applied to a Solar Seawater Desalination Plant”

[31]: Carballo et al. (2018), “Optimal Operating Conditions Analysis for a Multi-Effect Distillation Plant According to Energetic and Exergetic Criteria.”

[32]: Chorak et al. (2017), “Experimental Characterization of a Multi-Effect Distillation System Coupled to a Flat Plate Solar Collector Field”

[30]: González et al. (2014), “Economic Optimal Control Applied to a Solar Seawater Desalination Plant”

[33]: Gil et al. (2019), “Hybrid NMPC Applied to a Solar-powered Membrane Distillation System”

for starting and stopping each subsystem and considers a two-day prediction horizon. This enables the optimization to balance current performance with the impact of present decisions on future operation. The method is based on an experimentally validated system model that includes the electrical consumption of each component, coupled with a comprehensive data-driven MED model.

2.4 Implementation software tools

2: Isaac Newton in a letter to Robert Hooke in 1676, acknowledging that his discoveries were built on the work of others; also the title of the fourth studio album by English rock band Oasis

[34]: Biscani et al. (2020), “A Parallel Global Multiobjective Framework for Optimization: Pagmo”

[35]: Marcellos et al. (2021), *PyEqulon*

Software development for this research relies on a variety of tools. Just as scientific knowledge is built on the shoulders of giants², software similarly builds upon thousands of—mostly open-source—tools. Listing every tool used would be impractical, so only the most relevant ones are presented below:

- ▶ [PyGMO](#) (Mozilla Public License Version 2.0) [34] is a Python library for massively parallel optimization. It provides a unified interface for optimization algorithms and problems, facilitating deployment in parallel environments.
- ▶ [GPy](#) (BSD-3-Clause License) is a Gaussian Process Regression framework written in Python, developed by the Sheffield Machine Learning group.
- ▶ [pytransitions](#) (MIT License) is a lightweight, object-oriented state machine implementation in Python with many extensions. Created by Tal Yarkoni and maintained by Alexander Neumann.
- ▶ [simple-pid](#) (MIT License) provides a simple and fast PID controller implementation in Python. Created by Martin Lundberg.
- ▶ [Apache Airflow](#) (Apache 2.0 License). A platform to programmatically author, schedule, and monitor workflows.
- ▶ [PyEqulon](#) (BSD 3-Clause License) [35] is a Python package for automatic speciation calculations of aqueous electrolyte solutions.
- ▶ Statistics and Machine Learning Toolbox (proprietary MATLAB license) provides functions and apps to describe, analyze, and model data, including tools for machine learning such as classification, regression, clustering, and dimensionality reduction.

Automation overview: modelling, optimization and control

3

Automation, and particularly process automation, is a multidisciplinary technology that, by integrating various fields of knowledge, aims to develop autonomous systems capable of operating with minimal human intervention, using resources efficiently, adapting to changing conditions, and ensuring safety and reliability.

This chapter provides an overview of the main aspects of automation, focusing on modelling, optimization and control which are particularly relevant to the development of this research work. These three pillars are essential for the development of advanced automation systems and are widely used in the industry. The chapter is structured as follows: first, an overview of modelling techniques is presented, including first-principles and data-driven approaches. Then, optimization methods are discussed, covering both single-objective and multi-objective optimization. Finally, control strategies are reviewed, with a focus on PID and hierarchical control.

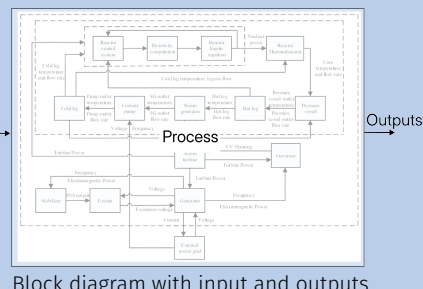
Dealing with complexity

Real systems are complex, with many elements interconnected. We first need to simplify them into simpler blocks or levels of abstraction that we can work with. These blocks or boxes have inputs and outputs, internally they hide some complexity, but from our abstraction we only care that we give some input to them, they perform some transformation, and then they return some output. These then can be interconnected to form a complex network or structure representing the real process.

This layering is common in many different fields, for example, processors are made up by thousands of layers, with modern processors going from city-like structures in the upper layers while reaching atomic scales in the lowest layers.



Zoomed-in microprocessor.
Source: [stylishpirate - Reddit](#)



Block diagram with input and outputs

3.1 Modelling and simulation

Models are useful approximations for the real-world, more precisely a mathematical representation of real-world systems. A model can depict a system at different levels of abstraction depending on the intended use. Models are useful in many applications [36]:

3.1 Modelling and simulation	15
3.1.1 First principle modelling	17
3.1.2 Data-driven modelling	17
3.1.3 Discrete modelling by means of Finite-State Machines (FSMs)	22
3.1.4 Forecasting and combinatory nature of FSMs	23
3.1.5 Performance metrics	23
3.2 Optimization	24
3.2.1 Non-Linear Programming (NLP) problems	25
3.2.2 Mixed Integer Non-Linear Programming (MINLP) problems	26
3.2.3 A discussion on constraint handling	26
3.2.4 Multi-objective optimization	27
3.2.5 Optimization algorithms	28
3.3 Control	32
3.3.1 PID controllers	33
3.4 Hierarchical control	34

[36]: Sokolowski et al. (2011), *Principles of Modeling and Simulation*

- ▶ Forecasting. They are used to predict the value of a variable at some time in the future.
- ▶ Simulation. Oftentimes experimentally evaluating real-world systems is impractical or infeasible, either because it is costly, time-consuming, or deteriorate the system, among other factors. Simulating a model enables the repeated observation of a system with just an associated computational cost.
- ▶ Control and optimization. In order to compute the optimal input to give to a real system, many control strategies are model-based, that is, they assess how inputs given to the real system will affect it by first evaluating them in a model.
- ▶ Via analysis, they enable to draw conclusions, verify and validate the research, and make recommendations in order to support decision-making.

Sensitivity analysis

Sensitivity analysis is one of the possible analysis tools. It involves systematically assessing how variations in input parameters impact the model outputs. One of the methods used in this research work is the Sobol method [37], which is a variance-based approach. This method decomposes the total variance of the model output into contributions from individual input parameters and their interactions.

All real world systems are fundamentally dynamical systems, that is, they evolve over time. For example a fluid flowing over a plane wing, the spread of a disease, the climate of a planet, the stock market, planets moving around the solar system. This behavior takes place continuously with respect to time for most physical systems, and can be described using differential equations. An alternative discrete representation can be achieved by performing a transformation from the continuous space to a discrete space sampling data at discrete time intervals and is described by difference equations. For an infinitesimal small time interval they are equivalent. In practice, the discrete representation is a simplification of continuous systems.

An example of the position (y) of an object free-falling by gravity could be represented:

- ▶ In a dynamic continuous space as $\frac{d^2y(t)}{dt^2} = -g$
- ▶ or with a discrete representation (sample time Δt and velocity v): $y_{k+1} = y_k + v_k \Delta t - \frac{1}{2}g(\Delta t)^2$

When a dynamic system is left unchanged for a sufficiently long period and an equilibrium is established between its inputs and outputs, it eventually reaches a stable or steady state. As long as the inputs remain constant, the outputs will also remain constant (visualized in Figure 3.1). Thermodynamic processes are often analyzed under these equilibrium conditions, since the main interest is typically the stable relationship between a given set of inputs and the resulting outputs, rather than the detailed trajectory of how the system evolves from one state to another. This approach makes it possible to evaluate the long-term performance of the system.

In many cases, a dynamic system can be approximated as a steady-state system if the transitions between equilibrium states are either negligible or irrelevant to the problem at hand. Such simplifications are appropriate when the system is expected to operate mostly under stable conditions, and the transient dynamics do not significantly affect performance. For example, in thermodynamic analyses, transient behavior is frequently treated as noise when evaluating efficiency or energy balances. This is especially valid for systems with fast dynamics —where

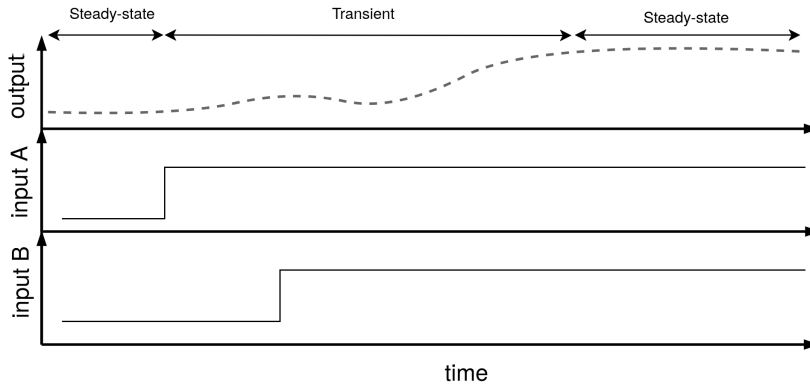


Figure 3.1: Dynamic response (reaction curve) of a process output to changes in its inputs'

transients settle within seconds—and that are only occasionally disturbed, meaning the system spends most of its time operating near steady state.

A model can be an incomplete and possibly incorrect representation of the phenomenon under study. This typically occurs when information about the phenomenon is lacking or when very complex processes are being modeled—such as biological systems that change their dynamics over time, or large-scale stochastic processes like climate, where small errors can propagate exponentially. All these factors contribute to uncertainty in modeling. Uncertainty is generally classified as aleatory or epistemic [36]. Aleatory uncertainty arises from inherent randomness in the system and is typically addressed through probabilistic or stochastic methods, though in some cases it may be simplified or ignored. Epistemic uncertainty, on the other hand, stems from incomplete knowledge, modeling assumptions, or limited data.

[36]: Sokolowski et al. (2011), *Principles of Modeling and Simulation*

Given a real-world scenario, the first step is to identify a problem to model, make reasonable assumptions about the process and collect data, choose a modelling approach, test the assumptions, refine the model as necessary and finally fit the model to data if appropriate. Two main categories of modelling exist: first-principle and data-driven, explained in the following.

3.1.1 First principle modelling

First-principle modelling¹ is an approach to representing a system by starting from the fundamental laws of nature —such as conservation of mass, energy, and momentum; Newton's laws of motion; thermodynamics; or chemical kinetics. In this framework, the model equations are derived from established physical, chemical, or biological principles that govern the system's behavior.

1: also called white-box modelling or physics-based modelling

The resulting models typically take the form of differential and algebraic equations, which describe how system states evolve over time as a function of inputs and parameters. Such models are valuable because they provide physical interpretability, can be extrapolated beyond measured operating points, and allow deeper insight into how design or operating conditions affect performance. However, they often require detailed process knowledge, accurate parameter estimation, and can become computationally intensive for complex systems.

3.1.2 Data-driven modelling

Data-driven modelling refers to the construction of models that rely primarily on measured or simulated data, rather than on explicit knowledge of the underlying physical laws. The central idea is to capture patterns, correlations, and dependencies in input-output data and use them for prediction, control, or

optimization. Unlike first-principle models, which are built from conservation laws and mechanistic equations, data-driven models treat the system as a black box, with little or no prior assumptions about its internal structure.

A large class of data-driven techniques can be framed within supervised learning, where the model learns a mapping from inputs to outputs based on labeled training data. Supervised learning methods are commonly divided into regression and classification problems: classification predicts discrete categories, while regression focuses on continuous quantities. In this research work the focus is mainly on regression approaches, since most engineering systems require the prediction of continuous variables such as temperatures, pressures, flows, or performance indices.

Data-driven regression models can range from simple, interpretable structures—such as polynomial regressions—to highly flexible nonlinear machine learning models such as Gaussian process regression or artificial neural networks. Each comes with its own trade-offs between accuracy, interpretability, data requirements, and computational cost. In the following, we discuss some representative examples of these approaches.

Data-driven approaches are particularly useful when: adequate experimental or simulated data is available, predictions are needed mainly within the range of observed data and simplicity and speed are prioritized over detailed physical interpretability.

Polynomial models

Polynomial models of arbitrary order approximate system behavior by expressing outputs as polynomial functions of the inputs. The degree of the polynomial determines how flexibly the model can capture nonlinear relationships: lower-order polynomials give simple trends, while higher-order ones can represent more complex patterns but risk overfitting and poor extrapolation outside the training range.

Polynomial regression is one of the most widely used empirical parametric-modeling techniques because it is easy to implement, computationally efficient, and provides closed-form solutions for the estimated coefficients. Despite its simplicity, it often delivers sufficiently accurate approximations for engineering applications.

Use cases include curve fitting, surrogate models for optimization problems, quick approximations in control design, and empirical correlations.

Gaussian Process Regression

A Gaussian Process (GP) is a powerful and flexible non-parametric model that defines a distribution over functions instead of assuming a specific functional form (such as a straight line in linear regression). In this framework, any possible function could explain the data, but functions that are *smoother* or *closer* together in input space are more likely. It consists of a collection of random variables, any finite number of which have a joint Gaussian (normal) distribution [38].

Gaussian-Process Regression (GPR) provides a flexible and probabilistic approach to modeling unknown functions. Consider a simple one-dimensional regression problem, mapping an input variable x to an output $f(x)$. In Figure 3.2 (a), several sample functions are drawn from a *prior* Gaussian Process, which expresses the assumed characteristics of functions before any data are observed. This prior favors smooth functions with an average (mean) value of zero across the input space². The shaded region represents the variability of these functions,

[38]: Rasmussen et al. (2006), *Gaussian Processes for Machine Learning*

2: Although the individual functions shown may not have a zero mean, the average of many such samples at any fixed x would approach zero

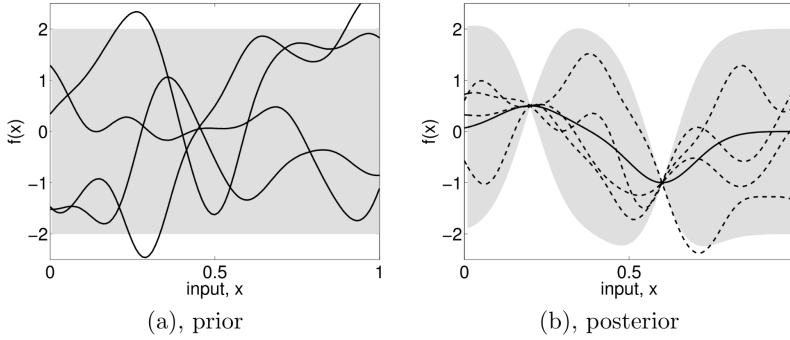


Figure 3.2: Illustration of Gaussian Process Regression. (a) Prior samples drawn from a Gaussian Process with zero mean and smooth covariance, representing the prior belief before observing any data. (b) Posterior samples and mean after conditioning on two observations, showing reduced uncertainty near the observed points.

Source: Rasmussen et al. [38]

corresponding to twice the pointwise standard deviation, which in this case is constant across x .

When a small dataset $\mathcal{D} = \{(x_1, y_1), (x_2, y_2)\}$ is observed, the process is updated to consider only functions consistent with these observations. This is illustrated in Figure 3.2 (b). The dashed lines represent sample functions that agree with the data, and the solid line indicates their mean. The uncertainty, represented by the shaded area, decreases near the observed points and remains higher where data are unavailable. This updated distribution is the *posterior* Gaussian Process, obtained by combining the prior assumptions with the observed data through Bayesian inference [39].

The choice of the prior, and particularly of the covariance (or kernel) function determines the characteristics of the functions the GP can represent, such as smoothness, amplitude, or characteristic length-scale (*i.e.* its shape)³. Adjusting the kernel parameters controls how quickly the functions vary with x , thereby tailoring the model to the data properties. In practice, learning with Gaussian Processes involves identifying the kernel and parameter values that best describe the observed data.

[39]: Gelman et al. (2013), *Bayesian Data Analysis, Third Edition*

3: Options such as the Squared Exponential (RBF) kernel produce smooth functions, while linear or periodic relationships can be captured using other kernels.

Artificial Neural networks

Artificial Neural Networks (ANNs), as the name suggests, have a behavior similar to biological neurons. Their structure is formed by a succession of layers, each one composed by nodes (or neurons) and they receive as input the output of the previous layer. This process is subsequently repeated until the final layer which has a number of neurons equal to the number of outputs [40].

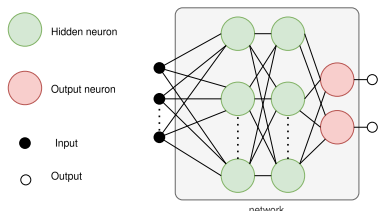
There are important aspects to be considered in the ANN model design, such as the model configuration, the network architecture and the network topology. They are discussed below.

[40]: Hagan et al. (2014), *Neural Network Design*

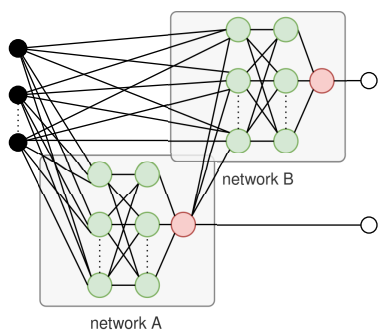
Model configuration. If the model has more than one output, several configurations are available for the implementation of the model as shown in Figure 3.3. The first one is a Multiple Inputs Multiple Outputs (MIMO) configuration, where a single network receives all the inputs and directly produces all predicted outputs. The second one is a cascade structure. This cascading approach involves training a network (*network A* in Figure 3.3 (b)) to predict one output using the available inputs. Subsequently, these inputs, along with the output from the first-output-predicting network, are fed into a second network (*network B* in Figure 3.3 (b)) that is in charge of forecasting the second output. This procedure can be repeated as many times as desired. A potential advantage of this configuration is that it may reduce the experimental data requirements to obtain satisfactory results. A third option is the combination of both configurations, where some networks may predict several outputs, while others are fed some of these outputs and subsequently use them as inputs.

Network architectures. Three network architectures have been explored in this research work:

4: Defined as $\text{logsig}(x) = 1/(1 + e^{-x})$, mapping any real input to a value between 0 and 1.



(a) MIMO configuration



(b) Cascade configuration

Figure 3.3: ANN model configurations

[41]: Beale et al. (2010), "Neural Network Toolbox"

5: The Z-score method rescales data so that each feature has a mean of 0 and a standard deviation of 1. It is computed as $z = \frac{x-\mu}{\sigma}$, where μ and σ are the feature's mean and standard deviation, respectively.

6: it refers to one complete pass of the entire training dataset through a learning algorithm during the training process of a model

[42]: Hamm et al. (2007), "Comparison of Stochastic Global Optimization Methods to Estimate Neural Network Weights"

1. Feed Forward (FF) network - Figure 3.4 (a). This is the base network architecture, where different layers are added sequentially and the flow of information is unidirectional. The transfer function adopted in the hidden layers is the differentiable *Log-Sigmoid*⁴, whereas the one employed in the output layer is a linear one with no saturations.
2. Cascade-forward (CF) network - Figure 3.4 (b). It is a variation on the feedforward network since it adds direct connections from the input and hidden layers to the output layer.
3. Radial Basis Function (RBF) network - Figure 3.4 (c). The transfer functions used in the first layer of the RBF network are different, they are local Gaussian like functions. Also, instead of multiplying by the weights, the distance between inputs and weights is computed and the bias is multiplied instead of added [40].

Network topology. Two-layer networks (one hidden and one output layer) can learn almost any input-output relationship, including non-linear ones. Adding more layers can improve the learning for more complex problems. However, increasing the number of layers or neurons per layer increases the training computational requirements, requires more data for a satisfactory model and can lead to overfitting. Therefore, the process usually starts with two layers and then the number of layers is increased if they do not perform satisfactorily [40].

Training process. The next important aspect to consider is the training process. For the FF and CF networks many Gradient- or Jacobian-based algorithms can be utilized like the Levenberg–Marquardt backpropagation algorithm [41]. It is a fast algorithm, ideal for multilayer networks with up to a few hundred weights and biases enabling efficient training. The training in this case is done in batches since sequential training is slower and does not produce better results. All data needs to be standardized applying methods like the Z-score normalization method⁵. The criteria established for deciding when to stop the training is the following one: when the performance on the validation set increases (worsens) for a number of iterations (also known as patience) or when the gradient is below a minimum (e.g. 1×10^{-7}) for a number of iterations or epochs⁶, or when a maximum number of epochs is reached (e.g. 1000). Finally, the selected network parameters are those of the best epoch.

For each network architecture, the training process is repeated a number of times (ten times is the recommended practice if the computational requirements allow it, since it guarantees reaching a global optimum with a high degree of confidence [42]). The optimal architecture and training is then selected according to a performance function evaluated with normalized values (e.g. Mean Squared Error (MSE) explained in a later section).

In the case of the RBF network, the training method consists in two stages which treats the two layers of the RBF network separately. The first layer weights and biases are tuned based on the orthogonal least squares method [40], while for the second layer are computed in one step using a linear least-squares algorithm. During training, neurons are added to the first layer (e.g. in increments of 20) trying to minimize a performance metric (e.g. MSE) to some goal. Finally, a parameter called spread is used to set the first layer biases. Larger values of this parameter promote a smoother approximation of the training data (more generalization), conversely, lower values provide a more exact fit to the training data.

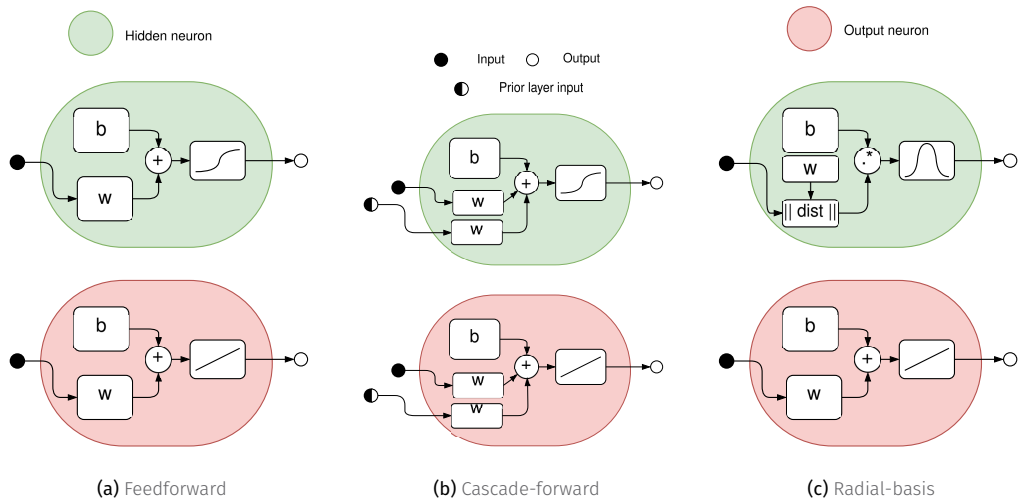


Figure 3.4: Considered ANN architectures

Other machine learning methods

- ▶ **Random Forest.** A random forest for regression is a method that combines many decision trees to make more accurate and stable predictions. A decision tree is a model that splits the data into smaller and smaller groups based on input features, creating a set of simple rules that lead to a prediction at the end of each branch. Each tree in a random forest is trained on a slightly different version of the data by randomly sampling both data points and features, and the forest's final prediction is obtained by averaging the outputs of all trees. As the number of trees increases, the prediction error stabilizes and approaches a fixed value. The performance of a random forest depends on how strong the individual trees are at predicting the target and how different they are from each other, and this balance allows the method to produce reliable predictions that are usually better than those of a single decision tree [43].
 - ▶ **Gradient-boosting** builds a strong predictive model by combining many weak models, usually decision trees, in a sequential way. Each new tree is trained to correct the errors (residuals) made by the previous ensemble, using the gradient of a loss function to guide the improvements [44].

[43]: Breiman (2001), “Random Forests”

[44]: Friedman (2001), “Greedy Function Approximation”

Surrogate Data-driven models from first-principles models. Synthetic dataset generation

One important advantage that first-principles models have over data-driven is their scalability, that is, the ability to adapt a model developed and validated in a pilot-scale system, to a large scale one. This is true for many systems as long as the system configuration remains the same. This allows to study and analyze pilot scale plants and extrapolate the results to industrial-sized plants. In addition, these type of models are also capable of predicting the behavior of the modelled systems in conditions that have not been tested (e.g. different operating or environmental conditions), although the reliability of the model could be lowered if these conditions move away from those experimentally used for some parameter calibration.

On the contrary, data-driven models are very specific to the system and operating ranges they are trained for. That is why training/calibrating a data-driven model

with a synthetic dataset generated from the evaluation of the first-principles model is common practice to obtain a surrogate model that can then be used in a larger range of operating conditions and that provides superior computational performance.

The process of generating samples from a first-principles model to train a data-driven model is called synthetic dataset generation. It consists of running the first-principles model for a set of input parameters, which can be selected randomly or following a specific distribution, and then using the outputs of the first-principles model as the training data for the data-driven model.

The first step is to define the input parameters and their ranges. This can be done by selecting the most relevant parameters for the system and determining their ranges based on the system's operating conditions. The next step is to generate a set of input parameters, which can be done using different methods such as Latin Hypercube Sampling, Monte Carlo Sampling, Sobol Sampling, or simply grid sampling [37, 45, 46]. These methods allow generating a set of input parameters that cover the entire range of the input parameters and ensure that the generated samples are representative of the system's behavior. Once the input parameters are defined, the first-principles model is run for each set of input parameters, and the outputs of the model are recorded. Finally, the recorded outputs are used to train the surrogate data-driven model.

[37]: Nossent et al. (2011), "Sobol'sensitivity Analysis of a Complex Environmental Model"

[45]: McKay et al. (1979), "A Comparison of Three Methods for Selecting Values of Input Variables in the Analysis of Output from a Computer Code"

[46]: Saltelli et al. (2000), *Sensitivity Analysis*

3.1.3 Discrete modelling by means of FSMs

Up to this point, the discussion has focused on the modeling of continuous systems, in which changes evolve smoothly over time and are typically described by differential equations. In contrast, discrete or event-driven modeling deals with systems whose states change only at distinct moments, triggered by the occurrence of specific events

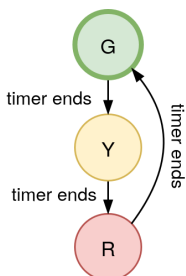
There are many ways of modeling the behavior of these systems, and the use of state machines is one of the oldest and best known. State machines allow us to think about the "state" of a system at a particular point in time and characterize the behavior of the system based on that state⁷.

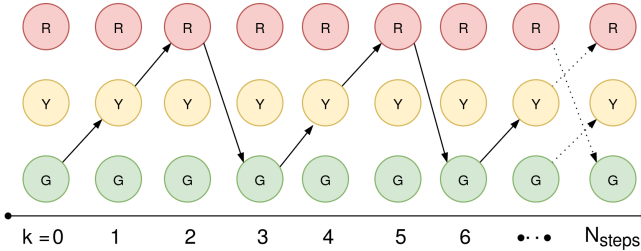
For example, a traffic light (see Figure 3.5) can be described as a finite state machine with three primary states: *green*, *yellow*, and *red*. In each state, the traffic light has a well-defined behavior (allowing vehicles to pass, warning them to slow down, or stopping them completely). The transitions between states are also clearly defined: green changes to yellow, yellow to red, and red back to green. Some transitions are possible, while others are not (e.g., green cannot jump directly to red without first passing through yellow).

So, a finite state machine is a model of behavior composed of a finite number of states and *transitions* between those states. Within each state and transition some *action* can be performed. A state machine needs to start at some *initial state*. Finite refers to a machine that has a limited number of possible states and at any given time it will be in one of those states. Its core components are described hereinafter:

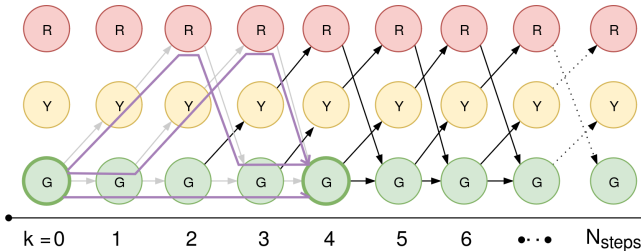
- ▶ **State.** A state represents a particular condition or stage in the machine. It represents a distinct mode of behavior or phase in a process.
- ▶ **Transition.** This is the process or event that causes the state machine to change from one state to another.
- ▶ **Action.** Specific operation or task that is performed when a certain event happens i.e. a state is entered, exited, or during a transition.
- ▶ **Model.** A stateful structure that holds information about the state of the machine. It gets updated during transitions and defines actions.

Figure 3.5: FSM representation of a traffic light





(a) Simple traffic light



(b) Traffic light with push-button

Figure 3.6: Evolution of different traffic-light FSMs assuming the timer takes one step to complete.

- **Machine.** This is the entity that manages and controls the model, states, transitions, and actions. It's the conductor that orchestrates the entire process of the state machine.

3.1.4 Forecasting and combinatory nature of FSMs

A traffic light is a simple example of a deterministic state machine, because its transitions are triggered by a single predictable input —the timer—and therefore its future trajectory is entirely fixed. From any given state, there is only one possible next step, so the entire cycle can be anticipated with certainty (see Figure 3.6 (a)). Many real systems, however, are not that simple. When the set of inputs that can trigger transitions is larger and each input leads to different successor states, the system no longer has just one linear trajectory but many possible ones. In such cases, the behavior of the machine can be represented as a branching tree, where each node corresponds to a state and each branch corresponds to a possible input event. This can be illustrated for the traffic light example if a push-button is added (see Figure 3.6 (b)). The state will be green-light unless the push-button is triggered. Starting from an initial state, evaluating now the possible paths that yield in an arbitrary final state given a number of steps becomes a combinatory problem.

This branching has important implications: while the machine is still finite in the number of states, the number of possible sequences of states over the horizon grows rapidly as more steps are considered. After just a few transitions, the tree of possible futures can expand exponentially.

3.1.5 Performance metrics

For models to be useful they need to accurately represent the real process. In order to quantitatively assess how good a model represents a real system different performance metrics are used. Four performance metrics are described: coefficient of determination (R^2), Root Mean Squared Error (RMSE), Mean Absolute Error (MAE) and Mean Absolute Percentage Error (MAPE).

8: also known as features
9: also referred as target

Coefficient of determination. Regression estimates the relationship between input variables⁸ and a continuous output variable⁹. R^2 is a direct measure of regression. It measures the proportion of the variance in the predicted variable that can be attributed to the independent variable(s), in this case the considered system inputs. Values close to one indicate a better prediction accuracy. It is calculated as follows:

$$R^2 = 1 - \frac{\sum_{i=1}^n (y_i - \hat{y}_i)^2}{\sum_{i=1}^n (y_i - \bar{y})^2},$$

where y_i is the measured or observed value for the output variable, in the i -th observation, \hat{y}_i is the estimated value of the same variable and n is the total number of observations. Finally, \bar{y} is the mean value of the experimental values.

Root Mean Square Error. RMSE is a statistical measure of the difference between the values predicted by a model and the observed values. It is calculated as the square root of the mean of the squared differences between the predicted and observed values, and it has its units.

$$\text{RMSE} = \sqrt{\frac{1}{n} \sum_{i=1}^n (y_i - \hat{y}_i)^2}$$

Mean Absolute Error. It represents the average absolute difference between predicted and measured values.

$$\text{MAE} = \frac{1}{n} \sum_{i=1}^n |y_i - \hat{y}_i|$$

Mean Absolute Percentage Error. As the MAE, it calculates the difference between the predicted and the actual values, but in this case it does so in relative terms:

$$\text{MAPE} = \frac{1}{n} \sum_{i=1}^n \left| \frac{y_i - \hat{y}_i}{y_i} \right| \times 100\%$$

3.2 Optimization

Optimization consists on finding the best solution, i.e. the optimal solution, to a problem under given circumstances. At its core, optimization seeks to determine the values of decision variables that minimize (or maximize) an objective function while respecting a set of constraints. These problems arise in diverse domains such as operations research, economics, energy systems, and machine learning, where they enable the systematic allocation of resources, the design of efficient processes, and the balancing of trade-offs between competing goals.

A general expression to define an optimization problem is:

$$\min_{\mathbf{x}, \mathbf{e}; \theta} J = f(\mathbf{x}, \mathbf{e}; \theta) \quad \text{s.t.} \quad g_i(\mathbf{x}) \leq 0, \quad i = 1, \dots, m \quad (3.1)$$

where \mathbf{x} is the vector of decision variables, \mathbf{e} the vector of environment variables, θ the list of parameters, $f(\mathbf{x})$ is the objective function to be minimized, and $g_i(\mathbf{x})$ are the constraints of the problem. The objective function is a scalar

function that maps the decision variables to a real number, representing the cost or performance of the system. The constraints are functions that restrict the feasible region of the problem, defining the set of values that the decision variables can take. The optimization problem is to find the values of the decision variables that minimize the objective function while satisfying the constraints.

Regarding the constraints, they can be categorized in two types depending whether they can be evaluated before evaluating the objective function or not:

- ▶ **Bounds** or box-bounds. These are constraints that limit the range of the decision variables, such as

$$x_i \in [l_i, u_i], \quad i = 1, \dots, n$$

where l_i and u_i are the lower and upper bounds of the decision variable x_i , respectively. They can be evaluated before evaluating the objective function.

- ▶ **Constraints**. These are constraints that restrict the feasible region (also known as domain) of the problem, such as

$$g_i(\mathbf{x}) \leq 0, \quad i = 1, \dots, m$$

where $g_i(\mathbf{x})$ are the constraint functions that depend on the decision variables \mathbf{x} , and m is the number of constraints. Its value can only be known after evaluating the problem.

These described components of an optimization problem are visualized in Figure 3.7.

3.2.1 NLP problems

A NLP problem refers to a *nonlinear programming* formulation in which both the objective function $f(\mathbf{x})$ and the constraint functions $g_i(\mathbf{x})$ can be nonlinear. These problems are generally more difficult to solve than linear programming (LP) problems, since the feasible region may be non-convex and the objective function may have multiple local minima. Solution techniques for NLP include gradient-based methods, sequential quadratic programming, interior-point methods, and heuristic approaches when derivatives are unavailable or the problem is highly non-convex.

Optimization concepts

- ▶ **Decision variables (\mathbf{x})**. These are the variables that can be controlled or adjusted in order to optimize the objective function.
- ▶ **Environment variables (\mathbf{e})**. These are the variables that cannot be controlled or adjusted, but they can affect the objective function and the constraints.
- ▶ **Objective function ($f(\mathbf{x})$)**. This is the function that needs to be minimized or maximized. It represents the goal of the optimization problem.
- ▶ **Constraints ($g(\mathbf{x})$)**. These are the restrictions or limitations that need to be satisfied in order to find a feasible solution. They can be equality or inequality constraints.
- ▶ **Search-space ($\mathcal{X} \subseteq \mathbb{R}^n$)**. This is the set of all possible values of the decision variables that satisfy the bounds.
- ▶ **Feasible region ($\mathcal{F} \subseteq \mathcal{X}$)**. This is the set of all possible values of the decision variables that satisfy the constraints. The optimal solution must lie within this region.
- ▶ **Optimal solution ($\mathbf{x}^* \in \mathcal{F}$)**. This is the set of values of the decision vari-

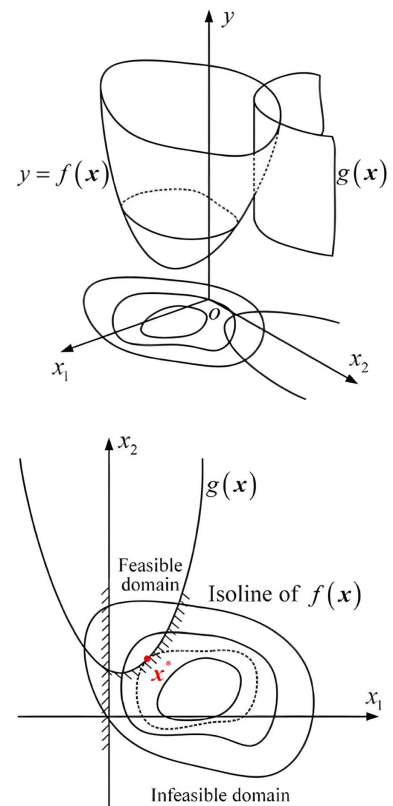


Figure 3.7: Constrained optimization problem. The goal is to minimize $y = f(\mathbf{x})$ with the two continuous decision variables x_1 and x_2 constrained to $g(\mathbf{x})$. The problem is NLP with a convex solution-space.
Source: Wang et al. [47]

ables that minimize or maximize the objective function while satisfying all the constraints.

- ▶ **Convexity.** A problem is convex if both the objective function and the feasible region are convex. Convex problems have a single global optimum, which can be found efficiently using various optimization algorithms. Non-convex problems may have multiple local optima, making them more challenging to solve.

3.2.2 MINLP problems

A Mixed Integer Non-Linear Programming (MINLP) problem, extends the NLP formulation by introducing integer (often binary) decision variables alongside continuous ones. The presence of discrete variables significantly increases the complexity of the problem, as the feasible set becomes combinatorial in nature, often leading to an exponential growth in the search space. MINLP problems naturally arise in many engineering problems where decisions such as on/off states, integer quantities, or logical relations must be combined with nonlinear models. Typical solution strategies include branch-and-bound, branch-and-cut, outer approximation, and decomposition methods.

As an example, consider the following MINLP problem:

$$\begin{aligned} \min_{x,y} \quad & (x - 3)^2 + y \\ \text{s.t.} \quad & x^2 \leq y, \\ & x \in \mathbb{R}, \quad y \in \{0, 1\}. \end{aligned} \tag{3.2}$$

In this formulation, x is a continuous variable, while y is binary. The feasible set is determined not only by the nonlinear constraint $x^2 \leq y$ but also by the discrete choice of y , which switches the constraint on or off depending on its value.

A common strategy for tackling MINLPs is by integer *relaxation*, in which the integer constraints on some variables are relaxed to continuous domains (e.g., replacing $y \in \{0, 1\}$ with $y \in [0, 1]$). The relaxed problem becomes a standard NLP, which is typically easier to solve. The solution of this relaxation can then be used to guide exact methods such as branch-and-bound or to construct valid lower bounds in global optimization algorithms. However, this is flawed in assuming the best solution of the relaxed problem is close to the full MINLP problem solution, or that the relaxed problem contains relevant information in its gradient.

3.2.3 A discussion on constraint handling

There are two main approaches to handle constraints in optimization problems:

- ▶ **Penalty methods.** These methods add a penalty term to the objective function to penalize the violation of the constraints. The penalty term is usually a function of the constraint violation, and it is added to the objective function to form a new objective function that is minimized. The penalty term can be linear or non-linear, and it can be adjusted during the optimization process to ensure that the constraints are satisfied. The main advantage of penalty methods is that they allow to handle constraints in a flexible way, and they can be used with any optimization algorithm. However, they can also lead to suboptimal solutions if the penalty term is not properly tuned, and they can also lead to numerical instability if the penalty term is too large.

- ▶ **Constraint handling methods.** These methods handle the constraints directly, by either rejecting solutions that violate the constraints or by modifying the optimization algorithm to ensure that the constraints are satisfied. The main advantage of constraint handling methods is that they guarantee that the constraints are satisfied, and they can also lead to better solutions than penalty methods. However, they can also be more complex to implement, and they can also lead to numerical instability if the constraints are too restrictive. Specific constraint-handling capable algorithms are required to solve these type of problems.

By using inequality constraints, the optimization algorithm is forced to find the best solution that satisfies these constraints. However, in problems with a horizon window, this would require returning a value of the constraint for each step within the horizon, thereby producing a large vector of inequality constraints and increasing the problem's dimension (*i.e.* its complexity). On the other hand, returning a single aggregated value for the entire episode provides much less information to the algorithm about which decisions violate the constraints and when. As a result, the optimizer may struggle to adapt its decision variables effectively and could fail to converge, or require an unfeasibly large number of objective function evaluations¹⁰.

Finally, non constraint-handling capable algorithms can be wrapped with constraint handling methods to solve problems with constraints [48], where they basically implement some type of penalty method.

¹⁰: Here, “unable” refers to requiring an unfeasible number of objective function evaluations, *i.e.*, too much time.

[48]: Farmani et al. (2003), “Self-Adaptive Fitness Formulation for Constrained Optimization”

3.2.4 Multi-objective optimization

When an optimization problem involves only one objective function, the task is called single-objective optimization. In contrast, when multiple objectives must be optimized simultaneously, the problem becomes one of multi-objective optimization. A key difference is that in the multi-objective case, objectives are often conflicting: improving one objective typically requires sacrificing performance in another [49]. As Johan Löfberg illustrates in the [YALMIP documentation](#):

It is impossible to design a car which is as light as possible, as cheap as possible, as fast as possible, and as durable as possible, all at the same time. In the end, the solution to the obviously multi-objective task of designing a car, will be a compromise. Multi-objective optimization is about finding the set of non-bad compromises, which is called the Pareto-optimal solutions.

Two main approaches are commonly used to address multi-objective problems [49]:

- ▶ Scalarization (or decomposition) methods, where the multi-objective problem is converted into a sequence of single-objective problems by combining objectives into one, for example using weighted sums or penalty methods. Each run of a single-objective solver yields one trade-off solution, so multiple runs with different scalarizations are required to approximate the Pareto set.
- ▶ Population-based methods, such as evolutionary algorithms¹¹, which evolve a set of solutions in parallel. Because they operate on a population rather than a single solution, these methods naturally approximate the entire Pareto front within a single run, capturing multiple trade-offs between conflicting objectives.

[49]: Deb (2011), “Multi-Objective Optimisation Using Evolutionary Algorithms: An Introduction”

¹¹: Described in the following section

3.2.5 Optimization algorithms

Optimization algorithms are methods designed to find the best solution to a problem by minimizing or maximizing an objective function under given constraints. Two categories are distinguished: local and global.

Local optimization

For convex problems and gradient-based methods, they typically use derivative information to guide the search efficiently.

[50]: Wächter et al. (2006), “On the Implementation of an Interior-Point Filter Line-Search Algorithm for Large-Scale Nonlinear Programming”

[51]: Kolda et al. (2003), “Optimization by Direct Search: New Perspectives on Some Classical and Modern Methods”

- ▶ **Interior Point OPTimizer (IPOPT)** [50] is a numerical optimization algorithm for large-scale NLP problems. It uses a primal-dual interior-point method, solving a sequence of barrier subproblems to handle inequality constraints while maintaining feasibility. At each iteration, IPOPT computes a Newton-type step by solving the sparse Karush-Kuhn-Tucker system, simultaneously updating primal and dual variables. Line search and barrier parameter updates ensure convergence, even for non-convex problems. It is highly efficient with sparse derivative matrices.
- ▶ **Compass search** [51] is a derivative-free local optimization method belonging to the class of direct search algorithms. At each iteration, the algorithm evaluates the objective function by probing in coordinate directions (north, south, east, west in two dimensions, or along each axis in higher dimensions) from the current point. If a trial move in any direction improves the objective, the algorithm accepts the move and continues from the new point; otherwise, the step size is reduced, and the process repeats. It is a slow but sure local optimization algorithm.
This algorithm is illustrated in Figure 3.10 (b).

Gradient-free global optimization

Global optimization: The holy grail!
60% of the time it works every time.

Johan Löfberg
Creator of YALMIP

12: they try to optimize a problem by iteratively trying to improve a candidate solution with regard to a given measure of quality

[52]: Holland (1992), *Adaptation in Natural and Artificial Systems*

[53]: Rechenberg (1989), “Evolution Strategy”

[54]: Schwefel (1981), *Numerical Optimization of Computer Models*

13: Crossover does exist in ES but plays a secondary role compared to GAs

Global gradient-free optimization refers to a family of optimization methods that aim to find the best solution to a problem without relying on gradient information. These methods are especially useful when the objective function is non-differentiable, noisy, discontinuous, or available only through expensive simulations where derivatives are impossible or impractical to compute. Unlike local optimization methods that may get trapped in nearby minima, global approaches search the entire solution space to increase the chances of finding the true global optimum.

Genetic Algorithms (GAs) and Evolutionary Strategys (ESs) are both part of the evolutionary computation family¹², but they emphasize different mechanisms. GAs, introduced by Holland [52], are inspired by biological evolution and work mainly with populations of candidate solutions represented as strings, often binary. They rely heavily on crossover (recombining parts of two solutions) along with mutation and selection, and are frequently applied to discrete or combinatorial problems. In contrast, ES, pioneered by P. Bienert, I. Rechenberg, and H. Schwefel in the 60s [53, 54], were designed for continuous optimization tasks and emphasize mutation as the primary search operator. A defining feature of ES is self-adaptation: not only the solutions but also the mutation parameters (such as step sizes or covariance structures) evolve over time, allowing the algorithm to adjust its own search dynamics¹³.

Genetic Algorithms versus Evolutionary Strategies

An interesting reflection from Francesco Biscani and Dario Izzo [34]:

Approximately during the same decades as Evolutionary Strategies were studied, a different group led by John Holland, and later by his student David Goldberg, introduced and studied an algorithmic framework called “genetic algorithms” that were, essentially, leveraging on the same idea but introducing also crossover as a genetic operator. This led to a few decades of confusion and discussions on what was an evolutionary strategy and what a genetic algorithm and on whether the crossover was a useful operator or mutation only algorithms were to be preferred.

Local versus gradient-free global optimization

When suitable, local optimization algorithms are generally preferable to heuristic approaches, as they typically achieve higher precision with far fewer function evaluations and offer more reliable convergence properties. Heuristic methods, in contrast, often demand significantly larger computational effort and may still fail to reach the desired solution quality. Their use should therefore be limited to situations where gradient information is unavailable or the problem structure prevents the application of more efficient local techniques.

Some of the algorithms presented here can theoretically, for any given finite problem, terminate with a global optimal solution as their parameters enable for a more extensive search. This theoretical result, however, is not particularly helpful, since the time required to ensure a significant probability of success will usually exceed the time required for a complete search of the solution space.

The focus is to try different algorithms and find the best alternative that, given a particular problem, can consistently find good solutions given some computational budget.

The following global optimization algorithms have been used in this research work:

- ▶ **(N+1)-ES Simple Evolutionary Algorithm (SEA)** [34, 53, 54]. Basic evolutionary strategy algorithm, where a population of individuals at each generation produces one offspring by randomly and uniformly mutating its best individual within the given bounds. Should the offspring be better than the worst individual in the population it will substitute it.
- ▶ **Simple Genetic Algorithm (SGA)** [52], [34]. Basic genetic algorithm where a population of individuals evolves through selection, crossover, and mutation. New offspring are generated by combining the genetic material of selected parents, and the population is updated by replacing less fit individuals with the newly created ones.
- ▶ **Covariance Matrix Adaptation Evolution Strategy (CMA-ES)** [55, 56], [34] iteratively samples candidate solutions from a multivariate normal distribution whose parameters are adapted over time. The distribution mean is updated toward successful candidate solutions, while the covariance matrix is incrementally adjusted to increase the likelihood of previously successful search directions, a process that can be interpreted as a natural gradient descent and as an iterated principal component analysis of successful steps. In addition, CMA-ES maintains two evolution paths that

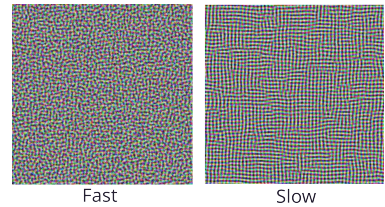


Figure 3.8: Simulated Annealing. Example illustrating the effect of cooling schedule on the performance of simulated annealing. The problem is to rearrange the pixels of an image so as to minimize a certain potential energy function, which causes similar colors to attract at short range and repel at a slightly larger distance. The elementary moves swap two adjacent pixels. These images were obtained with a fast cooling schedule (left) and a slow cooling schedule (right), producing results similar to amorphous and crystalline solids, respectively.

Source: Wikipedia

[34]: Biscani et al. (2020), “A Parallel Global Multiobjective Framework for Optimization: Pagmo”

[53]: Rechenberg (1989), “Evolution Strategy”

[54]: Schwefel (1981), *Numerical Optimization of Computer Models*

[52]: Holland (1992), *Adaptation in Natural and Artificial Systems*

[55]: Hansen (2006), “The CMA Evolution Strategy”

[56]: Gendreau et al. (2010), *Handbook of Metaheuristics*

[57]: Schlüter et al. (2009), "Extended Ant Colony Optimization for Non-Convex Mixed Integer Nonlinear Programming"

[58]: Kennedy et al. (1995), "Particle Swarm Optimization"

[59]: Gad (2022), "Particle Swarm Optimization Algorithm and Its Applications"

[60]: Storn et al. (1997), "Differential Evolution – A Simple and Efficient Heuristic for Global Optimization over Continuous Spaces"

[61]: Brest et al. (2006), "Self-Adapting Control Parameters in Differential Evolution"

[62]: Elsayed et al. (2011), "Differential Evolution with Multiple Strategies for Solving CEC2011 Real-World Numerical Optimization Problems"

[63]: Corana et al. (1987), "Minimizing Multi-modal Functions of Continuous Variables with the "Simulated Annealing" Algorithm—Corrigenda for This Article Is Available Here"

[64]: Geem et al. (2001), "A New Heuristic Optimization Algorithm"

track the correlation between consecutive steps: one path accelerates the adaptation of the covariance matrix by reinforcing favorable directions, while the other provides a robust mechanism for step-size control. This dynamic adaptation of both the covariance structure and step size allows CMA-ES to balance exploration and exploitation effectively, prevent premature convergence, and achieve fast progress toward optima even in high-dimensional, ill-conditioned, or nonconvex landscapes. The algorithm is illustrated in Figure 3.10 (a).

- ▶ **Extended Ant Colony Optimization (GACO)** [57], [34]. Ant Colony Optimization (ACO) is a class of optimization algorithms inspired by the foraging behavior of ants. Artificial ‘ants’ explore a parameter space representing all possible solutions, recording their positions and solution quality. Similar to real ants laying pheromones to guide others, simulated ants use this information so that future iterations increasingly focus on better solutions. An extended version called Extended ACO [57] generates new solutions using a multi-kernel Gaussian distribution based on pheromone-like values derived from previous solution quality. Solutions are ranked using an oracle penalty method. Extended ACO can handle box-bounded single-objective problems, both constrained and unconstrained, with continuous or integer variables.
- ▶ **Particle Swarm Optimization (PSO)** [58, 59], [34] is a population-based, derivative-free optimization algorithm inspired by the collective behavior of bird flocks. Each particle represents a candidate solution and moves through the search space with a velocity influenced by its personal best position and the global or neighborhood best positions. Through iterative updates of positions and velocities, the swarm balances exploration and exploitation to converge toward optimal solutions. The algorithm is illustrated in Figure 3.9.
- ▶ **Self-adaptive Differential Evolution (SADE)** [60–62], [34]. In the original differential evolution algorithm [60], at each iteration, new candidate solutions are generated by combining the weighted difference of randomly selected individuals with another individual from the population. This mutation step is followed by crossover to increase diversity, and selection ensures that only the better solutions survive. Many different proposals have been made to self-adapt both the crossover probability and the differential weight parameters of the original differential evolution algorithm. The used optimization library [34] implements two different mechanisms-Brest et al. [61] and Elsayed et al. [62] - together with their own addition.
- ▶ **Simulated annealing - Corana's version (SA)** [63], [34, 56] is a stochastic, derivative-free optimization algorithm inspired by the annealing process in metallurgy. The defining feature of simulated annealing is its use of a temperature parameter that decreases gradually during the search. The algorithm begins with a high initial temperature, allowing it to explore the search space freely and accept worse solutions with higher probability. As the temperature is reduced according to an annealing schedule specified by the user, the algorithm increasingly focuses on low-energy (or low-cost) regions and eventually behaves like a steepest descent method. This cooling process helps the system move from broad exploration toward fine-grained exploitation. Corana's version of SA introduces coordinate-wise temperature adaptation, where each variable has its own temperature schedule, and the step size is adjusted based on the success rate of previous moves. This allows the algorithm to adaptively balance exploration and exploitation for each dimension, improving convergence on high-dimensional or rugged landscapes. The algorithm is illustrated in Figure 3.8.
- ▶ **(Improved) Harmony Search (IHS)** [64], [34] inspired by the improvisation process of musicians, each musician represents a decision variable where each note corresponds to a value, and the aim is to achieve the best

possible harmony —analogous to finding the global optimum. In practice, every member of the population contributes to the search. At each iteration, a new solution is generated and, if it performs better than the worst individual in the population, it replaces it. The number of fitness function evaluations is therefore equal to the number of iterations. An improved version in Biscani *et al.* [34] of HS introduces dynamic parameters: the probability of reusing values from the decision vector is adjusted linearly, while the mutation rate decreases exponentially over time. These refinements are designed to balance exploration and exploitation more effectively¹⁴.

In this research work the two problems that are going to be presented on each part are non linear and non-convex. One of them also includes constraints. Meta-algorithms enable adapting algorithms that would otherwise be limited to certain types of problems. This is achieved by wrapping them with the so-called meta-algorithm. In this study two meta-algorithms are used:

- ▶ **Monotonic Basin Hopping (MBH)** [34] is an optimization algorithm that combines local search with stochastic exploration. It repeatedly perturbs candidate solutions within a neighborhood and applies a local optimization algorithm to find nearby minima. If the best solution improves, it is updated; otherwise, the search resets. This iterative approach allows the algorithm to escape local minima and efficiently explore the landscape in search of the global optimum.
- ▶ **Self-adaptive fitness formulation for constrained optimization (CSTR-SA)** [48]. The self-adaptive constraint-handling meta-algorithm allows any single-objective unconstrained algorithm to solve constrained problems. It adapts its parameters based on the current population, using a penalty approach that accounts for constraint violations. Each individual is evaluated by both objective value and normalized constraint infeasibility, and the population is evolved using the wrapped algorithm with penalized objectives. The best individuals are reinserted immediately, influencing the next generation, making this approach compatible with non-generational evolutionary algorithms.

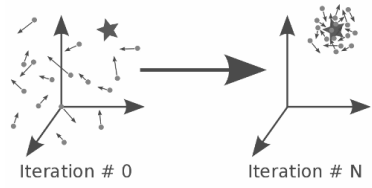


Figure 3.9: Particle Swarm Optimization concept. Each particle adjusts its velocity based on its own experience and that of neighboring particles to explore the search space and converge towards optimal solutions.
Source: Pagmo 2.19.1 documentation

¹⁴: While HS has demonstrated competitive results, it has also been criticized for its metaphor: the musical analogy adds little explanatory value and may obscure the algorithm's mechanics, which in essence resemble those of ESSs or GAs, relying on concepts such as mutation and crossover.

[48]: Farmani *et al.* (2003), "Self-Adaptive Fitness Formulation for Constrained Optimization"

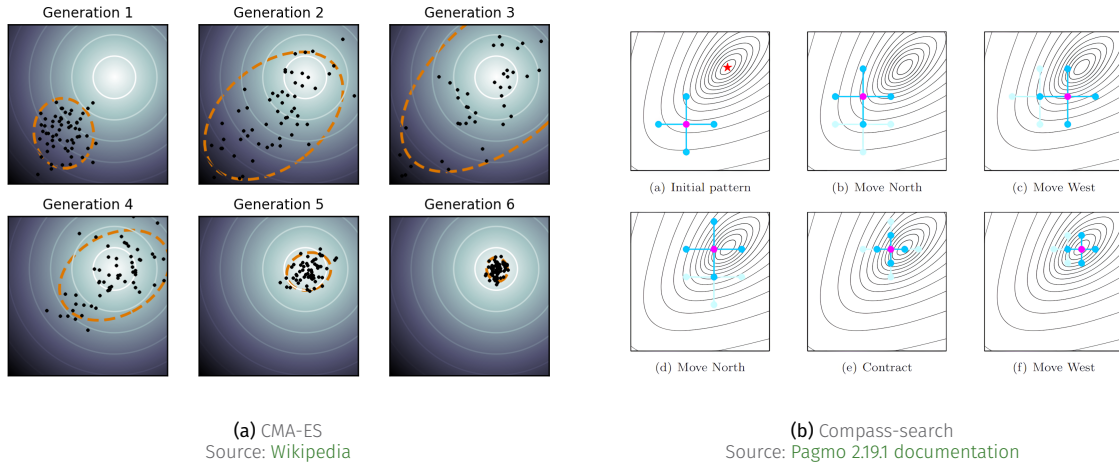


Figure 3.10: Illustration of optimization runs for two algorithms. In CMA-ES (a) it shows the covariance matrix adaptation on a simple two-dimensional problem. The spherical optimization landscape is depicted with solid lines of equal f -values. It shows how the distribution (dotted line) of the population (dots) changes during the optimization. On this simple problem, the population concentrates over the global optimum within a few generations.

3.3 Control

Controllers are mechanisms that allow us to manipulate the behavior of a system. While modeling and simulation provide a way to passively describe and predict how a system evolves, controllers take the next step by actively influencing the system in order to promote a desired behavior. In this way, controllers are fundamental to turning a passive system description into an autonomous system capable of regulating itself and achieving specific goals.

The general workflow of control engineering is: start with a dynamical system of interest, develop a mathematical model that captures its essential behavior, and then design a control policy that drives the system toward the desired performance. Depending on how this is achieved, different types of control strategies can be distinguished:

- ▶ Passive control: The desired behavior is embedded into the design of the system itself, without requiring active intervention. For example, designing a building with proper thermal insulation ensures it maintains stable indoor temperatures without external control actions.
- ▶ Active control: The controller actively supplies energy or signals to the system in order to adjust its behavior. Active control can be further classified into:

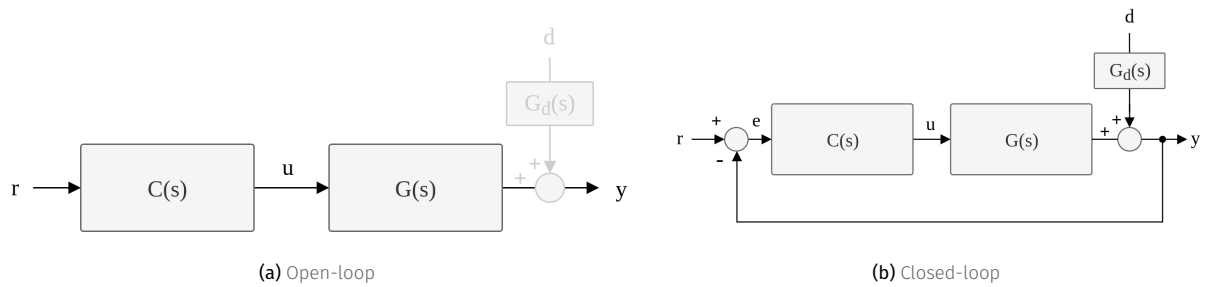


Figure 3.11: Control diagrams

- Open-loop control: A sequence of control actions (or a predefined trajectory) is computed in advance and applied to the system without measuring its actual response. This approach is simple but fragile, since it assumes the system will behave exactly as predicted.
- **Closed-loop (feedback) control:** The controller continuously measures the outputs of the system and adjusts its actions based on the observed behavior. This feedback mechanism allows the system to autonomously correct deviations and respond to changes in real time.

Feedback control, in particular, offers several fundamental advantages over open-loop strategies:

- ▶ Robustness to uncertainty: Real systems are never perfectly known —models are approximations, and parameters may vary. Feedback allows the controller to adapt its actions on the fly, reducing the impact of modeling errors.
- ▶ Rejection of disturbances: External disturbances, whether measurable or not, can affect the system output. Feedback enables the controller to partially or fully counteract these disturbances.
- ▶ Stability enhancement: A system that is unstable when uncontrolled (open-loop) can often be stabilized through properly designed feedback, ensuring safe and predictable behavior.

In short, control theory provides a framework that transforms dynamical systems from passive entities into actively regulated, autonomous ones. Through feedback, controllers achieve robustness, disturbance rejection, and stability.

3.3.1 PID controllers

A PID controller is one of the most widely used feedback control strategies in engineering¹⁵ because it combines three complementary mechanisms that work together to regulate a system effectively [66]. The proportional term (P) generates a control action directly proportional to the instantaneous error $e(t)$, which is the difference between the desired setpoint and the actual process variable; this provides an immediate response that reduces deviations. However, proportional action alone often leaves a steady-state error, which is corrected by the integral term (I). By integrating the error over time, the integral term accumulates past deviations and adjusts the control signal until the steady-state error is eliminated, ensuring that the system output eventually matches the setpoint exactly. While proportional and integral actions ensure responsiveness and accuracy, they may lead to sluggishness or overshoot if the system changes rapidly. To address this, the derivative term (D) predicts future behavior by considering the rate of change of the error, effectively damping oscillations and improving stability by anticipating trends before they cause large deviations. Together, these three terms balance immediate reaction, long-term correction, and predictive adjustment, resulting in the general PID control law¹⁶:

$$u(t) = K \left(e(t) + \frac{1}{T_i} \int_0^t e(t) dt + T_d \frac{de(t)}{dt} \right), \quad (3.3)$$

where K is the proportional gain, T_i the integral time, and T_d the derivative time. By tuning these parameters appropriately, the PID controller can be adapted to a wide variety of dynamic systems, offering both robustness and simplicity, which explains its success and popularity in industrial and scientific applications. PI controllers are sufficient for many control problems, particularly when process dynamics are benign and the performance requirements are modest. This is the

¹⁵: Honorable mention here to MPC control, not used in this research work but widely used in the industry for complex and effective process control, it shares many similarities to the optimization just described above and the reader is referred to Camacho et al. [65]

[66]: Hägglund et al. (2006), *Advanced PID Control*

¹⁶: In ideal form, other representations exist like the parallel representation

case of the processes of this research work. However, some enhancements can be applied to extend the basic PID scheme:

- ▶ **Anti-windup on the integral action:** prevents the integrator from accumulating error when the actuator saturates, avoiding overshoot and slow recovery once the control signal returns within bounds.
- ▶ **Feedforward:** improves disturbance rejection and setpoint tracking by adding a direct control action based on measurable inputs or known process dynamics, reducing the burden on the feedback loop.
- ▶ **Gain scheduling:** adapts controller parameters to changing operating conditions, maintaining performance and stability across a wide range of process regimes. It compensates for nonlinearities and varying dynamics by switching or interpolating between different sets of controller gains based on the current operating point or system state.

3.4 Hierarchical control: how optimization and control come together

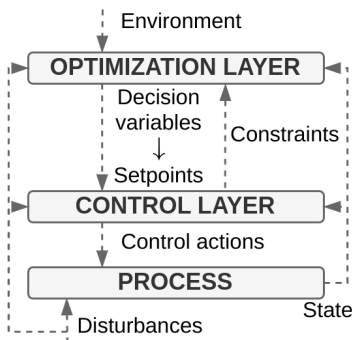


Figure 3.12: Hierarchical control architecture

[67]: Scattolini (2009), “Architectures for Distributed and Hierarchical Model Predictive Control – A Review”

17: depends on the particular problem, they can get very complex too

Ideally, a centralized solution would handle both low-level process control tasks and higher-level resource management and distribution optimization. However, this is rarely the case. For instance, planning the optimal distribution of resources on a monthly basis may require solving a complex optimization problem, often with a combinatorial component. Such optimization is computationally expensive, so it is typically addressed using simplified process models with long sampling periods, and the computation of new decisions is performed only occasionally.

In contrast, low-level process control requires frequent updates of control actions that must be computed quickly. A single centralized system attempting to address both high- and low-level problems would therefore face major challenges. Moreover, in large-scale systems, any failure of this centralized solution could compromise many —often critical— processes. For these reasons, decentralized and distributed approaches are often preferred.

In such approaches, complexity is divided among different agents (or layers). Each agent has a limited, problem-specific set of responsibilities. Various architectures exist for managing the information exchange between these agents. Summarizing, the factors that justify the need of a decentralized solution are [67]:

- ▶ Different time scales between low- (in the order of seconds) and high-level (in the order of hours) layers
- ▶ Different dynamic behavior: usually fast for regulatory control, slow or static for upper layers.
- ▶ Different computing requirements: complex resource optimization compared to generally more straightforward process control¹⁷
- ▶ Decoupling between optimization and critical process control

In this research work, a hierarchical two-layer control architecture is adopted as visualized in Figure 3.12. At the upper layer, a Real-Time Optimization (RTO) determines the optimal operating conditions with respect to an economic performance metric, using a detailed but pseudo-dynamic nonlinear physical model of the system. The lower layer relies on a simpler linear dynamic model, often derived through identification experiments, to design regulators such as MPC or PID controllers that ensure the RTO targets are met, while also providing bottom-up feedback on constraints and performance. Although the RTO model is inherently static, it should be periodically updated through reconciliation procedures to account for slow disturbances. Consistency must be maintained

between the models used in the upper and lower control layers, and the steady-state optimization should ensure that the computed input and output references are both feasible and as close as possible to the desired setpoints [67].

Just some phrase, it may be longer, it might
be shorter, but in the end, it's a phrase.
Aren't we all phrases? Well, no

Someone else answering someone

Part I

ENERGY MANAGEMENT IN MED PROCESSES DRIVEN BY VARIABLE ENERGY SOURCES

Just some phrase, it may be longer, it might
be shorter, but in the end, it's a phrase.
Aren't we all phrases? Well, no

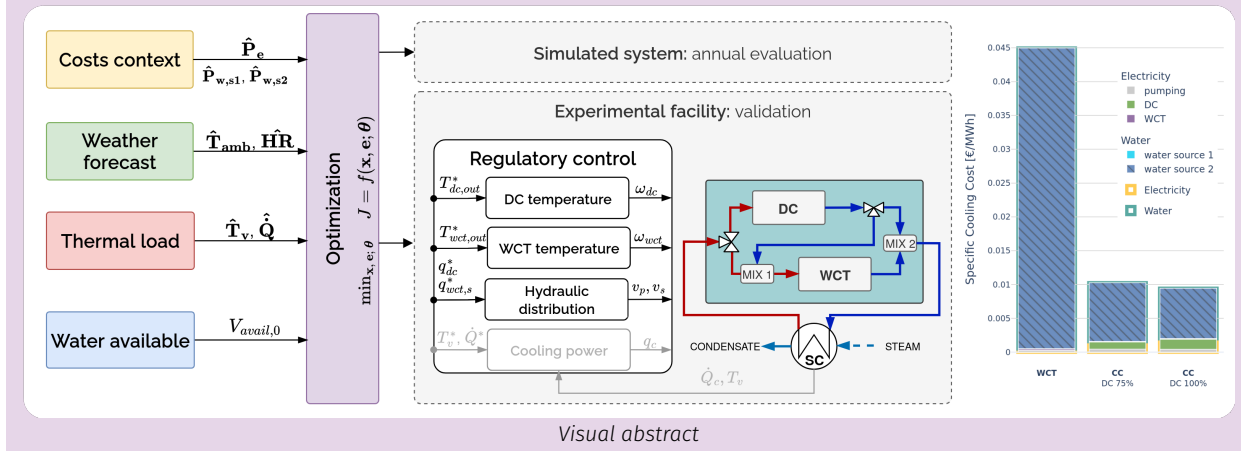
Someone else answering someone

To-davía por hacer el TL;DR cuando se tengan resultados de optimización. De momento solo está copiado de la otra parte

TL;DR

To enhance the applicability and sustainability of solar thermal technologies, this work investigates a novel cooling system for the power block of a CSP plant, combining dry and wet cooling components. A model of the CCS was developed alongside a two-stage optimization strategy. The methodology was validated using an experimental pilot plant, achieving R^2 values above 0.9 for the main output variables and successfully adapting the plant's operation to changing conditions.

A case study is presented for a commercial 50 MWe CSP plant with 8 hours of storage, Andasol-II, using annual simulations under a water-scarcity scenario where the current wet-only cooling system is replaced with the proposed CCS. Results indicate a potential 80 % reduction in cooling costs and a 48 % reduction in mean annual water use, but more importantly, a 38 % reduction during the driest and hottest months, demonstrating the significant potential of the system when operated optimally.



Part structure

This part is structured as follows: first in Chapter ?? (??) a context of concentrated solar thermal technologies is provided and their relationship with the water resource, specifically for the case of CSP. Then, the experimental CCS pilot at PSA is presented in Chapter ?? . The methodology for modelling and optimizing the operation of the system are described in Chapter ?? and Chapter ??, respectively. Both are validated in the experimental plant as showcased in Chapter ?? . Finally, Chapter ?? (??), describes and analyzes the results of the annual simulations performed for a commercial CSP plant using the proposed cooling system.

4

Thermal desalination

TL;DR

Desalination is often seen as a solution to mitigate freshwater scarcity in the face of climate change and population growth [68, 69]. It already plays a fundamental role in many regions [70], but, as more frequent droughts and water shortages are expected, the demand for desalinated water is likely to increase.

However, desalination also faces several challenges, the most important being the intense energy required to separate salts from seawater, which makes it an expensive process compared to other methods to obtain fresh water.

Low-temperature Multi-Effect Distillation (MED) systems constitute a mature, robust, and technically sound solution for brine concentration and resource recovery, especially when paired with waste or renewable heat sources. Rather than being seen as outdated compared to mechanical desalination, modern MED configurations play a complementary role in integrated water-energy systems aimed at sustainability and near-zero discharge.

4.1 Water crisis

One of the many bad consequences of climate change is the rapid desertification of the planet. According to World Resources Institute projections [71] (See Figure 4:1), 51 countries will suffer from high water stress by 2050. Many regions, including the Arabian Peninsula, Iran, India, and North Africa, are expected to consume at least 80 % of their water supply. The issue is not confined to emerging economies, as Southern European countries like Spain, Italy, and Portugal are also significantly affected with projections of extremely high water scarcity.

Desalination is often seen as a solution to mitigate freshwater scarcity in the face of climate change and population growth [68, 69]. It already plays a fundamental role in many regions [70], but, as more frequent droughts and water shortages are expected, the demand for desalinated water is likely to increase [72]. However, desalination also faces several challenges, the most important being the intense energy required to separate salts from seawater, which makes it an expensive process compared to other methods to obtain fresh water.

In a water scarcity scenario, the priority should always be to reduce the water demand in the first place [73]. Secondly, to recycle as much water as possible so that it can be reused [74]. However, for many parts of the world, these are only palliative measures. Simply put, there will not be enough water available to satisfy its needs, and thus the energy intense process of desalination is the only viable alternative.

Great efforts are being made to reduce the energy consumption of desalination and use renewable energies to increase its sustainability [75–77]. Another path to follow is to generate added value from the separation process.

4.1	Water crisis	41
4.2	Brine concentration and mining	42
4.3	Overview of Desalination Technologies	43
4.3.1	Mechanical Technologies	43
4.3.2	Thermal Technologies	43
4.3.3	Thermal desalination timeline and comparison with Reverse Osmosis (RO)	44
4.4	(Variable) Energy sources for thermal separation processes	46
4.4.1	Solar thermal	46
4.4.2	Waste heat	47

[71]: Kuzma et al. (2023), "Aqueduct 4.0"

[68]: Pltonykova et al. (2020), "The United Nations World Water Development Report 2020: Water and Climate Change."

[69]: Jones et al. (2019), "The State of Desalination and Brine Production"

[70]: Eke et al. (2020), "The Global Status of Desalination"

[72]: Mekonnen et al. (2016), "Four Billion People Facing Severe Water Scarcity"

[73]: Semiat (2008), "Energy Issues in Desalination Processes"

[74]: Howe et al. (2012), *Principles of Water Treatment*

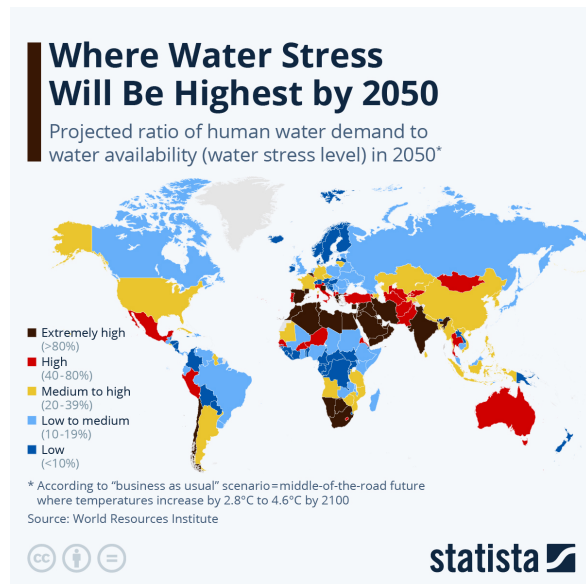
[75]: Shekarchi et al. (2019), "A Comprehensive Review of Solar-Driven Desalination Technologies for off-Grid Greenhouses"

[76]: Allouhi et al. (2024), "Towards Green Desalination"

[77]: Schär et al. (2023), "Optimization of Sustainable Seawater Desalination"

Figure 4.1: Global water stress map.

Source: Statista.



4.2 Brine concentration and mining

[78]: Panagopoulos (2022), "Study and Evaluation of the Characteristics of Saline Wastewater (Brine) Produced by Desalination and Industrial Plants"

[79]: Panagopoulos et al. (2020), "Environmental Impacts of Desalination and Brine Treatment - Challenges and Mitigation Measures"

A byproduct of the desalination process, brine typically exhibits salinities 1.6–2.1 times higher than seawater, along with residual process chemicals such as coagulants, antiscalants, and disinfectants [78]. Its conventional disposal methods—such as marine discharge, deep-well injection, evaporation ponds, and land application—are often unsustainable, leading to marine ecosystem stress, soil salinization, and groundwater contamination [79]. High-salinity plumes can cause osmotic shock in marine organisms, disrupt seagrass and coral communities, and alter local biogeochemical conditions. These impacts are particularly pronounced in semi-enclosed basins such as the Mediterranean or Red Sea, where dilution capacity is limited.

At the same time, desalination brine represents a largely untapped resource. Brines are rich in sodium, chloride, magnesium, calcium, and potassium, as well as trace valuable metals like lithium, rubidium, and cesium, which have high commercial value [79]. This recognition has led to growing interest in brine management and valorization, an approach that aligns with the principles of a circular water economy. Through Minimum Liquid Discharge (MLD) and Zero Liquid Discharge (ZLD) systems, it is possible to recover up to 95–100 % of freshwater and extract valuable salts and minerals, turning waste into a secondary source of raw materials [79]. This strategy not only reduces environmental impacts but also offers potential economic benefits, offsetting part of the desalination cost.

However, technical and economic barriers still limit large-scale implementation of brine mining. Challenges include high energy demand, low extraction efficiencies for trace elements, and the immaturity of integrated hybrid systems combining membrane, thermal, and chemical processes. Moreover, the dominance of sodium chloride—by far the most abundant constituent—means that saturation processes generate vast quantities of common salt, creating logistical and market challenges for its reuse. Recent studies are exploring new applications for desalination brines, such as using them as sources of chloride and nitrate ions in hydrometallurgical leaching or as inputs for industrial chemical production [80].

[80]: Hernández et al. (2020), "Use of Seawater/Brine and Caliche's Salts as Clean and Environmentally Friendly Sources of Chloride and Nitrate Ions for Chalcopyrite Concentrate Leaching"

4.3 Overview of Desalination Technologies

Desalination refers to the set of processes that remove dissolved salts and impurities from saline water to produce freshwater suitable for drinking, irrigation, or industrial use. These technologies can be broadly divided into thermal and mechanical-based processes, depending on the dominant physical mechanism of salt separation [81].

[81]: El-Dessouky et al. (2002), *Fundamentals of Salt Water Desalination*

4.3.1 Mechanical Technologies

Membrane processes rely on selective transport through semipermeable membranes, driven by pressure, concentration, or electrical potential differences, without phase change. They have become dominant in global desalination capacity because of lower energy requirements and modular scalability. The main categories are:

- ▶ Reverse Osmosis (RO). The most widely adopted method, where high-pressure pumps (50-80 bar for seawater) force water through semipermeable membranes, rejecting dissolved salts. RO systems achieve high recovery and energy efficiency, particularly when coupled with modern energy recovery devices, but require careful pretreatment to prevent fouling and scaling.
- ▶ Nanofiltration (NF) and Forward Osmosis (FO). Emerging variants designed for partial desalination, pretreatment, or hybrid systems that improve overall process efficiency.

4.3.2 Thermal Technologies

Thermal desalination processes are based on phase change, involving the evaporation of saline water and condensation of vapor as pure distillate. They were the first large-scale desalination methods to be commercialized and remain widely used, particularly in areas with access to low-cost fuel or waste heat. The main thermal processes are:

- ▶ Multi-Stage Flash (MSF). In MSF, seawater is heated and then flashed into vapor in a series of chambers operating at successively lower pressures. The vapor is condensed to produce distilled water, and the released heat is recovered to preheat the feed. MSF systems are robust and well-proven for large capacities but have high thermal and electrical energy requirements.
- ▶ Multi-Effect Distillation (MED). MED involves a sequence of evaporation-condensation stages (or “effects”) at decreasing pressures. Vapor produced in one effect serves as the heating medium for the next, significantly improving thermal efficiency. MED systems typically operate at 60–70 °C to minimize scaling but can reach up to 120 °C when properly pretreated. They are highly reliable and well-suited to integration with waste heat or solar thermal sources.
- ▶ Vapor Compression (VC). In Vapor Compression, the vapor generated from the feed is compressed either mechanically (MVC) or thermally (TVC) to raise its temperature and pressure so it can serve as the heat source for further evaporation. MVC systems are compact and efficient for small to medium capacities, while TVC is often combined with MED to improve energy recovery.
- ▶ Membrane Distillation (MD). Membrane Distillation bridges the gap between thermal and membrane technologies. It operates on the principle of vapor-phase transport through a hydrophobic, microporous membrane. The driving force is a vapor pressure difference generated by a temperature gradient across the membrane, rather than hydraulic pressure. The

[82]: Milow et al. (1997), "Advanced MED Solar Desalination Plants. Configurations, Costs, Future — Seven Years of Experience at the Plataforma Solar de Almeria (Spain)"

[83]: Alarcón-Padilla et al. (2007), "Application of Absorption Heat Pumps to Multi-Effect Distillation"

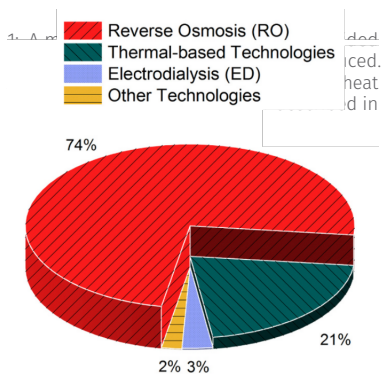


Figure 4.2: Desalination technologies used at plants worldwide in 2019

Source: Panagopoulos et al. [79]

[84]: Bouma et al. (2020). "Metrics Matter"

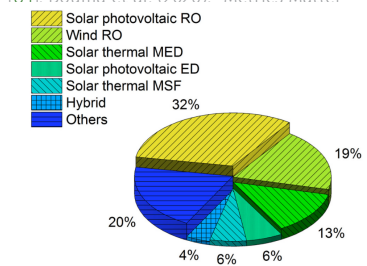


Figure 4.3: Desalination technologies coupled with renewable energy sources at plants worldwide.

Source: Panagopoulos et al. [79]

hot saline feed partially evaporates at the membrane surface, and the vapor diffuses through the membrane pores to condense on the cooler permeate side. MD can utilize low-grade or waste heat (< 80 °C), tolerate very high salinity feeds (even near saturation), and achieve high rejection rates (>99.9 %). Common configurations include Direct Contact MD (DCMD), Air-Gap MD (AGMD), Vacuum MD (VMD), and Sweeping-Gas MD (SGMD). Although still emerging at industrial scale, MD is particularly promising for brine concentration, ZLD systems, and solar-driven desalination.

4.3.3 Thermal desalination timeline and comparison with RO

Thermal desalination technologies, such as MED, MSF, and newer hybrid configurations, have evolved through several decades of incremental improvements focused primarily on maximizing thermal efficiency and reducing specific energy consumption. Early developments emphasized heat recovery, exemplified by the integration of Thermal Vapor Compression (TVC) [82] and absorption heat pumps (DEAHP) [83], both designed to increase the gain output ratio¹ by reusing latent heat more effectively. Research throughout the 1980s and 1990s concentrated on optimizing heat exchanger design, corrosion resistance, and system modularity, leading to steady improvements in performance and reliability. However, despite these advances, the fundamental thermodynamic limits of phase-change separation and the high capital cost of metallic heat exchangers have constrained further cost reductions and scalability.

By the late 1990s and early 2000s, it became increasingly clear that mechanically driven separation—particularly reverse osmosis (RO)—offered superior performance from both energetic and economic perspectives. RO's rise was enabled by major advances in polymer science, leading to thin-film composite membranes with high salt rejection and flux, as well as by the widespread deployment of energy recovery devices that dramatically lowered specific energy consumption.

A variety of metrics can be used to measure the energy efficiency of a desalination plant, each with different purposes and conveying different information. Primary energy consumption is the metric most closely tied to fuel consumption and, ultimately, to operating costs. This metric provides the fairest comparison between desalination technologies. Under any accurately defined metric in use today, RO outperforms MED on the basis of primary energy consumption. RO's efficiency advantage results from the cost and "conductivity" advantages of membranes over heat exchangers. Significant improvements in heat exchanger costs or heat transfer coefficients would be needed to make thermal desalination technologies such as MED competitive in this respect [84]. If we extend the comparison to primary energy consumption, which correlates directly with fuel usage. While MED uses approximately three times the exergy of an RO system at the desalination system inlet, it requires less than twice the primary energy (11.3 % compared to 20.6 %). The smaller gap arises because of the thermodynamic penalty associated with converting primary energy into electricity rather than into steam. Thus, while RO remains more efficient overall, the difference narrows when considering primary energy or co-generation scenarios, where electricity and water are produced together. In such cases, overall second-law efficiencies can approach 70 %, with only about a 1 % difference between RO and thermal technologies [84, *-8].

In all thermodynamic comparisons, RO has consistently outperformed MED. However, economic factors are equally decisive. Desalination plants are designed to minimize the leveled cost of water (LCOW), which depends not only on energy consumption but also on capital costs, material properties, and maintenance requirements. For example, while the cost of energy is comparable in co-production systems, RO benefits from the lower material and fabrication

costs of polymer membranes compared to the metallic heat exchangers used in thermal systems. Furthermore, membranes exhibit much higher effective conductance than heat exchangers, contributing to their overall economic and energetic advantage. Within the thermal technologies, this primary energy analysis also reveals that lower temperature and simpler systems results in higher overall efficiencies².

RO technology is the most prevalent, with 74 % of the world's installed capacity using this technology in 2019, while another 21 % and 3 % remained in the use of thermal technologies (namely, MED and MSF) and ED [79]. However, There has been a renewed research focus on low-temperature, small-scale thermal desalination. This resurgence is driven by the increasing availability of low-grade or waste heat, the desire for robust, low-maintenance systems in off-grid or remote regions, and the need for brine concentration and zero-liquid discharge applications where RO performance declines sharply. The development of membrane distillation (MD) –a hybrid thermal-membrane process— is an example of this shift.

The Case for Multi-Effect Distillation

In light of the comparative analysis between thermal and membrane desalination technologies, Multi-Effect Distillation stands out as a resilient and adaptable option —particularly for brine concentration and ZLD applications [85]. While RO dominates conventional seawater desalination due to its lower specific energy consumption, thermal systems offer unique advantages in scenarios where high salinity, waste heat availability, or stringent water quality requirements become critical factors.

Recent studies reinforce the viability of modern MED configurations. Panagopoulos [86] developed a comprehensive techno-economic model for a MED-thermal vapor compression (MED-TVC) system designed to treat high-salinity brines. The analysis demonstrated that a four-effect MED-TVC unit operating with 120 °C steam achieved the lowest freshwater production cost ($\approx 3.0 \text{ USD}_{2020} \cdot \text{m}^{-3}$) under conventional heat supply. When integrated with industrial waste heat, the cost decreased substantially to $\approx 1.7 \text{ USD}_{2020} \cdot \text{m}^{-3}$, with a payback period below two years. These results confirm that waste-heat-driven MED represents an economically viable pathway for sustainable brine management and resource recovery.

From a thermodynamic perspective, MED processes are capable of concentrating brines up to ZLD conditions, particularly when constructed with advanced corrosion-resistant alloys (e.g., super-duplex or hyper-duplex stainless steels) that withstand chloride concentrations above 18,000 mg/L. Exergy analyses from Panagopoulos [86] show that the largest irreversibilities occur in the thermal vapor compressor and evaporation stages; nonetheless, the overall exergy efficiency remains competitive for low-temperature thermal systems. Moreover, the recovered freshwater consistently meets high-quality standards (< 50 mg/L TDS), offering added economic and environmental value.

Consequently, low-temperature MED systems can be regarded as a mature, robust, and technically sound solution for brine concentration and resource recovery, especially when coupled with renewable or waste heat sources. Far from being obsolete, modern thermal configurations complement mechanical desalination technologies in integrated water-energy systems aimed at achieving sustainability, resource circularity, and near-zero discharge.

Overall, thermal desalination processes are characterized by high reliability, excellent product water quality, and strong compatibility with co-generation and heat-integration strategies. Although their specific energy consumption remains higher than that of RO, this gap diminishes in high-salinity and brine

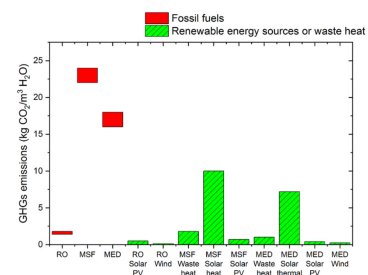


Figure 4.4: Greenhouse Gas (GHG)s emissions per cubic meter of freshwater produced
Source: Panagopoulos et al. [79].

[85]: Zaragoza et al. (2022), "Coupling of Nanofiltration with Multi-Effect Distillation for Solar-Powered Seawater Desalination towards Brine Mining and Water Production for Agriculture"

[86]: Panagopoulos (2020), "Process Simulation and Techno-Economic Assessment of a Zero Liquid Discharge/Multi-Effect Desalination/Thermal Vapor Compression (ZLD/MED/TVC) System"

[87]: Lienhard et al. (2017), "Thermodynamics, Exergy, and Energy Efficiency in Desalination Systems"

concentration applications, where mechanically driven processes suffer sharp efficiency losses due to osmotic limitations [87].

In conclusion, while RO remains the benchmark technology for large-scale seawater desalination, thermal and hybrid systems –particularly MED and MED-TVC– play an indispensable complementary role. They enable the efficient use of low-grade heat, ensure superior product water quality, and provide a sustainable route for brine minimization and resource recovery.

4.4 (Variable) Energy sources for thermal separation processes

[88]: Gude (2018), "Emerging Technologies for Sustainable Desalination Handbook"

Coupling desalination plants with renewable energy sources such as solar energy, geothermal energy, wind power, tidal power or other alternative energy sources such as waste heat from industrial processes. As compared to fossil fuels, renewable energy sources are abundant and more sustainable. Moreover, Figure 4.4 (green bars) presents the GHGs emissions per m³ of freshwater produced by the major desalination technologies when renewable energy sources or waste heat are used. As shown in Figure 4.4, GHGs emissions are significantly lower when using renewable sources of energy or waste heat. Fig. 6 shows the desalination plant types which are based on renewable energy sources [88]. Furthermore, some desalination technologies are self-sufficient and use excess energy from one stage of the cycle to lower pressure or boost temperature at another stage, such as in the thermal-based technologies (MSF and MED).

4.4.1 Solar thermal

There are two ways in which solar thermal energy can be coupled with thermal desalination processes. Either a solar field can be purposely built to drive the desalination process (standalone or partially with other heat source), or using a co-generation scheme of energy and water in a Concentrated Solar Power + Desalination (CSP+D) configuration. This integration offers significant advantages, including reduced costs for co-producing electricity and freshwater, improved cost-effectiveness through shared infrastructure and economies of scale, and additional savings in greenhouse gas emissions. One critical synergy arises from the fact that during high solar irradiance periods, when solar plants generate maximum (even excess) power coincides with water scarcity periods, making solar-driven desalination particularly effective. The choice between Concentrated Solar Power (CSP)+MED and CSP+RO is highly dependent on regional conditions [89]:

- ▶ In regions with low seawater salinity and lower ambient temperatures (like the Mediterranean), CSP+RO is generally more favorable. The penalty on power production from integrating MED is often higher than the electricity consumption of RO in these conditions.
- ▶ In regions with high seawater salinity and temperature (like the Arabian Gulf), CSP+MED becomes more attractive. The high salinity increases RO's electricity consumption, making the thermal route more efficient and cost-effective, especially when dry cooling is used for the power cycle.

To mitigate the risks of fully replacing the power plant's condenser with a desalination unit (which makes power production dependent on the desalination plant), hybrid configurations like LT-MED-TVC have been developed. This concept uses a combination of exhaust steam and extracted steam to drive the desalination, offering a good balance of efficiency and operational flexibility. In some cases, especially with dry cooling, it can outperform CSP+RO.

[89]: Palenzuela et al. (2015), *Concentrating Solar Power and Desalination Plants*

Furthermore, hybrid desalination systems that combine both membrane (RO) and thermal (MED) processes with a CSP plant are also seen as a promising path for combined desalination and brine concentration applications.

One example of a CSP+D system is Sundrop Farms in Port Augusta, South Australia, representing the world's first commercial application using concentrated solar thermal power to co-generate electricity, freshwater, and heating for horticulture [90]. Its central solar tower, targeted by 23,000 mirrors, produces steam to generate electricity, heat and cool greenhouses, and power a desalination plant. The system annually yields 1,700 MWh of electricity, 250,000 m³ of desalinated water from the saline Spencer Gulf, and 20,000 MWh of thermal energy. The freshwater is used in the greenhouses and then recycled, while the resulting brine is managed by sending it to existing power station outflows, with ongoing research into mineral recovery.

[90]: Palenzuela et al. (2019), "Concentrating Solar Power and Desalination Plants"

4.4.2 Waste heat

A significant portion of the world's primary energy consumption³ is ultimately released as waste heat from industrial processes and power generation facilities [91, 92]. This thermal energy, often regarded as a byproduct or liability, represents an immense and largely untapped resource. Instead of being vented to the environment, it can be harnessed either directly or through conversion systems to supply energy for various desalination technologies, thereby lowering operational costs and reducing the environmental footprint of freshwater production.

3: estimated between 20 and 50 %

Waste heat has therefore emerged as one of the most promising sustainable heat sources for low-temperature thermal desalination systems. Its integration into desalination processes can take several forms. In hybrid configurations, waste heat can be combined with other renewable sources, such as solar thermal energy, to increase the overall temperature level or availability of heat supplied to the thermal separator [93]. Alternatively, depending on the quantity and temperature of the available waste stream, it can operate standalone, driving thermally based desalination units without external fuel input.

[91]: Elsaid et al. (2020), "Recent Progress on the Utilization of Waste Heat for Desalination"

The temperature grade of waste heat⁴ plays a decisive role in determining its recovery potential and the appropriate desalination technology [92]. This classification is crucial because it dictates not only the technical feasibility but also the economic viability of energy recovery.

[92]: Brückner et al. (2015), "Industrial Waste Heat Recovery Technologies"

Broadly speaking, two main recovery pathways exist. The first involves direct heat-to-heat recovery, typically implemented through heat exchangers or heat pumps. This route is highly efficient and is particularly well suited to thermally driven desalination processes, such MED, MSF and MD. The second approach converts waste heat into mechanical work or electricity, most commonly using an Organic Rankine cycle systems or other thermodynamic engines. The generated power can then drive electricity-based desalination units.

[93]: Christ et al. (2015), "Boosted Multi-Effect Distillation for Sensible Low-Grade Heat Sources"

In both cases, effective utilization of waste heat not only enhances overall energy efficiency but also contributes to decarbonization efforts in the water and energy sectors. However, challenges remain in terms of temporal availability, temperature matching, and economic competitiveness

4: generally categorized into low (<100 °C), medium (100–400 °C), and high (>400 °C)

Solar energy and waste heat are free – so why care about efficiency?

Is it not solar energy free? Yes and no. This has been a recurring topic of debate in the literature. Although the fuel, the Sun, is indeed free and practically inexhaustible, converting that energy into a useful form (whether electrical, thermal, or otherwise) requires a transformation process that

entails costs.

In the case of solar fields, whether photovoltaic or solar-thermal, the more energy you need, the larger the field area must be, and consequently, the higher the investment cost. Therefore, renewable sources do not provide free energy. A similar argument applies to waste heat: to obtain usable heat for a thermal separator, a transformation process is often required, typically involving costly heat exchangers.

In summary, generating electricity or heat solely to power a thermal separation process (renewable or not) is generally inefficient and capital-intensive.

A separate question —explored in Chapter 7 (Performance evaluation in MED processes)— is what we actually mean by efficiency, and how it should be defined depending on the energy source.

SolarMED pilot plant

TL;DR

The Multi-Effect Distillation (MED) pilot plant at Plataforma Solar de Almería (PSA) is one of the first demonstration plants of solar-powered desalination in the world and one of the first facilities at PSA. Over the years it has followed the evolution of thermal desalination: from the seek for high-temperature, high-efficiency complex systems (Thermal Vapor Compressions (TVCs), Double-Effect Absorption Heat Pumps (DEAHPs)) to the realization of preferable simpler, lower-temperature systems. Today, it operates as a MED plant powered by a flat-plate collector solar field and a two-tank thermal storage system, with water as the heat transfer fluid. This chapter describes the main components of the facility, focusing on the MED plant, its particularities, instrumentation, and specifications.

At the end of the 1980s, CIEMAT (Centro de Investigaciones Energéticas, Medioambientales y Tecnológicas, Spain) and DLR (German Aerospace Center, Germany) joined efforts to develop an advanced desalination system powered by solar thermal energy and coupled to a TVC. This initiative, known as the Solar Thermal Desalination (STD) Project (1987–1994) [94], sought to demonstrate the feasibility of coupling large-scale seawater desalination with solar energy. During the first phase, a pilot plant was built at the PSA, combining a MED unit with a parabolic-trough solar field and thermal oil storage. The system operated with synthetic oil heated to drive steam generation, reaching promising efficiencies and demonstrating high reliability. However, the setup was complex and operated at relatively high temperatures, requiring precise control and maintenance [82].

In the second phase of the STD Project [82], researchers focused on improving energy efficiency and reducing consumption through system integration. A DEAHP ($\text{LiBr}-\text{H}_2\text{O}$) was coupled to the MED unit, significantly lowering thermal demand and increasing performance ratios. While these advancements confirmed the technical potential of solar-powered desalination, they also highlighted the challenges of operating high-temperature, oil-based systems. This realization guided subsequent efforts toward simpler and more robust configurations.

A decade later, the AQUASOL I [83, 95] project built upon this experience by shifting to lower-temperature and more practical designs. The parabolic-trough field was replaced with a 500 m² stationary compound parabolic collector (CPC) field using liquid water as the heat transfer fluid and with a direct connection to the MED. It included two small tanks to attenuate fluctuations in thermal energy availability. The system could operate in solar, fossil, or hybrid modes, offering greater flexibility and easier operation. This transition marked a decisive move from complex, high-temperature solar technologies toward simpler, water-based systems, better suited for reliable and cost-effective desalination under real-world conditions.

In its current configuration, result of the AQUASOL-II project [32, 96], the Solar-driven Multi-Effect Distillation (SolarMED) system consists of an MED plant powered by a flat-plate solar collector field coupled to a two-tank thermal energy storage system (larger than previously), as shown in Figure 1.4. The main components are interconnected as illustrated in Figure 5.1: a flat-plate collector field serving as the heat source, a pressurized hot-water two-tank storage system, and an MED unit that utilizes this thermal energy to separate seawater into freshwater and brine. The solar field and the storage circuit are thermally

5.1 Solar field	50
5.2 Thermal storage	50
5.3 Multi-Effect Distillation	51

[94]: Gregorzewski et al. (1991), “The Solar Thermal Desalination Research Project at the Plataforma Solar de Almeria”

[82]: Milow et al. (1997), “Advanced MED Solar Desalination Plants. Configurations, Costs, Future — Seven Years of Experience at the Plataforma Solar de Almeria (Spain)”

[83]: Alarcón-Padilla et al. (2007), “Application of Absorption Heat Pumps to Multi-Effect Distillation”

[95]: Blanco et al. (2011), “The AQUASOL System”

[32]: Chorak et al. (2017), “Experimental Characterization of a Multi-Effect Distillation System Coupled to a Flat Plate Solar Collector Field”

[96]: Ampuño et al. (2018), “Modeling and Simulation of a Solar Field Based on Flat-Plate Collectors”

coupled through a heat exchanger. Two subsystems can be distinguished: the Solar Field and Thermal Storage subsystem (**sfts**), responsible for collecting and storing solar energy, and the thermal load, which in this case corresponds to the MED plant performing the separation process (separation subsystem).

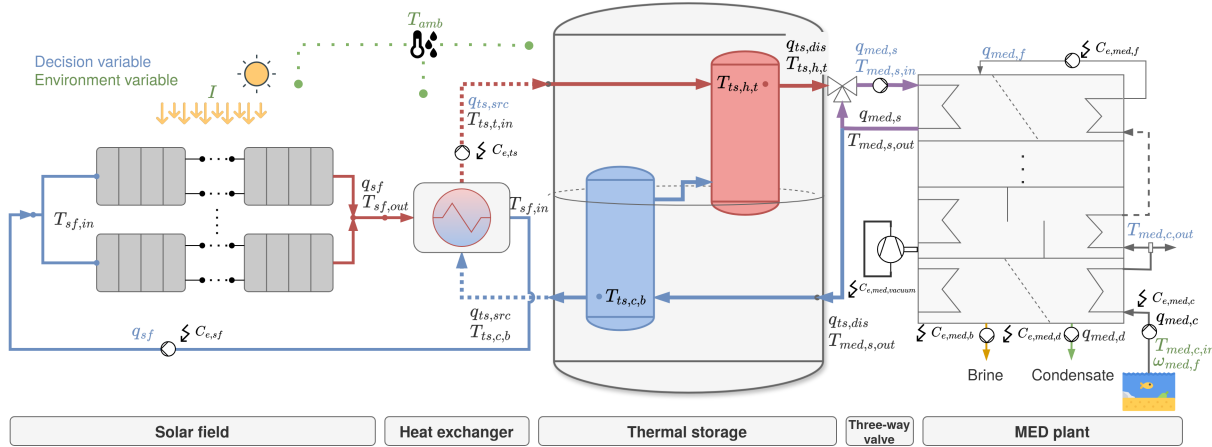


Figure 5.1: SolarMED process diagram

5.1 Solar field

1: See Figure 5.1 - Solar field

2: Depicted in Figure 5.2 (a)

[97]: Roca et al. (2024), "Modelo de parámetros concentrados para captadores solares planos con reflectores"

3: Even though this addition was performed recently and not considered in this research work

The AQUASOL-II solar field¹ consists of 60 static collector modules (Wagner LBM 10HTF model) with a total aperture area of 606 m², connected to a 40 m³ thermal storage system through a heat exchanger². The solar field is arranged in a small loop (Loop 1) with 4 collector modules connected in parallel, and four larger loops (Loops 2–5), each composed of 14 collector modules (each loop consists of two rows connected in series, and each row is formed by 7 collector modules in parallel). All flat-plate collectors are oriented south and tilted 35° with respect to the horizontal plane [97].

Each collector module is composed of five individual collectors through which water circulates as the heat transfer fluid via a zigzag-shaped absorber tube. As water moves across the tube, it absorbs solar radiation, increasing its temperature before exiting the collector. Recently, the solar field has been equipped with movable flat mirrors installed south of each collector row. These mirrors automatically track the Sun and reflect direct solar radiation onto the collectors, thereby increasing the solar irradiance incident on them³. The design of the solar field allows independent operation of each loop through its own valves and pumping system. Each loop is connected to an individual heat exchanger, providing flexibility to couple different loads according to experimental requirements.

5.2 Thermal storage

4: See Figure 5.1 - Thermal storage

[98]: Duffie et al. (2013), "Energy Storage"

The thermal storage system⁴ consists of a two-tank system. It has a total capacity of 40 m³ (depicted in Figure 5.2 (b)). The system is based on the design principles outlined by Duffie and Beckman [98], and consists of two thermally insulated tanks: a hot tank (the red tank in the diagram) operating at a higher temperature and a cold tank (blue tank in the diagram), each serving distinct roles in the thermal cycle (i.e. ensure thermal stratification). In normal operation, heat is extracted from the bottom of the cold tank, and after being heated, it is injected



Figure 5.2: Heat generation and storage subsystem facilities

into the top of the hot tank. The load extracts heat from the top of the hot tank, and returns it to the bottom of the cold tank, completing the cycle. The tanks are connected from top of the cold tank to the bottom of the hot tank, allowing for recirculation of the fluid between the two tanks.

5.3 Multi-Effect Distillation

To understand the Multi-Effect Distillation (MED) process, it is useful to first describe the operation of a single-effect distillation unit. Such a system mainly consists of an evaporator and a condenser. In the evaporator, an external heat source (typically hot water or steam from a boiler or power plant) transfers energy to seawater sprayed over a tube bundle, forming a thin film that partially evaporates. The generated vapor passes through a demister, which prevents salt droplets from being carried over, and then condenses in the condenser by transferring its latent heat to the seawater flowing inside the tubes. This process yields two products: the distillate (condensed vapor) and the brine (concentrated saline water).

The condenser's cooling water removes the excess heat not used for evaporation, and this water is discharged back to the sea. Since a single-effect unit has low efficiency, multiple stages are connected in series in an MED plant. In this configuration, the vapor produced in one stage serves as the heat source for the next, operating at progressively lower temperatures and pressures. Thus, evaporation and condensation occur simultaneously in each effect, requiring only one external heat source. The vapor condensed within all stages contributes to the total distillate production, while the final stage's condenser preheats the incoming seawater. Finally, the concentrated brine is discharged [89].

The experimental MED plant at PSA is a 14 effect, vertically stacked, forward-feed plant initially built to use low-pressure saturated steam as heat source (70°C , 0.31 bar) for the first effect and, as mentioned, later replaced to use hot water. An image of the facility in its current state can be seen in Figure 5.3. It has been operated in different experimental campaigns and configurations robustly for more than three decades. A summary of its main specifications is shown at Table 5.1.

The first campaign from 2009 to 2012 is a comprehensive campaign covering the operating range of the plant and described in Palenzuela *et al.* [99]. Within the



Figure 5.3: MED plant at PSA with open effects for maintenance

[89]: Palenzuela *et al.* (2015), *Concentrating Solar Power and Desalination Plants*

[99]: Palenzuela *et al.* (2016), "Experimental Parametric Analysis of a Solar Pilot-Scale Multi-Effect Distillation Plant"

5: Each experimental campaign requires a significant number of test days due to the large number of target operating points. Achieving a valid steady state takes approximately 20–30 minutes, not including the transition time between operating points. On a good day, 3–4 stable operating points can be reached; on a bad day, due to for example unfavorable environmental conditions, none may be achieved. This makes the experimental campaigns complex and extensive, making it highly suitable for extensive automation

Table 5.1: MED plant at PSA specifications and nominal operating conditions

Parameter	Value
Capacity	72 m ³ /day
Number of effects	14
Feed type	Forward feed
Physical arrangement	Vertically stacked
Heat exchanger configuration	90/10 Cu-Ni HTE
Heat source type	Hot water
Vacuum system	Hydro-ejectors
Heat source flow rate	12 L/s
Feed water flow rate	8 m ³ /h
Brine rejection	5 m ³ /h
Distillate production	3 m ³ /h
Cooling flow rate at condenser	8-20 m ³ /h (10-25 °C)
Thermal power consumption	190 kW
Top Brine Temperature (TBT)	70 °C
Condenser temperature	35 °C

Table 5.2: MED plant available experimental data range.

Variable	\bar{x}	\bar{x}	Unit
q_s	10.50	44.35	m ³ /h
$T_{s,in}$	52.01	80.98	°C
q_f	4.98	8.27	m ³ /h
$T_{c,in}$	12.14	33.64	°C
$T_{c,out}$	19.36	39.89	°C
q_d	1.61	3.08	m ³ /h
$T_{s,out}$	50.05	77.31	°C
q_c	8.03	23.13	m ³ /h

research work presented in this thesis, a second experimental campaign took place between 2021 and 2025, in order to validate a standardization methodology proposal and experimentally characterize the behavior of the system at higher temperatures (see Section 7.5). It is not as extensive as the first one but extends the operation range of the heat source temperature. In total, the experimental data spans 6 years of operation and make available 549 operation points with the range per variable shown in Table 5.2⁵.

Some particularities of this system are explained hereinafter:

- ▶ As an energy efficiency measure, the plant is equipped with 13 preheaters, which using a fraction of the vapor generated in the effects, preheat the feedwater before entering the first effect. The fourteenth “preheater” would be the condenser.
- ▶ As mentioned, the external heat source driving the process, is hot water from a thermal storage system. Water is drawn from one of the tanks and mixed with the water at the outlet of the first effect through a three-way valve (See Figure 5.1 - *Three-way valve*), allowing independent regulation of flow and temperature.
- ▶ The inland location of this experimental plant is another particularity of the system. A fixed amount of seawater (30 m³), stored in a reservoir, is available to be used in the process and replenished as needed. The effluents from the plant are mixed in a different reservoir (5 m³), and returned to the feed in a close loop operation. Because water exits the process at a higher temperature than when it enters, this type of operation implies an ever-increasing heat sink temperature. A wet cooling tower, installed between the two reservoirs, is used to mitigate this effect.
- ▶ The previous particularity leads to a significant variation in the inlet water temperature from day to day and also within the same day depending on the operation conditions. To ensure the stability of the condenser (i.e. a constant vapor pressure and outlet cooling water temperature), the cooling flow rate is regulated. This allows to have a stable system representative of a real plant operating under normal conditions. However, this can lead to variable electrical consumption of the cooling pump.
- ▶ The vacuum system of the plant is based on two hydro-ejectors and a pump. The pump is operated always at fixed speed and its electrical consumption has been characterized with measurements under various conditions as being near-constant and independent of the operation conditions. Its associated nominal power is 5 kW_e.
- ▶ The salinity of the feedwater is checked before every test measuring its conductivity with a conductivity meter (see Table 5.3).

The experimental facility is a complex system of considerable size for a pilot plant. It includes over 100 variables, between inputs and monitored outputs. Its instrumentation is shown in Table 5.3 and the placement in the system can be seen in Figure 5.4. Platinum temperature transducer, 100 ohms at 0 °C (PT100) sensors are used to measure all liquid temperatures (TT01..TT05), while a PT1000 sensor is used to measure the ambient temperature (TT06). The pressure inside the first effect and condenser (PT01 and PT02, respectively) is measured by two different pressure transducers which fundamentally differ in their measurement range. To monitor the power consumption of the system, various subsystems have been individually instrumented using a power meter (JT01..JT04). Conductivity is measured using a portable conductivity meter (CT01, CT02), to which a calibration is periodically performed to convert conductivity to salinity. Flow rates (FT01..FT04) are measured using different types of flowmeters depending on the characteristics of the fluid being evaluated. Electromagnetic flowmeters are used for conductive fluids, while vortex flowmeters are used for non-conductive fluids. All sensors transmit a 4–20 mA analog signal that is converted to digital by Analog-to-Digital Converter (ADC)

Table 5.3: Characteristics of the instrumentation installed at MED-PSA unit (^a value of the measured temperature in °C, ^b of reading, ^c full scale).

Measured variable	Instrument	Model	Range	Measurement uncertainty
Water temperature, TT01...TT0N	PT100 Class A	SEDEM OF112871	0 - 100°C	± 0.15 + 0.002·T ^a
Distillate flow rate, FT03	Vortex flow meter	ABB TRIO-WIRL VT4	1.6 - 18 m ³ /h	± 0.75% o.r. ^b
Hot water flow rate, FT01	Electromagnetic	Endress+Hauser Proline Promag 50P	2.42 - 78.33 L/s	± 0.5% o.r.
Feedwater flow rate, FT02	Electromagnetic	Endress+Hauser Proline Promag P 300	2.1 - 66 m ³ /h	± 0.5% o.r.
Ambient temperature, TT05	PT1000	-	-40 - 60 °C	± 0.15 + 0.002·T
Pressure, PT01	Pressure capacitive	Endress+Hauser Cerabar T-PMC131	0 - 1 bar	± 0.5% FS ^c
Pressure, PT02	Piezoresistive sensor	WIKA S-10	0 - 0.6 bar	± 0.5% FS
Level, LT01, LT02	Magnetic level gauge	IGEMA NA7-50	0-750 mm	± 5 mm
Power, JT01...JT04	Power meter Class 1 IEC 62053-21	Circutor CM31	0-7 kW	±1% o.r.
Conductivity, CT01...CT02	Conductivity meter	Prominent Portamess 911	0.1µS/cm - 1000 mS/cm	± 0.5% o.r. < 500 mS/cm ± 1% o.r. ≥ 500 mS/cm

converters. Variable Frequency Drives (VFDs) are used to control all flow rates in the system: heat source, cooling, feed, brine and distillate.

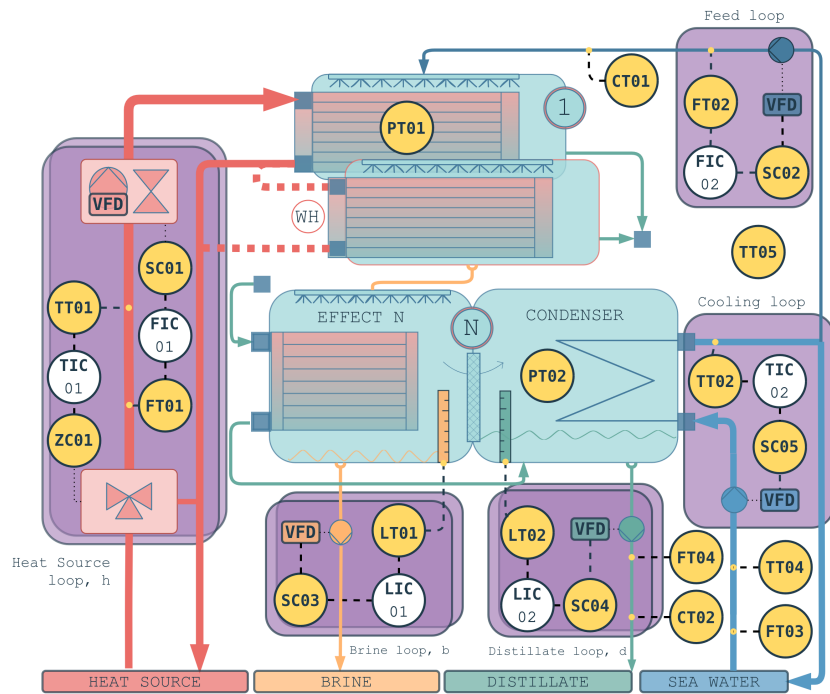


Figure 5.4: Piping and Instrumentation Diagram (P&ID) representative of the MED-PSA plant with the installed instrumentation, Key Process Variables (KPVs), and implemented control loops (ANSI/ISA 5.1-2022).

6

Hybrid modelling of a solar driven MED system

TL;DR

This chapter presents the discrete and complete dynamic modelling of the Solar-driven Multi-Effect Distillation (SolarMED) system. First, continuous physics-based and data-driven models for the solar field, heat exchanger, thermal storage, three-way valve, and Multi-Effect Distillation (MED) plant. These dynamic models are then combined with the discrete behavior of the installation. This is represented by means of two supervisory Finite-State Machines (FSMs) that define the operation states of the heat generation and storage subsystem (Solar Field and Thermal Storage subsystem (**sfts**)) and the multi-effect distillation subsystem (Separation subsystem (**med**)). Each FSM determines subsystem activation and transitions based on system inputs, internal rules, and configurable parameters such as cooldown or startup durations.

The integrated hybrid model is evaluated under realistic operation conditions with different prediction horizons, showing good agreement with experimental data. Results demonstrate that the model accurately reproduces the coupled dynamics of the system, maintaining Mean Absolute Percentage Error (MAPE) below 15% for multi-hour predictions while preserving computational efficiency.

6.1	Introduction	55
6.2	Dynamic modelling	55
6.2.1	Solar field	56
6.2.2	Thermal storage	60
6.2.3	Heat exchanger	64
6.2.4	MED	67
6.3	Discrete modelling	71
6.3.1	Heat generation and storage subsystem (sfts)	71
6.3.2	Separation subsystem (med)	71
6.3.3	Validation	73
6.4	Complete system model	74
6.4.1	Validation	76

6.1 Introduction

The behavior of the SolarMED process can be abstracted into two components, a continuous and a discrete one. Each component is described and validated in the respective Section 6.2 (Dynamic modelling. Process variables) and Section 6.3 (Discrete modelling. Operation state). Then, they are combined to create a complete model of the SolarMED process in Section 6.4 (Complete system model).

6.2 Dynamic modelling. Process variables

The dynamic behavior of the SolarMED governs the evolution of the continuous process variables. It is represented by a set of models, one for each system component. A discrete representation¹ is used: process variables are sampled at a fixed interval, T_s , and system dynamics are expressed through difference equations.

In most cases, this representation captures the transient behavior of the system. However, some models described in the following sections are steady-state approximations. While this can introduce discrepancies during transient events, the impact is minor. The model is intended primarily for optimization, with sampling times on the order of minutes. Moreover, inputs to slower components are adjusted infrequently (typically at intervals of 30 minutes or more) allowing sufficient time for the system to reach steady state².

1: Not to be confused with the discrete model, see Section 3.1.3

2: Further discussed in Section 3.1 (Modelling and simulation)

6.2.1 Solar field

The (flat-plate collector) solar field is basically a converter of electrical to thermal energy subject to irradiance availability. The main outputs, in terms of operation of the solar field, are the thermal power obtained, \dot{Q}_{sf} (kW_{th}), at what temperature that heat is obtained, $T_{sf,out}$ (°C), and the electricity needed to do so, $C_{e,sf}$ (kW_e).

3: i.e., a balanced flow distribution with similar collectors, which is the case in the experimental facility for the considered loops 2 to 5

[96]: Ampuño et al. (2018), "Modeling and Simulation of a Solar Field Based on Flat-Plate Collectors"

4: Also called model and fixed model parameters, respectively

[100]: Ampuño et al. (2019), "Apparent Delay Analysis for a Flat-Plate Solar Field Model Designed for Control Purposes"

5: Transport delays are a common feature in dynamic systems, where the response of the system to an input is not instantaneous, but rather delayed by a certain amount of time. This delay can be caused by various factors, in this particular system, is due to the time it takes for the water to flow through the solar field and reach the temperature sensors. The apparent delay is the result of adding up the individual - different delays of each collector cell

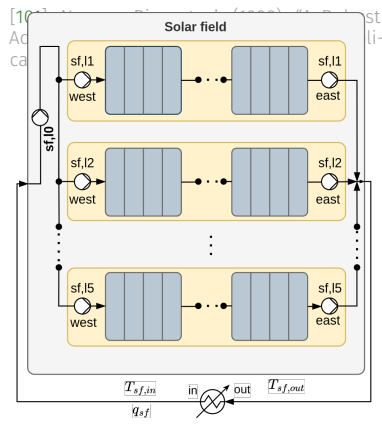


Figure 6.1: Solar field process diagram.

The diagram in Figure 6.1 illustrates the individual loops that make up the field. In the model, it is assumed that all loops have equal flow rates and temperatures³. As a result, the system can be simplified to a single loop with a collector area equal to the sum of the collector areas of the individual rows of collector loops.

A first-principles model (see Model 6.1) based on the one presented in Ampuño et al. [96] is used to model the solar field. The model has two types of parameters: dynamic and constant⁴. The dynamic parameters are the thermal loss coefficient, H_{sf} ($\frac{J}{s \cdot C}$), which relates thermal losses to the environment and the gain coefficient, β (m), encompassing the collector transmissivity and absorstane. It determines the amount of irradiance that is transferred to the working fluid. These two dynamic parameters are calibrated using experimental data which together with the constant parameters can be found in Table 6.4.

The main difference with respect to the model presented in [96] is how the apparent transport delay is modelled [100]⁵. In this implementation, the transport delay is simplified to a single steady state parameter based on the work presented in Normey-Rico et al. [101] since delays vary less than 30% from this nominal value.

Model 6.1: Solar field

$$\begin{aligned}
 T_{out}(k) &= sf\text{ model}\left(T_{out,k-1}, T_{in,k-n:k}, q_{k-n:k}, I_k, T_{amb,k}; \beta, H, \theta\right) \\
 L_{pipe,eq} &= \frac{T_s}{A_{pipe,eq}} \sum_{k=0}^n q_{sf}[k] && \text{Equivalent pipe length [m]} \\
 L_{eq} &= n_{c,s} \cdot L_t && \text{Eq. collector tube length [m]} \\
 c_f &= n_{c-loop} \cdot n_{tub_c} && \text{Conversion factor [-]} \\
 K_1 &= \beta / (\rho \cdot c_p \cdot A_{cs}) && [K \cdot m^2/J] \\
 K_2 &= H / (L_{pipe,eq} \cdot A_{cs} \cdot \rho \cdot c_p) && [1/s] \\
 K_3 &= 1 / (L_{pipe,eq} \cdot A_{cs} \cdot c_f) \cdot (1/3600) && [h/(3600 \cdot m^3 \cdot s)] \\
 T_{out}(k) &= T_{out}(k-1) + \left(\begin{array}{l} + K_1 \cdot I \\ - K_2 \cdot (\bar{T} - T_{amb}) \\ - K_3 \cdot q_{k-n_d} (T_{out,k-1} - T_{in,k-n_d}) \end{array} \right) \cdot T_s && \begin{array}{l} \text{Solar contribution [K/s]} \\ \text{Environment losses [K/s]} \\ \text{Heat absorbed [K/s]} \end{array}
 \end{aligned}$$

The number of delay samples depends on the model sample time and a system parameter called the equivalent length. The following procedure was followed to estimate it:

1. Using a reference test with a fixed sample time, T_s , the number of delay samples (n_d) was manually fitted to the data, by visually inspecting the response of the system to a step change in the input flow.
2. Estimate the equivalent length of the solar field by taking the average flow rate (\bar{q}_{sf}) across the delay samples span⁶, and divide it by a fixed parameter- the solar field pipe equivalent cross-sectional area, $A_{pipe,eq}$.

6: In reverse order, from newest to oldest

$$\bar{q}_{sf} = \sum_{k=-n_d}^{k=0} q(k)/n_d$$

$$L_{pipe,eq} = \frac{\bar{q}_{sf} \times T_s \times n_d}{A_{pipe,eq}}$$

3. With this equivalent length ($L_{pipe,eq}$), the number of delay samples can be estimated for any sample time T_s and flows vector \mathbf{q}_{sf} by iteratively adding the distance that flow travels at each sample time until the equivalent length is reached.

Electrical consumption

Definition 6.2.1 Step train test. Variations in the Variable Frequency Drive (VFD) pump speed from a minimum to a maximum value, with fixed increments.

The AQUASOL solar field consists of a set of pumps that recirculate water through the system. The pumps are controlled by VFDs that allow to vary the flow rate through the solar field. A main recirculation pump (P_{10}) is responsible for the primary flow, while additional pumps (P_{11}, P_{12} , etc.) are used in the individual loops to either increase the total flow rate or to operate with the isolated loop. This redundancy means that the same flow rate can be achieved with different pump configurations.

The electrical consumption of the solar field is characterized by determining the relationship between flow rate and power consumption for each configuration. This allows for the identification of the configuration that minimizes electrical consumption across the range of operating flow rates. Once this characterization is established, the overall electrical consumption of the solar field can then be modelled.

A series of tests were performed as can be seen in Figure 6.2. The tests were carried out in two different dates since they have to be performed early, before the solar field is irradiated by the sun and the field heats up⁷. In the first day, step trains are applied to the main loop and individual isolated loops⁸. On the second day, different speeds levels were set for the main recirculation pump (10% - 100%, 10% increments) while step trains were applied to the individual loops (40% - 100%, 20% increments)⁹.

7: Observe the trend in Figure 6.2 - Temperatures

8: 20240925 07:15 – 08:30

9: In Figure 6.2, from 20240927 07:35 to 08:20

Figure 6.3 shows the relationship between flow rate and power consumptions for different configuration and pump speeds. Up to 91.9 l/min the best configuration is to just use the main recirculation pump. Above this flow rate, the main pump is used in combination with the individual loop pumps. First, a combination of main pump from 85 to 100% and individual loops fixed at their 40% minimum speed up until 105 l/min, then the main pump fixed at 100% and individual loops at increasing values from 40 to 100% until a maximum achievable flow rate of 148 l/min.

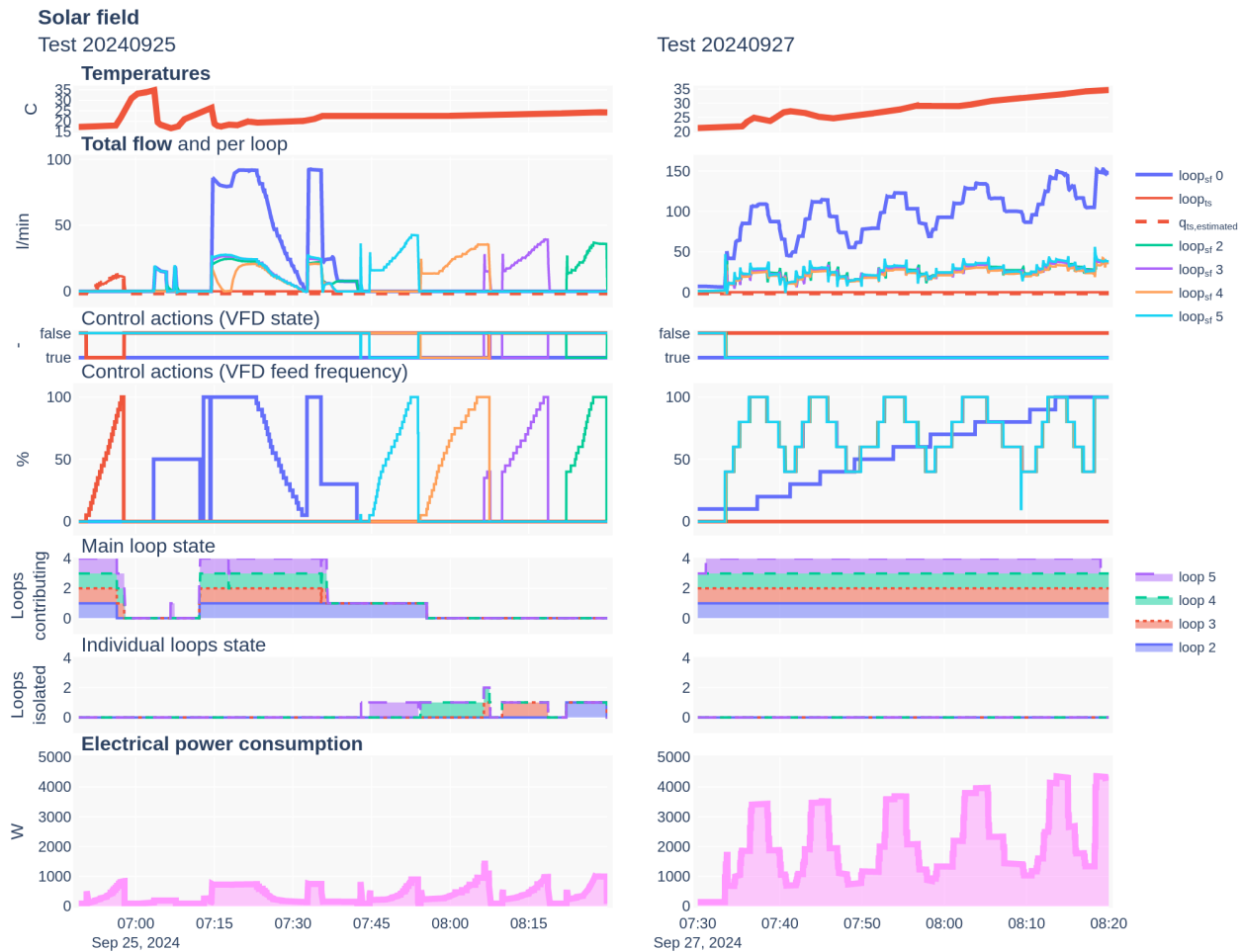
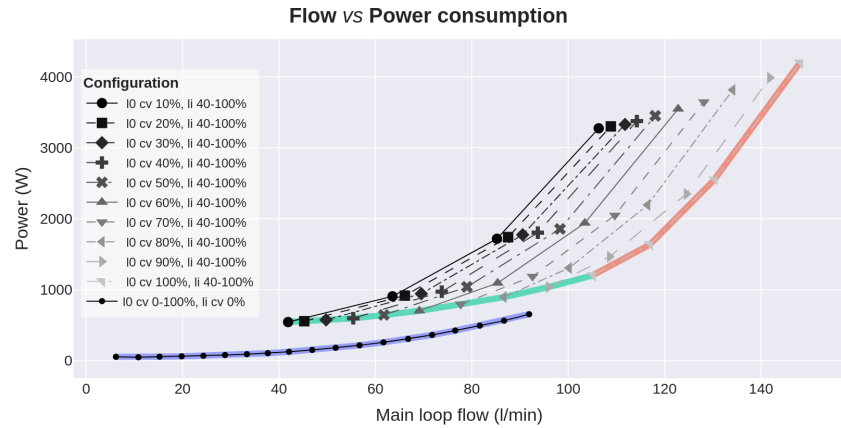


Figure 6.2: Solar field and thermal storage electrical characterization tests.



Figure 6.3: Solar field flow for different pump configurations and their associated power consumption.



$$\text{Optimal configuration}(q_{sf}) = \begin{cases} l_{0,cv} \in [0, 100] \% \wedge l_{i,cv} = 0\%, & 6.2 < q_{sf} \leq 91.9 \text{ (l/min)} \\ l_{0,cv} \in [0, 100] \% \wedge l_{i,cv} = 40, & 91.9 < q_{sf} \leq 105 \\ l_{0,cv} = 100 \wedge l_{i,cv} \in [40, 100], & 105 < q_{sf} \leq 148 \end{cases} \quad (6.1)$$

With this selection, a third-order polynomial regression is fitted to the data, with a coefficient of determination of $R^2 = 0.99$.

Model 6.2: Solar field electrical consumption

$$C_{e,sf} [\text{kW}_e] = \text{sf electrical consumption}(q_{sf} [\text{m}^3/\text{h}])$$

$$C_{e,sf} = 1.3 \cdot 10^{-5} \cdot q_{sf}^3 + -8.72 \cdot 10^{-4} \cdot q_{sf}^2 + 2.29 \cdot 10^{-2} \cdot q_{sf} + -8.48 \cdot 10^{-2}$$

Summarizing, the electrical consumption of the solar field is modelled as a function of the flow rate through the solar field from a minimum value of 3.7 m³/h (50 W) to a maximum value of 88.84 m³/h (4.2 kW). This is achieved as the result of different combinations of the main recirculation pump and the individual loops depending on the working flow range.

Validation

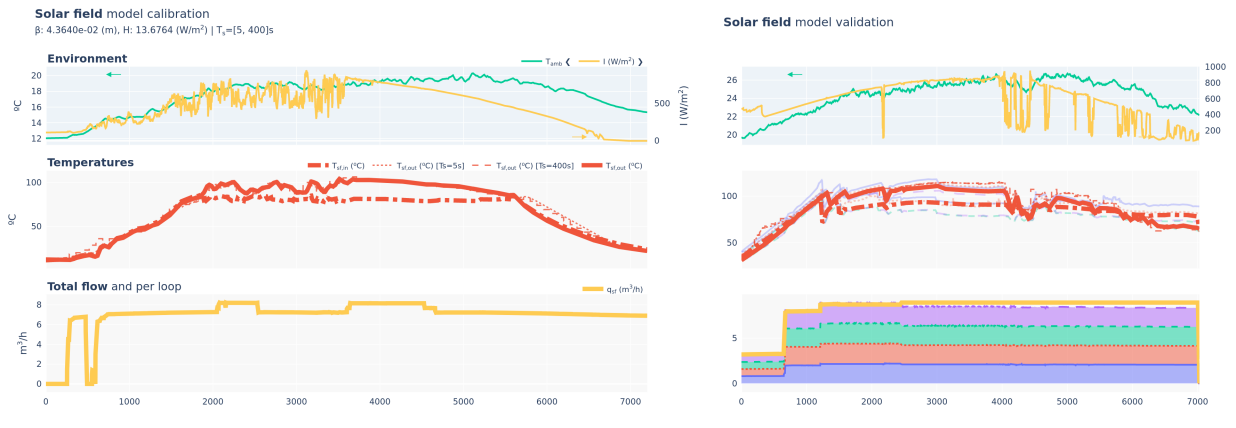


Figure 6.4: Solar field model calibration and validation tests.



In order to calibrate the model parameters (β and H), one representative experimental test is used¹⁰ where the parameters are fitted. Compared to the results presented in Ampuño *et al.* [96], double the gain coefficient is obtained while higher losses are found. This could be explained by the fact that the calibration was performed including the warm-up and cooldown periods of the solar field.

10: See Figure 6.4– left

As can be seen in the figure, most of the error is accumulated during the cooldown of the field. In Figure 6.4– right the dynamic behavior of the model is

Table 6.1: Summary table of the prediction results obtained with the solar field model for different test days and sample times.

Predicted variable	Sample time (s)	Test date	Performance metric						Time (s)	
			R ² (-)		MAE (s.u.)		MAPE (%)			
			Test	Avg.	Test	Avg.	Test	Avg.	Test	Avg.
$T_{sf,out}$ (°C)	5	20231030	0.97		4.41		9.17		1.48	
		20231106	0.97		2.97		6.25		1.40	
		20230630	0.81		9.77		17.95		1.70	
		20230703	0.92		5.07		6.05		1.60	
		20230508	0.89	0.96	5.59	2.50	7.86	9.37	1.42	1.43
		20230628	0.90		4.93		6.30		1.61	
		20230511	0.87		5.02		6.30		1.43	
		20230629	0.85		7.22		11.61		1.58	
		20230505	0.76		10.13		13.74		1.52	
		20231031	0.96		2.50		9.37		1.43	
400	400	20231030	0.96		4.99		10.71		0.02	
		20231106	0.97		3.69		8.28		0.02	
		20230630	0.79		10.20		18.52		0.02	
		20230703	0.93		4.73		5.56		0.02	
		20230508	0.88	0.93	5.71	2.84	7.81	10.21	0.02	0.02
		20230628	0.91		4.74		5.92		0.02	
		20230511	0.80		6.15		7.64		0.02	
		20230629	0.87		6.93		11.03		0.02	
		20230505	0.78		9.34		12.58		0.02	
		20231031	0.93		2.84		10.21		0.02	

s.u. stands for same units as the predicted variable

validated with another test. The dynamic response obtained is very similar to the one experimentally measured for most of the test, similar to the calibration test despite the cloudy conditions. A higher error is observed between calibration and the particular validation test shown: $R^2=0.97$ compared to 0.87, but this can be explained because during the latter part of the experiment the irradiance was very intermittent while a high flow was kept which even manages to invert outlet and inlet temperature. Nonetheless, in relative terms very similar errors are obtained¹¹.

11: 6.25 compared to 6.3 in terms of MAPE

Several more tests (10) are evaluated, and the performance obtained is shown in Table 6.3. Here it can be seen than for many tests performance close to the calibration tests are obtained. There is a notable difference in the performance of the model depending on the sample rate used. R^2 goes from 0.96 to 0.93, and Mean Absolute Error (MAE) from 2.50 to 2.84 °C, when moving from a fast sample rate ($T_s = 5$ s) to a slow one ($T_s = 400$ s). This is expected since the model loses performance in transient periods which are a constant in cloudy days. However, the average error is still accurate enough for the intended use of the model while having a significant reduction in computational time, from 1.43 s to 0.02 s, 71 times faster.

In general, good metrics are obtained for most tests, with maximum percentage errors below 10 % MAPE, and in those who do not, the error is usually accumulated while the solar field is heating up or cooling down, that is, when no heat is being delivered to the load.

6.2.2 Thermal storage

A first-principles model of a two-tank thermal storage system is developed to capture the key thermodynamic and fluid dynamic phenomena governing energy transfer and stratification [98].

[98]: Duffie et al. (2013), “Energy Storage”

The governing model equations and boundary conditions to simulate the transient thermal behavior of the storage system, including mass and energy balances, heat transfer mechanisms, and the stratification dynamics are shown in Model 6.3.

Model 6.3: Thermal storage

$$\mathbf{T}_h(k), \mathbf{T}_c(k) = \text{thermal storage model}(\mathbf{T}_h(k-1), \mathbf{T}_c(k-1), T_{src}(k), \\ T_{dis}(k), \dot{m}_{src}(k), \dot{m}_{dis}(k), T_{amb}(k); \theta_h, \theta_c)$$

if $\dot{m}_{dis}(k) > \dot{m}_{src}(k)$: *(cold to hot recirculation)*

$$\mathbf{T}_c(k) = \text{single tank model}(\mathbf{T}_c(k-1), T_T=0, T_B=T_{dis}(k), T_{amb}(k), \\ \dot{m}_{in,T}=0, \dot{m}_{in,B}=\dot{m}_{dis}(k), \dot{m}_{out,T}=\dot{m}_{dis}(k) - \dot{m}_{src}(k), \dot{m}_{out,B}=\dot{m}_{src}(k); \theta_c)$$

$$\mathbf{T}_h(k) = \text{single tank model}(\mathbf{T}_h(k-1), T_T=T_{src}(k), T_B=T_c^{out}(k), T_{amb}(k), \\ \dot{m}_{in,T}=\dot{m}_{src}(k), \dot{m}_{in,B}=\dot{m}_{dis}(k) - \dot{m}_{src}(k), \dot{m}_{out,T}=\dot{m}_{dis}(k), \dot{m}_{out,B}=0; \theta_h)$$

else: *(hot to cold recirculation)*

$$\mathbf{T}_h(k) = \text{single tank model}(\mathbf{T}_h(k-1), T_T=T_{src}(k), T_B=0, T_{amb}(k), \\ \dot{m}_{in,T}=\dot{m}_{src}(k), \dot{m}_{in,B}=0, \dot{m}_{out,T}=\dot{m}_{dis}(k), \dot{m}_{out,B}=\dot{m}_{src}(k) - \dot{m}_{dis}(k); \theta_h)$$

$$\mathbf{T}_c(k) = \text{single tank model}(\mathbf{T}_c(k-1), T_T=T_h^{out}(k), T_B=T_{dis}(k), T_{amb}(k), \\ \dot{m}_{in,T}=\dot{m}_{src}(k) - \dot{m}_{dis}(k), \dot{m}_{in,B}=\dot{m}_{dis}(k), \dot{m}_{out,T}=0, \dot{m}_{out,B}=\dot{m}_{src}(k); \theta_c)$$

where:

$$\mathbf{T}(k) = \text{single tank model}(\mathbf{T}(k-1), T_{T,in}(k), T_{B,in}(k), \dot{m}_{in,T}(k), \dot{m}_{in,B}(k), \\ \dot{m}_{out,T}(k), \dot{m}_{out,B}(k), T_{amb}(k); \theta;)$$

► Top volume

$$-\rho \cdot V_T \cdot c_p \cdot \frac{T_{T,k} - T_{T,k-1}}{T_s} + \dot{m}_{src} \cdot T_{T,in} \cdot c_p - \dot{m}_{dis} \cdot T_{T,k} \cdot c_p \\ - \dot{m}_{src} \cdot T_{T,k} \cdot c_p + \dot{m}_{dis} \cdot T_{T,k} \cdot c_p - H_T \cdot (T_{T,k} - T_{amb}) = 0$$

► Bottom volume

$$-\rho \cdot V_B \cdot c_p \cdot \frac{T_{B,k} - T_{B,k-1}}{T_s} + \dot{m}_{src} \cdot T_{B,in} \cdot c_p + \dot{m}_{dis} \cdot T_{B,in} \cdot c_p \\ - \dot{m}_{src} \cdot T_{B,k} \cdot c_p - \dot{m}_{dis} \cdot T_{B,k} \cdot c_p - H_N \cdot (T_{B,k} - T_{amb}) = 0$$

► Inner volume

$$-\rho \cdot V_i \cdot c_p \cdot \frac{T_{i,k} - T_{i,k-1}}{T_s} + \dot{m}_{src} \cdot T_{i-1,k} \cdot c_p - \dot{m}_{dis} \cdot T_{i,k} \cdot c_p \\ - \dot{m}_{src} \cdot T_{i,k} \cdot c_p + \dot{m}_{dis} \cdot T_{i+1,k} \cdot c_p - H_i \cdot (T_{i,k} - T_{amb}) = 0$$

Three types of volumes are defined: the inner volume, the top volume and the bottom volume:

- ▶ Top volume (V_T): can receive external heat, and have heat extracted from it. It interacts with the inner volume that it interfaces with.
- ▶ Bottom volume (V_B): can also have external interactions, and exchanges with the inner volume above it.
- ▶ Inner volume (V_i): is any volume that is not the top or bottom, that is, is surrounded by other volumes with which it exchanges heat and mass by inner recirculation.

Similar to the solar field model, it has two parameters that need to be calibrated using experimental data. These dynamic parameters are the thermal loss coefficient (H_i ($\frac{J}{s \cdot C}$)) which relates heat losses to the environment and the volume of each of the considered control volumes (V_i). Three temperature sensors are available in the experimental facility, so three volume divisions are used to model the thermal storage. With two tanks, this results in a total of 12 parameters to be calibrated.

Electrical consumption

The first step train given in Figure 6.2 – 20250925 from 06:50 to 07:15 is used to characterize the electrical consumption of recirculating water ($q_{ts,src}$) in the thermal storage circuit. The electrical consumption is modelled as a function of the flow rate through the thermal storage from a minimum value of $1.4 \text{ m}^3/\text{h} - 0.05 \text{ kW}_e$ to a maximum value of $8.4 \text{ m}^3/\text{h} - 0.75 \text{ kW}_e$ with a second-order polynomial regression, with a coefficient of determination of $R^2 = 0.99$.

Model 6.4: Thermal storage electrical consumption

$$C_{e,ts} [\text{kW}_e] = \text{ts electrical consumption} (q_{ts,src} [\text{m}^3/\text{h}])$$

$$C_{e,ts} = 4.88 \cdot 10^{-1} \cdot q_{ts,src}^2 + -6.95 \cdot 10^{-3} \cdot q_{ts,src} + 0.01$$

Validation

In order to calibrate the model parameters (H_i and V_i), data from the system was recorded during four consecutive days under different operating conditions (see Figure 6.6 - left). The first and last days included both charge and discharge cycles, while the middle two days were dedicated to charging-only operations. In between these days, the system was left idle to observe the natural thermal losses. The model parameters were fitted to minimize a combined metric averaging the three temperature measurements available per tank¹², obtaining a low thermal loss coefficient in the order of 10^{-2} to 10^{-4} (W/K). On the other hand, adding the volumes of the three control volumes totals around the 15 m^3 of the actual tank volume, which is a good indication that the model is capturing the thermal behavior of the system well. However, they are not distributed evenly; for both tanks the bottom volumes are significantly smaller than the upper ones. This can be explained by the fact that the temperature transmitters are not spaced evenly, and the bottom transmitter is located near the tank's bottom.

12: See Table 6.4

In Figure 6.6 – right, the model is validated with a different test. It can be observed that the error between calibration and validation is similar, 1.11°C (MAE)

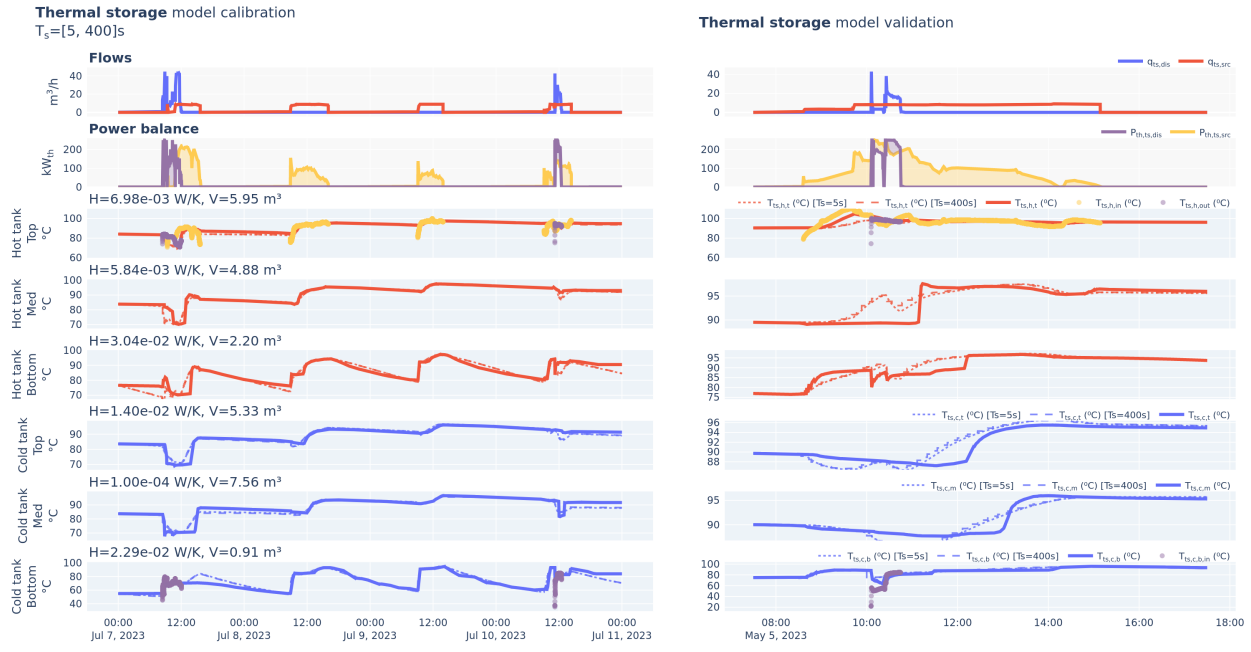


Figure 6.6: Thermal storage model calibration and validation tests.



sample time 5 sec
400 seconds sam-
ples are observed for
better value ob-
tained to calibration

compared to $1.14 \text{ }^{\circ}\text{C}^{13}$. The model seems to have a slower dynamic response to changes in the load-discharge balance than the actual system, which strangely stays impassive despite the changes in the load until some point where it reacts more aggressively. This could be explained by the interconnection between tanks. While the model assumes instantaneous and continuous flow recirculation between tanks, in reality it seems that the flow is discontinuous, only starting to flow when a certain pressure difference is reached. Nonetheless, both model and experimental data converge to similar values for all three measurements once the system stabilizes. Furthermore, the two most important measurements, the top of the hot tank and the bottom of the cold tank, which are the ones that interface with the rest of the system, have a very low error throughout the test.

Finally, several more tests (7) are evaluated, and the performance obtained is shown in Table 6.2. It should be noted that this model only receives feedback from the process initially, and then outputs are forecasted based on the inputs and the model own previously forecasted states. This means that any error in the prediction will be accumulated over time. This makes metrics like R^2 not representative of the model performance, as a small offset in the prediction will make R^2 drop significantly. For this reason, more emphasis is put on the MAE and MAPE metrics. In general, almost identical performance is obtained with the fast ($T_s = 5 \text{ s}$) and slow ($T_s = 400 \text{ s}$) sample rates, while the computational time is significantly reduced, from 5.45 s to 0.07 s, almost 80 times faster. This is explained because the model on each iteration needs to solve a system of equations, so it has associated a higher time per iteration, making potential savings in the number of iterations more significant. On the other hand, less accuracy is lost when reducing the sample rate compared to the solar field since the dynamics of this system are naturally slower due to the high thermal inertia of the tanks, thus making it more insensitive to the sampling.

Table 6.2: Summary table of the prediction results obtained with the thermal storage model for different test days and sample times.

Predicted variable	Sample time (s)	Test date	Performance metric						Time (s)	
			R ² (-)		MAE (s.u.)		MAPE (%)			
			Test	Avg.	Test	Avg.	Test	Avg.		
$T_{ts,h}$ (°C)	5	20230630	0.13		0.99		1.03		5.91	
		20230508	0.79		1.47		1.58		5.36	
		20230707	0.88		1.11		1.27		55.49	
		20230628	0.76	0.51	1.02	1.14	1.16	1.15	5.89	
		20230511	0.22		2.26		2.52		5.28	
		20230629	0.98		0.34		0.36		5.84	
		20230505	0.51		1.14		1.15		5.35	
		20230630	0.52		2.11		2.56		5.91	
		20230508	0.83		1.05		1.37		5.36	
		20230707	0.87		3.15		4.35		55.49	
$T_{ts,c}$ (°C)	400	20230628	0.68	0.88	2.86	1.78	3.78	2.14	5.89	
		20230511	0.96		1.75		2.17		5.28	
		20230629	0.88		2.02		2.52		5.84	
		20230505	0.88		1.78		2.14		5.35	
		20230630	0.18		1.07		1.11		0.09	
		20230508	0.79		1.47		1.58		0.08	
		20230707	0.88		1.10		1.26		0.63	
		20230628	0.76	0.54	1.03	1.14	1.18	1.14	0.07	
		20230511	0.21		2.33		2.59		0.07	
		20230629	0.98		0.36		0.38		0.07	
$T_{ts,c}$ (°C)	400	20230505	0.54		1.14		1.14		0.07	
		20230630	0.41		2.22		2.69		0.09	
		20230508	0.74		1.25		1.60		0.08	
		20230707	0.87		3.09		4.26		0.63	
		20230628	0.68	0.84	2.81	2.05	3.73	2.44	0.07	
		20230511	0.94		1.89		2.40		0.07	
		20230629	0.88		1.97		2.47		0.07	
		20230505	0.84		2.05		2.44		0.07	

s.u. stands for same units as the predicted variable. Alias: $T_{ts,h} == T_{ts,h,t}$ and $T_{ts,c} == T_{ts,c,b}$

Analyzing the performance in terms of the point of measurement, the top of the hot tank has the lowest error, with a MAE of 1.14 °C, while the bottom of the cold tank has a slight higher error, with 1.78 °C. Overall good agreement between model and experimental data is observed with maximum errors below 3 % MAPE. This means than the state of the thermal storage can be predicted with a reasonable accuracy for hours ahead.

6.2.3 Heat exchanger

The solar field and thermal storage are interfaced by a Heat Exchanger (hex) or hx , particularly a water-to-water counter-flow heat exchanger. The component is modelled using a first-principles steady state model based on the effectiveness-NTU method [102, 103]. The following assumptions need to be considered [102]:

- ▶ It has been assumed that the rate of change for the temperature of both fluids is proportional to the temperature difference; this assumption is valid for fluids with a constant specific heat, which is a good description of fluids changing temperature over a relatively small range. However, if the specific heat changes, the Logarithmic Mean Temperature Difference (LMTD) approach will no longer be accurate.
- ▶ It has also been assumed that the heat transfer coefficient (U) is constant, and not a function of temperature.
- ▶ No phase change during heat transfer.

[102]: Çengel et al. (2015), *Heat and Mass Transfer*

[103]: Kays et al. (1958), *Compact Heat Exchangers*

- Changes in kinetic energy and potential energy are neglected.

The model is described in Model 6.5. It returns the outlet temperatures from both primary circuit (solar field side), p , and secondary circuit s , the thermal storage side. As shown in Model 6.5, first the heat capacity C is determined in order to calculate the effectiveness (ϵ) of the heat exchanger. Finally, after determining the maximum heat transfer rate (\dot{Q}_{max}), the outlet temperatures can be obtained.

Validation

In order to calibrate the only parameter of this model (UA_{hx}), one representative experimental test is used where the parameters are fitted in order to obtain the *least-squares error* between the model and the experimental data. A heat transfer conductance value of 13 547 W/K is obtained. In Figure 6.8 the dynamic behavior of the model is validated with another test. It can be seen than the model performs fairly well even in transient conditions, with a MAE of $T_{hx,p,out} = 1.38^\circ\text{C}$, $T_{hx,s,out} = 1.39^\circ\text{C}$ and a coefficient of determination $R^2 = 99\%$ for both outputs¹⁴.

14: With fast sample rate – 5 seconds

Model 6.5: Heat exchanger

$$\begin{aligned}
 T_{hx,p,out}, T_{hx,s,out} &= \text{hx model}(T_{hx,p,in}, T_{hx,s,in}, \dot{m}_p, \dot{m}_s, T_{amb}; (UA)_{hx}) \\
 C_{hx,p} &= \dot{m}_{hx,p} \cdot c_{p,Tp,in} && \text{Primary side heat cap. [J/Ks]} \\
 C_{hx,s} &= \dot{m}_{hx,s} \cdot c_{p,Ts,in} && \text{Secondary side heat cap. [J/Ks]} \\
 C_{min} &= \min(C_{hx,p}, C_{hx,s}) \\
 C_{max} &= \max(C_{hx,p}, C_{hx,s}) \\
 C &= \frac{C_{min}}{C_{max}} \\
 \dot{Q}_{max} &= C_{min} \cdot (T_{hx,p,in} - T_{hx,s,in}) \\
 NTU &= UA/C_{min} \\
 \epsilon &= \frac{1 - e^{(-NTU \cdot (1-C))}}{1 - C \cdot e^{-NTU \cdot (1-C)}} && \text{Effectiveness [-]} \\
 T_{hx,p,out} &= T_{hx,p,in} - (\dot{Q}_{max} \cdot \epsilon) / (C_{hx,p}) \\
 T_{hx,s,out} &= T_{hx,s,in} + (\dot{Q}_{max} \cdot \epsilon) / (C_{hx,s})
 \end{aligned}$$

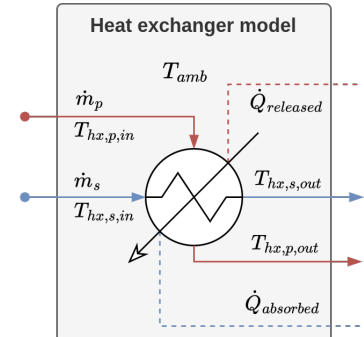


Figure 6.7: Heat exchanger process diagram.

Several more tests (11) are evaluated, and the performance obtained is shown in Table 6.3. In general, almost identical performance is obtained with the fast ($T_s = 5$ s) and slow ($T_s = 400$ s) sample rates, but as in the previous models, the computational time is significantly reduced, from 0.45 s to 0.01 s, an order of magnitude faster. In terms of accuracy, there seems to be a systematic higher error in the outlet of the secondary circuit with respect to the primary side, with double the error (MAE: 1.08 compared to 2.16 °C). Overall good agreement between model and experimental data is observed with maximum errors below 8 % MAPE.

Table 6.3: Summary table of the prediction results obtained with the heat exchanger model for different test days and sample times.

Predicted variable	Sample time (s)	Test date	Performance metric					
			R ² (-)		MAE (s.u.)		MAPE (%)	
			Test	Avg.	Test	Avg.	Test	Avg.
$T_{hx,p,out}$ (°C)	5	20231030	0.99	0.99	0.86	1.38	1.70	0.48
		20231106	0.99		0.68		3.14	0.49
		20230630	0.99		0.53		1.11	0.56
		20230703	0.99		1.24		0.67	0.60
		20230508	0.99				1.76	0.58
		20230707	0.99	0.99	1.64	1.08	5.15	3.58
		20230628	0.99		0.73		0.93	0.58
		20230511	0.98		1.40		1.92	0.54
		20230629	0.99		0.58		0.80	0.59
		20230505	0.99		1.22		1.67	0.54
		20231031	0.99		1.08		3.58	0.45
		20231030	0.98		2.58		5.54	0.48
		20231106	0.97		3.19		6.88	0.49
		20230630	0.98		2.71		4.63	0.56
		20230703	0.98		1.72		2.47	0.60
$T_{hx,s,out}$ (°C)	400	20230508	0.96		2.57		3.70	0.58
		20230707	0.98	0.96	2.90	2.16	7.24	7.55
		20230628	0.95		2.78		3.96	0.58
		20230511	0.95		2.88		3.95	0.54
		20230629	0.98		2.46		4.05	0.59
		20230505	0.97		2.93		4.31	0.54
		20231031	0.96		2.16		7.55	0.45
		20231030	0.99		0.87		1.74	0.01
		20231106	0.99		1.39		3.17	0.01
		20230630	0.99		0.70		1.16	0.01
		20230703	0.99		0.55		0.70	0.01
		20230508	0.99		1.26		1.82	0.01
		20230707	0.99	0.99	1.63	1.08	5.14	3.60
		20230628	0.99		0.71		0.93	0.01
		20230511	0.98		1.45		2.01	0.01
		20230629	0.99		0.58		0.81	0.01
$T_{hx,s,out}$ (°C)	400	20230505	0.99		1.23		1.71	0.01
		20231031	0.99		1.08		3.60	0.01
		20231030	0.98		2.60		5.64	0.01
		20231106	0.98		3.19		6.93	0.01
		20230630	0.98		2.69		4.65	0.01
		20230703	0.98		1.77		2.60	0.01
		20230508	0.96		2.61		3.79	0.01
		20230707	0.98	0.96	2.92	2.13	7.26	7.46
		20230628	0.95		2.77		3.98	0.01
		20230511	0.95		2.84		3.90	0.01
		20230629	0.98		2.52		4.19	0.01
		20230505	0.97		2.92		4.34	0.01
		20231031	0.96		2.13		7.46	0.01

s.u. stands for same units as the predicted variable

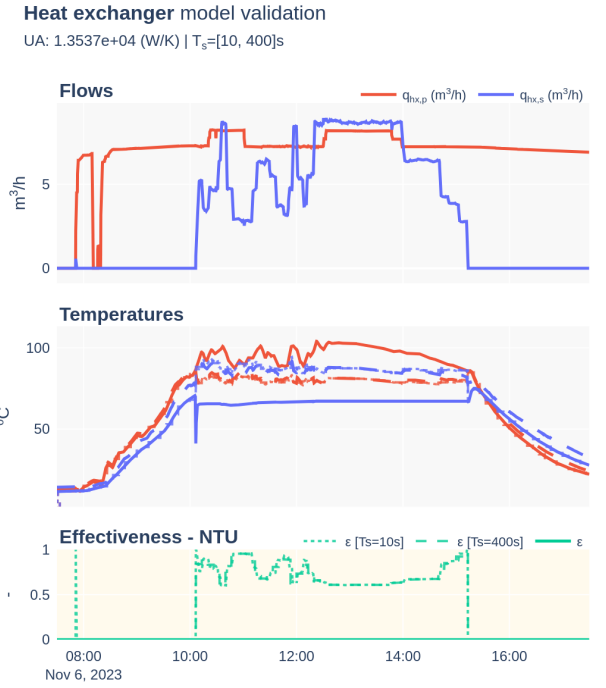


Figure 6.8: Heat exchanger model validation for a particular test. The effectiveness–NTU is limited to the model because it is an estimated parameter.



6.2.4 MED

The MED is modelled statically, considering changes in the system operating conditions happen at a slow enough rate that the dynamic behavior between stable states can be neglected, and thus, only those stable states are considered. Two models are developed for the MED: a data-driven model based on experimental data from the pilot plant, and a first-principles model based on thermodynamic equations. The data-driven model is the one integrated in the overall plant model used in optimization applications (See Chapter 8), while the first-principles model is used for comparison purposes and to gain insight into the operation of the MED (See Chapter 7).

Data-driven model

A Gaussian-Process Regression (GPR) model calibrated using data from two experimental campaigns described in Section 5.3.

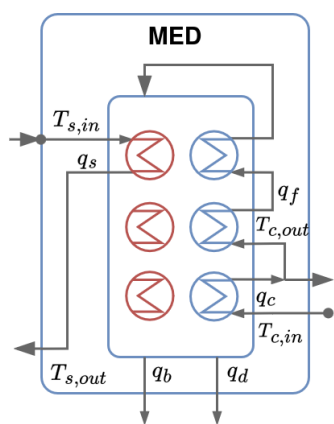


Figure 6.9: MED process diagram.

Model 6.6: MED model

$$q_d, T_{s,out}, q_c, T_{c,out} = f(q_s, q_f, T_{s,in}, T_{c,out}, T_{c,in})$$

$$q_d, T_{s,out}, q_c = f_{bb,q}(q_s, q_f, T_{s,in}, T_{c,out}, T_{c,in})$$

if $q_c > \bar{q}_c : q_c = \bar{q}_c$

or if $q_c < \underline{q}_c : q_c = \underline{q}_c$

then:

$$T_{c,out} = f_{bb,T}(q_s, q_f, T_{s,in}, q_c, T_{c,in})$$

$$q_d, T_{s,out} = f_{bb,q}(q_s, q_f, T_{s,in}, T_{c,out}, T_{c,in})$$

As observed in Model 6.6, the model has five inputs: the heat source flow rate ($q_{med,s}$), the feedwater flow rate ($q_{med,f}$), the inlet temperature of the heat source ($T_{med,s,in}$), the inlet temperature of the cooling water ($T_{med,c,in}$) and the outlet temperature of the cooling water ($T_{med,c,out}$). The model returns three main outputs: the distillate flow rate ($q_{med,d}$), the outlet temperature of the heat source ($T_{med,s,out}$) and the cooling water flow rate ($q_{med,c}$). An additional output is included with a validated value for the condenser outlet temperature ($T_{med,c,out}$), in cases where an unfeasible temperature is given as input. In Model 6.6, the functions $f_{bb,q}$ and $f_{bb,T}$ represent the black-box GPR models for the model with the main outputs and the auxiliary output, respectively.

First-principles model

The first-principles model is based on thermodynamic equations and mass and energy balances. A detailed description of the model can be found in the Appendix, Chapter B (MED First-Principles Model).

Electrical consumption

A similar procedure to the one for the solar field and thermal storage was followed, with some particular considerations:

The extraction pumps need to be evaluated under vacuum conditions, since this has a direct influence on the intake conditions (lower head pressure). The brine pump is evaluated with a step train test while the plant is inactive (no thermal input), in vacuum conditions and with feedwater being pumped. The water will naturally fall by gravity to the final effect¹⁵. The power consumption is measured using the VFD integrated power meter. For the distillate pump, water does not reach the final condenser unless vapor is generated, so the pump is evaluated with the plant active and distillate being produced. A test that produces distillate at the midrange working conditions of the VFD: ≈ 35 Hz. The step train is then performed by alternating high and low values¹⁶ and making sure the level stays within the operating range.

15: Given the plant vertically-stacked configuration

16: For example, 35 → 40 → 30 → 45 → 25 → 50 → 20 Hz

For the rest of the system pumps: heat source, feedwater and cooling water, a simple step train test is performed. Finally, the obtained electrical model is shown in Model 6.7.

Validation

As explained, two GPR models are used, so two models need to be calibrated, one for the aforementioned desired system outputs ($q_{med,d}$, $T_{med,s,out}$ and $q_{med,c}$) and an additional one for the condenser outlet temperature. An 80/20 training/validation split is used. The training is performed using an Radial Basis Function (RBF) kernel. The regression model is defined with the **GPy** library, which includes a Gaussian likelihood with a noise term by default. The kernel hyperparameters (variance, lengthscale, and noise variance) are optimized by maximizing the log-marginal likelihood using GPy's [104] built-in L-BFGS local optimizer.

[104]: GPy (), GPy: A Gaussian Process Framework in Python

Model 6.7: MED electrical consumption

$$\begin{aligned}
 C_{e,med} &= \text{med electrical consumption}(q_{med,s}, q_{med,f}, q_{med,c}, q_{med,d}, q_{med,b}) \\
 C_{e,med,s} &= 0.0104 - 0.025 q_{med,s} + 0.0339 q_{med,s}^2 \quad \text{m}^3/\text{h} \rightarrow \text{kW}_e \\
 C_{e,med,f} &= 0.704 - 0.0947 q_{med,f} + 0.0191 q_{med,f}^2 \quad \text{m}^3/\text{h} \rightarrow \text{kW}_e \\
 C_{e,med,c} &= 5.218 - 0.924 q_{med,c} + 0.0567 q_{med,c}^2 \quad \text{m}^3/\text{h} \rightarrow \text{kW}_e \\
 C_{e,med,d} &= 4.150 - 3.657 q_{med,d} + 0.948 q_{med,d}^2 \quad \text{m}^3/\text{h} \rightarrow \text{kW}_e \\
 C_{e,med,b} &= 0.031 - 0.019 q_{med,b} + 1.33 \times 10^{-3} q_{med,b}^2 \quad \text{m}^3/\text{h} \rightarrow \text{kW}_e \\
 C_{e,med,vac} &= \begin{cases} 5, & \text{if } med_{vac} = 2 \\ 1, & \text{if } med_{vac} = 1 \\ 0, & \text{if } med_{vac} = 0 \end{cases} \\
 C_{e,med} &= C_{e,med,s} + C_{e,med,f} + C_{e,med,c} + C_{e,med,d} + C_{e,med,b} + C_{e,med,vac}
 \end{aligned}$$

[View Model 6.7 in the GitHub repository](#)

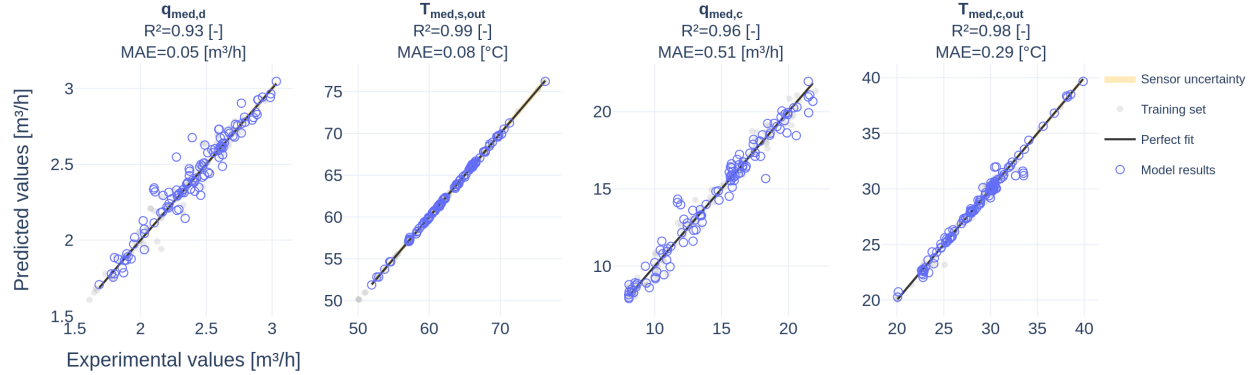


Figure 6.10: MED GPR model regression for different outputs. Dataset includes data spanning 6 years of operation.



From Figure 6.11, several observations can be drawn. First, the model shows high accuracy in predicting both distillate production and the heat source outlet temperature, even during transient phases such as those observed in the early part of the 31032023 test (Figure 6.11, left).

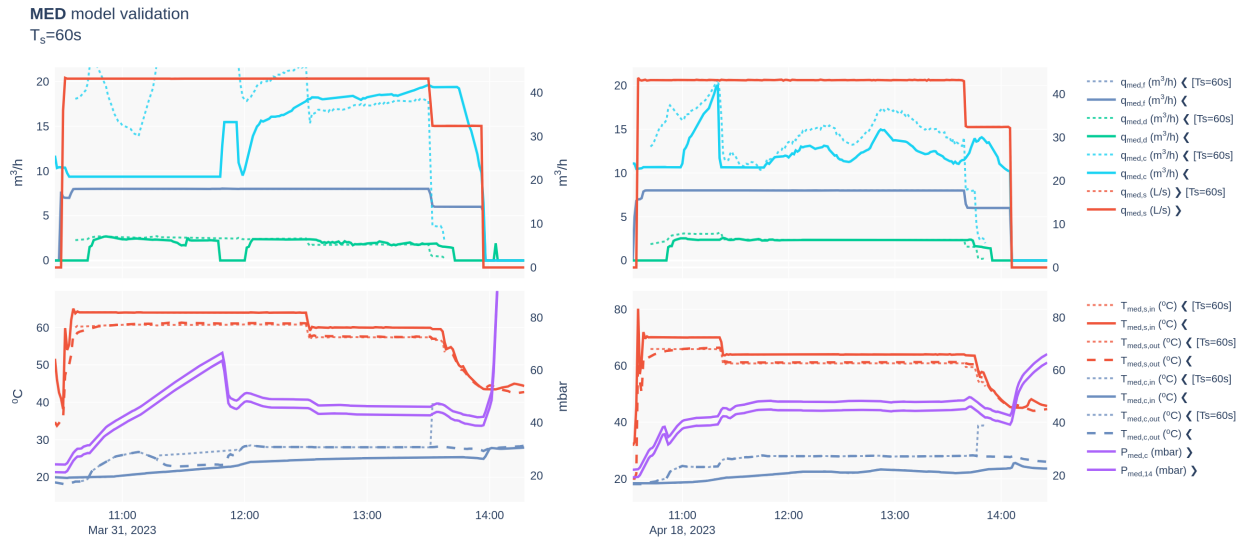


Figure 6.11: MED model validation tests.



In contrast, the cooling water predictions are less reliable during these transitions. As vapor gradually accumulates—visible as a pressure ramp in the condenser between 10:30 and 12:30 in the 202303031 test—it becomes difficult to predict how much vapor ultimately reaches the final condenser. Once stable conditions are established, however, the model can accurately estimate the cooling water demand required to maintain equilibrium at a given operating point, even under varying inlet water temperatures. This is evident in the later phase of the 202303031 test and throughout most of the 20230418 test.

17: Operating in a closed loop

A further observation is the system's strong sensitivity to the cooling water inlet temperature. In the pilot plant, which operates in a closed loop¹⁷, these inlet conditions are constantly shifting. Despite this, the static model is able to capture the condenser's overall behavior once the system stabilizes and the inlet temperature becomes the primary changing variable.

Subsystem	Parameter	Description	Value	Units
Model parameters				
Solar field	β	Gain coefficient	4.36×10^{-2}	m
	H	Heat loss coefficient	13.67	W/m ²
	V_p	Volume of control volume	[5.94, 4.87, 2.19]	m ³
Thermal storage	H_n	Heat loss coefficient	$[6.98, 5.84, 30.41] \times 10^{-3}$	W/K
	V_c	Volume of control volume	[5.33, 7.56, 0.9]	m ³
Heat exchanger	H_c	Heat loss coefficient	$[0.013.96, 0.1, 0.022] \times 10^{-3}$	W/K
	UA	Heat transfer conductance	1.35×10^4	W/K
Fixed model parameters				
Solar field	A_{cs}	Collector tube cross-section area	7.85×10^{-5}	m ²
	n_{tub-c}	Number of parallel tubes per collector	1	-
	n_{c-loop}	Number of parallel collectors per loop	7×5	-
	L_t	Individual collector tube length	23	m
	$n_{c,s}$	Number of collector row's in series	2	-
	T_{max}	Maximum working temperature	120	°C

Table 6.4: Models parameters

6.3 Discrete modelling. Operation state

The second modelling component defines the discrete state of the system, that is, its *operation state*. This component is modelled by means of FSMs. In order to determine its state, the Finite-State Machine (FSM) uses information from both its inputs, its internal state and the configured parameters.

The complete system is divided into two subsystems: the heat generation and storage subsystem (**sfts**) and the separation subsystem (**med**).

6.3.1 Heat generation and storage subsystem (**sfts**)

This subsystem encompasses the Solar Field (**sf**) and the Thermal Storage (**ts**). The subsystem can be modelled with a simple FSM. The FSM has two inputs, the recirculation flow rate on each circuit (q_{sf} and $q_{ts,src}$), and the FSM states are computed based on whether water is being recirculated on each. Four states are defined as shown in Table 6.5 and the possible transitions are visualized in Figure 6.12 (a). The states involve:

- ▶ **Off** (0). The system is off, no water is being recirculated in either circuit.
- ▶ **Warming up solar field** (1). Water is being recirculated in the solar field circuit but not in the thermal storage circuit. The solar field is being heated up.
- ▶ **Recirculating thermal storage** (2). Water is being recirculated in the thermal storage circuit but not in the solar field circuit. The thermal storage is being mixed.
- ▶ **Solar field heating up thermal storage** (3). Water is being recirculated in both circuits. The solar field is heating up the thermal storage.

Additionally, some conditions are configured with the following parameters¹⁸:

- ▶ **Enable recirculating thermal storage** (false). Allow to recirculate water in the thermal storage circuit while no water is being heated in the solar field. This would be used to mix the hot and cold tanks.
- ▶ **Active cooldown time** (10 minutes). Time to wait before activating the system again after stopping it.

6.3.2 Separation subsystem (**med**)

Two inputs are used in this machine, one logical which indicates the active state the system when all of the required pumps for operation are enabled. The other is an integer variable that regulates the vacuum state. This latter variable has three possible values: 0 when the vacuum pump is off, 1 when the vacuum pump operates at low speed (maintaining vacuum) and 2 when the vacuum pump

Reminder: FSMs

A finite state machine is a model of behavior composed of a finite number of states and transitions between those states. Within each state and transition some action can be performed^a.

^a See Section 3.1.3 (Discrete modelling by means of FSMs) for a more detailed description.

Table 6.5: **sfts** FSM states definitions. \wedge represents the logical AND operator and \Rightarrow represents that all meet the condition.

State	Name	Condition
0 (00)	Off	$q_{sf} \wedge q_{ts,src} == 0$
1 (01)	Warming up Solar Field (sf)	$q_{sf} > 0 \wedge q_{ts,src} == 0$
2 (10)	Recirculating Thermal Storage (ts)	$q_{sf} == 0 \wedge q_{ts,src} > 0$
3 (11)	sf heating up ts	$q_{sf} \wedge q_{ts,src} > 0$

18: In parentheses the value used

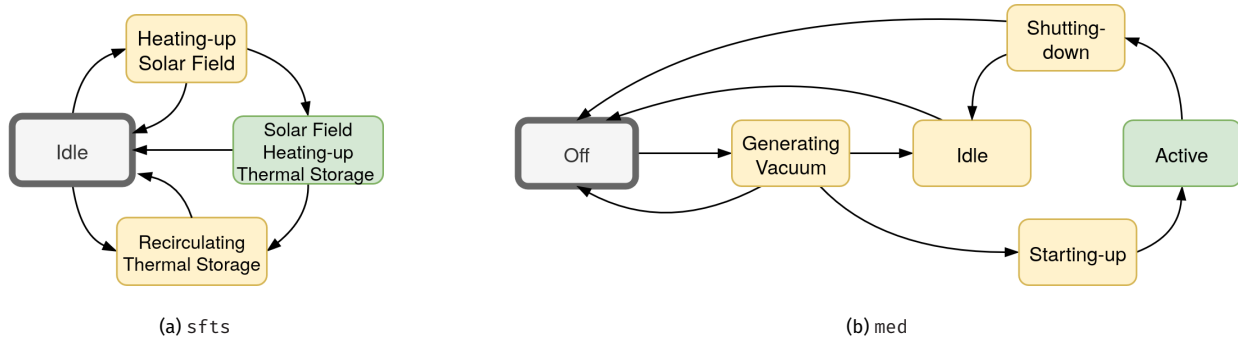


Figure 6.12: Finite-state machines for the different subsystems

operates at high speed (generating vacuum). The FSM states are computed based on these two inputs based on the conditions shown in Table 6.6 and the possible transitions are visualized in Figure 6.12 (b). The states are described in the following:

- ▶ **Off** (0). The system is off, no pumps are operating and no vacuum is being generated.
- ▶ **Generating vacuum** (1). The system is off, no pumps are operating but vacuum is being generated.
- ▶ **Idle** (2). The system is off, no pumps are operating but vacuum is maintained.
- ▶ **Starting-up** (3). The system is starting up, all pumps start operation following the procedure outlined in Section 7.5. No distillate is produced at this stage and temperature and pressure progressively ramp up until reaching equilibrium for the given inputs.
- ▶ **Shutting down** (4). The system is being shut down, distillate production has stopped and the system is cooled-down progressively. Extraction pumps start cycles of operation to empty the system. Vacuum may or may not be maintained at this stage.
- ▶ **Active** (5). The system is active, all pumps are operating and distillate is being produced.

As in the previous machine, the machine has additional FSM parameters that regulate its behavior, specifically:

- ▶ **Vacuum duration time** (30 minutes). Time to generate vacuum in the MED system.
- ▶ **Brine emptying time** (60 minutes). Time to extract brine from MED plant.
- ▶ **Startup duration time** (20 minutes). Time to start up the MED plant, once vacuum is generated.
- ▶ **Off cooldown time** (12 hours). Time to wait before activating the MED plant again after shutting it off.
- ▶ **Active cooldown time** (2 hours). Time to wait before activating the MED plant again after shutting it off or suspending it.

Finally, the machine has internal states that are updated during the machine evaluation in order to keep track of the progress of the different timed actions and whether they have been completed or not. These are for example the vacuum elapsed samples, the startup elapsed samples or the brine emptying elapsed samples. The associated logical states would be whether vacuum has been generated, whether the startup procedure has been completed or whether the brine emptying has been completed.

State	Name	Condition
0	Off	$\forall q == 0$
1	Generating vacuum	$med_{vac} == 2$
2	Idle	$\forall q == 0 \wedge med_{vac} == 1$
3	Starting-up	$\forall q > \underline{q} \wedge med_{vac} \geq 1$
4	Shutting down	$\exists q < \underline{q}$
5	Active	$\forall q > \underline{q} \wedge med_{vac} \geq 1$

Table 6.6: med FSM states definitions. \wedge represents the logical AND operator, \exists represents that at least one meets the condition, and \forall represents that all meet the condition.

6.3.3 Validation

Figure 6.13 shows the evolution of the states of both FSMs during a test. Particularly, the same test that is visualized in Figure ?? so that the actual inputs and subsystems states can be compared. It can be seen how both machines evolve in parallel in the bottom plot, while the upper one shows the cumulative input values¹⁹. The sfts first starts with the heating up of the solar field state triggered by the activation of the solar field pump (`sf_active`), and once the temperature is high enough after few samples the thermal storage starts recirculating (`ts_active`). This continues until the end of the tests when the temperature decreases so it gets deactivated (at sample 80 in Figure 6.13).

For the med, there is no measurement for the vacuum state of the system so it is assumed that it is set at a high-level from the beginning and kept until the end of the test. The system starts in the off state, and once vacuum is generated the start-up procedure gets triggered at sample 12-13. The system then stays active producing separation until it is shut-off at sample 56 for two samples, equivalent to over 10 minutes.

19: All variables are shown as integers and aliases are created to group the logical active conditions e.g. `med_active = $\forall q > \underline{q}$`

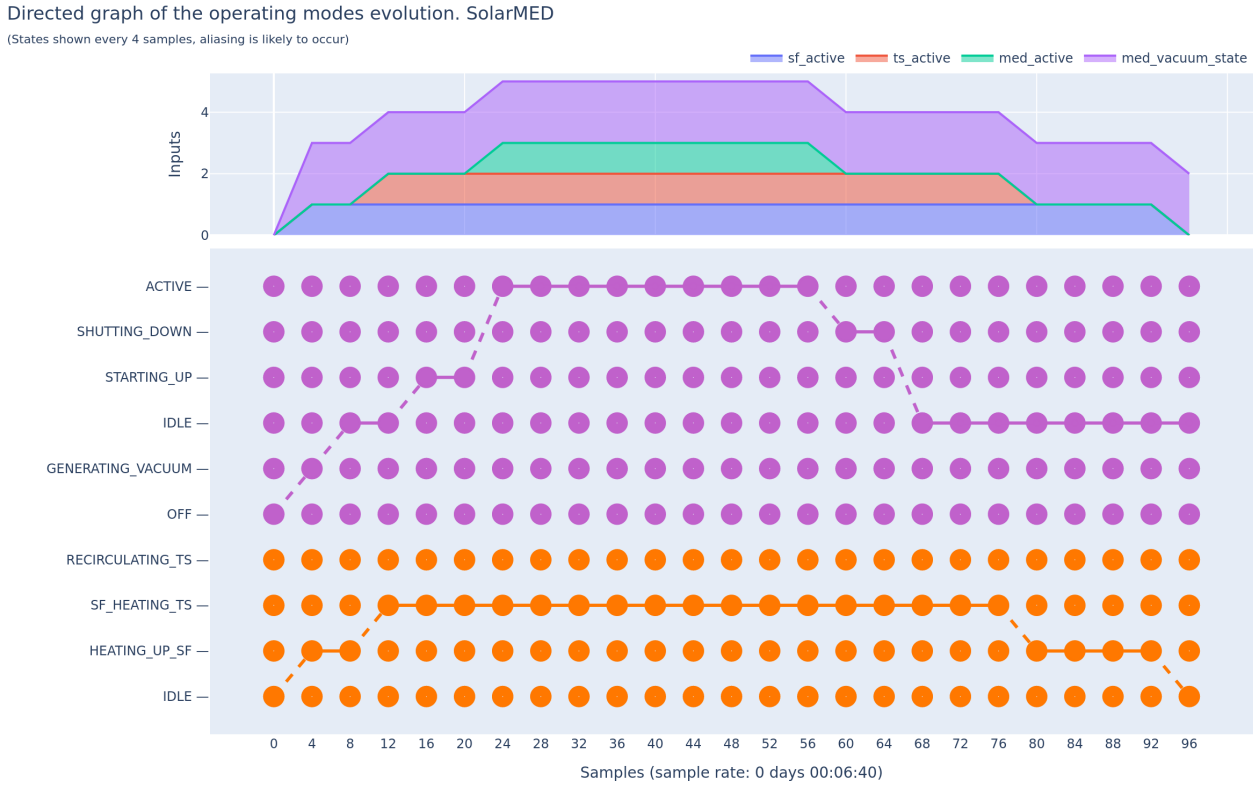


Figure 6.13: SolarMED FSM states evolution during a test on 20230703. Purple represents the `med` state and orange the `sfts`.
Note: `med active` is equivalent to the condition $\forall q_{med,i} > \underline{q}_{med,i}$

6.4 Complete system model

Finally, all the individual components described above (continuous and discrete) are combined to form the complete system model. The complete model is a hybrid model that orchestrates physics models for the solar field, heat exchanger, thermal storage, three-way valve and data-driven for the MED, plus two supervisory finite state machines. The continuous states are the outputs of the different subsystems, while the discrete states are the states of the two FSMs.

20: Specifically as a Python class

The model –defined in Model 6.8– is implemented following an object-oriented approach²⁰. Once it is initialized provided with the initial discrete states (e.g. vacuum generated, brine emptied from final effect, etc) and system parameters (e.g. thermal storage volumes, heat exchanger transfer conductance, med timings, etc). Also need to be initialized the initial temperatures for the solar field and thermal storage.

Each step takes environment inputs (irradiance I , ambient temperature T_{amb} , seawater temperature $T_{med,c,in}$) and operation decisions (e.g., q_{sf}^* , $q_{ts,src}^*$, $q_{med,s}^*$, $q_{med,f}^*$, $T_{med,s,in}^*$, $T_{med,c,out}^*$). Setpoints reflect operator/optimizer intent, the model then validates and turns them into realized outputs. Each step advances the plant one sampling interval. Physically, the model treats the installation as three hydraulic/thermal loops that exchange energy, all embedded in ambient conditions and subject to equipment limits.

Model 6.8: SolarMED model

$$\begin{aligned}
 q_{med,d}, C_e &= f(q_{med,s}, q_{med,f}, T_{med,s,in}, T_{med,c,out}, \\
 &q_{ts,src}, q_{sf}, med_{vac,st}, T_{med,c,in}, T_{amb}, l; \\
 &\theta_{sf}, \theta_{hx}, \theta_{med}, \theta_{softs}^{fsm}, \theta_{med}^{fsm}, \theta_\infty) \\
 st_{softs} &= soft fsm model(q_{sf}, q_{ts,src}; \theta_{softs}^{fsm}) \\
 st_{med} &= med fsm model(q_{med,s}, q_{med,f}, T_{med,c}; \theta_{med}^{fsm}) \\
 T_{sf,out} &= sf model(T_{sf,out,k-1}, T_{sf,in,k-n:k}, q_{sf,k-n:k}, l, T_{amb}; \theta_{sf}) \\
 T_{ts,h}, T_{ts,c} &= ts model(\\
 &T_{ts,h}(k-1), T_{ts,c}(k-1), T_{hx,s,out}, \\
 &T_{med,s,out}, q_{ts,src}, q_{ts,dis}, T_{amb}; \theta_{ts} \\
) \\
 T_{sf,in}, T_{hx,s,out} &= hx model(T_{sf,out}, T_{ts,c,b}, q_{sf}, q_{ts,src}, T_{amb}; \theta_{hx}) \\
 q_{ts,dis} &= 3WV model(q_{med,s}, T_{med,s,in}, T_{med,s,out}) \\
 q_{med,d}, T_{med,s,out}, q_{med,c}, T_{med,c,out} &= med model(\\
 &q_{med,s}, q_{med,f}, T_{med,s,in}, T_{med,c,out}, T_{med,c,in} \\
) \\
 C_{e,sf} &= sf electrical consumption(q_{sf}) \\
 C_{e,ts} &= ts electrical consumption(q_{ts,src}) \\
 C_{e,med} &= med electrical cons.(q_{med,s}, q_{med,f}, q_{med,c}, q_{med,d}, q_{med,b}) \\
 C_e &= C_{e,sf} + C_{e,ts} + C_{e,med}
 \end{aligned}$$

The supervisory logic (*i.e.*, FSMs) first decides which subsystems are allowed to act (solar field circulating, storage charging/discharging, MED producing). That logic turns setpoints into admissible operating points: a requested flow or temperature may be permitted as is, clipped to a limit, or forced to zero if a component is inactive, or set to a predefined value²¹. Once the discrete state of the system is fixed for the current step, the physics is evaluated in a sequence that mirrors causality and heat flow. This set of dependencies between the different subsystems is visualized in Figure 6.14.

The MED is solved first because it defines the thermal demand that the rest of the system must support. With the MED demand known, the three-way valve determines how much hot water must be extracted from storage and how to mix it to meet the MED hot-side inlet target. Physically, it blends water drawn from the top of the hot tank with the MED return, choosing a mix ratio and discharge flow that close the MED's energy balance. That fixes the storage discharge flow and the thermal duty the storage must deliver this step.

Next, the heat supply side is computed. When the solar field is circulating and storage is being recharged, the solar field, heat exchanger, and tanks are thermally coupled: the solar outlet temperature, the heat exchanger prima-

21: For example, if the MED subsystem is in the shutting down process, no thermal load is extracted from the thermal storage, and only the electrical consumption of the extraction pumps is considered (and of the vacuum if kept active)

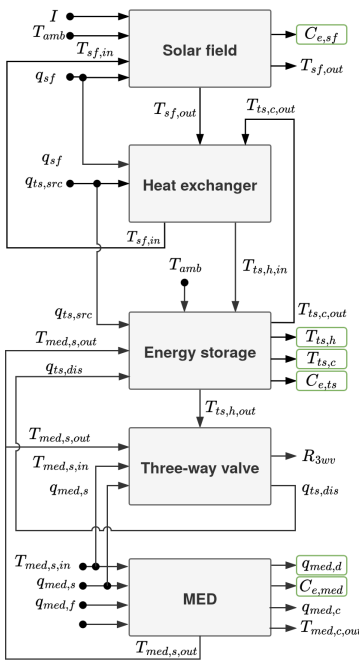


Figure 6.14: Complete SolarMED model architecture.

22: Figure 6.15 – Solar field from 06:00 to 10:00 and from 15:00 to 17:45

23: At the end of operation (15:00), for the 8-hour horizon: $T_{ts,h,t} = 96.98^\circ\text{C}$ vs 95.69 and $T_{ts,c,b} = 80.2^\circ\text{C}$ vs 81.7. In terms of energy stored: $Q_{ts,c} = 194.45 \text{ kWh}_{th}$ vs 211.36 and $Q_{ts,c} = 170.24 \text{ kWh}_{th}$ vs 173.52

24: Figure 6.15 – Thermal storage – Energy

25: Figure 6.15 – MED – Temperatures (right)
 $-P_{v,14}$

ry/secondary outlet temperatures, and the evolving tank stratification all depend on each other. In that coupled case, a small nonlinear subproblem is solved so that energy balances are simultaneously satisfied across generation, transfer, and load (storage), considering the previous tank states. When the field and storage are not simultaneously active (for example, idle storage or field, or storage discharging), the supply side decouples: the solar field is first evaluated alone, producing a primary-side outlet temperature ; then the tanks update their stratified temperatures by applying the computed inlet/outlet temperatures and the discharge flows.

Once temperatures and flows are settled, the model computes electrical powers using the actuators fitted curves. Finally, time-dependent states are rolled forward: solar loop histories are shifted to carry the new inlet/outlet values into the next step, and the tank stratification produced this step becomes the initial condition for the next.

6.4.1 Validation

Figure 6.15 and Table 6.7 show the results obtained for some days when evaluating the complete model. The model is evaluated with a sample time of 400 s but four different prediction horizons. In Figure 6.15 two of them are shown, 1 hour and 8 hours. This means, e.g., that for a horizon of 1 hour, the model is evaluated for 1 hour with no feedback from measured data. Then the model is updated with the actual measured state at that time and the process is repeated for the rest of the test. Finally, the error is computed between the model output and the actual measurement.

In Figure 6.15, while all subsystems are active, it can be seen a good agreement between the model prediction and the actual measurements for both horizons. A higher error is observed during startup and shutdown for the solar field²² (which propagates to the heat exchanger).

The MED, since it is a static model, is not affected by the horizon time (as long as the hot tank top temperature is above the operating temperature), while the solar field, and specially the thermal storage, show a higher error that accumulates over time. As expected, the 8-hour horizon shows a higher error than the 1-hour horizon, since the model is not updated with actual measurements for the whole duration of the test. Nonetheless, the final state of the thermal storage temperature profiles is not too far from the actual measurements²³, showing that the model is able to capture the overall behavior of the system. This is confirmed by the good agreement observed in the energy stored throughout the test²⁴.

For the MED, as commented in the component section, the output with the highest error is the cooling water flow rate, showing higher errors at the beginning where there is a heat source temperature mismatch (the actual temperature is higher than the upper limit of the data-driven model so is clipped) and in the second part of the test where the inlet cooling water temperature increases significantly, and since the flow was kept constant in the test the condenser is not stable anymore²⁵.

Table 6.7 shows the results obtained for different metrics (MAE, MAPE) for two different test days. This time two additional horizons are included, 30 minutes and 4 hours. The table also shows the computation time required to evaluate the model for each prediction horizon.

As mentioned, static variables such as the distillate production show no variation with the prediction horizon (e.g. MAE: $q_{med,d} = 0.15 \text{ m}^3/\text{h}$ for all horizon times in test 20230414), while dynamic variables such as the thermal storage hot tank top temperature show a clear increase in error with longer horizons (e.g. MAE

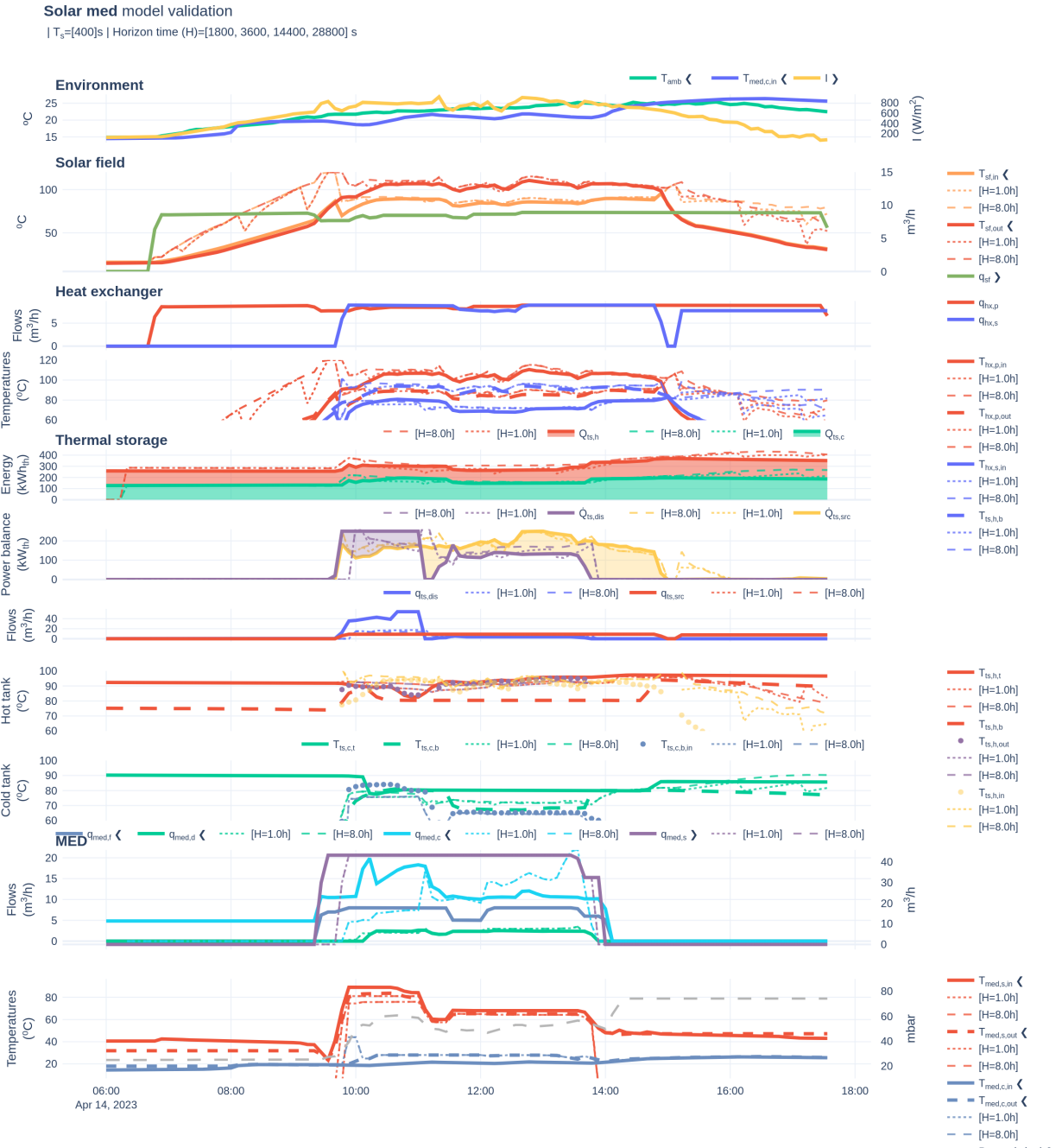


Figure 6.15: SolarMED model validation



$T_{ts,h} = 2.36^\circ\text{C}$ for a 30-minute horizon and $T_{ts,h} = 3.59^\circ\text{C}$ for a 4-hour horizon in test 20230414).

When judging the performance metrics, it is important to keep in mind that for the complete model, feedback from the real system is only available at the

Extended validation results

A visualization of all evaluated tests for every model validation are available in the thesis repository as a compressed folder



beginning of the day. From that point on, most subsystem inputs depend on states from other subsystems. For example, the solar field inlet temperature depends on the heat exchanger output, which in turn depends on the thermal storage state, which itself depends on the MED plant operation and, ultimately, on the solar field. Consequently, errors can propagate and accumulate over time.

Therefore, achieving consistent accuracy for multi-hour horizons in a fully coupled system is challenging. For standalone component models, MAPE values above 5–10 % would typically be considered poor; however, for the complete integrated system, maintaining MAPE values below roughly 15 % across several hours is a commendable result. This is particularly the case for thermal state variables such as $T_{ts,h}$ and $T_{ts,c}$, where the model captures the general dynamic behavior well even at long horizons. The computation times shown in the last column remain reasonable, with the 8-hours horizon evaluation taking around 5 s.

Predicted variable	Test date	Horizon time (s)	Performance metric		
			MAE (s.u.)	MAPE (%)	Time (s)
$q_{med,d}$ (m^3/h)	20230414	1800	0.15	16.80	13.42
		3600	0.15	16.80	22.13
		14400	0.15	16.80	8.15
		28800	0.15	16.80	5.86
	20230418	1800	0.07	9.99	7.83
		3600	0.07	9.99	4.52
		14400	0.07	9.99	2.64
		28800	0.07	9.99	2.52
	20230414	1800	2.36	2.50	13.42
		3600	3.15	3.32	22.13
		14400	3.59	3.78	8.15
		28800	3.18	3.37	5.86
$T_{ts,h}$ ($^\circ\text{C}$)	20230418	1800	0.48	0.52	7.83
		3600	1.09	1.18	4.52
		14400	3.95	4.29	2.64
		28800	5.87	6.38	2.52
	20230414	1800	2.66	3.76	13.42
		3600	3.03	4.27	22.13
		14400	4.20	5.93	8.15
		28800	4.31	6.20	5.86
	20230418	1800	2.76	3.94	7.83
		3600	3.19	4.52	4.52
		14400	5.37	7.59	2.64
		28800	6.85	9.74	2.52
$T_{ts,c}$ ($^\circ\text{C}$)	20230414	1800	14.12	16.85	13.42
		3600	13.37	16.18	22.13
		14400	13.71	15.79	8.15
		28800	13.80	15.92	5.86
	20230418	1800	15.93	43.31	7.83
		3600	18.35	47.19	4.52
		14400	13.04	33.59	2.64
		28800	12.85	30.99	2.52
	20230414	1800	25.02	30.60	13.42
		3600	23.59	30.07	22.13
		14400	26.78	37.01	8.15
		28800	25.81	36.43	5.86
$\dot{Q}_{ts,src}$ (kW_{th})	20230418	1800	13.02	45.83	7.83
		3600	12.69	44.46	4.52
		14400	19.82	78.38	2.64
		28800	26.58	97.08	2.52
	20230414	1800	20.57	15.29	13.42
		3600	17.02	12.65	22.13
		14400	14.90	11.34	8.15
		28800	19.23	15.01	5.86
	20230418	1800	8.73	6.23	7.83
		3600	8.71	6.23	4.52
		14400	16.92	11.64	2.64
		28800	21.01	14.35	2.52
$Q_{ts,h}$ (kWh_{th})	20230414	1800	11.82	6.87	13.42
		3600	14.58	8.17	22.13
		14400	26.15	14.61	8.15
		28800	22.15	12.37	5.86
	20230418	1800	9.30	4.64	7.83
		3600	10.37	5.12	4.52
		14400	21.75	10.76	2.64
		28800	30.39	15.11	2.52

Table 6.7: Summary table of the prediction results obtained with the SolarMED model for different test days, sample time set to 400s and different prediction horizons.

s.u. stands for same units as the predicted variable

Performance evaluation in MED processes: standard methodology proposal and high TBT experimental campaign

7

TL;DR

This chapter presents a standardized method for evaluating the performance of Multi-Effect Distillation (MED) processes, which can also be extended to other thermal separation technologies. The method addresses key aspects such as instrumentation requirements, process control, and the suitability of performance metrics, including the uncertainties associated with their determination. Additionally, an algorithm has been developed for the automatic detection of steady-state operation, enhancing the reliability and robustness of evaluations under variable conditions. Experimental results confirm that the proposed method is both robust and reliable, enabling fair comparisons of MED processes across different operating scenarios.

The experimentation includes the evaluation of the process at high Top Brine Temperatures (TBTs). The results are analyzed using different performance metrics and the scale formation risk is estimated by the Ryznar Stability Index (RSI). The results show that the MED process can be operated at high TBTs without significant scale formation and achieve higher concentrations, but without significant improvements in thermal performance and limited concentration capacity if no changes to its design are made.

Introduction

The future of MED in desalination and brine concentration applications depends on the technical development of the process and its integration with other technologies [25, 26]. The performance of this technology and how it is evaluated plays an important role in this development.

Although efforts have been made to propose performance metrics to evaluate the multi-effect evaporation process, there is neither consensus in which metrics are the most suitable [27] nor standards on how to evaluate the experimental process. The only standard existing in MED is not related to performance evaluation, but to cost structures and determinants [28].

For the performance evaluation of MED processes, originally, the index Gain Output Ratio (GOR) was used for plants operating with steam as external energy source. In order not to be limited to steam-driven systems and to take into account sensible heat sources, a new performance index was defined: the Performance Ratio (PR) [81, 105], which is currently the most widely adopted for MED performance evaluation although it is constrained by using a reference enthalpy of 2326 kJ equivalent to 1000 BTU. In [106], a variation of this metric called the Waste Heat Performance Ratio (PR_{WH}) was suggested to account for the potential of low-grade waste heat sources. Another widespread thermal performance metric that has been used in MED is the Specific Thermal Energy Consumption (STEC) and its electrical equivalent, the Specific Electrical Energy Consumption (SEEC). However, there are certain limitations in the aforementioned metrics that challenge making a fair comparison between desalination systems that use different energy sources *i.e.* electrical and thermal¹. Furthermore, the ability of thermal energy to perform work changes with its temperature, so it is essential to consider the quality of the thermal energy used in desalination processes. This limitation of traditional energetic metrics was showcased in Bouma *et al.* [84] where they compared four different configurations of MED plants: a low

7.1	Process analysis	84
7.2	Performance metrics	85
7.2.1	Separation metrics	85
7.2.2	Energetic metrics	86
7.2.3	Exergetic metrics	88
7.3	Instrumentation	89
7.3.1	Key Process Variables (KPVs) .	89
7.3.2	Instrumentation requirements	90
7.3.3	Uncertainty determination . .	92
7.4	Monitoring and process control	92
7.4.1	Monitoring: steady-state identification	92
7.4.2	Control system	94
7.5	Methodology validation and high TBT results	96

[25]: Ghenai *et al.* (2021), "Performance Analysis and Optimization of Hybrid Multi-Effect Distillation Adsorption Desalination System Powered with Solar Thermal Energy for High Salinity Sea Water"

[26]: Son *et al.* (2020), "Pilot Studies on Synergistic Impacts of Energy Utilization in Hybrid Desalination System"

[27]: Burgess *et al.* (2000), "Solar Thermal Powered Desalination: Membrane versus Distillation Technologies"

[28]: Pinto *et al.* (2017), "Desalination Projects Economic Feasibility"

[81]: El-Dessouky *et al.* (2002), *Fundamentals of Salt Water Desalination*

[105]: Mistry *et al.* (2011), "Entropy Generation Analysis of Desalination Technologies"

[106]: Christ *et al.* (2014), "Thermodynamic Optimisation of Multi Effect Distillation Driven by Sensible Heat Sources"

1: the value of 1 kWh electric differs from that of 1 kWh thermal in terms of their ability to produce work, as the latter is constrained by the Carnot efficiency [87]

[84]: Bouma *et al.* (2020), "Metrics Matter"

temperature MED configuration (LT-MED), a MED unit incorporating Thermal Vapor Compression (MED-TVC), a MED unit using nanofiltration (NF-LT-MED) for feedwater pretreatment, and a combination of TVC and nanofiltration. Although the Specific Thermal Energy Consumption (STEC) values favored the use of TVC, a more rigorous—exergetic—analysis revealed that the most efficient systems were those that used lower temperature heat sources (LT-MED and NF-LT-MED).

[107]: Darwish et al. (2006), “Multi-Effect Boiling Systems from an Energy Viewpoint”

[108]: Shahzad et al. (2019), “A Standard Primary Energy Approach for Comparing Desalination Processes”

[87]: Lienhard et al. (2017), “Thermodynamics, Exergy, and Energy Efficiency in Desalination Systems”

[109]: Brogioli et al. (2018), “Thermodynamic Analysis and Energy Efficiency of Thermal Desalination Processes”

[110]: Spiegler et al. (2001), “El-Sayed, Y.M.”

[111]: Sharqawy et al. (2011), “On Exergy Calculations of Seawater with Applications in Desalination Systems”

[112]: Sharqawy et al. (2010), “Formulation of Seawater Flow Exergy Using Accurate Thermo-dynamic Data”

[113]: Mistry et al. (2012), “Effect of Nonideal Solution Behavior on Desalination of a Sodium Chloride (NaCl) Solution and Comparison to Seawater”

[114]: Mistry et al. (2013), “Generalized Least Energy of Separation for Desalination and Other Chemical Separation Processes”

[115]: Thiel et al. (2015), “Energy Consumption in Desalinating Produced Water from Shale Oil and Gas Extraction”

[116]: Valenzuela et al. (2014), “Optical and Thermal Performance of Large-Size Parabolic-Trough Solar Collectors from Outdoor Experiments”

[117]: Prahil et al. (2018), *Protocol for Characterization of Complete Solar Concentrators Using Photogrammetry or Deflectometry*

[118]: Bayón et al. (2019), “Development of a New Methodology for Validating Thermal Storage Media”

Some authors have carried out exergy analysis to overcome the limitations aforementioned of energy performance metrics. Darwish et al. [107] proposed two new metrics: Specific Fuel Energy and Equivalent Specific Work. The first compares the energy used for the desalination process that could otherwise be used for energy generation in a turbine for which it was assumed a value for the efficiency of the power plant. The second sets the work potential of the extracted steam as a baseline, considering the desalination plant separation efficiency and adding the energy consumption for pumping. The problem of this study is that it is limited to cogeneration schemes (joint electricity and water production) and would not be useful in the case of desalination with low-temperature sources. Shahzad et al. [108] developed an approach based on the second law of thermodynamics, which is also useful only for cogeneration schemes. They proposed a common metric called the Standard Universal Performance Ratio to compare desalination processes using different kinds of energy, which is based on conversion of different types and grades of energies to standard primary energy. In this case, conversion factors were proposed to convert the derived energy input to the standard primary energy. Other authors have performed exergy analyses for stand-alone desalination processes, as is the case of Lienhard et al. [87] and Brogioli et al. [109], who considered desalination processes as a black box and the ideal work or the thermodynamic limit for the separation of dissolved salts in seawater as the Carnot work.

The problem with the exergy analyses is that they are more complex [110] due to the need to consider several aspects not present in simple energetic metrics: definition of dead state and control volume [111], chemical exergy modeling of seawater [112, 113] and minimum energy reference (least and minimum work of separation) [114, 115]. Probably because of their complexity, they have not been widespread in the performance evaluation of practical setups. Also, none of the works published so far in the scientific literature addresses specifically the exergetic evaluation when using non-conventional energy sources such as waste heat.

Two important requirements for an accurate and reliable performance assessment are the steady state identification and the uncertainty of both the direct measurement and that associated with the performance metric determination. With respect to the former, it is highly recommended to use automatic procedures that increase the reliability of the measurements. The steady state evaluation carried out manually so far by qualified operators [116–118], leads to high time consumption and full dependence on the operators’ attention, leading to potential unreliable identifications. With respect to the latter, it allows for a more comprehensive and nuanced approach to performance evaluation, since it increases the robustness of the evaluation while providing information on the reliability of the results. Neither of these two aspects have yet been addressed in the performance assessment of thermal desalination plants. There is a gap in the establishment of standard methodologies that include all the necessary requirements for the reliable assessment of the performance of thermal desalination processes. This chapter aims to address this gap by proposing a method with potential for a broader application in other thermal desalination processes. The method is applied and validated in the MED-Plataforma Solar de Almería (PSA) plant as part of a high TBT experimental campaign.

Evaluation at high Top Brine Temperature

The performance of a thermal process, such as MED, is dictated by the Carnot cycle [109], which sets the theoretical maximum efficiency for any heat engine. The efficiency of the Carnot cycle is limited by the temperature difference between the hot and cold sinks, which determine the amount of thermal energy that can be converted into useful (separation) work.

An approach to bring the MED closer to its thermodynamic limit can be achieved by raising the Top Brine Temperature (TBT) (from 70 to 80–90°C), which allows to increase the number of effects [119] while maintaining an optimal temperature drop across them (*pinch*)². This leads to an improvement in the thermal performance of traditional desalination applications and an increase in the concentration factors achievable [85].

High TBT does not mean high heat source temperature

MED-Thermal Vapor Compression (TVC) plants even when operating at low TBT require motive steam at *high* temperatures (120–150°C) [89]. However, the extension of the MED process to higher TBT values in the range of 80–90°C still requires relatively low temperature heat (<100°C), so it can still be considered low-temperature and compatible with low-grade waste heat sources.

In practice, the TBT in the MED system is limited to 70°C, since higher TBTs increase the risk of precipitation of divalent ions, which tend to form incrustations on the heat exchange surfaces. These deposits reduce heat transfer efficiency, as extensively analyzed by Glade *et al.* [120, 121].

Ryznar Stability Index (RSI)

The Ryznar Stability Index (RSI) is an empirical indicator used in water chemistry to predict the tendency of water to form scale (calcium carbonate deposits) or to cause corrosion. It is based on the Langelier Saturation Index (LSI) but is formulated to better correlate with observed scaling and corrosion behavior [122]. It is defined as:

$$RSI = 2pH_s - pH,$$

where pH is the measured pH of the water sample and pH_s is the pH at which the water is saturated with calcium carbonate (CaCO_3).

Figure 7.1 shows the RSI of seawater at different temperatures and concentrations, where the background surface color represents the RSI. For un-treated feedwater this risk of precipitation is present at almost any temperature due to its composition (RSI below 4, see Table 7.1). This situation can be attenuated either by the use of an anti-scalant, or by treating the feedwater to remove the divalent ions. One promising option to achieve the latter is to use selective nanofiltration membranes [123]. A nanofiltration pretreatment can be used to selectively remove the divalent ions while leaving relatively unaffected the components to be separated in the MED process, *i.e.* NaCl. This allows the operation of MED processes at higher TBTs or higher feed concentrations.

This second feature potentially enables hybrid systems combining two separation phases *e.g.*: an initial Reverse Osmosis (RO) stage for traditional seawater desalination followed by a MED brine concentrator that tolerates higher feed concentrations.

The chapter is structured as follows. First, in Section 7.1, a process analysis focused on performance evaluation is presented to clearly define the eval-

[109]: Brogioli *et al.* (2018), “Thermodynamic Analysis and Energy Efficiency of Thermal Desalination Processes”

2: With limitations, as in each effect a considerable amount of exergy is destroyed and a minimum pinch is required

[85]: Zaragoza *et al.* (2022), “Coupling of Nanofiltration with Multi-Effect Distillation for Solar-Powered Seawater Desalination towards Brine Mining and Water Production for Agriculture”

[120]: Glade *et al.* (2010), “Scale Formation of Mixed Salts in Multiple-Effect Distillers”

[121]: Krömer *et al.* (2015), “Scale Formation and Mitigation of Mixed Salts in Horizontal Tube Falling Film Evaporators for Seawater Desalination”

[123]: Schafer *et al.* (2021), *Nanofiltration: Principles, Applications, and New Materials*

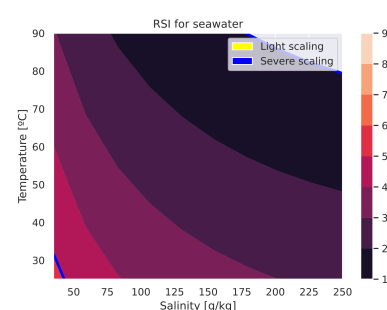


Figure 7.1: RSI of seawater at different temperatures and concentrations

Table 7.1: Ryznar Stability Index (RSI) values and their interpretation in terms of scaling and corrosion risk [122].

RSI > 9	Severe corrosion
7.5 < RSI < 9	Heavy corrosion
7 < RSI < 7.5	Significant corrosion
6 < RSI < 7	Stable water
5 < RSI < 6	Moderate to light scaling
4 < RSI < 5	Severe scaling

3: e.g. a design metric would be the specific area [81]

[84]: Bouma et al. (2020), "Metrics Matter"

4: The use of electrical energy will always be desired to be minimized, so the distinction is not needed.

5: e.g. a less efficient system will require a larger heat exchanger area to extract more energy from the waste heat source, leading to increased system costs

[124]: Mistry et al. (2013), "An Economics-Based Second Law Efficiency"

[125]: Christ et al. (2017), "Techno-Economic Analysis of Geothermal Desalination Using Hot Sedimentary Aquifers"

[93]: Christ et al. (2015), "Boosted Multi-Effect Distillation for Sensible Low-Grade Heat Sources"

[106]: Christ et al. (2014), "Thermodynamic Optimisation of Multi Effect Distillation Driven by Sensible Heat Sources"

[126]: Christ et al. (2015), "Application of the Boosted MED Process for Low-Grade Heat Sources – A Pilot Plant"

ation scope as well as the process inputs and outputs. Then, in Section 7.2, the performance metrics are introduced, including separation, energetic, and exergetic criteria. Section 7.3 describes the system instrumentation, covering Key Process Variables (KPVs), instrumentation requirements, and the uncertainty determination for both direct measurements and derived metrics. Section 7.4 presents the proposed steady-state identification algorithm for stable operation monitoring, together with the control strategies to be implemented. Finally, in Section 7.5, the proposed methodology is applied to a case study—an experimental campaign at the MED-PSA plant—to experimentally characterize the system under high TBTs. The results of this high-TBT operation are also analyzed in this section.

7.1 Process analysis

Metrics are defined based on some criteria, and this criteria is of paramount importance because resources and efforts are invested in optimizing the process in its direction. In order to adequately define these criteria, it is important to have an overall perspective of the process: defining its inputs and useful outputs—from a qualitative point of view—as well as a clear delineation of the scope of the evaluation.

Metrics can be related either to the operation or to the design of the system³. In terms of scope, they can span from primary energy sources [84] or the isolated MED process. This chapter focuses on the **operation** of an **isolated** MED system. Additionally, for the determination of the performance metrics, the following aspects are considered:

Application. Two applications are distinguished:

- ▶ **Seawater desalination.** The objective is to obtain fresh water. The level of separation achieved is a secondary (not useful) output.
- ▶ **Brine concentration.** The objective is to extract resources from the brine in order to valorize it. Here, the level of separation is a crucial factor to consider.

External heat source type. Two types of external heat sources are distinguished⁴:

- ▶ **Process heat.** Process heat is the heat utilized by a system and its associated costs are related to the amount of energy consumed.
- ▶ **Waste heat.** Waste heat is the heat utilized by a system that would otherwise be lost to the environment. It has no associated costs to the amount of heat used, though there are other costs associated with its use⁵ [124, 125]. Here the goal is to maximize the amount of product by maximizing the utilization of the waste source [93, 106, 126].

Process heat vs waste heat take on efficiency

In a process heat driven system, between two plants that produce the same amount of useful product, the most efficient one is the one that uses the least external heat to do so, whereas in a waste heat driven system, the two plants would be considered as efficient since the unused heat would be wasted to the environment. A more intuitive definition would be:

Given two plants that consume the same waste heat, the most efficient one is the one that produces the most product with that available heat.

Based on the above considerations, Figure 7.2 shows the control volume of the MED process with the inputs and outputs used for the definition of the

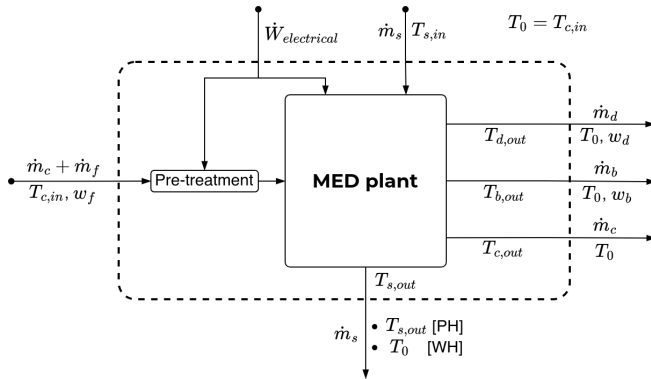


Figure 7.2: Inputs and outputs variables in an MED process. The dash line delimits the control volume

performance metrics. From left to right, seawater (including cooling water, c , and feed, f) enters the control volume at the seawater intake conditions ($T_{c,in}$). The cooling water is rejected at $T_{c,out}$. On the right side, the distillate and the brine are discharged from the MED system at temperatures $T_{d,out}$ and $T_{b,out}$ and mass fractions w_d and w_b , respectively. The temperatures of all these outlet streams, from a qualitative (*i.e.* exergetic) point of view, are useless and thus considered to be at T_0 when leaving the control volume⁶.

From top to bottom, the energy sources for the system are depicted. Electrical work is depicted as $\dot{W}_{electrical}$ and includes pumping, vacuum system, and feed water pretreatment, among others. The heat source is represented by the subscript (s) and as shown in the figure, it enters the MED plant at $T_{s,in}$ and leaves it at $T_{s,out}$ after releasing part of its energy. When leaving the control volume, $T_{s,out}$ value depends on the type of heat source:

- ▶ Process heat (PH). The value of $T_{s,out}$ does not change. In case steam is used as heat source, the primary energy driver is the latent heat of phase change and $T_{s,out}$ is usually similar to or equal to $T_{s,in}$. In case a sensible heat source is used, the driving force is the temperature difference and $T_{s,out}$ is between $T_{s,in}$ and T_0 .
- ▶ Waste heat source (WH). In this case, $T_{s,out}$ is considered to leave at the sink conditions (T_0) since this heat is not reused but lost to the environment.

6: It is heat that is lost to the environment, and thus no additional work can be feasibly extracted from these streams

7.2 Performance metrics

A performance metric is a quantitative measure used to evaluate the effectiveness or efficiency of a system. It provides objective information that can be used to monitor progress, identify areas for improvement, and inform decision making. A metrics division in three categories is proposed: separation, energetic, and exergetic metrics. A detailed description of each of them within each category is presented below.

7.2.1 Separation metrics

Recovery Ratio. The Recovery Ratio (RR) represents the flow ratio of unit of distillate produced per unit of feed and is very useful in seawater brine concentration applications [69]. It is related to electricity consumption, since the lower the Recovery Ratio (RR) the higher the feed pumping needs are for the same distillate production [89]. It is determined as follows:

[69]: Jones et al. (2019), “The State of Desalination and Brine Production”

[89]: Palenzuela et al. (2015), *Concentrating Solar Power and Desalination Plants*

$$RR = \frac{\dot{m}_d}{\dot{m}_f} \times 100 [\%], \quad (7.1)$$

where \dot{m}_d is the mass flow rate of distillate and \dot{m}_f is the feedwater mass flow rate, both in kg/s.

Concentration Factor. An equivalent metric is the concentration factor, which accounts for how many times the brine is concentrated with respect to the feed concentration:

$$CF = \frac{w_b}{w_f} = \frac{\dot{m}_f}{\dot{m}_f - \dot{m}_d} [-], \quad (7.2)$$

where w_b is the brine concentration and w_f is the feedwater concentration, both in g/kg.

Reconcentration Index. Apart from the already known previous metrics, a new one is proposed in this work that can be useful for seawater brine concentration applications. This metric is called Reconcentration Index (RI), and it allows to determine how close the separation achieved (RR) is to the theoretical maximum recovery ratio (RR_{max}). It is defined as:

$$RI = RR/RR_{max} [-], \quad (7.3)$$

[115]: Thiel et al. (2015), "Energy Consumption in Desalinating Produced Water from Shale Oil and Gas Extraction"

7: sodium chloride is the only solute considered, as it sets the concentration limit being the solute in seawater with the highest concentration and the greatest solubility [115]

8: Limited to steam or 1000 BTU as arbitrary conversion factor

[127]: Lienhard V et al. (2012), "SOLAR DESALINATION"

$$RR_{max} = w_{w,f} \left(1 - \frac{b_{NaCl,f}}{b_{NaCl,sat}} \right) \times 100 [\%], \quad (7.4)$$

where $w_{w,f}$ is the water mass fraction in the feed (which is $1 - w_{sol,f}$, where $w_{sol,f}$ is the mass fraction of the solutes in the feed) and $b_{NaCl,f}$ is the molality of sodium chloride in the feed, in mol_{NaCl}/kg_w (both can be obtained from a feedwater chemical analysis). On the other hand, $b_{NaCl,sat}$ is the molality of sodium chloride at saturation conditions⁷ (see Section A.3 (Separation metrics calculation) for more details of its estimation).

7.2.2 Energetic metrics

The energetic metrics are metrics that consider only the first law of thermodynamics (*i.e.* quantity). They are: Gain Output Ratio (GOR), Specific Thermal Energy Consumption (STEC), and Specific Electrical Energy Consumption (SEEC) and are described in the following.

Gain Output Ratio. Regarding the Gain Output Ratio (GOR), a universal definition of this metric that avoids the limitations of some of the commonly used definitions mentioned⁸ is the ratio between the energy in the form of latent heat required to vaporize all the distillate produced and the external thermal energy contributed to the system (Equation 7.5) [127].

$$GOR = \frac{\dot{m}_d \cdot \Delta h_{avg}}{\dot{Q}_{in}} \quad (7.5)$$

where Δh_{avg} is the latent heat of vaporization at the average vapor temperature between the first effect and the last effect, in kJ/kg, and \dot{Q}_{in} is the external

thermal energy consumption required to drive the process, in kW. In case process heat is used, it is determined by \dot{m}_s (mass flow rate of the external energy source supplied in the first effect, in kg/s) and Δh_s , which can be calculated as $h_{s,in} - h_{s,out}$ (in case of sensible heat) or as $h_{s,sat,vap} - h_{s,sat,liq}$ (in case of latent heat of phase change at saturation conditions from vapor to liquid at temperature $T_{s,in}$).

In case waste heat is used as external thermal energy source for the MED system, \dot{Q}_{in} is determined with \dot{m}_s and Δh but referred to the lowest temperature of the system ($T_{c,in}$).

Specific Thermal Energy Consumption. Another performance index widely used in thermal desalination is the Specific Thermal Energy Consumption (STEC). For desalination applications, it is defined as the input heat to the system per unit of product (distillate). If process heat is used, this index has units of energy per fraction of volume and its expression is shown in Equation 7.6.

$$STEC = \frac{\dot{m}_s \cdot (h_{s,in} - h_{s,out})}{\dot{m}_d} \cdot \rho_d \cdot \frac{1 \text{ kWh}}{3600 \text{ kJ}} \left[\frac{\text{kWh}_{th}}{\text{m}^3} \right]. \quad (7.6)$$

For brine concentration applications, it is named as $STEC_{bc}$ and it is determined as the energy required (in kJ) per unit of feed (in kg) (i.e. \dot{m}_f in the denominator) [128].

Both STEC and GOR are equivalent and are related via Equation 7.7.

[128]: Chen et al. (2021), "A Zero Liquid Discharge System Integrating Multi-Effect Distillation and Evaporative Crystallization for Desalination Brine Treatment"

$$STEC = \frac{2326 \text{ kJ/kg}}{GOR} \cdot \rho_d \cdot \frac{1 \text{ kWh}}{3600 \text{ kJ}}, \quad (7.7)$$

where ρ_d is the density of the distillate in kg/m^3 .

For the cases in which waste heat source is used as energy source, a variation of the STEC is proposed: the waste heat STEC ($STEC_{wh}$). For desalination applications, it is determined as follows:

$$STEC_{wh} = \frac{\dot{m}_s \cdot (h_{s,in} - h_{c,in})}{\dot{m}_d} \cdot \rho_d \cdot \frac{1 \text{ kWh}}{3600 \text{ kJ}} \left[\frac{\text{kWh}_{th}}{\text{m}^3} \right]. \quad (7.8)$$

As before, for brine concentration applications, \dot{m}_d would be replaced by \dot{m}_f in the denominator.

Specific Electrical Energy Consumption. Another important index in desalination is the Specific Electrical Energy Consumption (SEEC), which represents the total electrical consumption of the plant per unit of distillate water produced. These are the subsystems that should be considered:

- ▶ J_s . External heat source pumping (if any)
- ▶ J_f . Feed pumping
- ▶ J_c . Cooling
- ▶ J_d, J_b . Discharge extractions
- ▶ J_{vacuum} . Vacuum system
- ▶ J_{aux} . Auxiliary consumptions. Represents any additional power that the system may require to function (e.g., electrical consumption for feedwater pretreatment such as nanofiltration)

For desalination applications, the following equation is used for the calculation of this metric:

$$SEEC = \frac{\sum_{i=1}^N (U_i)}{\dot{m}_d} \left[\frac{\text{kWh}_e}{\text{m}^3} \right], \quad (7.9)$$

where J_i is the electrical consumption of the i_{th} subsystem. In the case of brine concentration applications, the index is called $SEEC_{bc}$ and the denominator would be replaced by \dot{m}_f .

7.2.3 Exergetic metrics

Exergy is the maximum amount of work achievable when a system is brought into equilibrium from its initial state to a reference state (known as the dead state and represented by the subscript "0") [111, 129]. This reference state is usually established for desalination applications as the seawater intake temperature ($T_{c,in}$). In contrast to the energetic metrics, it considers not only the first law of thermodynamics (quantity), but also the second law (quality).

Second law efficiency. The most widespread exergetic metric is the second law efficiency (η_{II}) [87], which accounts for irreversible losses within a system. It is calculated as the ratio of the useful exergy output of a system ($\dot{E}x_{out,useful}$) to the exergy input given to the system ($\dot{E}x_{in}$) (a further explanation of how to determine the different exergy flows can be found in Section A.2 (Exergy calculations)):

$$\eta_{II} = \frac{\dot{E}x_{out,useful}}{\dot{E}x_{in}} \times 100 [\%]. \quad (7.10)$$

Considering exergy losses, which are the sum of the exergy destroyed in each individual component ($\dot{E}x_{destroyed}$) and exergy losses due to discharge streams in disequilibrium to the environment ($\dot{E}x_{streams}$), the previous equation can be written as follows:

$$\eta_{II} = 1 - \frac{\dot{E}x_{destroyed} + \dot{E}x_{streams}}{\dot{E}x_{in}} \times 100 [\%]. \quad (7.11)$$

Specific Exergy Consumption. Another useful metric is the Specific Exergy Consumption (SEXC), which was firstly referenced as specific consumed available energy in [107]. Similarly to Specific Electrical Energy Consumption (SEEC) and STEC, it accounts for the exergy input to the system per unit of distillate produced (Equation 7.12) and it is determined as follows [84]:

$$SEXC = \frac{\dot{E}x_{in}}{\dot{m}_d} \left[\frac{\text{kWh}_{ex}}{\text{m}^3} \right]. \quad (7.12)$$

It is important to note that the terms $\dot{E}x_{out,useful}$ and $\dot{E}x_{in}$ from the previous exergetic metrics are determined depending on what is considered as useful exergy leaving the process and what is deemed as exergy input to the system⁹:

- ▶ **Useful exergy output.** The useful exergy output of the system ($\dot{E}x_{out,useful}$) depends on what is considered the valuable product generated by the process. In a separator in which the objective is to separate water and brine, the useful exergy is the chemical exergy of separation. As discussed in [87], for seawater desalination applications, where the valuable product

[107]: Darwish et al. (2006), "Multi-Effect Boiling Systems from an Energy Viewpoint"

[84]: Bouma et al. (2020), "Metrics Matter"

9: It mirrors the qualitative analysis presented in Section 7.1

[87]: Lienhard et al. (2017), "Thermodynamics, Exergy, and Energy Efficiency in Desalination Systems"

is fresh / pure water, the chemical exergy of separation corresponds to that of a reference ideal separator that achieves the *minimum separation work* ($\dot{W}_{\text{least}}^{\min} = \dot{W}_{\text{least}}|_{RR \rightarrow 0}$). The objective is to minimize the required energy consumption to produce fresh / pure water, regardless of how much separation takes place ($RR \rightarrow 0$), so $\dot{Ex}_{\text{out,useful}} = \dot{W}_{\text{least}}^{\min}$.

On the other hand, in brine concentration applications, since the objective is to maximize the separation achieved, the separator takes into account the amount of separation achieved ($\dot{W}_{\text{least}}|_{RR}$), and $\dot{Ex}_{\text{out,useful}} = \dot{W}_{\text{least}}$ ^[115].

The definition and determination of the least and minimum least work of separation can be found in Section A.2.

[115]: Thiel et al. (2015), "Energy Consumption in Desalinating Produced Water from Shale Oil and Gas Extraction"

- **Exergy input.** The exergy input (\dot{Ex}_{in}) is determined according to the type of external heat source. In case process heat is used, the exergy input is determined as:

$$\dot{Ex}_{in} = \dot{Ex}_{s,in} - \dot{Ex}_{s,out} + \sum_i \dot{E}_i, \quad (7.13)$$

where $\dot{Ex}_{s,in}$ and $\dot{Ex}_{s,out}$ are the exergy flows associated with the thermal energy source at the inlet and outlet, respectively.

When using waste heat sources, the exergy input is determined as:

$$\dot{Ex}_{in} = \dot{Ex}_{s,in} - \dot{Ex}_{s,out}^{wh} + \sum_i \dot{E}_i, \quad (7.14)$$

where $\dot{Ex}_{s,out}^{wh}$ is the outlet heat source exergy flow, which is evaluated at temperature T_0 (dead state).

Thus, for brine concentration applications or in case waste heat is used, the metric should include the subscript *bc* or *wh*, respectively, to distinguish between the application and external energy source types.

7.3 Instrumentation

7.3.1 Key Process Variables (KPVs)

The KPVs are those variables that uniquely define an operating point, which is obtained by averaging all monitored variables when stable operation is achieved. In other words, any change in the key variables is associated with a different operating point, since the plant outputs are affected accordingly. The following selected variables apply to any MED plant with any configuration in terms of seawater flow direction, tube arrangement in tube bundles, or effect layout [89]. They are represented in Figure 7.3 and described hereinafter:

[89]: Palenzuela et al. (2015), *Concentrating Solar Power and Desalination Plants*

- **Heat source flow rate** (\dot{m}_s - FT01), inlet temperature and pressure ($T_{s,in}$ and $P_{s,in}$ - TT01 and PT03) for sensible heat sources, and just **FT01** and **TT01** if saturated steam is used (otherwise steam quality needs to be estimated). They determine the hot side conditions, which usually take place in the first effect that is at the highest temperature and pressure. If multiple effects receive external heat sources, each one has to be monitored.
- **Feed water flow rate** (\dot{m}_f - FT02), which affect the overall plant operation conditions. A precise and stable input feed flow rate ensures consistent heat transfer rates, residence times, and separation efficiencies.

- ▶ **Distillate flow rate (\dot{m}_d - FT03).** It is a basic variable that gives information about the production of the system. As long as this output variable is stable, it can be assumed that the sum of it plus the brine flow rate is equal to the feed flow rate.
- ▶ **Condenser pressure / temperature ($P_{v,c}$ - PT02 / $T_{v,c}$)** or condenser outlet temperature ($T_{c,out}$ - TT02). The stability of any of these variables, together with that of the distillate production, establish a stable heat sink.
- ▶ **Effect pressure / temperature ($P_{v,1}$ - PT01 / $T_{v,1}$)** or heat source outlet temperature ($T_{s,out}$ - TT05), which is always required in case that sensible heat source is considered as the external energy source. The stability of this output variable determines a stable hot side. In case other effects, apart from the first one, receive external heat sources, each one has to be monitored.
- ▶ **Feed water salinity (w_f - CT01).** It affects the overall plant operation conditions since any stream with different salinity would have different thermodynamic properties (i.e. boiling point elevation) and therefore, different energy requirements are needed to perform the separation.
- ▶ **Condensate salinity (w_d - CT02).** This variable together with the distillate flow rate gives information on the achieved levels of salt separation.
- ▶ **Ambient temperature (T_{amb} - TT06).** The ambient conditions determine the losses to the environment which can change the results for the –otherwise— same operating conditions.
- ▶ **Seawater temperature** or condenser inlet temperature ($T_{c,in}$ - TT04). It is another environment variable that sets the minimum achievable temperature in the system.
- ▶ **Last effect (L_b - LT01)** and condenser (L_d - LT02) levels. In the case of the final condenser, it is a vessel in which the vapor coming from the final effect condenses, producing distillate that is continuously extracted from the system. The stability in this vessel is achieved when the extraction rate is equal to the condensate production rate. A higher extraction rate would eventually lead to unstable production, while a lower extraction rate would cause an increase in the vapor pressure, which would lead to induced lower production caused by misoperation. A stable level throughout the operation can ensure that the extraction and production rates (\dot{m}_d) are in balance. In the case of the last effect, it is important to keep the level as low as possible in order to avoid brine contamination in the distillate. variables are not relevant to the operating point, but are relevant to the plant operation.

7.3.2 Instrumentation requirements

The installed instrumentation must measure magnitudes such as flow rate (mass or volumetric), temperature, pressure, water conductivity, level, and power. First, it is important to account for the influence of the quality of each measured variable on the reliability of the performance metrics, which is determined by a sensitivity analysis.

Reminder: How to interpret Sensitivity Analysis (SA) results

The results include different sensitivity indices, namely first-order, second-order, and total-order indices. The first-order index measures the direct effect of an input variable on the output, excluding interactions with other variables. The second-order index quantifies the interaction effects between pairs of variables. Finally, the total-order index represents the overall contribution of an input variable, including both its direct and interaction effects.^a

^a More details are shown in Section 3.1 (Modelling and simulation)

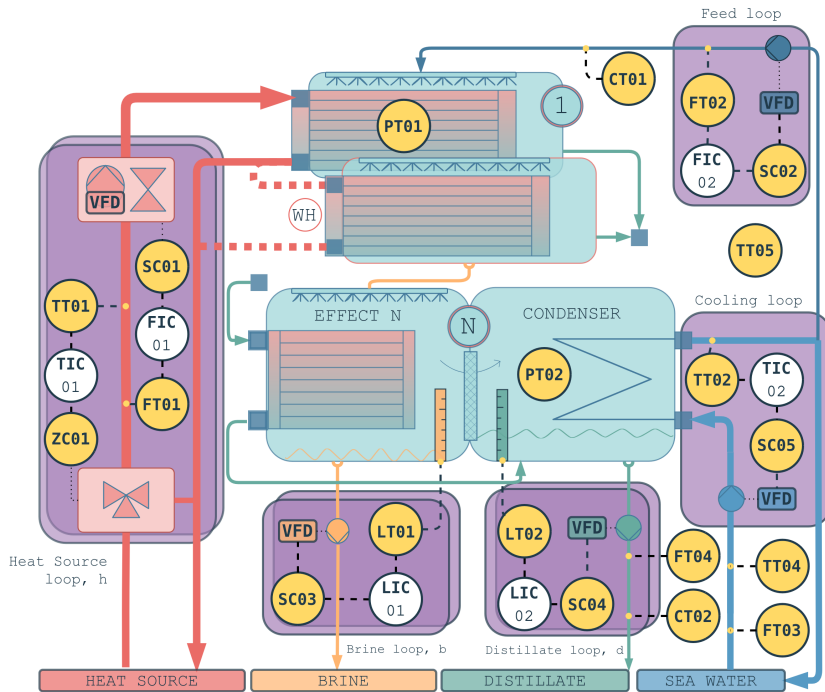


Figure 7.4 shows the results obtained from the sensitivity analysis in terms of total-order Sensitivity Index (SI). The closer the SI is to 1, the greater the influence of the variable (shown on the left axis) on the reliability of the performance metric (shown on the top). In other words, the quality of the variable measurement should be higher for variables with a higher SI. The cases where no sensitivity index is obtained indicate that the variable has no effect on the metric.

In general, monitoring of these variables must be performed online for each operating point evaluated. However, some of the variables rarely change and can be measured periodically or offline. This is the case of environment variables such as w_f , w_d , T_{amb} .

Another aspect that deserves careful consideration is the measurement of the temperature of the heat source. To determine the thermal efficiency of the system when a sensible heat source is utilized, it is crucial to accurately measure the temperature difference between the inlet and outlet of this energy source (ΔT_s). Using temperature transmitters with high accuracy rates (*i.e.* Platinum temperature transducer, 100 ohms at 0 °C (PT100)), uncertainties of about 0.5 °C or below 1 % for the absolute temperature can be expected at temperatures exceeding 60 °C. However, when considering the small temperature differences between the inlet and outlet, which can be as low as 2 °C, the resulting relative uncertainty could be up to 25 %. To address this problem, it is recommended that both temperature transmitters are identical and calibrated simultaneously, using the same calibration pattern, which translates into observed values for the uncertainty of the temperature difference in the range of 0.1 °C or 5 %.

On the other hand, the total electrical energy consumption (represented as JT01 in Figure 7.3) can be monitored as global system consumption, or independently per subsystem (J_s , J_c , J_f , J_d , J_b , J_{vacuum} , J_{aux}).

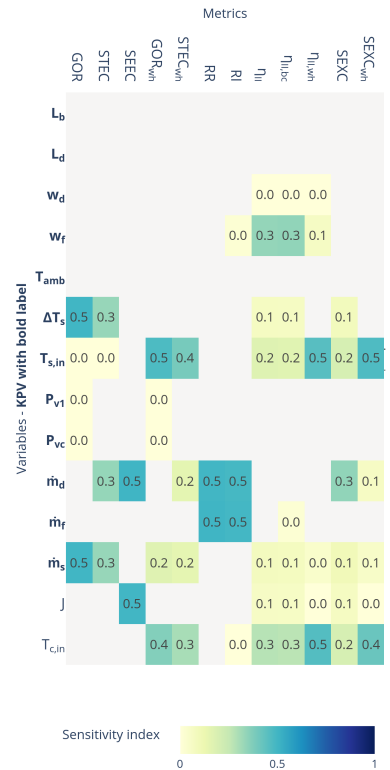


Figure 7.4: Sensitivity index results for different variables. Useful to assess the impact of the different measured variables uncertainty on the performance metrics. KPIs are shown in bold notation

All KPIs must be monitored regardless of their influence on the performance metric being evaluated because, as mentioned above, the average values of these variables at steady state conditions define an operating point.

7.3.3 Uncertainty determination

[130]: BIPM (2008), JCGM 100:2008. GUM 1995 with Minor Corrections. Evaluation of Measurement Data — Guide to the Expression of Uncertainty in Measurement

Uncertainty determination is particularly valuable in assessing the reliability and validity of predictions, forecasts, or results evaluation. The framework on which the uncertainty assessment of this proposed methodology is based is the **JCGM 100:2008** [130].

In an uncertainty analysis, the uncertainties of direct measurements must be firstly determined. The uncertainty of each direct measure (ΔX_i) consists of the sum of two components, as indicated below:

$$\Delta X_i = \Delta X_{\text{sensor}} + \Delta X_{\text{control}}$$

where:

- ▶ ΔX_{sensor} is the contribution of the sensor, which depends on its accuracy, calibration and conversion errors, and should be available from the instrument datasheet.
- ▶ $\Delta X_{\text{control}}$ is the uncertainty attributed to the quality of the control and is estimated using the standard deviation of the measurement throughout the period considered as stable.

[131]: Smith (2013), *Uncertainty Quantification*

On the other hand, when working with derived variables, *i.e.* quantities that are calculated based on other measured or known quantities, the uncertainty is determined through uncertainty propagation. There are several analytical and numerical methods to propagate uncertainty [131]. One simple approach is the use of first-order Taylor series approximation, obtained calculating the partial derivative of the different direct measurements ($X_i = 1..N$) that take part in the calculation of an output (Y):

$$Y = f(X_1, \dots, X_N),$$

$$\Delta Y = \left(\sum_{i=1}^N \left(\left| \frac{\partial Y}{\partial X_i} \right| \Delta X_i \right) \right)^{1/2},$$

[132]: NIST (), “NIST Guidelines for Evaluating and Expressing the Uncertainty of NIST Measurement Results Cover”

where ΔY can be expressed in terms of absolute uncertainty, relative, or standard uncertainty [132]. This alternative provides a simple mathematical expression to directly estimate uncertainty. Expressions for the uncertainty estimation of energetic and separation metrics of MED processes with this approach are available in Section A.1. However, first-order Taylor series approximation has certain limitations, being the main one that it is not adequate for highly non-linear models, where a higher order Taylor expansion is required, or when uncertainties are far from the mean. Also, when working with complex models, as in the case of exergetic metrics, its expression can not be practically obtainable. For these cases, the recommended approach are numerical methods, specifically the Monte Carlo method [133], which despite its higher computational requirements does not have the aforementioned limitations [134].

[133]: BIPM (2008), JCGM101:2008. Evaluation of Measurement Data — Supplement 1 to the “Guide to the Expression of Uncertainty in Measurement” — Propagation of Distributions Using a Monte Carlo Method

[134]: Wolff (2007), “Monte Carlo Errors with Less Errors”

7.4 Monitoring and process control

7.4.1 Monitoring: steady-state identification

The evaluation of the system performance must be carried out when the plant is at steady state conditions, that is, when the mass and energy balances are in equilibrium and thus do not change with time; otherwise, erroneous results can be obtained. Steady-state conditions can be identified by observation

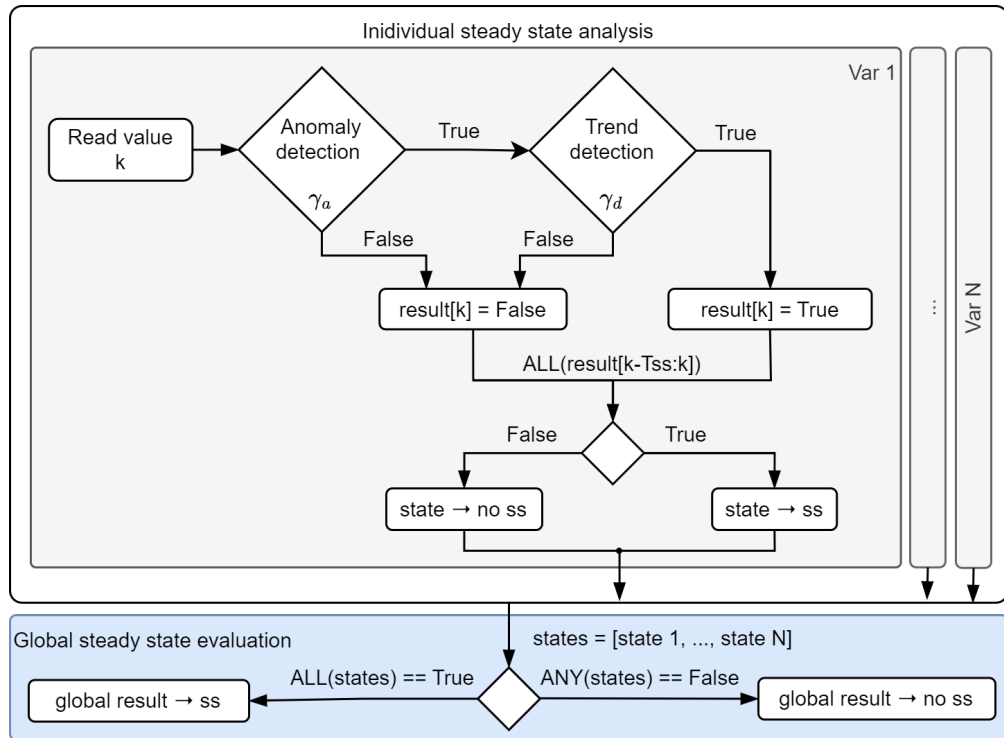


Figure 7.5: Diagram of the steady-state identification procedure

by qualified and experienced plant operators. However, the use of automatic detection algorithms is recommended for experimental facilities where a wide range of operating conditions are involved. In this work, an automatic detection algorithm has been purposely developed and implemented to identify the steady state of the process.

The methodology is based on the idea presented by M. Korbel *et al.* [135] and consists of combining an algorithm to detect anomalies, such as the wavelet transform [136, 137] (which allows detecting abrupt signal changes and distinguishing between high-frequency noise, transient states and steady states), with a trend detection method to identify smooth ramps as non-steady states. Whereas M. Korbel [135] *et al* propose a statistical trend detection approach, in this paper the derivative of the signal is used due to its simplicity since in this case, a threshold is the only parameter that has to be established. A diagram of the steady-state detection procedure is shown in Figure 7.5, where three parameters are mainly required: wavelet transform threshold (γ_a), derivative threshold (γ_d) and time window duration (T_{ss}).

[135]: Korbel et al. (2014), "Steady State Identification for On-Line Data Reconciliation Based on Wavelet Transform and Filtering"

[136]: Jiang et al. (2003), "Application of Steady-State Detection Method Based on Wavelet Transform"

[137]: Jiang et al. (2000), "Industrial Application of Wavelet Transform to the On-Line Prediction of Side Draw Qualities of Crude Unit"

[135]: Korbel et al. (2014), "Steady State Identification for On-Line Data Reconciliation Based on Wavelet Transform and Filtering"

At each sampling time k , a new value is read, and the *Anomaly Detection* algorithm (in this case, the wavelet transform) is applied. If the output is positive (true, meaning no anomaly is detected), the next step is *Trend Detection*. The variable is considered to be under steady-state (ss) conditions only if all elements in the results vector are positive over the period T_{ss} . Finally, the *Global Steady-State Evaluation* identifies a steady-state period when all N variables involved have been classified as steady-state.

7.4.2 Control system

Figure 7.3 shows the control loops to be implemented in an MED unit, whose subsystems and their control are described below:

- ▶ **Heat source** (*Heat Source loop* in Figure 7.3). Both the inlet temperature (TT01) / pressure (PT03) and the flow rate of the heat source (FT01) must be controlled. It can be done either by direct control over the source heat generating heat under the required operating conditions (flow and temperature/pressure), or by performing a transformation. Depending on the heat source characteristics, this transformation involves:
For sensible heat sources, independent variation of temperature and flow rate can be achieved by means of: 1) a mixing three-way valve that mixes part of the return fluid, at temperature TT05, with the inlet fluid, at TT01 by acting over the control signal for temperature regulation ZC01 and; 2) flow (FT01) regulation by acting over the control signal SC01, which can be a Variable Frequency Drive (VFD) or valve. This decoupled regulation is shown in Figure 7.3. The flow rate regulation (FT01) is achieved by acting on the selected actuator (SC01), which can be a VFD or a valve¹⁰.
For latent heat sources (steam), the pressure-flow-independent regulation is not possible since they are intrinsically coupled variables. In this case, a pressure regulator valve (ZC01) can be used to control either the flow rate (FT01) or the pressure (PT03).
- ▶ **Cooling** (*Cooling Loop* in Figure 7.3). The pressure inside the condenser (PT02) or the condenser outlet temperature (TT02) can be controlled by regulating the cooling flow rate (FT03), being the cooling water inlet temperature (TT04) a disturbance. This control loop (TIC02) consists in turn in two control loops (cascade control [138]), where an outer loop sets a reference flow rate value to achieve the desired condenser outlet temperature (or pressure), and an inner loop (not shown in Figure 7.3) acts on SC05 (VFD's frequency) to achieve the desired flow rate. Direct regulation of condenser outlet temperature using the VFD is also valid in case the measurement of the cooling flow rate is not available.
- ▶ **Brine extraction** (*Brine loop* in Figure 7.3). The brine level in the last effect (LT01), or in all effects if a parallel feed configuration is used, is controlled by the brine flow rate –see control loop LIC01 in Figure 7.3. In this case, the controller can act directly on the VFD frequency (SC03) to avoid the need for an additional flow meter.
- ▶ **Distillate extraction** (*Distillate loop* in Figure 7.3). As in the previous case, the distillate level (LT02) is controlled by acting on the control variable (SC04).
- ▶ **Feedwater** (*Feed loop* in Figure 7.3). The feed water flow rate is regulated by the FIC02 control loop, using a VFD (SC02) and a flow meter (FT02).

Startup and shutdown procedures

On MED systems with discontinuous operation, such as experimental plants, or plants driven by intermittent energy sources (e.g. solar energy), the startup and shutdown procedures are critical for ensuring safe and efficient operation. It is a repetitive and sufficiently complex process that requires an experienced operator. Manual management of the a process leads to errors that cause setbacks or, in the worst cases, premature failures in the facility: contamination of the condenser with brine due to erratic draining of the last effect, accumulation of scale on the surfaces of heat exchangers due to rapid cooling after shutdown, pumps cavitating because they are not stopped when the water flow at the intake ceases, etc. Thus this procedure should be automated.

10: It should be noted that this decoupling comes at the cost of an inefficient energy mixing process.

[138]: Åström et al. (1995), *PID Controllers: Theory, Design, and Tuning*

This can be achieved through the implementation of two finite state machines that manage the startup and shutdown of the facility, respectively. These have been designed to perform a sequence of operations that take the plant from an initial state to a final state following proper operating practices. A diagram of the process is shown in Figure 7.6.

The machines are responsible for managing the activation and deactivation of devices as well as controllers. Additionally, they set reference values for these based on a previously established configuration and evaluate whether the reference has been reached before proceeding to the next step. They also adjust certain parameters of the control system (level control) and restore the initial values once the task is completed.

The startup procedure follows an activation sequence of the different subsystems: extractions → cooling → feedwater and heat source. Then the system is left to stabilize and the startup sequence is complete.

Regarding the shutdown procedure, the two most delicate processes are the progressive cooldown of the first effect¹¹ and the complete draining of the last effect and condenser. For the gradual temperature decrease of the first effect, after the plant shutdown signal, the hot water temperature is reduced in 5-minute steps starting from the last recorded value until a final temperature of 50°C is reached (and then left to cooldown to ambient temperature). To drain the levels, a reference value well below the normal operating level is set, and the controller parameters are changed to more aggressive ones. Additionally, the device is deactivated each time the reference is reached and is not reactivated until the level reaches a specified value. This activation and deactivation process continues while the feedwater finishes draining from the upper effects of the plant. Once the control system has been deactivated for longer than a preset time, the plant shutdown procedure is considered complete, and the level controller parameters are restored.

¹¹: which has the highest scaling potential if not handled properly

A standard method for performance evaluation of thermal separation processes

1. Define the Key Process Variables (Section 7.3.1)
2. Select the required performance metrics to be evaluated according to the application and type of energy source(s) (Section 7.1).
3. Define the required instrumentation of the KPVs and of any additional variables needed for the target performance metrics (Section 7.3.2).
4. Define the uncertainty associated with the measurement and that associated with the performance metric determination (Section 7.3.3)
5. Implement the required actuators and integrate them into a control system to ensure the stability of the plant operation (Section 7.4.2).
6. Identify a time window where stable operation is achieved (Section 7.4.1).

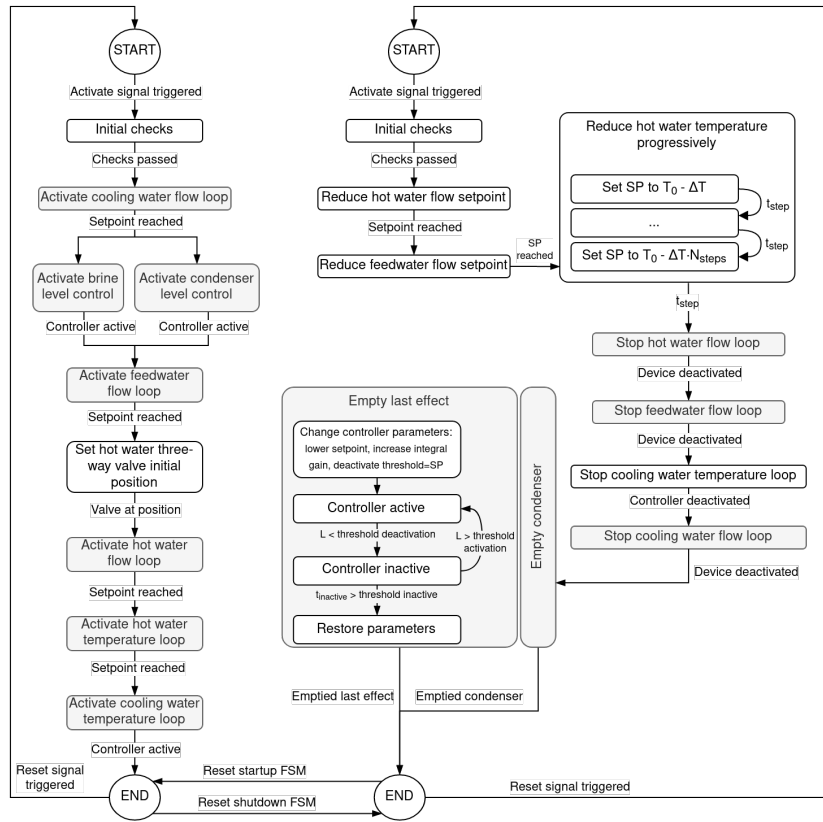


Figure 7.6: Flowchart of finite state machines for plant start-up (left) and shutdown (right)

7.5 Case study: methodology validation and results analysis in a high TBT experimental campaign at the MED-PSA plant

To showcase the application and usefulness of the proposed methodology, a case study consisting on the application of the methodology to an experimental campaign at the Solar-driven Multi-Effect Distillation (SolarMED) pilot plant is presented. The campaign was designed to evaluate the performance of the MED process under different operating conditions (see Table 7.2 and Figure 7.7), with the aim of improving its thermal performance and assessing the feasibility of using higher Top Brine Temperatures.

The following sections describe the implementation of the methodology, which is showcased in Figure 7.8 for one particular test and further discussed in the following.

Monitoring and control system implementation results

Finite state machines. In Figure 7.8 the activation sequence can be visualized at the beginning of the test (09:49–10:00): extractions → cooling → feedwater and heat source. The Flows are activated in about two minutes followed by another minute for the inlet temperature. Then the system is left to stabilize. At 09:52 the delay between activating the feedwater and it reaching the last effect is completed and the brine extraction pump starts operating. Pressures, temperatures and the distillate level in the system progressively evolve up to 10:00 when the conditions are changed for the first operation point for the day. The distillate level control action is delayed further until 10:04 when the first distillate is produced.

Table 7.2: Experimental campaign design specifications

Variable	Unit	Range
$T_{s,in}$	°C	60-89
q_s	l/s	7-14
$T_{c,out}$	°C	20-40
q_f	m ³ /h	5-9
w_f	g/kg	40

The shutdown procedure can be observed in Figure 7.8 starting from 13:07. After a decrease in flow rates, the first effect heat load is progressively decreased until 13:34. From this time, pumps are stopped and the extraction cycles begin as can be noted by the high oscillations in the *Electrical consumption – J_b* and J_d and *Levels*.

Steady state identification. The steady state identification algorithm has been implemented in the control system. It allows the automatic detection of stable operation points. This is done by monitoring the KPVs and applying the algorithm described in Section 7.4.1. In Figure 7.8, steady state periods are highlighted with a yellow background, which indicates that the algorithm has detected a stable operation point. Two are detected, the first one from 11:00 to 11:55 and the second one from 12:16 to 12:59.

Control. In terms of control, a Proportional-Integral-Derivative controller (PID) control has been implemented to effectively regulate and maintain the desired setpoints of the subsystems mentioned in Section 7.4.2. This approach enables the system to respond quickly to changes, minimize steady state errors, reject disturbances, and enhance overall performance and reliability. Figure 7.9 shows the development procedure for one of the main loops, the condenser outlet temperature control. To tune the controller, the system was excited with a Pseudo-Random Binary Sequence (PRBS) signal Figure 7.9 (a), obtaining an ARX model ($n_a = 20$, $n_b = 49$, $n_k = 5$, 96.38% fit) using the *System Identification Toolbox* from MATLAB. It allowed to extract an approximate first-order dynamic with which to tune the controller. Figure 7.9 (b) shows the controller performance for a particular test. Initially, the control signal (q_c) increases to compensate for the trend observed in the condenser inlet temperature. At 11:45, the setpoint is changed to 24 °C, to which the controller immediately adapts by decreasing its input, allowing the temperature to rise. The system progressively evolves toward the new setpoint, which is reached at 12:30. The controller then maintains the desired temperature, compensating for other disturbances (not shown in the figure). A similar behavior can be observed in the test shown in Figure 7.8 – *Temperatures and Flows*. For the first operating point (11:00 onwards), the continuously increasing inlet temperature ($T_{c,in}$) is compensated by the controller, which increases the cooling flow rate to maintain the condenser outlet temperature at the setpoint. For the second operating point (12:16), the simultaneous change of outlet temperature to a higher value, and the activation of the cooling tower –not shown in the figure— allows the inlet temperature to stabilize. This permits the controller to reduce the cooling flow rate and remain relatively unchanged from that point onwards.

Uncertainty propagation. The chosen uncertainty propagation method has been the Monte Carlo method, in which, given the time-series signals of the directly measured variables with their associated uncertainties, a normally distributed random signal is generated with a certain number of samples. The metric is then evaluated as many times as samples are available and thus a vector is obtained for the evaluated metric.

Reproducibility and the effect of the steady state duration

The operation points pairs 1–2 and 3–4 in Table 7.3 are the same test, *i.e.* the same operating conditions, but performed on different dates. Particularly for points 1–2, the duration of the steady state is significantly different (16 and 76 minutes, respectively). The obtained performance metrics are similar, with almost identical values for the energetic (GOR, STEC) and separation metrics (RR, RI). Minor differences, but still within the uncertainty margin are observed in metrics influenced by electrical consumption (η_{II} , SEXC, SEEC)—which varies between tests. The observed differences are mainly due to variations in the cooling water inlet temperature, which in turn affect the required cooling water

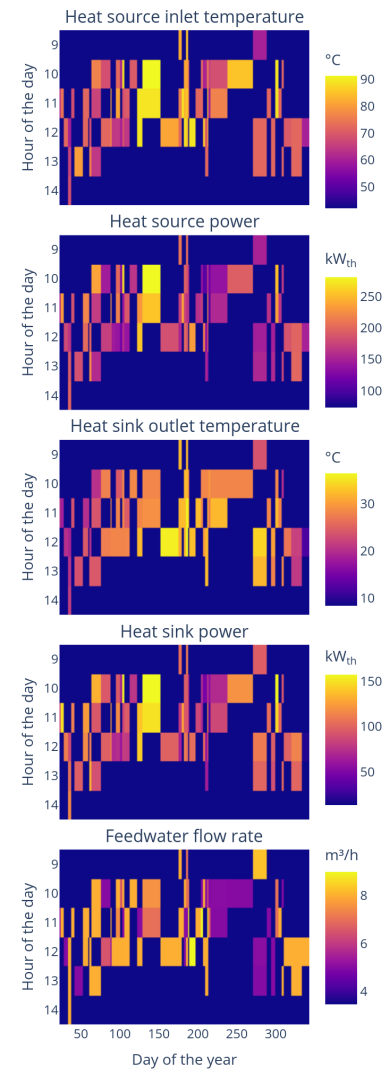


Figure 7.7: Visualization of the different process inputs values during the experimental campaign.



Parameters for both the control system and the steady-state identification algorithm can be found in the Appendix, Section A.4.

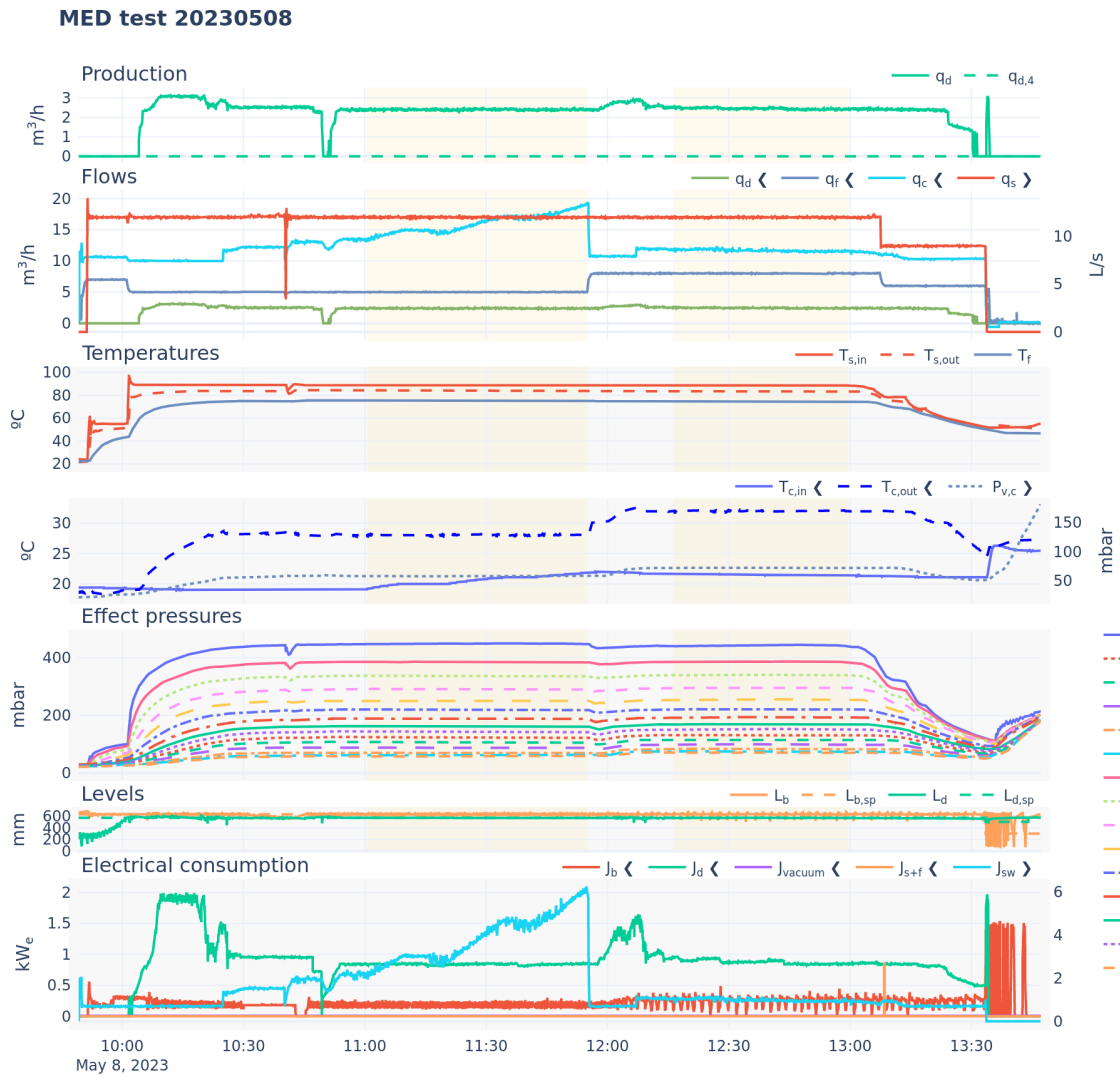


Figure 7.8: Test results. Several days available in interactive version



flow rate. For point 1, the inlet condenser temperature ($T_{c,in}$) is 24.5°C , requiring a cooling water flow rate of $17 \text{ m}^3/\text{h}$ ($J=8.0\pm0.2 \text{ kW}_e$), whereas for point 2, $T_{c,in}$ is 23°C , requiring $13 \text{ m}^3/\text{h}$ ($J=8.1\pm0.2 \text{ kW}_e$). These differences result in a 0.3% variation in the second-law efficiency and $0.1 \text{ kWh}_e/\text{m}^3$ in the SEEC. In contrast, for points 3 and 4, the inlet condenser temperatures are similar enough (22.6 and 21.4°C , respectively), making the differences in all performance metrics negligible ($J=8.1\pm0.2 \text{ kW}_e$ for both points).

Thus, it can be stated that the proposed methodology provides reproducible results and that the quality of stable operation and the ability to correctly identify it are of greater importance than the specific duration of the steady state.

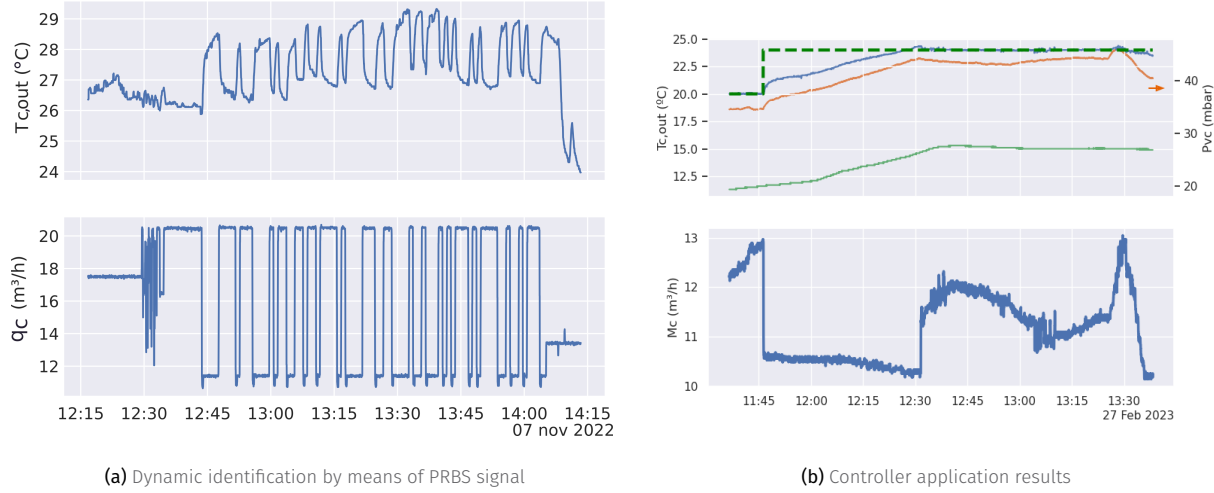


Figure 7.9: Condenser outlet temperature controller implementation. On (b) the perturbation (inlet temperature) is shown with a solid-green line, while the output (condenser outlet temperature) is shown with a solid-blue line. The reference is a thick dashed-green line.

Experimental evaluation at high Top Brine Temperatures

As mentioned in the introduction, in practice, the TBT in the MED system is typically limited to 70 °C or below to prevent scaling. This limitation can be assessed using the RSI, which requires knowledge of the water pH. To obtain this parameter, a laboratory analysis of the water composition was carried out for both the untreated seawater at the intake of the MED system and the pretreated water after the nanofiltration unit. The results of this analysis are presented in Figure 7.10 (center bar plot). Subsequently, the *PyEqulon* open-source library [35] was used to estimate the pH at various temperatures and concentration factors. For the latter, it was assumed that all ions scale uniformly, *i.e.*, that the concentration factor is identical for all species. Based on these values, the RSI was computed for different temperatures and concentrations.

For un-treated feedwater (Figure 7.10 - left) the risk of precipitation is present at almost any temperature due to its composition¹². A nanofiltration pretreatment¹³ is used to selectively remove the divalent ions while leaving relatively unaffected the monovalent ones, *i.e.* NaCl. After pretreatment, severe scaling –RSI values below 4— can only be observed above 80°C and ≈ 100 g/kg as shown in Figure 7.10 – right.

[35]: Marcellos et al. (2021), *PyEqulon*

12: Figure 7.10 – seawater in center bar plot

13: Figure 7.10 – pretreated water in center bar plot

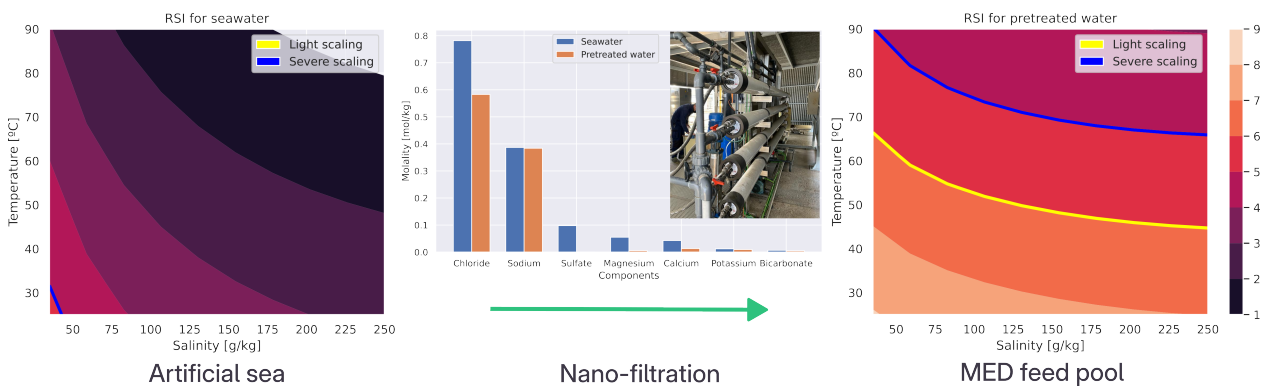


Figure 7.10: RSI values as a function of temperature and concentration before (left) and after (right) pretreatment using nanofiltration.

Using a physical model of the plant¹⁴, a better insight into the inner working of

14: A detailed description of the model can be found in the Appendix, Chapter B (MED First-Principles Model)

Table 7.3: Measured variables and performance metrics for some operation points of the experimental campaign. The values are expressed as mean \pm standard deviation with a coverage factor of 2 (95% confidence interval). D is the duration of the steady state period.

	Test date (UTC)	D (min)	Performance metrics						
			GOR (-)	STEC ($\text{KW}_{th}/\text{m}^3$)	SEEC (KW_e/m^3)	RR (-)	RI (-)	η_{II} (%)	SEXC ($\text{kWh}_{ex}/\text{m}^3$)
1	20230331 12:15	16	11 \pm 1	60 \pm 6	3.9 \pm 0.2	29 \pm 1	0.35 \pm 0.02	8.0 \pm 0.6	10.9 \pm 0.8
2	20230418 12:22	76	11 \pm 1	59 \pm 6	4.0 \pm 0.2	29 \pm 2	0.35 \pm 0.02	7.7 \pm 0.6	11.3 \pm 0.9
3	20230329 13:10	24	10.1 \pm 0.7	66 \pm 5	3.9 \pm 0.2	30 \pm 2	0.35 \pm 0.02	6.9 \pm 0.4	12.7 \pm 0.8
4	20230414 12:51	27	10.2 \pm 0.7	65 \pm 5	3.9 \pm 0.2	30 \pm 2	0.36 \pm 0.02	6.8 \pm 0.4	12.8 \pm 0.8
5	20230511 11:23	32	8.1 \pm 0.4	81 \pm 4	3.2 \pm 0.2	44 \pm 2	0.52 \pm 0.02	4.6 \pm 0.3	17.8 \pm 0.9
6	20230414 11:49	18	11 \pm 1	59 \pm 5	3.8 \pm 0.2	47 \pm 3	0.56 \pm 0.03	7.2 \pm 0.5	11.9 \pm 0.9
7	20230508 11:00	54	7.0 \pm 0.4	93 \pm 6	3.7 \pm 0.2	48 \pm 3	0.57 \pm 0.03	3.9 \pm 0.3	21 \pm 1

Measured variables											
	$T_{s,in}$ ($^{\circ}\text{C}$)	$T_{c,out}$ ($^{\circ}\text{C}$)	q_s ($\text{L}\cdot\text{s}^{-1}$)	q_f ($\text{m}^3\cdot\text{h}^{-1}$)	q_d ($\text{m}^3\cdot\text{h}^{-1}$)	$T_{s,out}$ ($^{\circ}\text{C}$)	$T_{c,in}$ ($^{\circ}\text{C}$)	w_f ($\text{mS}\cdot\text{cm}^{-1}$)	w_d ($\mu\text{S}\cdot\text{cm}^{-1}$)	q_c ($\text{m}^3\cdot\text{h}^{-1}$)	J (kW)
1	64.0 \pm 0.8	28.1 \pm 0.6	12.0 \pm 0.2	8.0 \pm 0.1	2.4 \pm 0.1	61.1 \pm 0.7	24.5 \pm 0.7	67.4 \pm 0.7	8.00 \pm 0.08	17 \pm 1	(8.0 \pm 0.2) $\times 10^3$
2	64.0 \pm 0.7	28.0 \pm 0.6	12.0 \pm 0.3	8.0 \pm 0.1	2.3 \pm 0.1	61.2 \pm 0.7	23 \pm 1	67.4 \pm 0.7	8.00 \pm 0.08	13 \pm 2	(8.1 \pm 0.2) $\times 10^3$
3	68.0 \pm 0.7	28.0 \pm 0.6	12.0 \pm 0.2	8.0 \pm 0.1	2.4 \pm 0.1	64.8 \pm 0.7	22.6 \pm 0.6	67.4 \pm 0.7	8.00 \pm 0.08	13.8 \pm 0.8	(8.1 \pm 0.2) $\times 10^3$
4	68.0 \pm 0.7	27.9 \pm 0.8	12.0 \pm 0.3	8.0 \pm 0.1	2.4 \pm 0.1	64.8 \pm 0.6	21.4 \pm 0.8	67.4 \pm 0.7	8.00 \pm 0.08	10.9 \pm 0.9	(8.1 \pm 0.2) $\times 10^3$
5	88.9 \pm 0.9	29 \pm 1	12.0 \pm 0.3	7.0 \pm 0.1	3.1 \pm 0.1	83.8 \pm 0.9	22 \pm 1	64.7 \pm 0.6	8.00 \pm 0.08	20.1 \pm 0.3	(7.9 \pm 0.3) $\times 10^3$
6	68.0 \pm 0.7	28.0 \pm 0.5	12.0 \pm 0.3	5.0 \pm 0.1	2.4 \pm 0.1	65.2 \pm 0.7	20.8 \pm 0.6	67.4 \pm 0.7	8.00 \pm 0.08	10.1 \pm 0.4	(7.9 \pm 0.3) $\times 10^3$
7	89.0 \pm 0.7	28.1 \pm 0.6	12.0 \pm 0.3	5.0 \pm 0.1	2.4 \pm 0.1	84.4 \pm 0.8	21 \pm 2	64.5 \pm 0.7	8.00 \pm 0.08	16 \pm 3	(7.8 \pm 0.3) $\times 10^3$

the plant can be obtained. The model is based on the energy and mass balances of the system, and it is used to estimate different outputs at the effect level, such as the temperature and pressure of the vapor, the distillate production, and the brine concentration.

Scaling assessment during high Top Brine Temperature operation

Using the aforementioned physical model of the plant, it is possible to analyze the temperature and concentration evolution and visualize them as shown in Figure 7.11 (a).

The figure shows the temperature and concentration evolution at each effect in the MED plant for several operation points: low-temperature operation points (4: 68–8, 6: 68–5) and high-temperature operation points (5: 89–8, 7: 89–5). According to the RSI, the high-temperature operation points (5, 7) enter the light scaling risk zone for the first seven effects —above the yellow line in Figure 7.11 (a)— while the low-temperature operation points (4, 6) remain within the stable water zone for all effects.

To assess whether scaling occurred during high-temperature operation, control tests were conducted both before the high-temperature tests and repeated after approximately 30 hours of high TBT operation. In Table 7.3, the same operation points used to validate reproducibility¹⁵, i.e., 1–2 and 3–4, can be used to draw conclusions. No significant differences can be observed for any of the performance indicators, with the values remaining consistent between tests. This suggests that the system operated efficiently, without significant fouling or scaling.

This is further confirmed by applying the physical model of the plant to estimate the heat transfer coefficients. Figure 7.11 (b) illustrates the comparison of heat transfer coefficients before and after the high-temperature campaign for both control tests. The results show only minor variations between the pre- and post-high-temperature operation. With measurements across all effects showing no systematic degradation trend. The consistency of the coefficients indicates that no measurable scaling occurred during the high TBT operation period.

15: Section 7.5 (Reproducibility and the effect of the steady state duration)

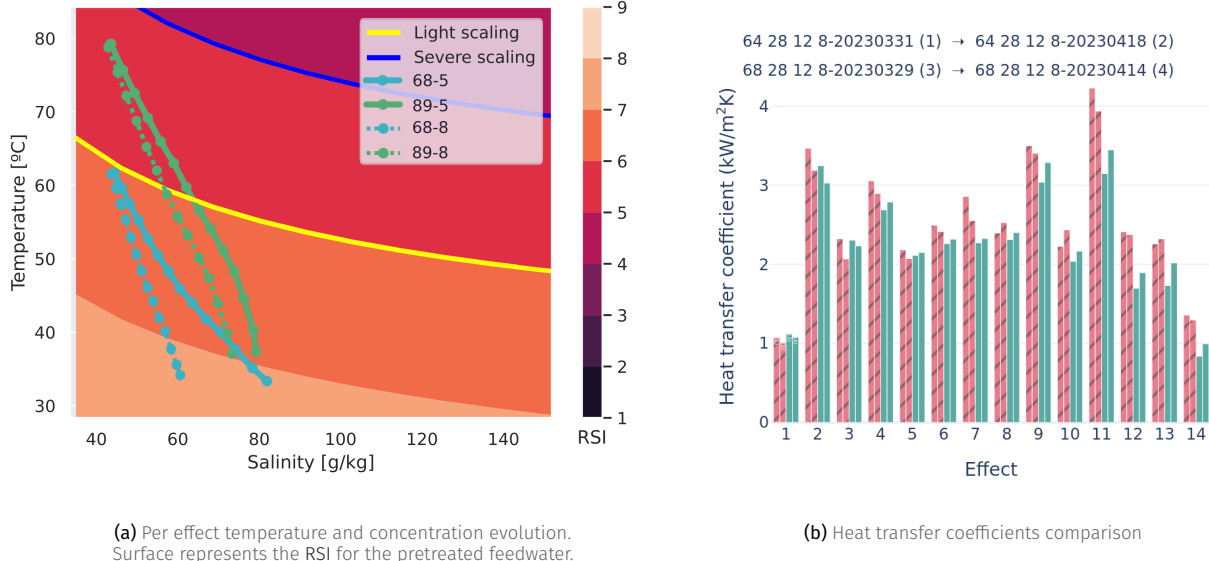


Figure 7.11: Scaling assessment during high TBT operation

Performance analysis at high Top Brine Temperature

In Table 7.3 operation points 4–5 and 6–7 compare low and high TBT operation. Two of them (4 and 6) receive heat at 68°C, while they differ in the feedwater flow rate (q_f), one (4) with a higher value (8 m³/h) and the other (6) at a lower one (5 m³/h). The other two operation points receive heat at 89°C and similar feedwater flow rate¹⁶. The first two operation points result in an approximate TBT of 61.5°C while the last two operation points have an approximate TBT of 79.2°C. This operation points selection is made to compare the performance of the plant at low and high TBT operation with otherwise equivalent conditions.

The first key observation is that, contrary to the statement in the introduction, the plant's performance does not improve with higher heat source temperatures; rather, it deteriorates significantly. The GOR decreases by approximately 20% and 36% for the low (4–5) and high (6–7) q_f scenarios, respectively. The results are even more pronounced in terms of second-law efficiency, with reductions of 32% and 46%, respectively. This decline occurs because higher-quality exergy is being destroyed in the process. More energy —of superior quality— is being consumed to produce distillate less efficiently.

16: Equal between 4 and 5, slightly different but comparable between 6 and 7

This behavior is expected and can be attributed to the fact that the increase in heat source temperature is not utilized to incorporate additional effects, which would be the driver enhancing system efficiency.

comprobar números

On the other hand, the concentration achieved does increase significantly for the high q_f scenario, with a 47% increase in the recovery ratio. This is not the case for the low q_f scenario, where the recovery ratio is similar to the low temperature operation point. A possible explanation is presented hereinafter.

A per effect comparison can also be made in terms of energy contribution for vapor generation. This is shown in Figure 7.12 in terms of energy contributions (a) and vapor generation mechanisms (b) for the low q_f (=5 m³/h) operation points. In Figure 7.12 (a) it can be seen how, in the first effect, the only contributor to vapor generation is the external heat source (red bar). For the following effects, most of the energy comes from the previous effect vapor (purple bar) with some

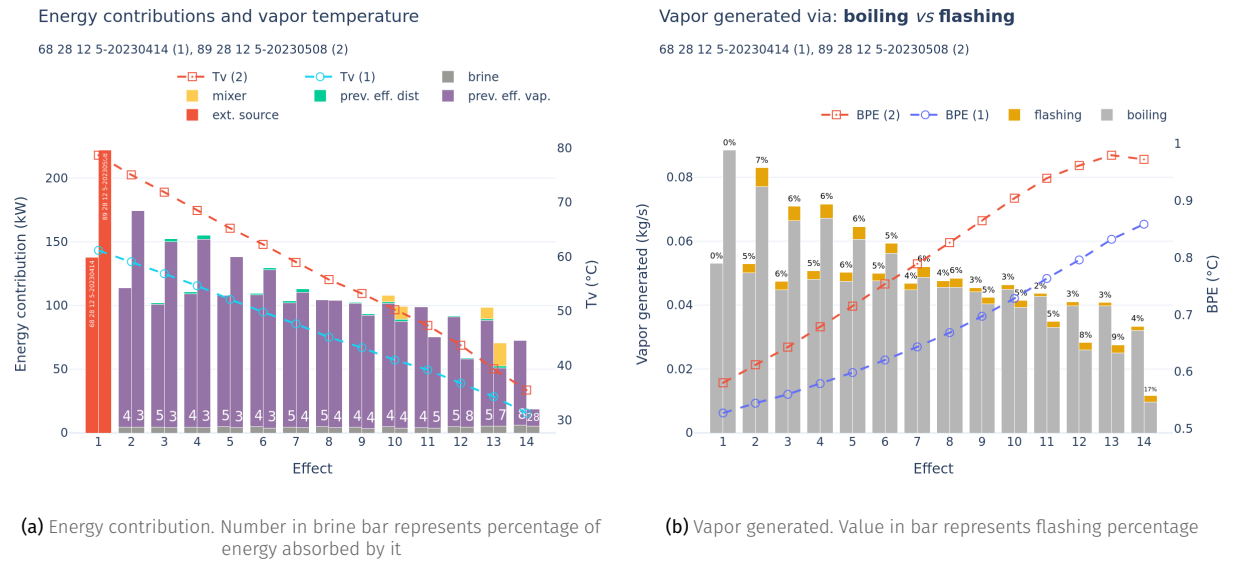


Figure 7.12: Per effect comparison between low and high TBT operation points

17: This is achieved by sacrificing the previous effects distillate (green bar) in some other effects

contribution at specific effects —10, 13— from distillate coming from previous effects (yellow bar, *mixer*)¹⁷. The only negative contributor (it absorbs heat instead of releasing it) is the brine (gray bar), which is warmed up. Also in the plot is shown the vapor temperature evolution.

Figure 7.12 (b) shows the vapor generation per effect deaggregated in terms of the different mechanisms: boiling (gray bars) and flashing (yellow bars). Additionally, the Boiling Point Elevation (BPE) of the brine is shown as dashed lines. In this plot, it can be seen how in general boiling is the main driver for vapor generation.

In the first effect a stark difference between low and high operation can be seen, with almost double the power released by the external source, producing almost double the vapor —Figure 7.12 (b). However this difference is not maintained in the following effects, but an opposite trend is observed. Effect 8 is the crossing point and from there on the low temperature operation point produces more vapor. Another interesting comparison is the *mixer* energy contribution, the higher temperature of the distillate produced in the first effects becomes a significant contributor in the later effects, with a greater impact compared to the low temperature operation. Thus, distillate distribution is more effective when total plant temperature differences are higher.

A possible explanation as to why vapor generation seems limited and thus the achieved concentration, can be that the BPE of the brine —Figure 7.12 (b)— is a function of temperature and concentration, increasing with the latter. This means that the temperature difference between the brine and the vapor is reduced, which in turn reduces the boiling driving force. In the visualized case, the final BPE value for the low-temperature operation is reached by effect 9 of the high temperature one. In an MED plant, the vapor generated in the previous effect is the driving force for the next effect —Figure 7.12 (a). Low vapor production on one effect means a diminished force for heat transfer in the next one, which in turn reduces the vapor production on that effect. It is an exponential decay process. That is why despite the larger energy availability in the first effects, the

better balanced effects of the low temperature operation turns out to ultimately produce similar levels of separation [139].

Also in this figure, it can be seen than flashing takes a more relevant role in vapor generation in the latter effects of the high temperature alternative, since it is not affected by BPE (8, 9 and 17% of the total vapor generated in effects 12, 13 and 14, respectively). This indicates that maybe flashing is a good alternative to increase the vapor production in the latter stages of a thermal brine concentrator plant.

[139]: Lienhard V (2019), "Energy Savings in Desalination Technologies"

Remark 7.5.1 A MED-MSF hybrid could be a good alternative to increase the brine concentration in the last effects, where the vapor production is limited by the BPE. Another option worth exploring is variable geometry effects, in order to increase temperature differences and maintain vapor production at higher concentrations.

Towards the optimal coupling and operation of a solar driven MED system

8

TL;DR

This chapter describes a method to develop an operational strategy enabling the seamless integration of a solar driven MED system in an autonomous and optimal manner, including decisions on when to start or stop each subsystem and how to regulate them during operation.

The method is based on a hierarchical control approach consisting of three layers, where the upper operation plan solves a Mixed Integer Non-Linear Programming (MINLP) problem. Results for a week long simulation of the system are compared against two alternative strategies: a baseline operation and only operation optimization strategies show that the proposed method is able to significantly increase the water production by XX % by taking full advantage of the solar resource and flexibility of the thermal storage.

8.1 Introduction

Most of the literature on automatic control of MED processes focuses on low-level control strategies. These are typically based on simple control loops, using either PID controllers [29] or Model Predictive Control (MPC) [30], with the main objective of maintaining desired temperature setpoints—primarily the heat source inlet temperature. A number of works have also addressed optimization of the MED process in isolation. For example, Carballo et al. [31] optimized the steady-state MED process using genetic algorithms under different criteria (*e.g.*, maximum production, highest performance ratio, minimum energy consumption, best second-law efficiency, and combinations thereof). However, their approach treated the inlet cooling/seawater flow as a decision variable, which is an uncontrolled input and thus invalidates the results. The condenser outlet temperature, which can be regulated through the cooling water flow, would have been the appropriate decision variable. Similarly, Chorak et al. [32] experimentally characterized the pilot plant described in Chapter 5 under a wide range of operating conditions. Their results highlighted how distillate production and thermal performance are highly sensitive to the chosen operating point: feedwater flow rate, condenser operating temperature, and heat source temperature have strong impacts, whereas the system is less sensitive to variations in heat source flow rate, owing to its sensible heat transfer nature.

There are inherent limitations in optimizing the MED process in isolation, without considering the complete system. As explained in Chapter 7, an MED plant (or any thermal separator) requires two forms of energy: heat and electricity. Electricity costs can be directly assigned using, for instance, market prices. For fossil-fuel-based thermal energy, it is straightforward to relate operating conditions to fuel consumption and cost. However, when thermal energy is provided by a variable source such as solar, the situation becomes more complex. Solar availability is intermittent, and both the operation and efficiency of the solar field depend strongly on how the MED load is managed. The two subsystems are intrinsically coupled. This complexity is further amplified by the presence of thermal storage, which enables time-shifting of solar energy use and adds another layer of operational decisions.

In short, the true cost of thermal energy in a solar-driven system is difficult to assess, and achieving optimal MED operation requires optimizing the entire coupled system.

8.1	Introduction	105
8.2	Problem description	107
8.2.1	Implementation discussion . .	108
8.3	Proposed strategy	110
8.4	Operation plan layer descrip- tion	111
8.4.1	Candidate problems genera- tion	111
8.4.2	Update times generation . . .	111
8.5	Operation optimization layer description	113
8.6	Optimization results	114
8.6.1	Choosing an algorithm	114
8.6.2	Choosing a candidate problem	114
8.6.3	Simulation results	114
8.6.4	Performance comparison with alternative strategies	117

[29]: Roca et al. (2008), “Solar Field Control for Desalination Plants”

[30]: González et al. (2014), “Economic Optimal Control Applied to a Solar Seawater Desalination Plant”

[31]: Carballo et al. (2018), “Optimal Operating Conditions Analysis for a Multi-Effect Distillation Plant According to Energetic and Exergetic Criteria.”

[32]: Chorak et al. (2017), “Experimental Charac-
terization of a Multi-Effect Distillation System
Coupled to a Flat Plate Solar Collector Field”

Several studies address this broader problem at different levels of complexity. González *et al.* [30] proposed a receding-horizon optimal control strategy with economic objectives—maximizing water production while minimizing electricity costs. Their work relied on a simplified linear model, optimizing only the solar field flow, while fixing the MED inlet temperature at a constant value. The most advanced optimization efforts in the literature, however, have been developed not for MED but for Membrane Distillation (MD).

[140]: Porrazzo *et al.* (2013), “A Neural Network-Based Optimizing Control System for a Seawater-Desalination Solar-Powered Membrane Distillation Unit”

In Porrazzo *et al.* [140], the authors developed a neural network-based optimizing control system for a solar-powered seawater Membrane Distillation (MD) unit. Because solar energy is intermittent and variable, efficient operation requires advanced control strategies. A neural network model, trained on experimental data, was used to capture the relationships between solar radiation, feed flow rate, inlet water temperature, and distillate production. This model was then applied to identify optimal feed flow conditions that maximize distillate output under varying conditions. The proposed feedforward control strategy was validated through simulations and tested in a pilot plant, demonstrating improved efficiency.

[33]: Gil *et al.* (2019), “Hybrid NMPC Applied to a Solar-powered Membrane Distillation System”

Gil *et al.* [33] extended this approach by recognizing that a solar MD plant does not operate as a single continuous process but transitions through distinct operating modes (*e.g.*, heating the solar field, charging the storage tank, or running the MD module) dictated by solar and thermal conditions. In their formulation, the switching logic is predefined: the solar field is started once irradiance exceeds a threshold, the tank is then charged, and the MD module only begins operation once its inlet temperature reaches a set value. In other words, the decision of when to start each subsystem is hardwired into the control rules. As a result, these operating modes are treated as part of the environment, not as free decision variables—representing a limitation of the work. To manage the predefined mode transitions, the authors modeled the facility as a hybrid system and developed a Hybrid Nonlinear Model Predictive Control (H-PNMPC) scheme. This framework optimizes flow rates while anticipating and coordinating the fixed transitions between modes. In doing so, it generalizes the earlier feedforward optimization into a predictive control framework that incorporates environmental constraints, enabling more robust operation. Simulation results showed that the H-PNMPC increased operating hours and slightly improved water production compared to rule-based control. Nevertheless, the choice of optimization parameters—operation time, operating temperature, and distillate production—together with the omission of electrical consumption, led to potentially inefficient outcomes. For instance, the system achieved an 11.31 % increase in operating time for only a 1.23 % gain in production, likely at the expense of higher auxiliary energy consumption.

Firstly, existing literature on the optimization of MED plants presents important limitations. Many studies either consider too few variables, rely on uncontrollable variables, or use overly simplified models. From the process analysis in Chapter X, it was concluded that the key controllable variables that fully define the operating conditions of an MED plant are: the heat source flow rate ($q_{med,s}$), the heat source inlet temperature ($T_{med,s,in}$), the feedwater flow rate (q_f), and the condenser outlet temperature ($T_{med,c,out}$). These should therefore serve as the decision variables when optimizing plant operation.

Secondly, the objective in optimizing desalination processes is to maximize distillate production while minimizing the resources required. In solar-driven processes, the solar resource itself has no direct cost. However, its use requires electricity to recirculate the working fluid through the solar field. Since the solar field essentially acts as a solar-to-heat converter, the only relevant consumption to be minimized in the optimization is the electricity demand of all system components.

A further consideration, often overlooked in the literature, concerns decisions on when to start and stop the operation of different subsystems in the presence of thermal storage. Thermal storage allows heat to be used independently of solar availability, within certain limits. Depending on its size, this makes the timing of subsystem operation—solar field and thermal separator—crucial for maximizing system performance both on the current day and over subsequent days. Relying on a fixed irradiance threshold to trigger the system startup sequence is therefore suboptimal, as it ignores the state of thermal storage and forecasts of solar availability that could enable longer or shorter operation of the heat source, or earlier or later startup of the load.

In this work, the operation of a solar-driven MED system is optimized with these aspects in mind. This is the first study to include explicit decisions on when to start and stop each subsystem, while also accounting for a two-day prediction horizon. This allows the optimization to consider not only immediate performance, but also the impact of present decisions on future production. The method relies on an experimentally validated system model that incorporates the electrical consumption of each component, combined with the most comprehensive data-driven MED model currently available in the literature.

This chapter is structured as follows: first, the optimization problem is described in Section 8.2, then the proposed optimization strategy to solve it is presented in Section 8.3. The strategy consists on two fundamental blocks which are detailed in Section 8.4 (Operation plan layer description) and Section 8.5 (Operation optimization layer description).

8.2 Problem description

The behavior of the SolarMED process is controlled by acting on two components, a discrete (operation state) and a continuous one (process variables).

The goal is to design an operational strategy that enables the seamless integration of both subsystems in an autonomous and optimal manner, including decisions on when to start or stop each subsystem and how to regulate them during operation. Therefore, considering the whole system as a Mixed Integer Non-Linear Programming (MINLP) optimization problem¹ that aims to maximize the water production while minimizing the (electrical) consumption of the system. Decisions on when to operate the system are weighted considering an optimization horizon, approximating the operation strategy of the system to the optimum:²

1: See Section 3.2.2 (MINLP problems)

2: In general q represents flow rates while T are temperatures. Figure 5.1 can be consulted for subscript reference.

Problem: SolarMED

$$\min_{\mathbf{x}, \mathbf{e}; \theta} J = f(\mathbf{x}, \mathbf{e}; \theta) = \sum_{i=1}^{n_{steps}} (J_{e,i} - J_{w,i})$$

with:

for $i = 1 \dots n_{steps}$:

$$J_{w,i} = q_{d,i} \cdot P_{w,i} \text{ if valid operation else } 0$$

$$J_{e,i} = C_{e,i} \cdot P_{e,i}$$

$$q_{d,i}, C_{e,i}, \text{ valid operation} = \text{solarmed model}(\mathbf{x}_{c,i}, \mathbf{x}_{p,i}, \dots)$$

- Decision variables

$$\mathbf{x} = [\mathbf{med}_{mode}, \mathbf{sfts}_{mode}, \mathbf{q}_{sf}, \mathbf{q}_{ts,src}, \mathbf{q}_{med,s}, \mathbf{q}_{med,f}, T_{med,s,in}, T_{med,c,out}]$$

$\forall i = 1 \dots n_{steps}$ is a notation to indicate that a condition must be held at every step i in the optimization horizon (n_{steps}).
Bold variables represent vectors.

where $\mathbf{x}_{nx \times \sum n_{updates,xi}} = [x_{1,i}, \dots, x_{1,n_{updates,x_1}}, \dots, x_{n_x,n_{updates,x_{nx}}}]$

- ▶ Environment variables

$$\mathbf{e} = [\mathbf{I}, \mathbf{T}_{\text{amb}}, \mathbf{P}_e, \mathbf{P}_w]$$

where $\mathbf{e} = [e_{1,1}, \dots, e_{1,n_{steps}}, \dots, e_{n_e,n_{steps}}]$

- ▶ Fixed parameters ??

$$\theta = [R_p = 1, R_s = 0, \omega_{dc} = 0]$$

subject to:

- ▶ Box-bounds

- $\text{med}_{\text{mode}} \in [0, 1] \subset \mathbb{Z}$
- $\text{sfts}_{\text{mode}} \in [0, 1] \subset \mathbb{Z}$
- $q_{sf} \in [\underline{q}_{sf}, \bar{q}_{sf}] \subset \mathbb{R}$
- $q_{ts,src} \in [\underline{q}_{ts,src}, \bar{q}_{ts,src}] \subset \mathbb{R}$
- $q_{med,s} \in [\underline{q}_{med,s}, \bar{q}_{med,s}] \subset \mathbb{R}$
- $q_{med,f} \in [\underline{q}_{med,f}, \bar{q}_{med,f}] \subset \mathbb{R}$
- $T_{\text{med,s,in}} \in [\underline{T}_{\text{med,s,in}}, \bar{T}_{\text{med,s,in}}] \subset \mathbb{R}$
- $T_{\text{med,c,out}} \in [\underline{T}_{\text{med,c,out}}, \bar{T}_{\text{med,c,out}}] \subset \mathbb{R}$

valid operation conditions, $\forall i = 1 \dots n_{steps}$:

- ▶ $T_{sf,out} \leq \bar{T}_{sf,out}$

Where the objective is to minimize the cumulative cost of operation (J). Fresh water ($q_{med,d}$) sold (J_w) at price P_w is the negative term while electrical consumptions (C_e) at price P_e make up the positive cost term (J_e). The benefit (B) of operation is simply the inverse of the cost of operation.

The environment is represented by the vector \mathbf{e} , which includes the global solar irradiance (\mathbf{I}), ambient temperature (\mathbf{T}_{amb}), and the prices of water (\mathbf{P}_w) and electricity (\mathbf{P}_e).

The decision vector \mathbf{x} is composed of the decision variables for both the discrete and the continuous space. Two decision variables are defined to manipulate the discrete state of each subsystem defined in Section 6.3: med_{mode} and $\text{sfts}_{\text{mode}}$. These binary ($\subset \mathbb{Z}$) variables establish whether the particular subsystem is active ($x_i = 1$) or inactive ($x_i = 0$). This is directly related to the operation state of the particular subsystem³⁴ and accounted for in the models by the integrated finite-state machines as explained in Section 6.3. For the continuous space, the decision variables include the ones that define the operating conditions (*i.e.* operation point) of the MED system, and the two recirculation flow rates that determine the conditions of the heat source (q_{sf} , $q_{ts,src}$).

3: As defined in Tables 6.5 and 6.6

4: Once the values for these decision variables are provided, the low-level control layer is in charge of safely transitioning between operation states *e.g.* $\text{med}_{\text{mode}} : 0 \rightarrow 1$, $\text{med}_{\text{state}} : \text{off} \rightarrow \text{generating vacuum} \rightarrow \text{starting-up} \rightarrow \text{active}$

8.2.1 Implementation discussion

On the constraint handling

The reader might notice that no constraints are explicitly defined in the problem definition. This is because the constraints are implicitly defined in the model equations, which are used to evaluate the objective function. This design decision is motivated to avoid the need for a constraint-handling capable optimization algorithm, limiting the choice for an already complex MINLP problem⁵. Specifically, two aspects demand further consideration:

5: See Section 3.2.3 (A discussion on constraint handling) for a more detailed discussion on the topic

1. The decision value for the MED outlet condenser temperature ($T_{med,c,out}$) is not a direct input to the system, but rather a setpoint to be followed by a low-level control loop by manipulating the cooling water flow rate ($q_{med,c}$). This input might saturate and thus not be able to achieve the desired setpoint. In this case, a new value for the decision variable is computed, which is the minimum value that can be achieved (with $\bar{q}_{med,c}$). In this case, the value used in the SolarMED and the output from the optimization to the low-level control layer would be the validated value for $T_{med,c,out}$. No additional actions are needed.
2. In the solar field, in order to not constantly interrupt the evaluation due to the solar field temperature going above $\bar{T}_{sf,out}$ (120 °C), the model saturates this temperature when going above and sets a flag. The limitation of this approach is that when there is low energy demand from the load, and likely because it favors energy transfer in the heat exchanger⁶, the optimizer tends to minimize the solar field flow, and systematically lets the solar field outlet temperature reach the limit. To avoid this situation, the positive term of the objective function is nullified in iterations where the constraint is not met.

Here, in order to ensure *valid operation* the fitness function is manipulated to de-incentivize decision variable values that lead to unfeasible operation.

⁶: greater temperature difference in primary side instead of greater mass flow rate with its associated increase in pumping power

On the prediction horizon

The problem is designed as an optimization problem with a shrinking horizon. The horizon size should be large enough so that decisions on how to operate the system are made with perspective, taking into account how they will affect the system in the future, but not so large that current decisions have no impact on the far future, and making the problem dimensionality become unmanageable.

For this case study, this parameter should be chosen based on the hours of capacity of the thermal storage to operate the MED system.

The thermal storage capacity is XXX which allows the system to operate with no supply from the solar field for up to XX hours. This means that depending on the charge state of the thermal storage, the system could start operation independently of the irradiance conditions, or operate at different levels of temperature. Considering this the optimization horizon, in time units, chosen was 36 hours. This means that if the optimization is evaluated at 5:00 on day 1, the fitness function is evaluated until 19:00 of day 2 *i.e.* including the end of operation for day 2.

On solving the optimization problem

Solving the optimization problem for this Mixed Integer Non-Linear Programming (MINLP) formulation presents significant challenges due to the combinatorial nature of the integer decision variables [141]. As shown in Figure 8.1, each combination of integer decisions, such as the operational modes of the separation subsystem (med_{mode}) and the solar field thermal storage subsystem ($sfts_{mode}$), leads to a different system trajectory along the prediction horizon⁷.

The number of possible operation trajectories increases exponentially with both the number of integer variables (n_{xi}) and the number of decision updates ($n_{updates,xi}$), following the expression⁸:

$$n_{problems} = n_{xi}^{n_{updates,xi}}. \quad (81)$$

Reminder: Shrinking horizon optimization

An optimization where the horizon end is fixed, and as time progresses, the start of the horizon moves forward.⁹

⁹ See Section 3.2 (Optimization)

[141]: Grossmann (2021), Advanced Optimization for Process Systems Engineering

⁷: This will be referred to as: operation plan

⁸: For example: $n_{updates,xi} = 6 \rightarrow n_{problems} = 64$, $n_{updates,xi} = 24 \rightarrow n_{problems} = 16\,777\,216$

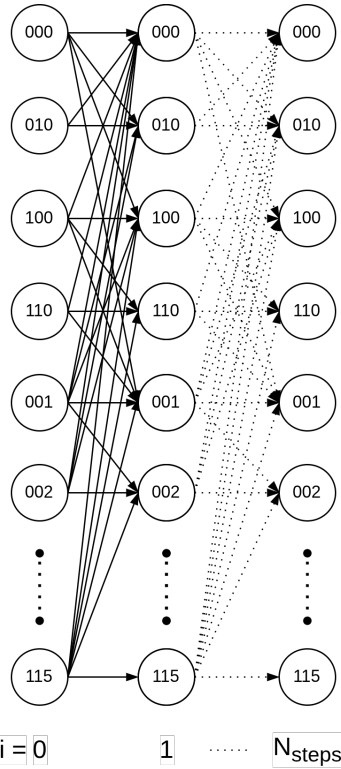


Figure 8.1: Decision tree resulting from the combinatorial nature of the integer part of the optimization problem. Text in nodes represents system states.

This exponential growth makes the search space extremely large and complex.

An important design consideration when solving the optimization problem is whether the sequence of integer decisions (*i.e.*, operational mode transitions over time) is predefined or whether the optimization algorithm is allowed to explore the decision tree freely and determine the optimal sequence. The latter case requires more computational effort but allows for potentially better-performing solutions by dynamically adjusting to system conditions.

On the decision variables update frequency

Apart from the integer decision variables, if a fixed decision variable update frequency is chosen for all continuous decision variables, the size of the decision vector for a large horizon like the one chosen can become large with diminishing returns. Instead, a new design parameter is introduced: the number of decision variable updates (n_{updates,x_i}) for each decision variable in the optimization problem.

Thus, the decision vector is formed by each individual decision variable repeated as many times as updates for it:

$$X_{n_x \times \sum n_{\text{updates},x_i}} = [x_{1,k}, \dots, x_{1,n_{\text{updates},x_1}}, \dots, x_{n_x, n_{\text{updates},x_n}}]$$

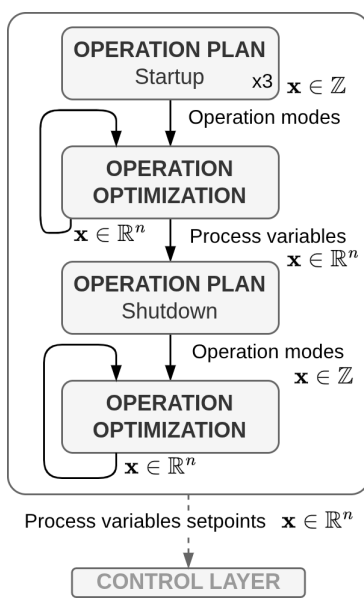
The number of updates of the decision variable ($n_{\text{updates},x_i} \in [1, n_{\text{steps}}]$) can be chosen individually. More updates are assigned to variables regulating faster dynamics ($q_{sf}, q_{ts,src}$), and these updates of the decision variables are evenly distributed throughout the active period of the subsystem within the horizon. This is a crucial design consideration since otherwise the limited number of updates would be assigned to long inactive periods (between end of operation in day 1 and start on day 2).

It also means that the continuous component of the decision vector can only be assigned timestamps after the integer part is defined. Once timestamps are associated with each decision variable, the decision vector values can be resampled to match the desired sampling time of the optimization problem. This is done by forward filling [142] the values of the decision vector until the next update time.

8.3 Proposed optimization strategy

A hierarchical control approach (see Figure 8.2) was chosen consisting of three layers: operation plan, operation optimization, and control. This scheme was chosen for two main reasons. On the one hand, the time scales of the different aspects of the operation of the system (operation mode changes, process variables setpoint changes, regulatory control, respectively) can differ substantially. Secondly, it allows to abstract process complexity from the more computationally demanding upper layers by allocating it into the downstream layers. The operation plan layer makes decisions for the *operation modes*, the operation optimization layer sets the setpoints given to the continuous *process variables* that are to be followed by the low-level regulatory control layer.

Both operation plan and operation optimization layers share the same underlying problem structure, the difference being that the operation plan layer evaluates a predefined library of n_{problems} combinations of the binary decision variables med_{mode} and $\text{sfts}_{\text{mode}}$ twice; once to decide the operation start, and another to end operation. The operation optimization layer periodically solves



a single Non-Linear Programming (NLP) problem with the selected values for these two variables fixed. They are further described in the following sections.

8.4 Operation plan layer description

This layer determines the integer decision variables of the MINLP problem, namely, the sequence of operation modes producing an operation plan. To make the problem computationally tractable, only a limited number of combinations, n_{problems} , are evaluated. This transforms the mixed-integer problem into a simpler form by moving the integer variables from the decision to the environment space. In effect, the original MINLP is decomposed into a library of nNLP problems that are individually evaluated⁹.

To improve robustness, the layer can be evaluated multiple times (n_{evals}) under different scenarios—typically reflecting variations in forecasted environmental conditions. The final operation plan is selected as the best compromise across these scenarios.

The time required to perform this layer's computation is denoted $\Delta t_{\text{eval,plan}}$.

8.4.1 Candidate problems generation

Given the available computational resources and the complexity of the objective function, it has been found feasible to evaluate in the order of $n_{\text{problems}} \sim 100$ candidate combinations. This constraint informs how many Degrees of Freedom (DoF) (i.e. number of updates available for the operation modes) can be defined by using Equation 8.1. The particular design choice for the number of updates per subsystem is shown in Table 8.1. In total, 101 distinct operation plans are generated for the start-up evaluation and 144 for the shutdown¹⁰.

Subsystem	Degrees of freedom				n_{problems}
	Day 1		Day 2		
	Start	Stop	Start	Stop	
Evaluation: Start-up (1)	sfts	3	3	1	1
	med	3	3	1	1
Evaluation: Shutdown (2)	sfts	-	3	2	2
	med	-	3	2	144

The number of updates available for each integer variable $n_{\text{updates},xi}$ will be interchangeably referred to as Degrees of Freedom (DoF).

9: MINLP → nNLP

10: Notice the total number does not match exactly Equation 8.1 since special cases are added (subsystem inactive)

Table 8.1: Operation plan. Start-up (1) and shutdown (2) degrees of freedom for changes in the operation state.

8.4.2 Update times generation

Up to this stage the operation plans generated just consist of a list of ones and zeros for each subsystem, indicating whether the subsystem is active or inactive in the particular update. The next step is to assign the operation mode updates to specific time instants, which then can be resampled to match the desired sampling time of the optimization problem¹¹.

In order to maintain the solution close to the optimal one, while keeping the number of problems reasonable, decision updates are distributed throughout the prediction horizon at strategic time instants. Since the case study system is fundamentally a solar process, the operation is strongly dependent on the irradiance availability, and thus operation changes are likely to take place at the start and end of the solar day.

The operation mode updates are distributed temporally as shown in Figure 8.3 (b) depending on the number of updates available (Degrees of Freedom (DoF)). These update times are dependent on the solar irradiance profile and are bounded by lower- and upper-level thresholds. Depending on the plan

11: As with the continuous component of the decision vector, this is done by forward filling [142] the values of the decision vector until the next update time. This is also known as *Last Observation Carried Forward*

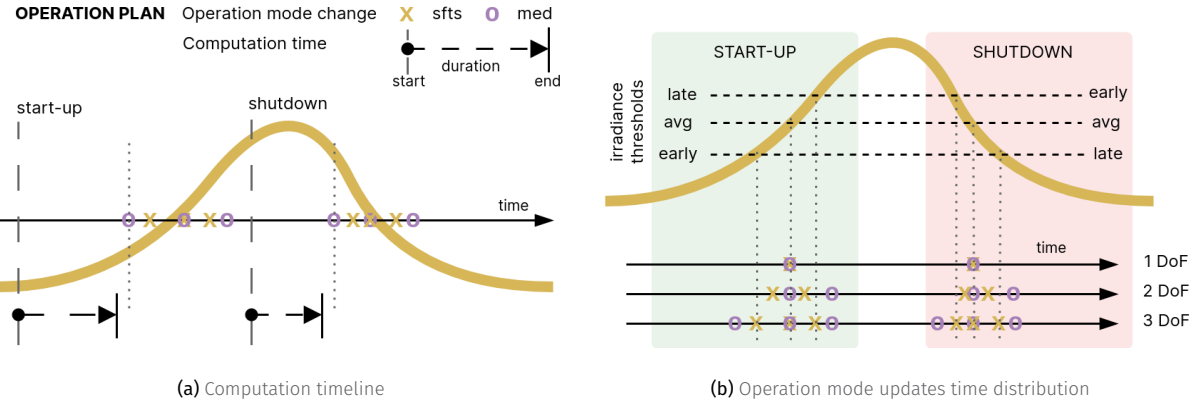


Figure 8.3: Operation plan layer computation and updates distribution. The yellow line represents the irradiance illustrating the solar day.

action (start-up or shutdown), they are named early-late start or early-late stop thresholds, respectively.

In Figure 8.3 (b) up to three DoF are visualized. If only one update is available, the update time is set at the mean of the early and late thresholds. If two DoF are available, for the Solar Field and Thermal Storage subsystem (sfts) subsystem, they are placed halfway between the early threshold and the mean, and the late threshold and the mean, respectively. For the MED subsystem, updates are delayed. Finally, with three DoF, updates for the sfts subsystem are placed at the early, mean and late thresholds, while for the MED subsystem, the leftmost and rightmost updates are shifted to the left and right, respectively. If more updates for the particular action are available *i.e.* DoF, additional thresholds can be added.

Given a number of updates per subsystem and the update times assigned. The potential operation time change candidates are defined as:

$$t_{mode-change,candidates} = [t_0, t_1, \dots, t_{max(n_{updates}, \forall x_i)}]$$

Ordered in ascending order, where t_0 is the earliest potential operation change time and $t_{max(n_{updates}, \forall x_i)}$ is the latest potential operation change time. Based on this definition, the earliest potential subsystem start-up would be at $t_{\uparrow, candidates}(0)$. Similarly, the earliest potential shutdown would be at $t_{\downarrow, candidates}(0)$.

Start-up

The most important aspect of this evaluation is to find the right time to bring the subsystems online, and secondary is to provide a preliminary estimate for their shutdown timing.

This is the first evaluation of the proposed methodology (see Figure 8.2) and is computed ahead of the first potential operation mode change (Figure 8.3 (a) - start-up), with enough lead time to complete the analysis before any potential change in operation mode ($t_{\uparrow, candidates}(0)$):

$$t = t_{\uparrow, candidates}(0) - (\Delta t_{eval, plan} \times n_{evals})$$

Being the earliest evaluation, it has the longest prediction horizon and thus the highest predicted variables uncertainty. As a counterpart, as shown in

Figure 8.3 (a), this early evaluation start allows sufficient computation time, even several hours in advance, to perform several evaluations. Specifically three evaluations (n_{evals}) are performed: a nominal scenario with the forecasted environmental conditions, a pessimist one with a 20% decrease in the expected solar irradiance and finally an optimist one with a 20% increase in the expected solar irradiance.

Shutdown

A second evaluation is performed later in the day (see Figure 8.2), before system shutdown. This aims to determine the most suitable time to stop operations using the most recent system state information. It includes DoF regarding the operation schedule for the following day, allowing the shutdown decision for day 1 to account for its impact on the start and end times of day 2¹².

Only one evaluation is performed, as the uncertainty in the prediction horizon is significantly lower than in the start-up evaluation. It is evaluated in parallel to the operation optimization layer and just before the earliest expected shutdown time of the subsystems from Section 11 (Start-up), $t_{\downarrow, candidates}(0)$, considering subsystem shutdown.

12: See Table 8.1

$$t = t_{\downarrow, candidates}(0) - (\Delta t_{eval, plan} \times \text{somenumber})$$

Once computed the integer decision are updated in this layer. The faster the computation the better, since it will allow the operation optimization layer to optimize operation for the actual shutdown time and adapt accordingly.

8.5 Operation optimization layer description

As mentioned, this middle layer establishes the setpoints for the continuous process variables, *i.e.* the continuous part of the MINLP problem. The operation optimization layer evaluates periodically, with a sample time $T_{eval, optim}$, a NLP problem where the integer decision variables are fixed to the values provided by the operation plan layer¹³. It uses the latest available state of the system and environment predictions to evaluate the objective function.

The layer computation time is named $\Delta t_{eval, optim}$.

13: It is exactly equivalent to the operation plan layer problem, just making $n_{problems} = 1$

SolarMED optimization methodology

1. Generate operation mode change candidates based on the available updates per subsystem and irradiance thresholds.
2. Before the first potential operation change and considering the evaluation time, $t = t_{\uparrow, candidates}(0) - (\Delta t_{eval, plan} \times n_{evals})$, evaluate the operation plan layer to establish the operation start of the subsystems and an estimation of when to stop.
3. Before the established startup and considering the layer evaluation time, $t = t_{\uparrow} - \Delta t_{eval, optim}$, start evaluating the operation optimization layer periodically ($T_{eval, optim}$) to establish the setpoints for the continuous process variables.
4. Before the earliest subsystem projected shutdown and considering the operation optimization layer evaluation time, $t = t_{\downarrow, candidates}(0) - \Delta t_{eval, plan}$, evaluate the operation plan layer, in parallel to the operation optimization layer, to establish the shutdown time of the subsystems.
5. Continue evaluating the operation optimization layer periodically

$(T_{eval,optim})$ until the last subsystem is shutdown.

8.6 Optimization results

8.6.1 Choosing an algorithm

Once the optimization problem(s) is defined, an algorithm must be chosen that explores the solution space and finds a decision vector that minimizes the objective function.

The solution space has proven to be non-convex, with many local minimums (poor results were obtained when using local-gradient-based algorithms). The size of the decision vector depends on the active periods duration, around 120 elements. In addition, simulation of two days of operation (even when inactive periods are skipped) requires 5-10 seconds of computation time. Algorithm parallelization capabilities are of no use in this case, since many candidate problems will already be evaluated in parallel. The objective is then to find a global large-scale optimization algorithm that can find near-optimal solutions with 200 to 300 objective function evaluations (totaling 2-4 hours of computation time). In order to find the best algorithm, one of the candidate problems is arbitrary chosen and a library of global-evolutionary optimization algorithms is used from the PyGMO open-source Python library, specifically: Differential Evolution (DE), Self-adaptive DE (SADE), (N+1)-ES Simple Evolutionary Algorithm (SAE), Covariance Matrix Adaptation Evolution Strategy (CMA-ES) and Particle Swarm Optimization (PSO). Evolution results are shown in Fig.??, showcasing that for this particular problem the best alternative is the (N+1)-ES Simple Evolutionary Algorithm.

8.6.2 Choosing a candidate problem

Once an algorithm was chosen, all $n_{problems}$ were evaluated where the algorithm is only required to choose values for the process variables (continuous). The results of this evaluation are shown in Fig.??, 101 problems were evaluated and visualized is their fitness evolution as a function of objective function evaluations. Problems 8, 18 and 48 resulted in the best fitness after the evolution process and their operation plan can be visualized in Fig. ??.

8.6.3 Simulation results

Figure ?? shows results for the simulated system in a total of X days. Where the first two days present favorable - sunny - conditions, followed by a cloudy day, and finishing with a sunny day (Figure ?? - Environment).

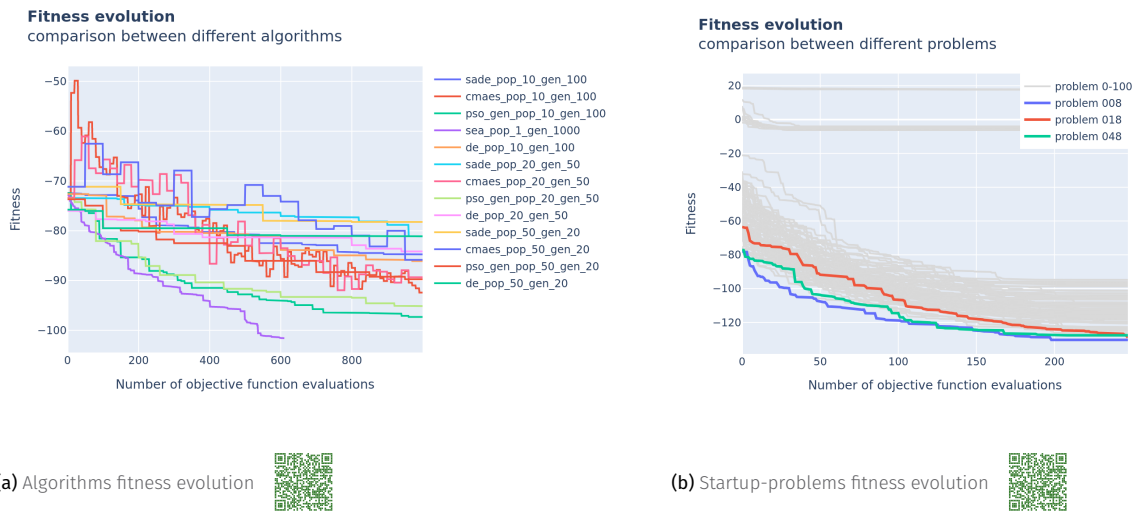
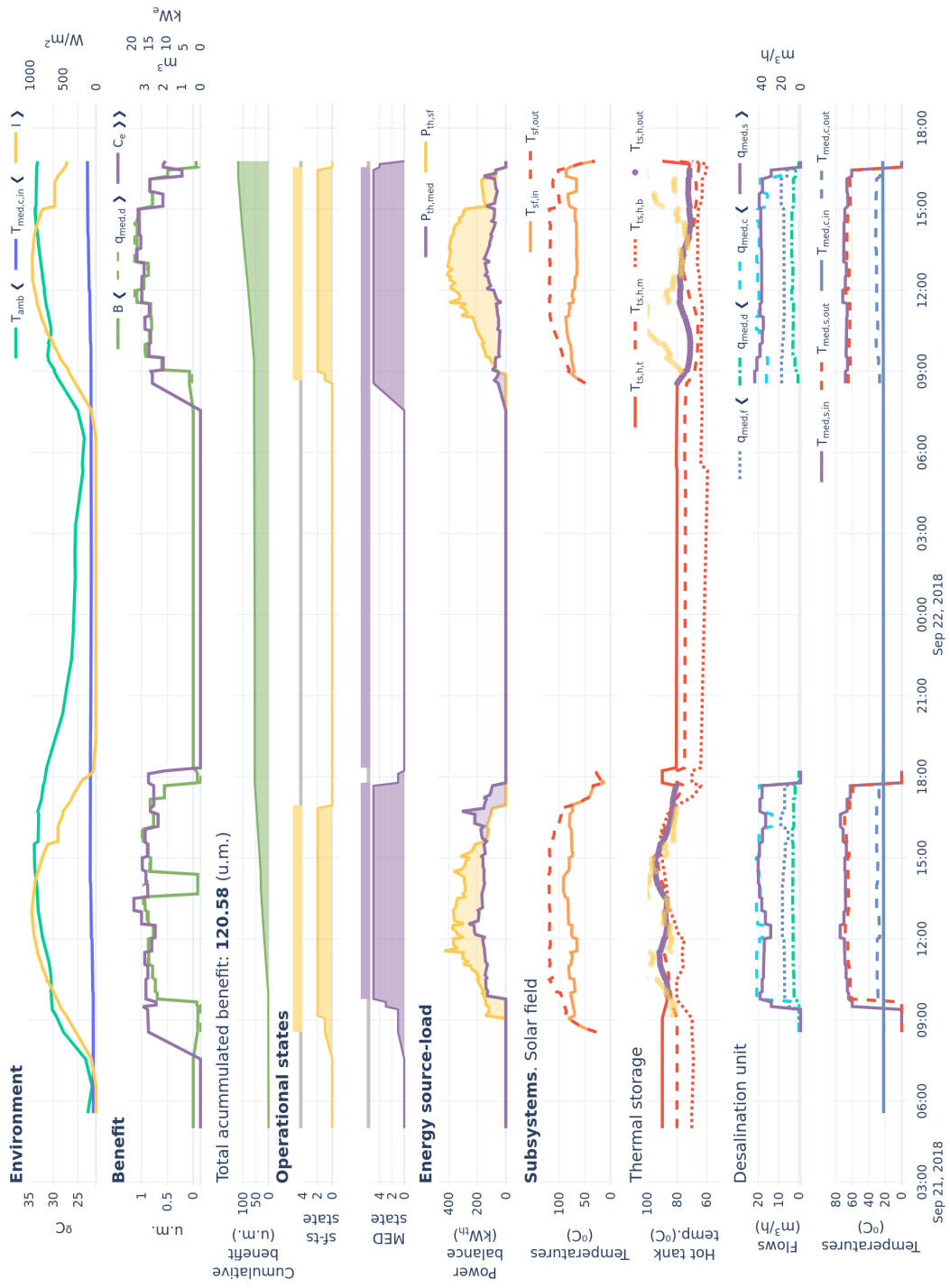


Figure 8.4: Fitness evolution for a particular startup-problem

Solar MED optimal coupling

Evaluation results



8.6.4 Performance comparison with alternative strategies

baseline operation and just operation optimization

CONCLUSIONS AND OUTLOOK

Just some phrase, it may be longer, it might
be shorter, but in the end, it's a phrase.
Aren't we all phrases? Well, no

Someone else answering someone

Conclusions

Outlook and future work

Optimal water and electricity management in a combined cooling system

Improved Pareto front computation. In the current optimization implementation, the Pareto front for each step in the optimization horizon is constructed using a grid search over the decision space. This approach can become computationally expensive, especially as the grid resolution increases. Additionally, the Pareto front must be recalculated from scratch at every step, even though the sequential steps are often very similar—cost parameters remain constant, and only the thermal load and weather conditions change, typically with small variations. A more efficient solution would be to use a multi-objective optimization algorithm, which can transfer evolved populations between successive evaluations, significantly reducing redundant computations.

Better water management In the current implementation, the primary water source is distributed evenly each day, so the optimization process uses up the entire supply daily. However, a more intelligent daily distribution—essentially, a new optimization problem—could improve water management by allocating different amounts on different days, based on expected weather conditions and predicted generation. This approach would likely be incorporated as a new upper layer in the hierarchical control structure.¹⁴ At the higher level a simpler and more abstract model would be considered to predict the long term behavior of the system and to optimize it over a long time horizon, probably considering the availability and capacity of a water reservoir.

Analyze different combined coolers configurations and within each configuration, different component sizes. The cooler analyzed has a combined dry and wet coolers which can either satisfy the nominal cooling load. Different ratios could be analyzed and one would probably be a better fit for the particular case study. Furthermore, the Air-Cooled Heat Exchanger (ACHE) is used for the Dry Cooler (DC), but other options could be considered and added to the comparison, such as an Air-Cooled Condenser (ACC) in parallel with a surface condenser together with a Wet Cooling Tower (WCT) or a deluged condenser.

This in itself is a design optimization problem that is not addressed in this thesis. However, it is important to integrate a method like the proposed optimization and include it in the design process to evaluate the performance of different configurations and sizes. In the end the decision of cooling system configuration and size will be informed by a techno-economic analysis.

Techno-economic analysis. The presented cooling alternatives comparative in this thesis focus on the operation cost of the system, but to get a better picture of the alternatives performance, a techno-economic analysis that includes the capital cost of the system and the expected lifetime of the components should be performed *i.e.* considering all costs associated with the system the plant's lifetime. This is currently being worked on as part of SOLHycool¹⁵, where the methodology presented here in terms of operation costs will be integrated in a techno-economic analysis for different case studies.

14: The resulting structure would be: 1. Water allocation, 2. Combined Cooling System (CCS) operation optimization, 3. Combined Cooler (CC) regulatory control.

15: <https://solhycool.psa.es/>

Energy management in MED processes driven by variable energy sources

Alternative configurations for an MED brine concentrator. Configuraciones alternativas para procesos MED para aplicaciones de concentración de salmueras:

geometría variable de efectos, fuentes externas en efectos distintos al primero, acoplamiento con MSF para efectos posteriores.

Alternative configurations for solar-driven MED. Configuraciones alternativas para el proceso solar MED (almacenamiento con distintos puntos de carga y descarga, MED con distintos puntos de fuente externa, etc. Incluir diagrama de draw.io con las distintas configuraciones) [77]

[77]: Schär et al. (2023), "Optimization of Sustainable Seawater Desalination"

The layout configuration of the facility focused on realibility and simplifying operation and maintenance, not strictly on thermodynamic efficiency. The efficiency of the system could be improved:

1. if direct coupling between solar field and thermal storage was used, avoiding the heat exchanger energy transfer associated losses
2. thermal storage allowed charge and discharge from different levels, in order to take advantage of the temperature stratification and avoid fluid mixing
- 3.
- 4.

These decisions were made to, on the one hand allow to separate the solar field and thermal storage into two distinct decoupled circuits, providing flexibility, reducing the volume of additives required (only added to the solar field circuit), and operational flexibility (other external loads can be connected to the solar field when the MED is not being operated).

In conclusion this system, although improvable, allows to validate the feasibility of the proposed approach by means of the implementation of a suitable control system, in such a way, that the ideas and techniques presented in this work, could be directly extrapolated to a commercial system just by modifying some of the decision variables to suit the particular implementation.

Derived scientific contributions

The author has published or submitted for publication several journal articles, contributed to conferences (national and international) and colloquiums:

Journal publications

- J. M. Serrano, P. Navarro, J. Ruiz, P. Palenzuela, Manuel Lucas, and L. Roca. "Wet Cooling Tower Performance Prediction in CSP Plants: A Comparison between Artificial Neural Networks and Poppe's Model." Energy, May 29, 2024, 131844.
DOI: <https://doi.org/10.1016/j.energy.2024.131844>.
- P. Navarro, J. M. Serrano, L. Roca, P. Palenzuela, M. Lucas, and J. Ruiz. "A Comparative Study on Predicting Wet Cooling Tower Performance in Combined Cooling Systems for Heat Rejection in CSP Plants." Applied Thermal Engineering, June 21, 2024, 123718.
DOI: <https://doi.org/10.1016/j.applthermaleng.2024.123718>.
- J. M. Serrano, P. Navarro, L. Roca, P. Bartolomé, ..., P. Palenzuela, M. Lucas, and J. Ruiz. "Combined cooling for CSP plants: Modeling, experimental validation and optimization analysis" Applied Thermal Engineering, December 21, 2025, 123718.
DOI: <https://doi.org/...> (Under review).

Contribution to conferences

- ▶ J. M. Serrano, J. D. Gil, J. Bonilla, P. Palenzuela, and L. Roca, "Optimal operation of a combined cooling system" in 4th IFAC International Conference on Advances in Proportional-Integral-Derivative Control, Almería, Spain, 2024-06-12/2024-06-14.
- ▶ J. M. Serrano, J. D. Gil Vergel, J. Bonilla, P. Palenzuela, and L. Roca, "Operación óptima de un sistema de refrigeración combinada," in XLIV Jornadas de Automática, Universidad de Zaragoza, 6, 7 y 8 de septiembre de 2023, Zaragoza, 2023rd ed., Aug. 2023, pp. 477-482.
DOI: [10.17979/spudc.9788497498609.477](https://doi.org/10.17979/spudc.9788497498609.477).
- ▶ P. Navarro, J. M. Serrano, J. Ruiz, M. Lucas, L. Roca, and P. Palenzuela. "Comparison Between an Artificial Neural Network and Poppe's Model for Wet Cooling Tower Performance Prediction in CSP Plants." Efficiency, Cost, Optimization, Simulation and Environmental Impact of Energy Systems. International Conference., ECOS 2023, June 25, 2023, 1609–20.
DOI: [10.52202/069564-0146](https://doi.org/10.52202/069564-0146).
- ▶ L. Roca, J. M. Serrano, J.D. Gil, G. Zaragoza, M. Beschi, and A. Visioli. "Modelo de parámetros concentrados para captadores solares planos con reflectores." Jornadas de Automática, no. 45 (July 2024): 45.
DOI: [10.17979/ja-cea.2024.45.10930](https://doi.org/10.17979/ja-cea.2024.45.10930)

Participation in conferences and colloquiums

- ▶ J.M. Serrano, L. Roca, P. Palenzuela. "Yearly Simulation of a Combined Cooling System Integrated into a Concentrating Solar Power Plant". SolarPACES. Almería, Spain (September 2025).
- ▶ J.M. Serrano, P. Palenzuela and L. Roca. "Methodology for the implementation of a steady state simulation model in a multi-effect distillation plant. Case study: PSA MED pilot plant". Desalination for the Environment, Clean Water and Energy (EDS). Las Palmas de Gran Canaria, Spain (2022).
- ▶ J.M. Serrano, P. Palenzuela and L. Roca. Experimental evaluation of MED at high top brine temperatures with no divalent ions in feed water. Desalination for the Environment, Clean Water and Energy (EDS). Limassol, Chipre (2023).
- ▶ Patri ponemos el EDS de Marruecos?
- ▶ 3rd SFERA-III Doctoral Colloquium:
 1. Technological developments for solar multi-effect distillation processes. Almería, Spain (2021).
 2. Modelling and automation of a multi-effect distillation plant for the optimal coupling with solar energy. ETH Zurich, Switzerland (2022).
 3. Towards the optimal coupling of multi-effect distillation with solar energy. DLR. Cologne, Germany (2023).

As a result of the work developed in the present research work, several repositories containing experimental datasets and open-source code have been made publicly available. Particularly, each of the parts of the thesis has an associated repository with the implementation of the presented results, in order to facilitate transparency, reproducibility, and reusability of the developed methods. Additionally, this thesis manuscript itself is also made available together with all its associated media:

Open datasets

- ▶ P. Palenzuela, L. Roca, J.M. Serrano (CIEMAT-PSA). "Steady-State Operation Dataset of an Experimental Wet Cooling Tower Pilot Plant Located at Plataforma Solar de Almería." Version 1.0.0. Zenodo, June 21, 2024. DOI: [10.5281/zenodo.10806201](https://doi.org/10.5281/zenodo.10806201).
- ▶ P. Palenzuela, L. Roca, J.M. Serrano (CIEMAT-PSA). "Steady-State Operation Dataset of an Experimental Air-Cooled Heat Exchanger Located at Plataforma Solar de Almería." Version 1.0.0. Zenodo, December? , 2025. DOI: [10.5281/zenodo.17312369](https://doi.org/10.5281/zenodo.17312369) (To be published).
- ▶ P. Palenzuela, L. Roca, J.M. Serrano (CIEMAT-PSA). "Steady-State Operation Dataset of an Experimental Surface Condenser Located at Plataforma Solar de Almería." Version 1.0.0. Zenodo, December? , 2025. DOI: [10.5281/zenodo.17312530](https://doi.org/10.5281/zenodo.17312530) (To be published).
- ▶ P. Palenzuela, L. Roca, J.M. Serrano (CIEMAT-PSA). "Steady-State Operation Dataset of an Experimental Combined Cooling System Located at Plataforma Solar de Almería." Version 1.0.0. Zenodo, December? , 2025. DOI:[10.5281/zenodo.17312546](https://doi.org/10.5281/zenodo.17312546) (To be published).

Open-source implementation

- ▶ J.M. Serrano, L. Roca. "Repository with the implementation source code for modeling, optimization and simulation of a combined cooling system (wet cooling tower, dry cooler and surface condenser) at Plataforma Solar de Almería as part of the SOLhycool research project". DOI: <https://doi.org/10.5281/zenodo.CHANGEME>
- ▶ J.M. Serrano, "Repository with the implementation and results of the modeling and optimization of a solar-driven multi-effect distillation system at Plataforma Solar de Almería". DOI: <https://doi.org/10.5281/zenodo.CHANGEME>
- ▶ J.M. Serrano, Repository with the source code for the PhD thesis manuscript: "Towards optimal resource management in solar thermal applications: CSP and desalination". DOI: [10.1596/XXX](https://doi.org/10.1596/XXX)

APPENDIX

Just some phrase, it may be longer, it might
be shorter, but in the end, it's a phrase.
Aren't we all phrases? Well, no

Someone else answering someone

A

MED Performance Evaluation

A.1 Uncertainty estimation through first-order Taylor series approximation

In this appendix, expressions for the uncertainty estimation of energetic and separation metrics are shown.

A.1.1 Specific Thermal Energy Consumption (STEC)

$$\Delta STEC = \left(\left(\left| \frac{\delta STEC}{\delta \dot{m}_d} \right| \Delta \dot{m}_d \right)^2 + \left(\left| \frac{\delta STEC}{\delta \dot{m}_s} \right| \Delta \dot{m}_s \right)^2 + \left(\left| \frac{\delta STEC}{\delta T_s} \right| \Delta T_s \right)^2 \right)^{1/2} \quad (\text{A.1})$$

Calculating the partial derivatives, the expression is obtained:

where: $T_s = T_{s,in} - T_{s,out} \rightarrow \Delta T_s = \Delta(T_{s,in} - T_{s,out})$.
If they are the same sensor and were calibrated at the same time using the same calibration standard

$$STEC \pm \Delta STEC \left[\frac{\text{kWh}_{\text{th}}}{\text{m}^3} \right] = \frac{\dot{m}_s c_p T_s}{\dot{m}_d} \pm \frac{c_p}{\dot{m}_d} \times \left[(T_s \Delta \dot{m}_s)^2 + (\dot{m}_s \Delta T_s)^2 + (\dot{m}_s T_s \dot{m}_d^{-1} \Delta \dot{m}_d)^2 \right]^{1/2} \quad (\text{A.2})$$

A.1.2 Specific Electrical Energy Consumption (SEEC)

$$SEEC \pm \Delta SEEC \left[\frac{\text{kWh}_e}{\text{m}^3} \right] = \frac{\sum_{i=1}^N E_i}{\dot{m}_d} \pm \left[\left(\frac{\sum_{i=1}^N \Delta E_i}{\dot{m}_d} \right)^2 + \left(\frac{\sum_{i=1}^N E_i}{\dot{m}_d^2} \Delta \dot{m}_d \right)^2 \right]^{1/2} \quad (\text{A.3})$$

A.1.3 Performance Ratio

$$PR \pm \Delta PR = \frac{\dot{m}_d \Delta h_{ref}}{\dot{m}_s \Delta h_s} \pm \frac{\Delta h_{ref}}{\dot{m}_s \Delta h_s} \left[(\Delta \dot{m}_d)^2 + \dot{m}_d^2 \left(\left(\frac{\Delta \dot{m}_s}{\dot{m}_s} \right)^2 + \left(\frac{\Delta(\Delta h_s)}{\Delta h_s} \right)^2 \right) \right]^{1/2} \quad (\text{A.4})$$

A.1.4 Waste heat performance ratio

$$PR_{WH} \pm \Delta PR_{WH} = \frac{\dot{m}_d}{\dot{m}_s T} \frac{\Delta h_{ref}}{c_p} \pm \frac{\Delta h_{ref}}{c_p} \frac{1}{\dot{m}_s T} \\ \times \left[(\Delta \dot{m}_d)^2 + \dot{m}_d^2 \left(\frac{\Delta \dot{m}_s}{\dot{m}_s} + \frac{\Delta T}{T} \right)^2 \right]^{1/2} \quad (A.5)$$

where: $T = T_{s,in} - T_{c,in} \rightarrow \Delta T = \Delta T_{s,in} + \Delta T_{c,in}$

A.1.5 Recovery ratio

$$RR \pm \Delta RR = \frac{\dot{m}_d}{\dot{m}_f} \pm \left(\left(\frac{1}{\dot{m}_f} \Delta \dot{m}_d \right)^2 + \left(\frac{\dot{m}_d}{\dot{m}_f^2} \Delta \dot{m}_f \right)^2 \right)^{1/2} \quad (A.6)$$

A.1.6 Concentration factor

$$CF \pm \Delta CF = \frac{\dot{m}_f}{\dot{m}_b} \pm \frac{1}{\dot{m}_b} \left(\left(1 + \frac{\dot{m}_f}{\dot{m}_b} \right)^2 \cdot \Delta \dot{m}_f^2 + \left(\dot{m}_f \cdot \Delta \dot{m}_b \right)^2 \right)^{1/2} \quad (A.7)$$

where: $\dot{m}_b = \dot{m}_f - \dot{m}_d \rightarrow \Delta \dot{m}_b = \Delta \dot{m}_f + \Delta \dot{m}_d$

A.2 Exergy calculations

Exergy consists on two components: thermomechanical exergy and chemical exergy. When performing an exergetic analysis, the balances of the exergy flows of interest are calculated given the control volume presented in Fig. ???. Any external stream entering the control volume is considered an exergy input (\dot{Ex}_{in}), while any stream leaving it is considered an exergy output (\dot{Ex}_{out}). A general expression to determine the specific exergy flow (\dot{e}_x) of a stream is given in Equation A.8, where the first two summands represent the thermomechanical component and the last the chemical component.

$$\dot{e}_x = (h - h^*) - T_0(s - s^*) + \sum_{i=1}^n w_i(\mu_i^* - \mu_i^0). \quad (A.8)$$

In Equation A.8, the variables h , s , μ , and w represent the specific enthalpy, specific entropy, chemical potential, and mass fraction, respectively. The properties denoted with an asterisk in the equation are calculated at the restricted dead state conditions (when the temperature and pressure of the system change to match the temperature and pressure of the environment). On the other hand, properties labeled with a superscript of “0” are determined at the global dead state (when the concentration is also changed to match that of the environment). The subscript i represents a species (NaCl, H₂O and others if considered). Notice that the chemical exergy component in this work has been calculated by two approaches: empirical correlations (i) and modelling seawater as an electrolyte for a solution of NaCl with the same concentration as the feedwater salinity (ii). In the latter case, the required activity coefficients have been determined by Pitzer equations [143].

Finally, in order to calculate the specific exergy flows, libraries in MATLAB [144, 145] and Python [romera_jjgomera_2021a] are available. However, they are limited to 120 kg/kg of concentration. For higher values, the approach used is the modelling of seawater as an electrolyte and in this case the chemical exergy

[143]: Pitzer (1973), “Thermodynamics of Electrolytes. I. Theoretical Basis and General Equations”

[144]: Sharqawy et al. (2010), “Thermophysical Properties of Seawater: A Review of Existing Correlations and Data”

[145]: Nayar et al. (2016), “Thermophysical Properties of Seawater”

flows are determined by the activity coefficients using a free and open source tool [35].

Least and minimum least work of separation. To determine how efficient a desalination plant is at separating fresh water from seawater, it is compared to the thermodynamic minimum. This is the least work required to accomplish the separation and is only achievable with an ideal reversible separator (without entropy generation). It has been analyzed and presented in different ways in the literature [87, 110, 111, 115]. A general expression is shown in Equation A.9 in terms of the Gibbs free energy (g).

$$\dot{W}_{\text{least}} = \dot{m}_d \cdot g_d + \dot{m}_b \cdot g_b - \dot{m}_f \cdot g_f. \quad (\text{A.9})$$

If it is normalized to the distillate production and the flows expressed in terms of the recovery ratio according to Equation 7.1, the expression becomes:

$$\frac{\dot{W}_{\text{least}}}{\dot{m}_d} = g_d + \frac{1 - RR}{RR} \cdot g_b - \frac{1}{RR} \cdot g_f. \quad (\text{A.10})$$

As can be seen in Equation A.10, the least work of separation depends on how much pure water is extracted per unit of feed (RR), and as proven in [105], the higher the RR, the higher the least energy required to produce the separation. In this context, the minimum least work of separation (W_{least}^{\min}) is determined when $RR \rightarrow 0$.

A.3 Separation metrics calculation

The molality of sodium chloride at saturation (see Equation 7.4) is determined using the following correlation that was established by [146] in terms of mass fraction and it is valid for a temperature range between 25 and 80 °C:

$$w_{\text{NaCl},\text{sat}} = a + b \cdot T + c \cdot T^2 + d \cdot T^3 \left[100 \text{g}_{\text{NaCl}} / \text{g}_w \right]$$

Likewise, the following conversion formula between mass fraction and molality can be used:

$$b_{\text{NaCl},\text{sat}} = \frac{w_{\text{NaCl},\text{sat}} / 100}{M_{\text{NaCl}} \left(1 - w_{\text{NaCl},\text{sat}} / 100 \right)} \left[\text{mol}_{\text{NaCl}} / \text{g}_w \right]$$

Where M_{NaCl} is the molecular weight of NaCl in g/mol.

A.4 Control system and steady state identification parameters

This appendix section provides reference tables outlining parameters used in the algorithms discussed in this document. Table A.2 summarizes the parameter values for the PID-based process control, while Table A.1 details those for steady-state detection. For the first, K_p , K_i , and K_d are the proportional, integral, and derivative gains, respectively (see Section 3.3.1 (PID controllers)). In the latter, γ_a represents the wavelet transform threshold, γ_d the derivative threshold and finally T_{ss} the time window duration. The algorithm they are used in is described in Section 7.4.1 (Monitoring: steady-state identification). In both tables, T_s represents the sample time.

[35]: Marcellos et al. (2021), PyEqulon

[87]: Lienhard et al. (2017), "Thermodynamics, Exergy, and Energy Efficiency in Desalination Systems"

[110]: Spiegler et al. (2001), "El-Sayed, Y.M."

[111]: Sharqawy et al. (2011), "On Exergy Calculations of Seawater with Applications in Desalination Systems"

[115]: Thiel et al. (2015), "Energy Consumption in Desalinating Produced Water from Shale Oil and Gas Extraction"

[105]: Mistry et al. (2011), "Entropy Generation Analysis of Desalination Technologies"

[146]: Pinho et al. (2005), "Solubility of NaCl, NaBr, and KCl in Water, Methanol, Ethanol, and Their Mixed Solvents"

where:

- $a = 5.671 \cdot 10^1$
- $b = -2.713 \cdot 10^{-1}$
- $c = 7.598 \cdot 10^{-4}$
- $d = -6.373 \cdot 10^{-7}$

Table A.1: Parameters for the steady-state detection algorithm, where s.u. represents that**Table A.2:** Parameters for the PID controller pre-tuned control, where i.u. represents the input variable units, and o.u. the output units.

Parameter	Variable				
	$P_{v,c}$	$P_{v,1}$	\dot{m}_d	\dot{m}_s	\dot{m}_f
γ_q [v.u.]	0.05	0.05	0.1	0.3	0.2
γ_d [v.u./s]	0.002	0.03	0.001	0.02	0.001
T_s [s]			1		
T_{ss} [s]			600		

Parameter	Subsystem					
	Brine level	Distillate level	Condenser outlet temperature	Heat source temperature	Heat source flow	Feedwater flow
Kp [i.u./o.u.]	-0.01	-0.05	-1.7526	1	5	4
Ki[i.u./(o.u.s)]	-0.02	-0.005	-0.0322	0.2	1	1
Kd [i.u./(o.u./s)]	0	0	0	0.5	0.8	0
Ts [s]	5	3	5	2	1	1
Configuration			Parallel configuration			

B

MED First-Principles Model

TL;DR

A first-principles model of a MED plant is presented in this appendix. It is based on thermodynamic equations and mass and energy balances and can be used in two modes depending on the application.

This model simulates thermal and mass transfer processes in a MED plant, such as the one at PSA. The MED process consists of a series of effects (evaporators) and preheaters connected in sequence. In each effect, seawater partially evaporates under decreasing pressure and temperature conditions, while in the preheaters, the feed water is gradually warmed using the condensation heat from the vapor produced in the effects.

The model is based on several assumptions to simplify the calculations:

- ▶ Steady-state operation.
- ▶ Negligible heat losses to the environment.
- ▶ Isothermal physical properties have been considered for all cases.

And is based on several works found in the literature [119, 147, 148] but extends them by including more detailed calculations for the different heat transfer modes (boiling, flashing), considering not-constant Non-Equilibrium Allowance (NEA) and BPE effects, and considering the flashing process of the distillate. It works both at nominal and partial load conditions.

To solve the model, an iterative process is followed where the model proceeds effect by effect, starting from the first stage. For each effect, it uses nonlinear solvers to solve a system of non linear equations (see Figures ??–??) ensuring consistent heat exchange and energy balances. The preheaters are solved in a similar manner. Throughout the process, mass and energy conservation are verified. After completing a cell, the model updates the inlet conditions for the next effect taking into consideration the distillate vapor lost in the preheater-effect distribution line, temperature losses and more importantly, the plant's condensate distribution layout (see Figure B.9).

The model can be used in two modes depending on the application: *calibration mode* and *simulation mode*. Both modes share the same equations and structure, but differ in the inputs required and the parameters used.

[119]: Mistry et al. (2013), "An Improved Model for Multiple Effect Distillation"

[147]: Palenzuela et al. (2014), "Steady State Model for Multi-Effect Distillation Case Study"

[148]: El-Dessouky et al. (1998), "Steady-State Analysis of the Multiple Effect Evaporation Desalination Process"

B.1 Nomenclature

Nomenclature inconsistency

Flows (either mass or volumetric) are represented with a capital M , different to the rest of the manuscript where lowercase \dot{m} is used for mass flows or q for volumetric flows.

Model parameters:

- ▶ Effect heat transfer coefficients (U_{ef})

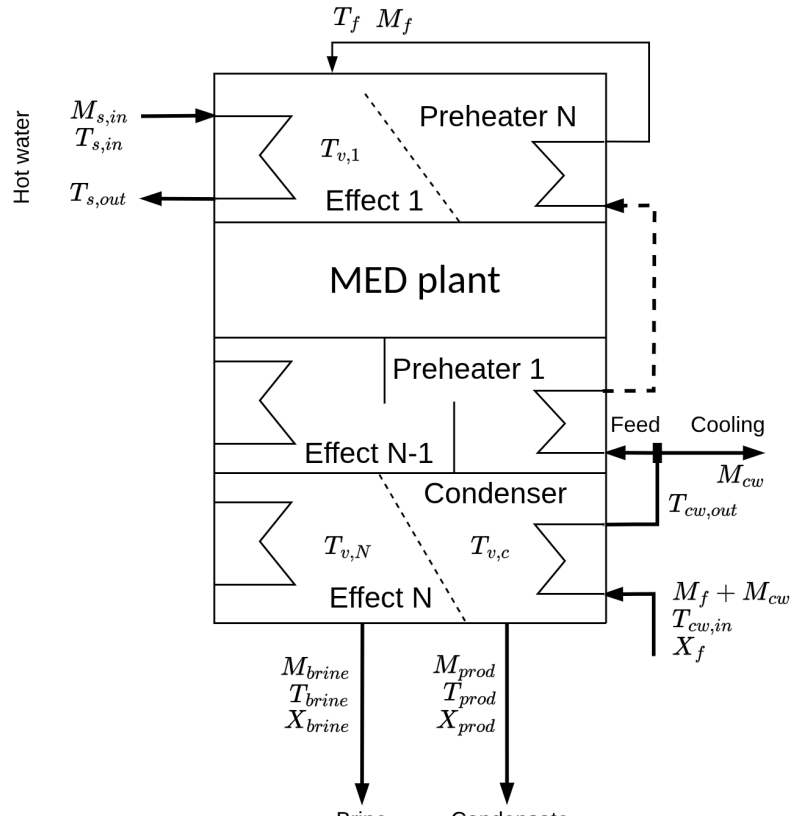


Figure B.1: Overall schematic of the MED model with inputs, outputs, main variables and components

- ▶ Preheater heat transfer coefficients (U_{ph})
- ▶ Preheater-effect distribution line vapor losses (ΔM_v) ...

Plant parameters:

- ▶ Mixer valve positions (Y)
- ▶ Effect and preheater areas ($A_{ef,i}, A_{ph,i}$)
- ▶ Condenser area (A_c)
- ▶ Number of effects and preheaters (N_{ef})

Model inputs:

- ▶ Heat source flow rate and inlet temperature ($M_s, T_{s,in}$)
- ▶ Cooling water flow rate and inlet temperature ($M_c, T_{c,in}$)
- ▶ Feedwater flow rate and inlet temperature ($M_f, T_{f,in}$)
- ▶ Operating pressures per effect and preheater ($P_{ef,i}, P_{ph,i}$)
- ▶ Number of effects and preheaters (N)
- ▶ Feedwater salinity (S_f)

Effects:

Preheaters:

B.1.1 Calibration mode

In the *calibration mode* (see Figure B.3), the model is used to obtain different detailed parameters/outputs of interest that cannot be measured directly, such as the heat transfer coefficients, the different heat transfer modes contribution (boiling, flashing, etc), per effect brine concentration, per effect distillate

$M_s, T_{s,in}, T_{s,out}$
 $M_{cw}, T_{cw,in}$
 M_f, X_f
 $T_{v,1:N}, T_{ph,1:N}, \Delta M_{v,0}$

production, etc.. The computed parameters in this mode can then be used to generate models for these parameters. For this purpose, the model requires an extended set of inputs, including measured temperatures or pressures per effect and preheater¹.

To solve it, an initial guess of ΔM_v is provided, and then the model iteratively solves for the heat transfer coefficients (U_{ef} and U_{ph}) and outlet conditions until the final condenser. The total distillate produced is compared with the measured value, and ΔM_v is adjusted accordingly. This process continues until the calculated distillate matches the measured value within a specified tolerance.

This mode can be used to identify loss of performance, fouling and other issues. Evaluated over time, it can provide trends and be integrated into predictive maintenance strategies. It can also be used to generate data-driven models for the different parameters, which can then be used in the *simulation mode*. Also, it provides more detailed outputs that can be used for further analysis by the O&M team.

Inputs

Outputs

- ▶ Model parameters ($U_{ef}, U_{ph}, \Delta M_v$)
- ▶ Detailed per effect and preheater outputs (temperatures, pressures, flows: condensate, flashed condensate, vapor produced by boiling, flashing, etc) concentration, heat transfer rates and more)
- ▶ Global outputs: Total distillate produced, brine concentration, heat source outlet temperature, etc.

B.1.2 Simulation mode

In this variant, the model is used to simulate the plant behavior, but given fewer inputs compared to the previous variant. It uses pre-trained models for the different parameters (i.e. heat transfer coefficients of the different effects and preheaters, vapor loss). Either empirical correlations from the literature or a data-driven model trained using the outputs from the *calibration mode* evaluated for a long enough experimental campaign can be used.

The model uses models (either pre-trained data-driven models, empirical correlations or physical models) for U_{ef} , U_{ph} , and ΔM_v . Thus, the iterative process to estimate ΔM_v is skipped. Also, during the sequential calculation of cell, the pre-trained models are given the current operating conditions and return the required parameters to solve each effect and preheater.

This mode provides a detailed operation steady state model of an MED plant with minimum assumptions and that does not require outputs of the plant as inputs.

B.2 Implementation

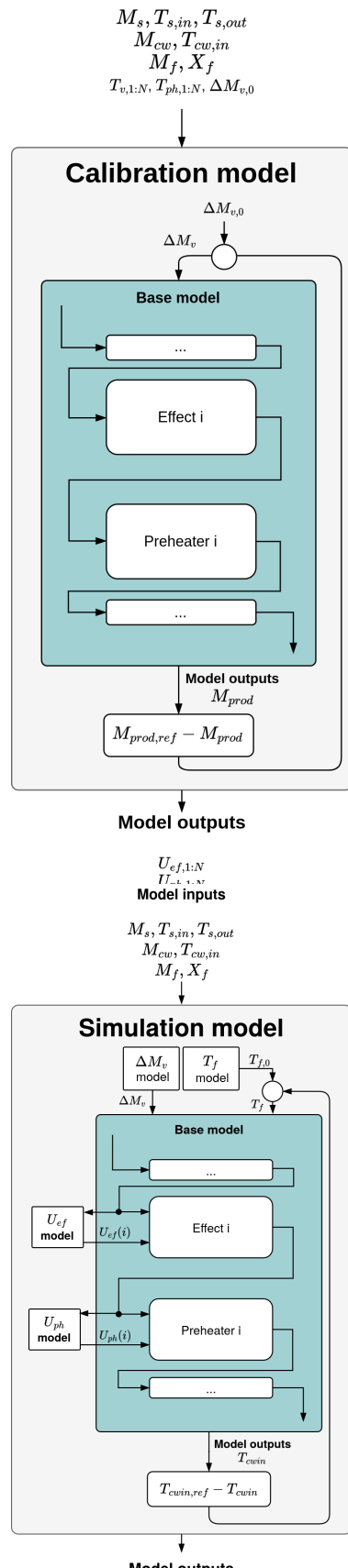


Figure B.3: MED model *simulation mode* diagram with inputs and outputs

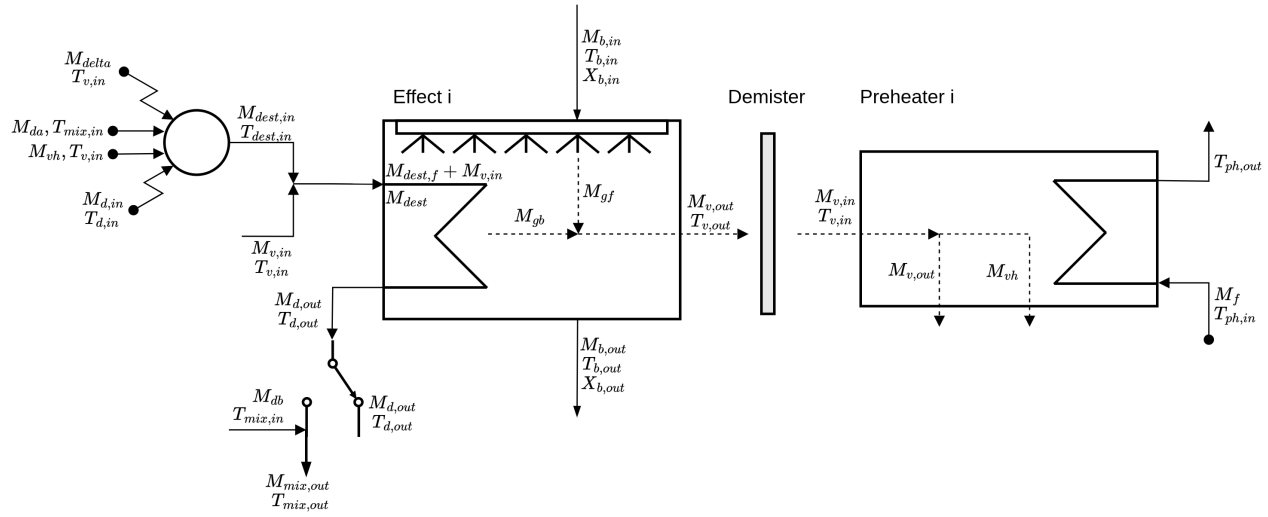


Figure B.4: Detailed schematic of a single cell in the MED containing the effect or evaporator (left) and the preheater (right)

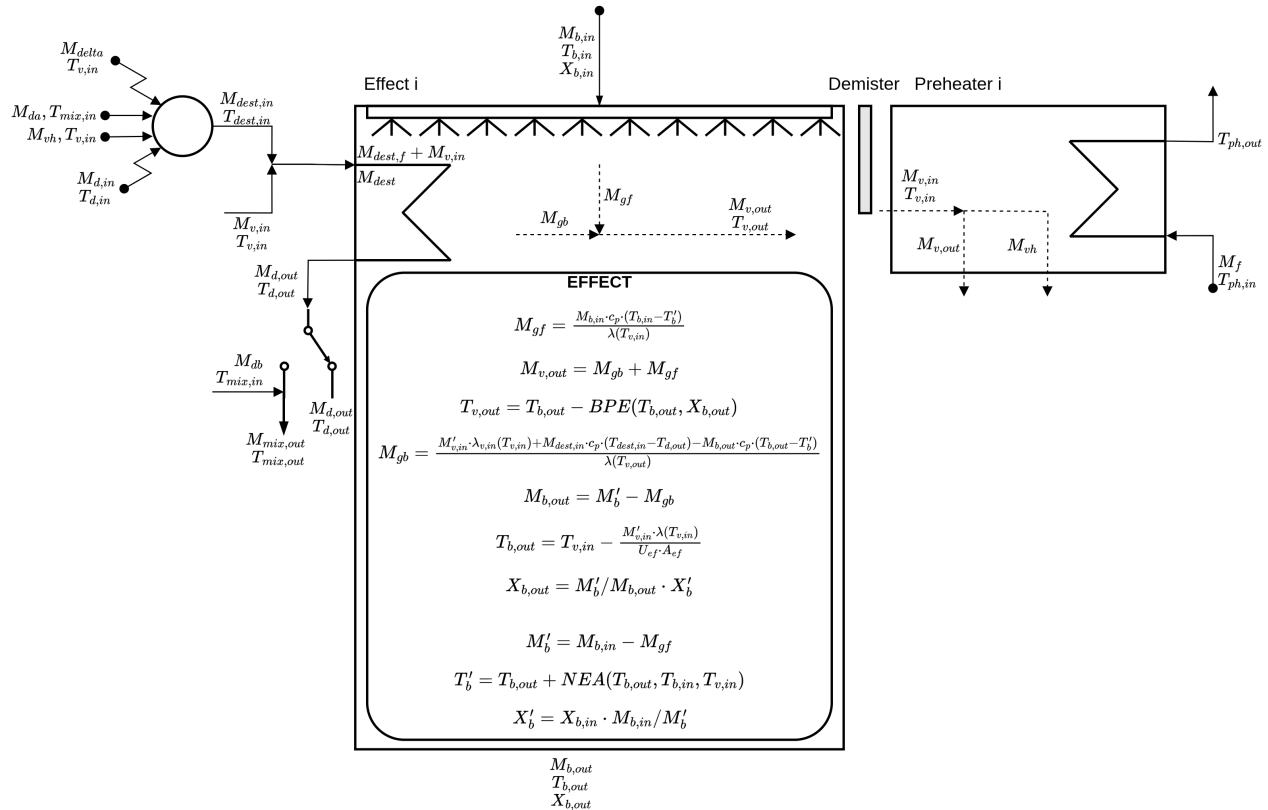


Figure B.5: Detailed schematic of a single cell in the MED with the effect's equations.

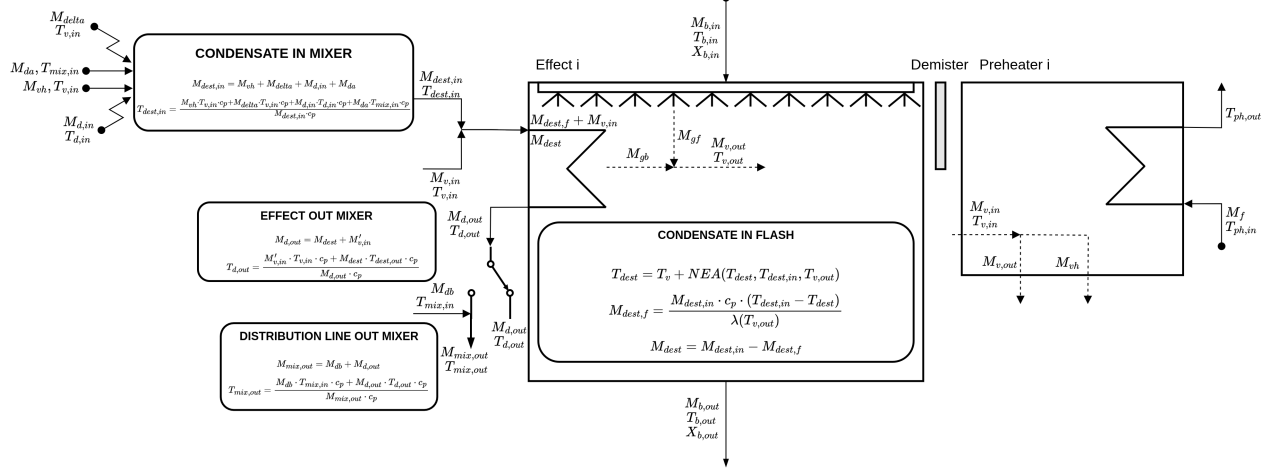


Figure B.6: Detailed schematic of a single cell in the MED with the energy source side equations and internal effect condensate flashing.

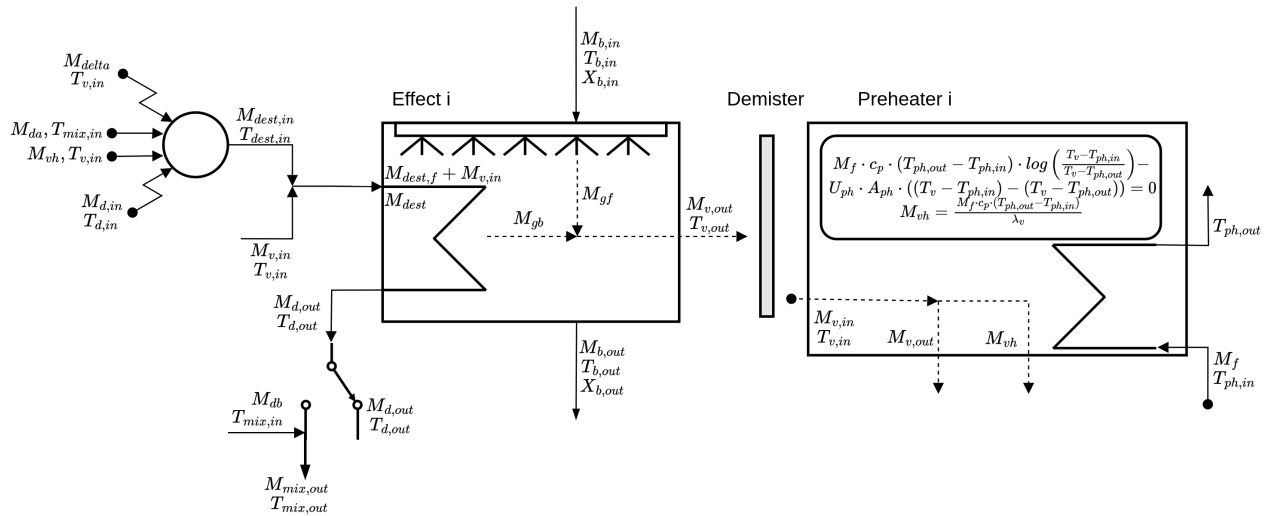


Figure B.7: Detailed schematic of a single cell in the MED with the preheater's equations.

B.3 Validation

[99]: Palenzuela et al. (2016), “Experimental Parametric Analysis of a Solar Pilot-Scale Multi-Effect Distillation Plant”

Using the same dataset presented in Section 6.2.4 (MED) – Palenzuela et al. [99], the *calibration mode* of the model is evaluated, with the results shown in Figure B.10 (a). Then it was divided in training and validation set and the training set was used to generate data-driven models for the different parameters required in the *simulation mode*. The *simulation mode* was then evaluated using the validation set and the results are presented in Figure B.10 (b).

The results demonstrate that both variants of the model can accurately predict the output variables such as the plant’s distillate production. As expected, the calibration model performs better since it uses more detailed inputs, but the simulation model also shows good accuracy. Finally, a comparison of both modes obtained heat transfer coefficients is shown in Figure B.8. They show similar trends except for part of the experimental dataset where higher discrepancies are observed for the latter effects (effects 11–14). This can probably be explained by the fact that the sequential calculation of the model coupled to its high non-linearity means that error is accumulated, where small deviations in the first effects can lead to larger errors in the latter ones. Nonetheless, both models overall provide similar results and trends.

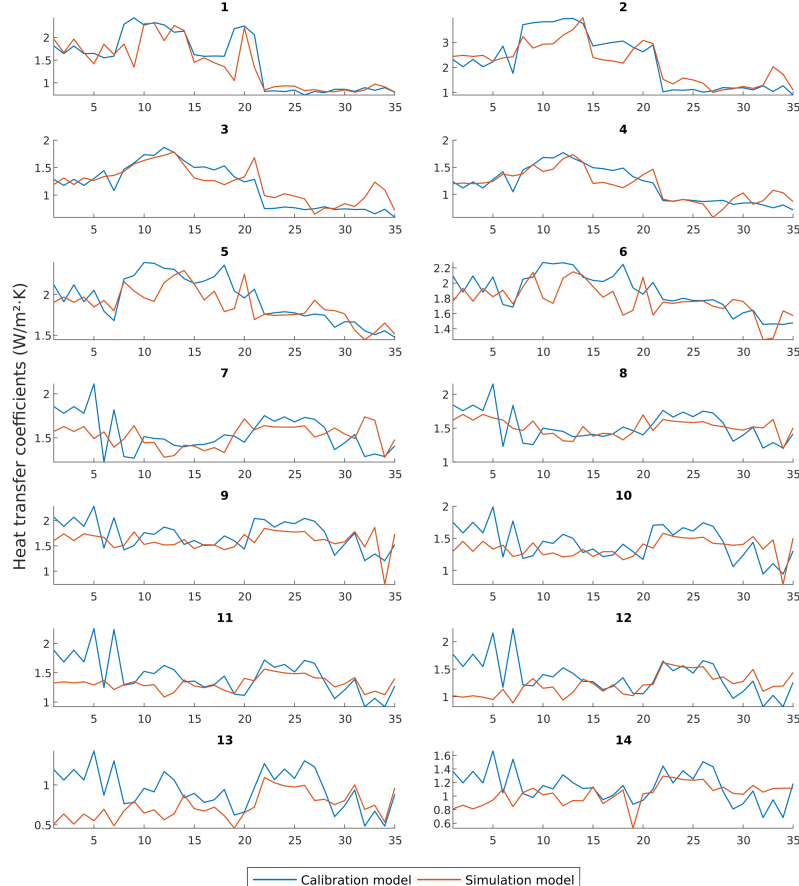


Figure B.8: Heat transfer coefficients comparison between *calibration mode* and *simulation mode* for the validation set

Figure B.11 shows the operation history of the plant (starting from 2009)

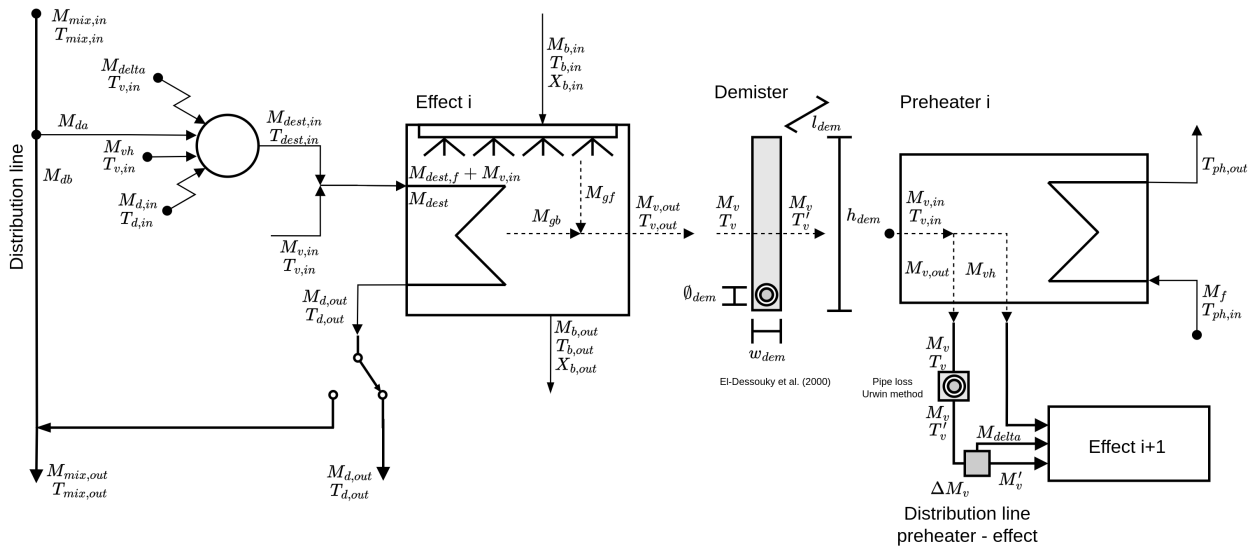
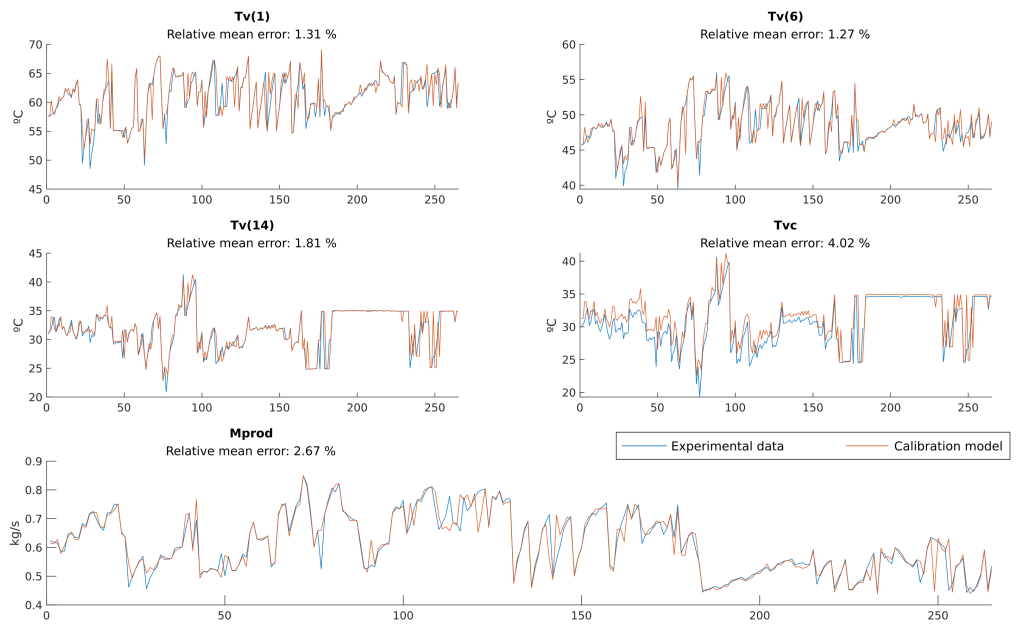
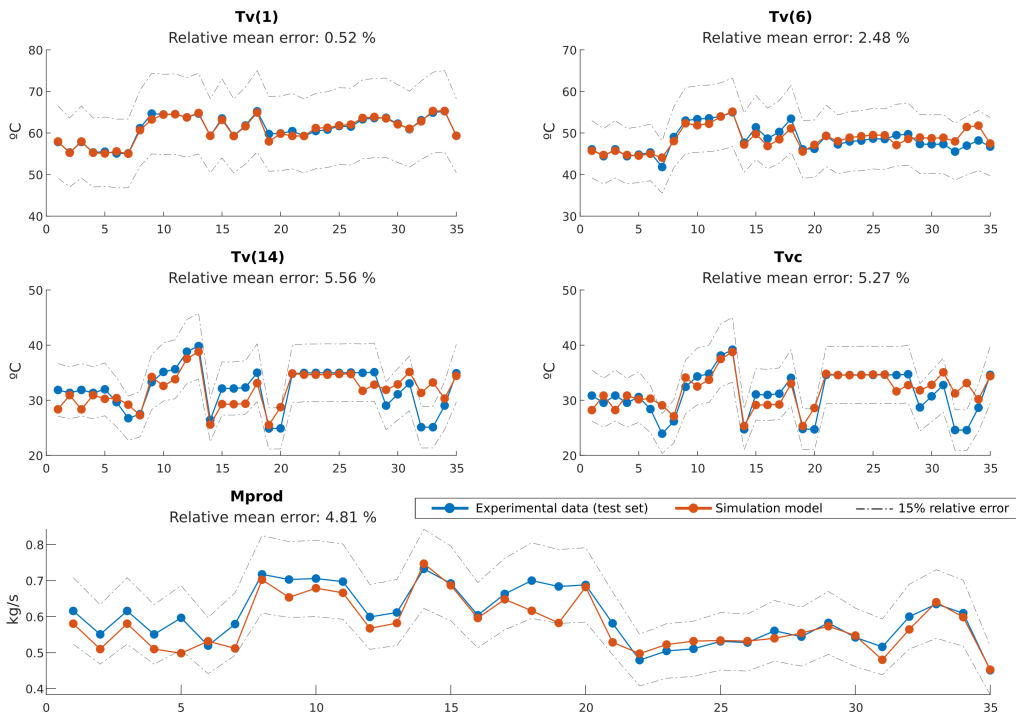


Figure B.9: Detailed schematic of a single cell in the MED with distribution lines for the energy source side and generated steam. Also auxiliary elements like demister and preheater-effect distribution line geometry.



(a) Calibration mode



(b) Simulation mode

Figure B.10: MED first-principles model validation

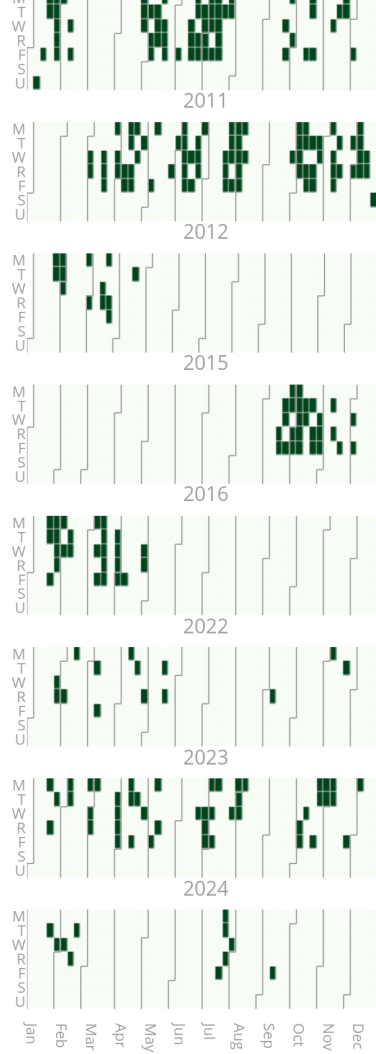


Figure B.11: Operation history of the pilot plant.



Bibliography

Here are the references in citation order.

- [1] Andrew Sayer. *Why We Can't Afford the Rich*. 1st ed. Bristol University Press, 2016. (Visited on 06/27/2024) (cited on page 7).
- [2] José Esquinas Alcázar. *Rumbo al Ecocidio: Cómo frenar la amenaza a nuestra supervivencia*. Barcelona: Espasa, 2023. 256 pp. (cited on page 7).
- [3] World Meteorological Organization. *State of the Global Climate 2024*. Vol. 1368. Geneva: United Nations, 2025 (cited on pages 7, 8).
- [4] IEA. *Global Energy Review 2025*. Paris, Mar. 24, 2025 (cited on page 7).
- [5] Lucas Henneman et al. "Mortality Risk from United States Coal Electricity Generation." In: *Science* 382.6673 (Nov. 24, 2023), pp. 941–946. doi: [10.1126/science.adf4915](https://doi.org/10.1126/science.adf4915). (Visited on 10/14/2025) (cited on page 7).
- [6] Roland Geyer, Jenna R. Jambeck, and Kara Lavender Law. "Production, Use, and Fate of All Plastics Ever Made." In: *Science Advances* 3.7 (July 19, 2017), e1700782. doi: [10.1126/sciadv.1700782](https://doi.org/10.1126/sciadv.1700782). (Visited on 10/14/2025) (cited on page 7).
- [7] Robert McSweeney and Ayesha Tandon. *Mapped. How Climate Change Affects Extreme Weather around the World*. Carbon Brief. Nov. 18, 2024. URL: <https://interactive.carbonbrief.org/attribution-studies/> (visited on 10/14/2025) (cited on pages 7, 9).
- [8] IRENA. *Press Release: World Breaks Renewable Records but Must Move Faster to Hit 2030 Tripling Goal*. Oct. 14, 2025. URL: <https://web.archive.org/web/20251014182847/https://mailchi.mp/79ce55416f16/press-release-world-breaks-renewable-records-but-must-move-faster-to-hit-2030-tripling-goal?e=fdf79ae0c8> (visited on 10/14/2025) (cited on page 7).
- [9] Columbia Law School. *President Trump Prioritizes Fossil Fuel Development and Rolls Back Climate Action in Energy / Sabin Center for Climate Change Law*. Oct. 5, 2025. URL: <https://web.archive.org/web/20251005195227/https://climate.law.columbia.edu/content/president-trump-prioritizes-fossil-fuel-development-and-rolls-back-climate-action-energy> (visited on 10/15/2025) (cited on page 7).
- [10] elDiario.es. *La Confusión Sobre Las Causas Del Apagón Recrudece La Batalla Ideológica Entre Renovables y Nuclear*. 2025. URL: https://web.archive.org/web/20251014183542/https://www.eldiario.es/economia/confusion-causas-apagon-recrudece-batalla-ideologica-renovables-nuclear_1_12258635.html (visited on 10/14/2025) (cited on page 7).
- [11] BARREAU Marie-Sophie Amelie. "The Future of Climate Migration." In: (2025) (cited on page 8).
- [12] Diana Hicks et al. "Bibliometrics. The Leiden Manifesto for Research Metrics." In: *Nature* 520.7548 (Apr. 2015), pp. 429–431. doi: [10.1038/520429a](https://doi.org/10.1038/520429a). (Visited on 05/01/2025) (cited on page 9).
- [13] Mark D. Wilkinson et al. "The FAIR Guiding Principles for Scientific Data Management and Stewardship." In: *Scientific Data* 3.1 (1 Mar. 15, 2016), p. 160018. doi: [10.1038/sdata.2016.18](https://doi.org/10.1038/sdata.2016.18). (Visited on 06/16/2023) (cited on page 9).
- [14] Faisal Asfand et al. "Thermodynamic Performance and Water Consumption of Hybrid Cooling System Configurations for Concentrated Solar Power Plants." In: *Sustainability* 12.11 (2020). doi: [10.3390/su12114739](https://doi.org/10.3390/su12114739) (cited on page 12).
- [15] Ayman Mdallal et al. "Modelling and Optimization of Concentrated Solar Power Using Response Surface Methodology: A Comparative Study of Air, Water, and Hybrid Cooling Techniques." In: *Energy Conversion and Management* 319 (Nov. 1, 2024), p. 118915. doi: [10.1016/j.enconman.2024.118915](https://doi.org/10.1016/j.enconman.2024.118915). (Visited on 06/17/2025) (cited on page 12).
- [16] Hemin Hu et al. "Thermodynamic Characteristics of Thermal Power Plant with Hybrid (Dry/Wet) Cooling System." In: *Energy* 147 (Mar. 15, 2018), pp. 729–741. doi: [10.1016/j.energy.2018.01.074](https://doi.org/10.1016/j.energy.2018.01.074). (Visited on 03/10/2023) (cited on page 12).
- [17] Tao Tang et al. "Study on Operating Characteristics of Power Plant with Dry and Wet Cooling Systems." In: *Energy and Power Engineering* 5.4 (4 June 30, 2013), pp. 651–656. doi: [10.4236/epc.2013.54B126](https://doi.org/10.4236/epc.2013.54B126). (Visited on 06/13/2025) (cited on page 12).

- [18] Wanchai Asvapoositkul and Mantheerapol Kuansathan. "Comparative Evaluation of Hybrid (Dry/Wet) Cooling Tower Performance." In: *Applied Thermal Engineering* 71.1 (Oct. 5, 2014), pp. 83–93. doi: [10.1016/j.applthermaleng.2014.06.023](https://doi.org/10.1016/j.applthermaleng.2014.06.023). (Visited on 03/10/2023) (cited on page 12).
- [19] G. Barigozzi, A. Perdichizzi, and S. Ravelli. "Performance Prediction and Optimization of a Waste-to-Energy Cogeneration Plant with Combined Wet and Dry Cooling System." In: *Applied Energy* 115 (Feb. 15, 2014), pp. 65–74. doi: [10.1016/j.apenergy.2013.11.024](https://doi.org/10.1016/j.apenergy.2013.11.024). (Visited on 03/10/2023) (cited on page 12).
- [20] Lidia Martín and Mariano Martín. "Optimal Year-Round Operation of a Concentrated Solar Energy Plant in the South of Europe." In: *Applied Thermal Engineering* 59.1 (Sept. 25, 2013), pp. 627–633. doi: [10.1016/j.applthermaleng.2013.06.031](https://doi.org/10.1016/j.applthermaleng.2013.06.031). (Visited on 06/13/2025) (cited on page 12).
- [21] Mariano Martín. "Optimal Annual Operation of the Dry Cooling System of a Concentrated Solar Energy Plant in the South of Spain." In: *Energy* 84 (May 1, 2015), pp. 774–782. doi: [10.1016/j.energy.2015.03.041](https://doi.org/10.1016/j.energy.2015.03.041). (Visited on 06/12/2025) (cited on page 12).
- [22] L. E. Wiles et al. *Description and Cost Analysis of a Deluge Dry/Wet Cooling System*. PNL-2498. Battelle Pacific Northwest Labs., Richland, WA (USA), June 1, 1978. doi: [10.2172/6700397](https://doi.org/10.2172/6700397). (Visited on 08/10/2025) (cited on page 12).
- [23] F. R. Zaloudek et al. *Study of the Comparative Costs of Five Wet/Dry Cooling Tower Concepts*. BNWL-2122. Battelle Pacific Northwest Labs., Richland, WA (USA), Sept. 1, 1976. doi: [10.2172/7101320](https://doi.org/10.2172/7101320). (Visited on 08/09/2025) (cited on page 12).
- [24] Shahab Rohani et al. "Optimization of Water Management Plans for CSP Plants through Simulation of Water Consumption and Cost of Treatment Based on Operational Data." In: *Solar Energy* 223 (July 15, 2021), pp. 278–292. doi: [10.1016/j.solener.2021.05.044](https://doi.org/10.1016/j.solener.2021.05.044). (Visited on 06/17/2025) (cited on page 12).
- [25] Chaouki Ghenai et al. "Performance Analysis and Optimization of Hybrid Multi-Effect Distillation Adsorption Desalination System Powered with Solar Thermal Energy for High Salinity Sea Water." In: *Energy* 215 (Jan. 15, 2021), p. 119212. doi: [10.1016/j.energy.2020.119212](https://doi.org/10.1016/j.energy.2020.119212). (Visited on 01/08/2023) (cited on pages 12, 81).
- [26] Hyuk Soo Son et al. "Pilot Studies on Synergetic Impacts of Energy Utilization in Hybrid Desalination System: Multi-effect Distillation and Adsorption Cycle (MED-AD)." In: *Desalination* 477 (Mar. 1, 2020), p. 114266. doi: [10.1016/j.desal.2019.114266](https://doi.org/10.1016/j.desal.2019.114266). (Visited on 01/07/2023) (cited on pages 12, 81).
- [27] Greg Burgess and Keith Lovegrove. "Solar Thermal Powered Desalination: Membrane versus Distillation Technologies." In: (Jan. 2000) (cited on pages 13, 81).
- [28] F. Silva Pinto and R. Cunha Marques. "Desalination Projects Economic Feasibility: A Standardization of Cost Determinants." In: *Renewable and Sustainable Energy Reviews* 78 (Oct. 2017), pp. 904–915. doi: [10.1016/j.rser.2017.05.024](https://doi.org/10.1016/j.rser.2017.05.024). (Visited on 07/27/2023) (cited on pages 13, 81).
- [29] Lidia Roca et al. "Solar Field Control for Desalination Plants." In: *Solar Energy* 82.9 (Sept. 1, 2008), pp. 772–786. doi: [10.1016/j.solener.2008.03.002](https://doi.org/10.1016/j.solener.2008.03.002). (Visited on 09/10/2025) (cited on pages 13, 105).
- [30] Ramón González, Lidia Roca, and Francisco Rodríguez. "Economic Optimal Control Applied to a Solar Seawater Desalination Plant." In: *Computers & Chemical Engineering* 71 (Dec. 4, 2014), pp. 554–562. doi: [10.1016/j.compchemeng.2014.10.005](https://doi.org/10.1016/j.compchemeng.2014.10.005). (Visited on 09/09/2025) (cited on pages 13, 105, 106).
- [31] Jose A. Carballo et al. "Optimal Operating Conditions Analysis for a Multi-Effect Distillation Plant According to Energetic and Exergetic Criteria." In: *Desalination*. Desalination Using Renewable Energy 435 (June 1, 2018), pp. 70–76. doi: [10.1016/j.desal.2017.12.013](https://doi.org/10.1016/j.desal.2017.12.013). (Visited on 06/17/2022) (cited on pages 13, 105).
- [32] Aicha Chorak et al. "Experimental Characterization of a Multi-Effect Distillation System Coupled to a Flat Plate Solar Collector Field: Empirical Correlations." In: *Applied Thermal Engineering* 120 (June 25, 2017), pp. 298–313. doi: [10.1016/j.applthermaleng.2017.03.115](https://doi.org/10.1016/j.applthermaleng.2017.03.115). (Visited on 09/10/2025) (cited on pages 13, 49, 105).
- [33] Juan D. Gil et al. "Hybrid NMPC Applied to a Solar-powered Membrane Distillation System." In: *IFAC-PapersOnLine*. 12th IFAC Symposium on Dynamics and Control of Process Systems, Including Biosystems DYCOPS 2019 52.1 (Jan. 1, 2019), pp. 124–129. doi: [10.1016/j.ifacol.2019.06.048](https://doi.org/10.1016/j.ifacol.2019.06.048). (Visited on 03/18/2024) (cited on pages 13, 106).
- [34] Francesco Biscani and Dario Izzo. "A Parallel Global Multiobjective Framework for Optimization: Pagmo." In: *Journal of Open Source Software* 5.53 (2020), p. 2338. doi: [10.21105/joss.02338](https://doi.org/10.21105/joss.02338) (cited on pages 14, 29–31).
- [35] Caio Felipe Curitiba Marcellos et al. *PyEquilon: A Python Package For Automatic Speciation Calculations of Aqueous Electrolyte Solutions*. May 2021. Pre-published (cited on pages 14, 99, 129).
- [36] John A. Sokolowski and Catherine M. Banks. *Principles of Modeling and Simulation: A Multidisciplinary Approach*. John Wiley & Sons, Sept. 20, 2011. 211 pp. (cited on pages 15, 17).

- [37] Jiri Nossent, Pieter Elsen, and Willy Bauwens. "Sobol'sensitivity Analysis of a Complex Environmental Model." In: *Environmental Modelling & Software* 26.12 (2011), pp. 1515–1525 (cited on pages 16, 22).
- [38] Carl Edward Rasmussen and Christopher K. I. Williams. *Gaussian Processes for Machine Learning*. Adaptive Computation and Machine Learning. Cambridge, Mass: MIT Press, 2006. 248 pp. (cited on pages 18, 19).
- [39] A. Gelman et al. *Bayesian Data Analysis, Third Edition*. Chapman & Hall/CRC Texts in Statistical Science. Taylor & Francis, 2013 (cited on page 19).
- [40] Martin T. Hagan et al. *Neural Network Design*. Martin Hagan, 2014. 800 pp. (cited on pages 19, 20).
- [41] Mark Hudson Beale, Martin T Hagan, and Howard B Demuth. "Neural Network Toolbox." In: *User's Guide, MathWorks* 2 (2010), pp. 77–81 (cited on page 20).
- [42] Lonnie Hamm, B. Wade Brorsen, and Martin T. Hagan. "Comparison of Stochastic Global Optimization Methods to Estimate Neural Network Weights." In: *Neural Processing Letters* 26.3 (Dec. 1, 2007), pp. 145–158. doi: [10.1007/s11063-007-9048-7](https://doi.org/10.1007/s11063-007-9048-7). (Visited on 03/16/2024) (cited on page 20).
- [43] Leo Breiman. "Random Forests." In: *Machine Learning* 45.1 (Oct. 1, 2001), pp. 5–32. doi: [10.1023/A:1010933404324](https://doi.org/10.1023/A:1010933404324). (Visited on 03/13/2024) (cited on page 21).
- [44] Jerome H. Friedman. "Greedy Function Approximation: A Gradient Boosting Machine." In: *The Annals of Statistics* 29.5 (Oct. 2001), pp. 1189–1232. doi: [10.1214/aos/1013203451](https://doi.org/10.1214/aos/1013203451). (Visited on 08/19/2025) (cited on page 21).
- [45] M. D. McKay, R. J. Beckman, and W. J. Conover. "A Comparison of Three Methods for Selecting Values of Input Variables in the Analysis of Output from a Computer Code." In: *Technometrics* 21.2 (1979), pp. 239–245. doi: [10.2307/1268522](https://doi.org/10.2307/1268522). (Visited on 10/13/2025) (cited on page 22).
- [46] Andrea Saltelli, K. Chan, and E. M. Scott. *Sensitivity Analysis: Gauging the Worth of Scientific Models*. John Wiley & Sons, Oct. 3, 2000. 515 pp. (cited on page 22).
- [47] Xiaojun Wang et al. "Structural Design Optimization Based on the Moving Baseline Strategy." In: *Acta Mechanica Solida Sinica* 33.3 (June 1, 2020), pp. 307–326. doi: [10.1007/s10338-019-00144-0](https://doi.org/10.1007/s10338-019-00144-0). (Visited on 08/24/2025) (cited on page 25).
- [48] R. Farmani and J.A. Wright. "Self-Adaptive Fitness Formulation for Constrained Optimization." In: *IEEE Transactions on Evolutionary Computation* 7.5 (Oct. 2003), pp. 445–455. doi: [10.1109/TEVC.2003.817236](https://doi.org/10.1109/TEVC.2003.817236). (Visited on 03/31/2025) (cited on pages 27, 31).
- [49] Kalyanmoy Deb. "Multi-Objective Optimisation Using Evolutionary Algorithms: An Introduction." In: *Multi-Objective Evolutionary Optimisation for Product Design and Manufacturing*. Springer, 2011, pp. 3–34 (cited on page 27).
- [50] Andreas Wächter and Lorenz T. Biegler. "On the Implementation of an Interior-Point Filter Line-Search Algorithm for Large-Scale Nonlinear Programming." In: *Mathematical Programming* 106.1 (Mar. 1, 2006), pp. 25–57. doi: [10.1007/s10107-004-0559-y](https://doi.org/10.1007/s10107-004-0559-y). (Visited on 08/19/2025) (cited on page 28).
- [51] Tamara G. Kolda, Robert Michael Lewis, and Virginia Torczon. "Optimization by Direct Search: New Perspectives on Some Classical and Modern Methods." In: *SIAM Review* 45.3 (2003), pp. 385–482. doi: [10.1137/S003614450242889](https://doi.org/10.1137/S003614450242889) (cited on page 28).
- [52] John H. Holland. *Adaptation in Natural and Artificial Systems: An Introductory Analysis with Applications to Biology, Control, and Artificial Intelligence*. The MIT Press, Apr. 29, 1992. (Visited on 08/19/2025) (cited on pages 28, 29).
- [53] Ingo Rechenberg. "Evolution Strategy: Nature's Way of Optimization." In: *Optimization: Methods and Applications, Possibilities and Limitations*. Ed. by H. W. Bergmann. Berlin, Heidelberg: Springer, 1989, pp. 106–126. doi: [10.1007/978-3-642-83814-9_6](https://doi.org/10.1007/978-3-642-83814-9_6) (cited on pages 28, 29).
- [54] Hans-Paul Schwefel. *Numerical Optimization of Computer Models*. USA: John Wiley & Sons, Inc., May 1981. 398 pp. (cited on pages 28, 29).
- [55] Nikolaus Hansen. "The CMA Evolution Strategy: A Comparing Review." In: *Towards a New Evolutionary Computation: Advances in the Estimation of Distribution Algorithms*. Ed. by Jose A. Lozano et al. Berlin, Heidelberg: Springer, 2006, pp. 75–102. doi: [10.1007/3-540-32494-1_4](https://doi.org/10.1007/3-540-32494-1_4). (Visited on 08/19/2025) (cited on page 29).
- [56] Michel Gendreau and Jean-Yves Potvin, eds. *Handbook of Metaheuristics*. Vol. 146. International Series in Operations Research & Management Science. Boston, MA: Springer US, 2010. (Visited on 01/02/2024) (cited on pages 29, 30).
- [57] Martin Schlüter, Jose A. Egea, and Julio R. Banga. "Extended Ant Colony Optimization for Non-Convex Mixed Integer Nonlinear Programming." In: *Computers & Operations Research* 36.7 (July 1, 2009), pp. 2217–2229. doi: [10.1016/j.cor.2008.08.015](https://doi.org/10.1016/j.cor.2008.08.015). (Visited on 08/19/2025) (cited on page 30).

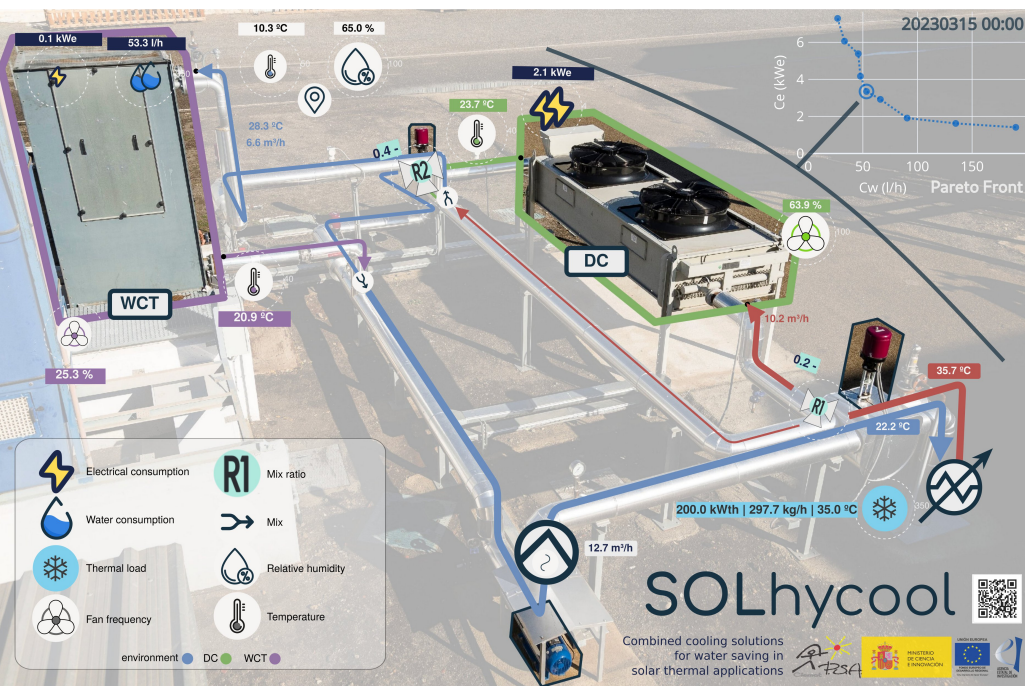
- [58] J. Kennedy and R. Eberhart. "Particle Swarm Optimization." In: *Proceedings of ICNN'95 - International Conference on Neural Networks*. ICNN'95 - International Conference on Neural Networks. Vol. 4. Nov. 1995, 1942–1948 vol.4. doi: [10.1109/ICNN.1995.488968](https://doi.org/10.1109/ICNN.1995.488968). (Visited on 08/19/2025) (cited on page 30).
- [59] Ahmed G. Gad. "Particle Swarm Optimization Algorithm and Its Applications: A Systematic Review." In: *Archives of Computational Methods in Engineering* 29.5 (Aug. 1, 2022), pp. 2531–2561. doi: [10.1007/s11831-021-09694-4](https://doi.org/10.1007/s11831-021-09694-4). (Visited on 08/19/2025) (cited on page 30).
- [60] Rainer Storn and Kenneth Price. "Differential Evolution – A Simple and Efficient Heuristic for Global Optimization over Continuous Spaces." In: *Journal of Global Optimization* 11.4 (Dec. 1, 1997), pp. 341–359. doi: [10.1023/A:1008202821328](https://doi.org/10.1023/A:1008202821328). (Visited on 08/20/2025) (cited on page 30).
- [61] Janez Brest et al. "Self-Adapting Control Parameters in Differential Evolution: A Comparative Study on Numerical Benchmark Problems." In: *IEEE Transactions on Evolutionary Computation* 10.6 (Dec. 2006), pp. 646–657. doi: [10.1109/TEVC.2006.872133](https://doi.org/10.1109/TEVC.2006.872133). (Visited on 08/20/2025) (cited on page 30).
- [62] Saber M. Elsayed, Ruhul A. Sarker, and Daryl L. Essam. "Differential Evolution with Multiple Strategies for Solving CEC2011 Real-World Numerical Optimization Problems." In: *2011 IEEE Congress of Evolutionary Computation (CEC)*. 2011 IEEE Congress on Evolutionary Computation (CEC). New Orleans, LA, USA: IEEE, June 2011, pp. 1041–1048. doi: [10.1109/CEC.2011.5949732](https://doi.org/10.1109/CEC.2011.5949732). (Visited on 08/20/2025) (cited on page 30).
- [63] A. Corana et al. "Minimizing Multimodal Functions of Continuous Variables with the "Simulated Annealing" Algorithm—Corrigenda for This Article Is Available Here." In: *ACM Trans. Math. Softw.* 13.3 (Sept. 1, 1987), pp. 262–280. doi: [10.1145/29380.29864](https://doi.org/10.1145/29380.29864). (Visited on 08/19/2025) (cited on page 30).
- [64] Zong Woo Geem, Joong Hoon Kim, and G.V. Loganathan. "A New Heuristic Optimization Algorithm: Harmony Search." In: *SIMULATION* 76.2 (Feb. 1, 2001), pp. 60–68. doi: [10.1177/003754970107600201](https://doi.org/10.1177/003754970107600201). (Visited on 06/16/2025) (cited on page 30).
- [65] E. F. Camacho and C. Bordons. *Model Predictive Control*. Red. by Michael J. Grimble and Michael A. Johnson. Advanced Textbooks in Control and Signal Processing. London: Springer, 2007. (Visited on 03/12/2024) (cited on page 33).
- [66] Karl J Hägglund and Tore Åström J. *Advanced PID Control*. Research Triangle Park, NC: ISA-The Instrumentation, Systems, and Automation Society, 2006 (cited on page 33).
- [67] Riccardo Scattolini. "Architectures for Distributed and Hierarchical Model Predictive Control – A Review." In: *Journal of Process Control* 19.5 (May 1, 2009), pp. 723–731. doi: [10.1016/j.jprocont.2009.02.003](https://doi.org/10.1016/j.jprocont.2009.02.003). (Visited on 08/21/2025) (cited on pages 34, 35).
- [68] Hanna Pltomykova et al. "The United Nations World Water Development Report 2020: Water and Climate Change." In: (2020) (cited on page 41).
- [69] Edward Jones et al. "The State of Desalination and Brine Production: A Global Outlook." In: *Science of The Total Environment* 657 (Mar. 20, 2019), pp. 1343–1356. doi: [10.1016/j.scitotenv.2018.12.076](https://doi.org/10.1016/j.scitotenv.2018.12.076). (Visited on 06/29/2022) (cited on pages 41, 85).
- [70] Joyner Eke et al. "The Global Status of Desalination: An Assessment of Current Desalination Technologies, Plants and Capacity." In: *Desalination* 495 (Dec. 1, 2020), p. 114633. doi: [10.1016/j.desal.2020.114633](https://doi.org/10.1016/j.desal.2020.114633). (Visited on 01/05/2023) (cited on page 41).
- [71] Samantha Kuzma et al. "Aquaduct 4.0: Updated Decision-Relevant Global Water Risk Indicators." In: (Aug. 16, 2023). (Visited on 08/09/2025) (cited on page 41).
- [72] Mesfin M Mekonnen and Arjen Y Hoekstra. "Four Billion People Facing Severe Water Scarcity." In: *Science advances* 2.2 (2016), e1500323 (cited on page 41).
- [73] Raphael Semiat. "Energy Issues in Desalination Processes." In: *Environmental Science & Technology* 42.22 (Nov. 15, 2008), pp. 8193–8201. doi: [10.1021/es801330u](https://doi.org/10.1021/es801330u). (Visited on 01/08/2023) (cited on page 41).
- [74] Kerry J. Howe et al. *Principles of Water Treatment*. John Wiley & Sons, Oct. 26, 2012. 674 pp. (cited on page 41).
- [75] Nooshin Shekarchi and Farhad Shahnia. "A Comprehensive Review of Solar-Driven Desalination Technologies for off-Grid Greenhouses." In: *International Journal of Energy Research* 43.4 (2019), pp. 1357–1386. doi: [10.1002/er.4268](https://doi.org/10.1002/er.4268). (Visited on 10/17/2024) (cited on page 41).
- [76] A. Alloushi and K. M. Almohammadi. "Towards Green Desalination: A Multi-Site Analysis of Hybrid Renewable Energy Integration in Saudi Arabian RO Plants." In: *Desalination* 592 (Dec. 21, 2024), p. 118087. doi: [10.1016/j.desal.2024.118087](https://doi.org/10.1016/j.desal.2024.118087). (Visited on 10/17/2024) (cited on page 41).

- [77] Sebastian Schär et al. "Optimization of Sustainable Seawater Desalination: Modeling Renewable Energy Integration and Energy Storage Concepts." In: *Energy Conversion and Management* 293 (Oct. 1, 2023), p. 117447. doi: [10.1016/j.enconman.2023.117447](https://doi.org/10.1016/j.enconman.2023.117447). (Visited on 10/17/2024) (cited on pages 41, 122).
- [78] Argyris Panagopoulos. "Study and Evaluation of the Characteristics of Saline Wastewater (Brine) Produced by Desalination and Industrial Plants." In: *Environmental Science and Pollution Research* 29:16 (Apr. 1, 2022), pp. 23736–23749. doi: [10.1007/s11356-021-17694-x](https://doi.org/10.1007/s11356-021-17694-x). (Visited on 10/16/2025) (cited on page 42).
- [79] Argyris Panagopoulos and Katherine-Joanne Haralambous. "Environmental Impacts of Desalination and Brine Treatment - Challenges and Mitigation Measures." In: *Marine Pollution Bulletin* 161 (Dec. 1, 2020), p. 111773. doi: [10.1016/j.marpolbul.2020.111773](https://doi.org/10.1016/j.marpolbul.2020.111773). (Visited on 10/16/2025) (cited on pages 42, 44, 45).
- [80] Pía Hernández et al. "Use of Seawater/Brine and Caliche's Salts as Clean and Environmentally Friendly Sources of Chloride and Nitrate Ions for Chalcopyrite Concentrate Leaching." In: *Minerals* 10:5 (May 2020), p. 477. doi: [10.3390/min10050477](https://doi.org/10.3390/min10050477). (Visited on 10/16/2025) (cited on page 42).
- [81] H. T. El-Dessouky and H. M. Ettouney. *Fundamentals of Salt Water Desalination*. Elsevier, Mar. 20, 2002. 691 pp. (cited on pages 43, 81, 84).
- [82] Bernhard Milow and Eduardo Zarza. "Advanced MED Solar Desalination Plants. Configurations, Costs, Future – Seven Years of Experience at the Plataforma Solar de Almeria (Spain)." In: *Desalination*. Annual Meeting of the European Desalination Society of Desalination Anf the Environment 108:1 (Feb. 1, 1997), pp. 51–58. doi: [10.1016/S0011-9164\(97\)00008-8](https://doi.org/10.1016/S0011-9164(97)00008-8). (Visited on 10/16/2025) (cited on pages 44, 49).
- [83] Diego-César Alarcón-Padilla and Lourdes García-Rodríguez. "Application of Absorption Heat Pumps to Multi-Effect Distillation: A Case Study of Solar Desalination." In: *Desalination* 212:1 (June 25, 2007), pp. 294–302. doi: [10.1016/j.desal.2006.10.014](https://doi.org/10.1016/j.desal.2006.10.014). (Visited on 10/16/2025) (cited on pages 44, 49).
- [84] Andrew T. Bouma, Jaichander Swaminathan, and John H. Lienhard V. "Metrics Matter: Accurately Defining Energy Efficiency in Desalination." In: *Journal of Heat Transfer* 142:12 (Oct. 7, 2020). doi: [10.1115/1.4048250](https://doi.org/10.1115/1.4048250). (Visited on 03/22/2023) (cited on pages 44, 45, 81, 84, 88).
- [85] Guillermo Zaragoza et al. "Coupling of Nanofiltration with Multi-Effect Distillation for Solar-Powered Seawater Desalination towards Brine Mining and Water Production for Agriculture." In: *Nanofiltration 2022 : Principles, Applications and New Materials*. Achalm, Reutlingen, June 26–30, 2022 (cited on pages 45, 83).
- [86] Argyris Panagopoulos. "Process Simulation and Techno-Economic Assessment of a Zero Liquid Discharge/Multi-Effect Desalination/Thermal Vapor Compression (ZLD/MED/TVC) System." In: *International Journal of Energy Research* 44:1 (2020), pp. 473–495. doi: [10.1002/er.4948](https://doi.org/10.1002/er.4948). (Visited on 01/06/2023) (cited on page 45).
- [87] John H. Lienhard et al. "Thermodynamics, Exergy, and Energy Efficiency in Desalination Systems." In: *Lienhard via Angie Locknar* (2017). (Visited on 04/04/2022) (cited on pages 46, 81, 82, 88, 129).
- [88] Gnaneswar Gude. "Emerging Technologies for Sustainable Desalination Handbook." In: (2018) (cited on page 46).
- [89] Patricia Palenzuela, Diego-César Alarcón-Padilla, and Guillermo Zaragoza. *Concentrating Solar Power and Desalination Plants*. Oct. 9, 2015 (cited on pages 46, 51, 83, 85, 89).
- [90] Patricia Palenzuela and Diego C. Alarcón-Padilla. "Concentrating Solar Power and Desalination Plants." In: *Solar Resources Mapping: Fundamentals and Applications*. Ed. by Jesús Polo, Luis Martín-Pomares, and Antonio Sanfilippo. Cham: Springer International Publishing, 2019, pp. 327–340. doi: [10.1007/978-3-319-97484-2_14](https://doi.org/10.1007/978-3-319-97484-2_14). (Visited on 10/16/2025) (cited on page 47).
- [91] Khaled Elsaïd et al. "Recent Progress on the Utilization of Waste Heat for Desalination: A Review." In: *Energy Conversion and Management* 221 (Oct. 1, 2020), p. 113105. doi: [10.1016/j.enconman.2020.113105](https://doi.org/10.1016/j.enconman.2020.113105). (Visited on 10/15/2025) (cited on page 47).
- [92] Sarah Brückner et al. "Industrial Waste Heat Recovery Technologies: An Economic Analysis of Heat Transformation Technologies." In: *Applied Energy* 151 (Aug. 1, 2015), pp. 157–167. doi: [10.1016/j.apenergy.2015.01.147](https://doi.org/10.1016/j.apenergy.2015.01.147). (Visited on 01/07/2023) (cited on page 47).
- [93] Alexander Christ, Klaus Regenauer-Lieb, and Hui Tong Chua. "Boosted Multi-Effect Distillation for Sensible Low-Grade Heat Sources: A Comparison with Feed Pre-Heating Multi-Effect Distillation." In: *Desalination*. Energy and Desalination 366 (June 15, 2015), pp. 32–46. doi: [10.1016/j.desal.2014.12.047](https://doi.org/10.1016/j.desal.2014.12.047). (Visited on 01/04/2023) (cited on pages 47, 84).
- [94] A. Gregorzewski et al. "The Solar Thermal Desalination Research Project at the Plataforma Solar de Almeria." In: *Desalination* 82:1–3 (1991), pp. 142–144 (cited on page 49).

- [95] Julián Blanco et al. "The AQUASOL System: Solar Collector Field Efficiency and Solar-Only Mode Performance." In: *Journal of Solar Energy Engineering* 133.011009 (Jan. 28, 2011). doi: [10.1115/1.4003291](https://doi.org/10.1115/1.4003291). (Visited on 10/20/2025) (cited on page 49).
- [96] Gary Ampuño et al. "Modeling and Simulation of a Solar Field Based on Flat-Plate Collectors." In: *Solar Energy* 170 (Aug. 1, 2018), pp. 369–378. doi: [10.1016/j.solener.2018.05.076](https://doi.org/10.1016/j.solener.2018.05.076). (Visited on 03/17/2023) (cited on pages 49, 56, 59).
- [97] Lidia Roca et al. "Modelo de parámetros concentrados para captadores solares planos con reflectores." In: *Jornadas de Automática* 45 (45 July 19, 2024). doi: [10.17979/ja-cea.2024.45.10930](https://doi.org/10.17979/ja-cea.2024.45.10930). (Visited on 08/25/2024) (cited on page 50).
- [98] John A. Duffie and William A. Beckman. "Energy Storage." In: *Solar Engineering of Thermal Processes*. John Wiley & Sons, Ltd, 2013, pp. 373–408. doi: [10.1002/9781118671603.ch8](https://doi.org/10.1002/9781118671603.ch8). (Visited on 07/15/2025) (cited on pages 50, 60).
- [99] Patricia Palenzuela, Diego C. Alarcón-Padilla, and Guillermo Zaragoza. "Experimental Parametric Analysis of a Solar Pilot-Scale Multi-Effect Distillation Plant." In: *Desalination and Water Treatment* 57:48–49 (Oct. 2016), pp. 23097–23109. doi: [10.1080/19443994.2016.1180481](https://doi.org/10.1080/19443994.2016.1180481). (Visited on 09/01/2025) (cited on pages 51, 136).
- [100] Gary Ampuño et al. "Apparent Delay Analysis for a Flat-Plate Solar Field Model Designed for Control Purposes." In: *Solar Energy* 177 (Jan. 1, 2019), pp. 241–254. doi: [10.1016/j.solener.2018.11.014](https://doi.org/10.1016/j.solener.2018.11.014). (Visited on 03/15/2023) (cited on page 56).
- [101] Julio E. Normey-Rico et al. "A Robust Adaptive Dead-Time Compensator with Application to A Solar Collector Field1." In: *IFAC Proceedings Volumes*. IFAC Workshop on Linear Time Delay Systems (LTDS '98), Grenoble, France, 6-7 July 31.19 (July 1, 1998), pp. 93–98. doi: [10.1016/S1474-6670\(17\)41134-7](https://doi.org/10.1016/S1474-6670(17)41134-7). (Visited on 02/19/2024) (cited on page 56).
- [102] Yunus A. Çengel and Afshin J. Ghajar. *Heat and Mass Transfer: Fundamentals & Applications*. Fifth edition. New York, NY: McGraw Hill Education, 2015. 968 pp. (cited on page 64).
- [103] William Morrow Kays and Alexander Louis London. *Compact Heat Exchangers: A Summary of Basic Heat Transfer and Flow Friction Design Data*. McGraw-Hill, 1958. 180 pp. (cited on page 64).
- [104] GPy. *GPy: A Gaussian Process Framework in Python*. URL: <http://github.com/SheffieldML/GPy> (cited on page 69).
- [105] Karan H. Mistry et al. "Entropy Generation Analysis of Desalination Technologies." In: *Entropy. An International and Interdisciplinary Journal of Entropy and Information Studies* 13.10 (2011), pp. 1829–1864. doi: [10.3390/e13101829](https://doi.org/10.3390/e13101829) (cited on pages 81, 129).
- [106] A. Christ, K. Regenauer-Lieb, and H.T. Chua. "Thermodynamic Optimisation of Multi Effect Distillation Driven by Sensible Heat Sources." In: *Desalination* 336.1 (2014), pp. 160–167. doi: [10.1016/j.desal.2013.12.006](https://doi.org/10.1016/j.desal.2013.12.006) (cited on pages 81, 84).
- [107] M. A. Darwish, Faisal Al-Juwayhel, and Hassan K. Abdulraheim. "Multi-Effect Boiling Systems from an Energy Viewpoint." In: *Desalination* 194.1 (June 10, 2006), pp. 22–39. doi: [10.1016/j.desal.2005.08.029](https://doi.org/10.1016/j.desal.2005.08.029). (Visited on 06/01/2022) (cited on pages 82, 88).
- [108] Muhammad Wakil Shahzad, Muhammad Burhan, and Kim Choom Ng. "A Standard Primary Energy Approach for Comparing Desalination Processes." In: *npj Clean Water* 2.1 (Jan. 7, 2019), pp. 1–7. doi: [10.1038/s41545-018-0028-4](https://doi.org/10.1038/s41545-018-0028-4). (Visited on 07/23/2024) (cited on page 82).
- [109] Dorianio Brogioli, Fabio La Mantia, and Ngai Yin Yip. "Thermodynamic Analysis and Energy Efficiency of Thermal Desalination Processes." In: *Desalination* 428 (Feb. 15, 2018), pp. 29–39. doi: [10.1016/j.desal.2017.11.010](https://doi.org/10.1016/j.desal.2017.11.010). (Visited on 01/05/2023) (cited on pages 82, 83).
- [110] K.S. Spiegler and Y.M. El-Sayed. "The Energetics of Desalination Processes." In: *Desalination* 134 (Apr. 1, 2001), pp. 109–128. doi: [10.1016/S0011-9164\(01\)00121-7](https://doi.org/10.1016/S0011-9164(01)00121-7) (cited on pages 82, 129).
- [111] Mostafa H. Sharqawy, John H. Lienhard V, and Syed M. Zubair. "On Exergy Calculations of Seawater with Applications in Desalination Systems." In: *International Journal of Thermal Sciences* 50.2 (Feb. 1, 2011), pp. 187–196. doi: [10.1016/j.ijthermalsci.2010.09.013](https://doi.org/10.1016/j.ijthermalsci.2010.09.013). (Visited on 03/22/2023) (cited on pages 82, 88, 129).
- [112] Mostafa H. Sharqawy, Syed M. Zubair, and John H. Lienhard. "Formulation of Seawater Flow Exergy Using Accurate Thermodynamic Data." In: *Prof. Lienhard via Angie Locknar* (Nov. 2010). (Visited on 04/13/2023) (cited on page 82).
- [113] Karan H. Mistry and John H. Lienhard V. "Effect of Nonideal Solution Behavior on Desalination of a Sodium Chloride (NaCl) Solution and Comparison to Seawater." In: *Karan Mistry* (Nov. 2012). (Visited on 04/22/2023) (cited on page 82).

- [114] Karan H. Mistry and John H. Lienhard. "Generalized Least Energy of Separation for Desalination and Other Chemical Separation Processes." In: *Entropy. An International and Interdisciplinary Journal of Entropy and Information Studies* 15.6 (2013), pp. 2046–2080. doi: [10.3390/e15062046](https://doi.org/10.3390/e15062046) (cited on page 82).
- [115] Gregory P. Thiel et al. "Energy Consumption in Desalinating Produced Water from Shale Oil and Gas Extraction." In: *Desalination. Energy and Desalination* 366 (June 15, 2015), pp. 94–112. doi: [10.1016/j.desal.2014.12.038](https://doi.org/10.1016/j.desal.2014.12.038). (Visited on 03/06/2023) (cited on pages 82, 86, 89, 129).
- [116] Loreto Valenzuela, Rafael López-Martín, and Eduardo Zarza. "Optical and Thermal Performance of Large-Size Parabolic-Trough Solar Collectors from Outdoor Experiments: A Test Method and a Case Study." In: *Energy* 70 (June 1, 2014), pp. 456–464. doi: [10.1016/j.energy.2014.04.016](https://doi.org/10.1016/j.energy.2014.04.016). (Visited on 07/17/2024) (cited on page 82).
- [117] Christoph Prahl, Christoph Happich, and Jesús Fernández. *Protocol for Characterization of Complete Solar Concentrators Using Photogrammetry or Deflectometry*. WP14 – Task 14.2. DLR, Feb. 2018 (cited on page 82).
- [118] Rocío Bayón and Esther Rojas. "Development of a New Methodology for Validating Thermal Storage Media: Application to Phase Change Materials." In: *International Journal of Energy Research* 43.12 (2019), pp. 6521–6541. doi: [10.1002/er.4589](https://doi.org/10.1002/er.4589). (Visited on 07/17/2024) (cited on page 82).
- [119] Karan H. Mistry, Mohamed A. Antar, and John H. Lienhard V. "An Improved Model for Multiple Effect Distillation." In: *Desalination and Water Treatment* 51.4–6 (Jan. 1, 2013), pp. 807–821. doi: [10.1080/19443994.2012.703383](https://doi.org/10.1080/19443994.2012.703383). (Visited on 06/01/2022) (cited on pages 83, 131).
- [120] Heike Glade et al. "Scale Formation of Mixed Salts in Multiple-Effect Distillers." In: *IDA Journal of Desalination and Water Reuse* 2.1 (Jan. 1, 2010), pp. 38–44. doi: [10.1179/ida.2010.2.1.38](https://doi.org/10.1179/ida.2010.2.1.38). (Visited on 06/16/2023) (cited on page 83).
- [121] Kerstin Krömer et al. "Scale Formation and Mitigation of Mixed Salts in Horizontal Tube Falling Film Evaporators for Seawater Desalination." In: *Heat Transfer Engineering* 36.7–8 (May 3, 2015), pp. 750–762. doi: [10.1080/01457632.2015.954961](https://doi.org/10.1080/01457632.2015.954961). (Visited on 07/10/2023) (cited on page 83).
- [122] John W Ryznar. "A New Index for Determining Amount of Calcium Carbonate Scale Formed by a Water." In: *Journal-American Water Works Association* 36.4 (1944), pp. 472–483 (cited on pages 83, 84).
- [123] Andrea Schafer and Anthony Fane. *Nanofiltration: Principles, Applications, and New Materials*. John Wiley \& Sons. 2021 (cited on page 83).
- [124] Karan H. Mistry and John H. Lienhard. "An Economics-Based Second Law Efficiency." In: *Entropy* 15.7 (7 July 2013), pp. 2736–2765. doi: [10.3390/e15072736](https://doi.org/10.3390/e15072736). (Visited on 03/22/2023) (cited on page 84).
- [125] Alexander Christ et al. "Techno-Economic Analysis of Geothermal Desalination Using Hot Sedimentary Aquifers: A Pre-Feasibility Study for Western Australia." In: *Desalination* 404 (Feb. 17, 2017), pp. 167–181. doi: [10.1016/j.desal.2016.11.009](https://doi.org/10.1016/j.desal.2016.11.009). (Visited on 01/05/2023) (cited on page 84).
- [126] Alexander Christ, Klaus Regenauer-Lieb, and Hui Tong Chua. "Application of the Boosted MED Process for Low-Grade Heat Sources – A Pilot Plant." In: *Desalination. Energy and Desalination* 366 (June 15, 2015), pp. 47–58. doi: [10.1016/j.desal.2014.10.032](https://doi.org/10.1016/j.desal.2014.10.032). (Visited on 01/04/2023) (cited on page 84).
- [127] John H. Lienhard V et al. "SOLAR DESALINATION." In: *Annual Review of Heat Transfer* 15 (2012). doi: [10.1615/AnnualRevHeatTransfer.2012004659](https://doi.org/10.1615/AnnualRevHeatTransfer.2012004659). (Visited on 10/17/2024) (cited on page 86).
- [128] Qian Chen et al. "A Zero Liquid Discharge System Integrating Multi-Effect Distillation and Evaporative Crystallization for Desalination Brine Treatment." In: *Desalination* 502 (Apr. 2021), p. 114928. doi: [10.1016/J.DESAL.2020.114928](https://doi.org/10.1016/J.DESAL.2020.114928) (cited on page 87).
- [129] Adrian Bejan. *Advanced Engineering Thermodynamics*. John Wiley & Sons, 2016 (cited on page 88).
- [130] BIPM. *JCGM 100:2008. GUM 1995 with Minor Corrections. Evaluation of Measurement Data – Guide to the Expression of Uncertainty in Measurement*. Joint Committee for Guides in Metrology, 2008. URL: https://www.bipm.org/documents/20126/2071204/JCGM_101_2008_E.pdf/325dcaad-c15a-407c-1105-8b7f322d651c (cited on page 92).
- [131] Ralph C. Smith. *Uncertainty Quantification: Theory, Implementation, and Applications*. SIAM, Dec. 2, 2013. 400 pp. (cited on page 92).
- [132] NIST. "NIST Guidelines for Evaluating and Expressing the Uncertainty of NIST Measurement Results Cover." In: *NIST* (). (Visited on 06/16/2023) (cited on page 92).
- [133] BIPM. *JCGM101:2008. Evaluation of Measurement Data – Supplement 1 to the "Guide to the Expression of Uncertainty in Measurement" – Propagation of Distributions Using a Monte Carlo Method*. Joint Committee for Guides in Metrology, 2008. URL: https://www.bipm.org/documents/20126/2071204/JCGM_101_2008_E.pdf/325dcaad-c15a-407c-1105-8b7f322d651c (cited on page 92).

- [134] Ulli Wolff. "Monte Carlo Errors with Less Errors." In: *Computer Physics Communications* 176.5 (Mar. 2007), p. 383. doi: [10.1016/j.cpc.2006.12.001](https://doi.org/10.1016/j.cpc.2006.12.001). (Visited on 06/19/2023) (cited on page 92).
- [135] Milan Korbel et al. "Steady State Identification for On-Line Data Reconciliation Based on Wavelet Transform and Filtering." In: *Computers & Chemical Engineering* 63 (Apr. 17, 2014), pp. 206–218. doi: [10.1016/j.compchemeng.2014.02.003](https://doi.org/10.1016/j.compchemeng.2014.02.003). (Visited on 12/14/2022) (cited on page 93).
- [136] Taiwen Jiang et al. "Application of Steady-State Detection Method Based on Wavelet Transform." In: *Computers & Chemical Engineering* 27.4 (Apr. 15, 2003), pp. 569–578. doi: [10.1016/S0098-1354\(02\)00235-1](https://doi.org/10.1016/S0098-1354(02)00235-1). (Visited on 01/03/2023) (cited on page 93).
- [137] Taiwen Jiang, Bingzhen Chen, and Xiaorong He. "Industrial Application of Wavelet Transform to the On-Line Prediction of Side Draw Qualities of Crude Unit." In: *Computers & Chemical Engineering* 24.2 (July 15, 2000), pp. 507–512. doi: [10.1016/S0098-1354\(00\)00520-2](https://doi.org/10.1016/S0098-1354(00)00520-2). (Visited on 12/27/2022) (cited on page 93).
- [138] Karl Johan Åström and Tore Hägglund. *PID Controllers: Theory, Design, and Tuning*. ISA - The Instrumentation, Systems and Automation Society, 1995 (cited on page 94).
- [139] John H. Lienhard V. "Energy Savings in Desalination Technologies: Reducing Entropy Generation by Transport Processes." In: *Journal of Heat Transfer* 141.7 (May 17, 2019). doi: [10.1115/1.4043571](https://doi.org/10.1115/1.4043571). (Visited on 03/30/2023) (cited on page 103).
- [140] R. Porrazzo et al. "A Neural Network-Based Optimizing Control System for a Seawater-Desalination Solar-Powered Membrane Distillation Unit." In: *Computers & Chemical Engineering* 54 (July 11, 2013), pp. 79–96. doi: [10.1016/j.compchemeng.2013.03.015](https://doi.org/10.1016/j.compchemeng.2013.03.015). (Visited on 09/09/2025) (cited on page 106).
- [141] Ignacio E. Grossmann. *Advanced Optimization for Process Systems Engineering*. Cambridge Series in Chemical Engineering. Cambridge: Cambridge University Press, 2021 (cited on page 109).
- [142] Rob J. Hyndman and George Athanasopoulos. *Forecasting: Principles and Practice*. 3rd ed. OTexts, 2021 (cited on pages 110, 111).
- [143] Kenneth S. Pitzer. "Thermodynamics of Electrolytes. I. Theoretical Basis and General Equations." In: *The Journal of Physical Chemistry* 77.2 (Jan. 1, 1973), pp. 268–277. doi: [10.1021/j100621a026](https://doi.org/10.1021/j100621a026). (Visited on 11/13/2023) (cited on page 128).
- [144] M. H. Sharqawy, J. H. Lienhard, and S. M. Zubair. "Thermophysical Properties of Seawater: A Review of Existing Correlations and Data." In: *Desalination and Water Treatment* 16.1–3 (Apr. 2010), pp. 354–380. doi: [10.5004/dwt.2010.1](https://doi.org/10.5004/dwt.2010.1) (cited on page 128).
- [145] Kishor G. Nayar et al. "Thermophysical Properties of Seawater: A Review and New Correlations That Include Pressure Dependence." In: *Desalination* 390 (July 15, 2016), pp. 1–24. doi: [10.1016/j.desal.2016.02.024](https://doi.org/10.1016/j.desal.2016.02.024). (Visited on 04/25/2023) (cited on page 128).
- [146] Simão P. Pinho and Eugénia A. Macedo. "Solubility of NaCl, NaBr, and KCl in Water, Methanol, Ethanol, and Their Mixed Solvents." In: *Journal of Chemical & Engineering Data* 50.1 (Jan. 1, 2005), pp. 29–32. doi: [10.1021/je049922y](https://doi.org/10.1021/je049922y). (Visited on 04/26/2023) (cited on page 129).
- [147] Patricia Palenzuela et al. "Steady State Model for Multi-Effect Distillation Case Study: Plataforma Solar de Almería MED Pilot Plant." In: *Desalination* 337 (Mar. 1, 2014), pp. 31–42. doi: [10.1016/j.desal.2013.12.029](https://doi.org/10.1016/j.desal.2013.12.029) (cited on page 131).
- [148] Hisham El-Dessouky et al. "Steady-State Analysis of the Multiple Effect Evaporation Desalination Process." In: *Chemical Engineering & Technology* 21.5 (1998), pp. 437–451. doi: [10.1002/\(SICI\)1521-4125\(199805\)21:5<437::AID-CEAT437>3.0.CO;2-D](https://doi.org/10.1002/(SICI)1521-4125(199805)21:5<437::AID-CEAT437>3.0.CO;2-D). (Visited on 06/01/2022) (cited on page 131).



Esta investigación abarca dos estudios complementarios sobre dos recursos intrínsecamente vinculados: el agua y la energía. La primera parte se centra en la gestión eficiente de los recursos hídricos para la generación eléctrica en una planta de energía solar concentrada, mientras que la segunda explora el uso eficiente de la energía solar para la producción de agua limpia en un proceso de destilación multi-efecto alimentado con energía solar térmica.

This research encompasses two complementary studies on two intrinsically linked resources: water and energy. The first part focuses on the efficient management of water resources for power generation in Concentrated Solar Power plants, while the second explores the efficient use of solar energy for clean water production in a solar-driven multi-effect distillation plant.